

Electrically Reconfigurable Optical Metasurfaces for Universal Wavefront Shaping

Thesis by
Prachi Thureja

In Partial Fulfillment of the Requirements for the
Degree of
Doctor of Philosophy

The logo for the California Institute of Technology (Caltech), featuring the word "Caltech" in a bold, orange, sans-serif font.

CALIFORNIA INSTITUTE OF TECHNOLOGY
Pasadena, California

2025
Defended February 19, 2025

© 2025

Prachi Thureja

ORCID: 0000-0003-3852-3395

All rights reserved

ACKNOWLEDGEMENTS

Completing this thesis has been a truly rewarding experience, and I am deeply grateful to those who have walked this path with me. I would not be here if it were not for their unwavering support, insightful advice, inspiration, and mentorship at every step in my journey.

First and foremost, I would like to express my deepest gratitude to my advisor, Prof. Harry A. Atwater, whose guidance and unwavering support have been instrumental from the very beginning of my PhD. His encouragement to embrace every opportunity has not only shaped my academic trajectory but also has led me to some of the most meaningful experiences and friendships over the past five years. I am profoundly thankful for his belief in me and for his steadfast support through every challenge. His leadership, marked with passion and positivity, has granted me the freedom to pursue my intellectual curiosities, explore new avenues of research, and evolve into the researcher I am today. His enthusiasm for science has been a constant source of motivation, and I aspire to carry forward the lessons I have learned from him and share them with future generations, as he has done so generously with me.

I would also like to extend my sincere thanks to my PhD thesis committee members for their time, expertise, and valuable insights at various stages of my PhD. I am grateful to Prof. Andrei Faraon for his support and for instilling in me the importance of critical thinking. I appreciate Prof. Kerry Vahala's guidance, especially in experimental work related to high-frequency and high-power metasurfaces. To Prof. Albert Polman, I am deeply thankful for his encouragement and unwavering support of my work since our first meeting at the Nanophotonics Gordon Conference in 2022. I am also grateful to Prof. Axel Scherer for serving on my candidacy committee and providing valuable inputs on metasurface fabrication.

I am incredibly fortunate to have worked alongside brilliant colleagues and teammates who played pivotal roles in the projects that shaped this thesis. To Dr. Ghazaleh Kafaie Shirmanesh, thank you for introducing me to the field of active metasurfaces and for your invaluable guidance during the early stages of my research. To Dr. Katherine T. Fountaine, I truly appreciate your insights on optimization methods and the thoughtful advice you shared about navigating career paths beyond graduate school. To Dr. Ruzan Sokhoyan, your guidance on the

theoretical aspects of active metasurfaces has been instrumental, and I am grateful for your mentorship during my formative years as a PhD student.

To Jared Sisler, my lab partner over multiple years, thank you for tackling challenges side by side and for the support and motivation we provided one another through all of it. To Dr. Meir Y. Grajower, thank you for teaching me to become a resilient researcher. To Dr. Michael D. Kelzenberg, for his incredible support and mentorship, especially during the development of electrical control units. To Ivy Huang, my summer undergraduate research fellow, thank you for allowing me to grow as a mentor.

To Andrew W. Nyholm, thank you for being not only a fantastic teammate but also a wonderful friend. I have truly enjoyed learning about spalling from you and will always treasure our adventures both in and outside of the lab. To Dr. Phillip R. Jahelka, your enthusiasm and wisdom have been an incredible inspiration to me, and I am grateful for your constant support in the lab. To Dr. Martin Thomaschewski, thank you for introducing me to electro-optic measurements and for your openness to new ideas as we navigated complex research topics together. To Julie Belleville, thank you for your dedication as a co-worker — I have no doubt that you will continue to excel as you take on some of the projects discussed in this thesis. To Samuel K. W. Seah, I sincerely appreciate the insights you shared on thin-film transfer techniques. And to Prof. Claudio U. Hail, thank you for your unwavering support and guidance, both in and outside of the lab.

I would also like to acknowledge Dr. Yury Tokpanov, Morgan Foley, Dr. Yonghwi Kim, Dr. Komron Shayegan, and Dr. Souvik Biswas for numerous thoughtful discussions and insights they provided throughout various stages of my PhD.

I am deeply grateful to my collaborators and research mentors outside of Caltech — Dr. Abhijit Biswas, Dr. Joseph M. Kovalik, Dr. William T. Roberts, Dr. Zhimin Shi, Dr. Renate Landig, Dr. Ramón Paniagua-Dominguez, Prof. Arseniy Kuznetsov, Prof. Mark L. Brongersma, Prof. Min Seok Jang, Jiwon Kang, Soh Uenoyama, and Dr. Junghyun Park — for enriching my research experience with their invaluable expertise and guidance.

The experimental work I conducted during my PhD would not have been possible without the exceptional dedication and trainings provided from the Kavli Nanoscience Institute (KNI) at Caltech. I am deeply grateful to both current and past staff members — Dr. Guy A. DeRose, Alex Wertheim, Bert Mendoza,

Dr. Annalena Wolff, Alireza Ghaffari, Kelly McKenzie, Nathan S. Lee, Tiffany Kimoto, Jennifer Palmer, and Sydney Garstang — for their invaluable support and for creating a truly special community of dedicated scientists that foster exceptional research.

While my scientific network has been integral to my academic journey, I could not have made it here without the amazing friends I have had the privilege to meet at Caltech. To Dr. Rebecca Glaudell, thank you for being by my side from day one. To Dr. Lucía B. De Rose, I am grateful for your guidance and for all our adventures around Los Angeles. To Scott Habermehl, thank you for sitting through hours of homework with me and for always being there — whether over early morning coffee or late-night ice cream. To Bilgehan Baspinar and Ian M. Foo, I appreciate your support, patience, and willingness to let me drag you on all sorts of LA adventures. To Nimisha Ramprasad, my ultimate hype girl, thank you for always lifting me up, no matter the day. To Ellis Spickermann, thank you for being an amazing adventure buddy and for always checking in on me. To Kyle Hunady, your friendship kept me grounded while wrapping up my thesis, reminding me to slow down and embrace the moment. To Elsie Loukiatchenko, for your trust and belief in me. To Rachel Tham, our foodie adventures will always be among my favorite memories. To Dr. Lucy Li, you are an amazing travel buddy and I will always look back fondly on our adventures in Hawaii. To Ramon Gao, your constant support and encouragement have meant so much to me. To Dr. Marianne Aellen, I will always cherish our mid-afternoon coffee chats and the fun moments we shared organizing the first A-Team Winter School together. To Dr. Megan E. Phelan, Dr. Cora Wyent, Dr. Hamidreza Akbari, and Prof. Wen-Hui (Sophia) Cheng, I am grateful for your friendship, support, and advice throughout different stages of my PhD. You provided just the right mix of wisdom, laughter, and encouragement when I needed it most. Finally, to the entire Atwater Research Group, thank you for being such an incredible group of people to work with. I have so many fond memories with all of you, and I will carry them with me as I step into my next adventure.

I also wish to extend my thanks to the Caltech administrative staff for their tireless efforts and for keeping us motivated throughout our journeys as PhD students. In particular, I would like to thank Thomasine V. Murphy, Jennifer N. Blankenship, Christine E. Jenstad, Angie Riley, Jonathan P. Gross, and Kamaljit Flower for their hard work, dedication, and care.

Beyond academics, Caltech has fostered a truly special community, and I am thankful for the people who brightened my days with their kindness — whether through a warm smile, a simple check-in, or a coffee prepared with extra love. Their everyday gestures made a huge difference.

One of the most fulfilling aspects of my PhD journey has been being part of two remarkable communities. First, I would like to acknowledge Womxn in EAS (Engineering and Applied Sciences) at Caltech for their unwavering support, inspiration, and the beautiful friendships that have grown over the years. I am especially thankful to Dr. Heather L. Lukas, Dr. Jacqueline R. Tawney, and Prof. Xueyue (Sherry) Zhang for their friendship and for being such a source of inspiration to me. I would also like to thank the younger generation of Womxn in EAS members for carrying our efforts forward. To Yazmin Gonzalez, thank you for your guidance and mentorship not only to the organization but to me personally — it truly meant the world.

Second, I am incredibly grateful for the friendships I formed through organizing the 2024 Gordon Research Seminar on Plasmonics & Nanophotonics. It has been a truly rewarding experience to help cultivate a passionate community of researchers and I deeply cherish the meaningful connections built along the way.

To my mentors from my time at ETH Zurich — Prof. Lisa V. Poulikakos, Prof. David J. Norris, and Dr. Eva De Leo — thank you for your invaluable guidance, support, and encouragement. You have played an essential role in my academic trajectory and I am grateful for the foundations and self-confidence you have instilled in me.

To my childhood friends — Ranjini Chithambaram and Jessica Theodore, to my ETH friends — Dr. Alexander C. Hernandez Oendra, Manuel Brändli, Annina Eichenberger, Noah Rothenberger, to the friends I have met through conferences — Prof. Eileen Otte, Sahitya Singh, Sedigheh K. Esfahani, Enrico Maria Renzi, Federico De Luca, and the entire New York family, thank you for the laughter, the adventures, and all the incredible memories.

Lastly, to my family — Mom, Dad, and my brother, Dr. Deepankur Thureja — thank you for believing in me when I doubted myself, for supporting my dreams and endeavors, for being patient through all the ups and downs, and for being my ultimate pillars of strength. Your infinite love and encouragement have been the foundation of my journey, and this achievement is as much yours as it is mine. Thank you for everything. You mean the world to me.

ABSTRACT

The ability to control the properties of light in a compact, reconfigurable platform is essential for advancing nanophotonic technologies. Active metasurfaces — flat optical components with tunable subwavelength elements — enable real-time manipulation of wavefronts and thus offer a path toward versatile optical systems. This thesis furthers the development of electrically programmable metasurfaces as a step toward a universal platform for independent and comprehensive wavefront control. By integrating system-level optimization strategies, novel operation modes, and advanced material platforms, we establish a framework for next-generation, on-demand optical processing components.

First, we introduce an array-level inverse design approach for beam steering metasurfaces, that co-optimizes the spatial amplitude and phase responses to enhance target functionalities. Using the platform of a plasmonic, indium tin oxide (ITO)-based active metasurfaces, we demonstrate non-intuitive configurations that achieve high-directivity, continuous-angle beam steering up to 70° . Experimental validation confirms the effectiveness of this approach, which we further extend to advanced applications including flat-top beams, tunable beam widths, and multi-beam steering.

To expand the functional channel capacity of active metasurfaces, we then explore space-time modulation as a means of enabling multi-frequency operation. By modulating ITO-based metasurfaces operating at near-infrared wavelengths with tailored waveforms at frequencies up to 10 MHz, we experimentally generate desired frequency harmonics, which appear as sidebands offset from the incident laser frequency. Introducing phase offsets between the driving waveforms enables tunable diffraction of frequency-shifted light. Theoretical extensions of this work highlight the potential of space-time metasurfaces to realize active multitasking components capable of dynamically performing multiple independent functions.

For improved efficiency and broadband operation, we investigate electro-optically tunable metasurfaces based on the Pockels effect in barium titanate (BTO). We develop a scalable fabrication technique to obtain high-quality, thin-film BTO via stress-induced exfoliation from single-crystal substrates, preserving its bulk electro-optic properties. The experimentally measured Pockels coefficient r_{33} exceeds that of commercially available thin-film lithium niobate, demonstrating the potential of

this material platform for integration into high-speed, low-loss optical metasurfaces. Leveraging these properties, we design transmissive BTO-based metasurfaces for high efficiency beam steering at visible wavelengths.

The results presented in this thesis lay the foundation for next-generation programmable metasurfaces by addressing key challenges in materials, design methodologies, and system-level control architectures. We conclude with a discussion of future directions, including the discovery of high-performance tunable materials, the development of advanced unit cell designs for independent control over multiple optical properties, and the miniaturization of control networks for large-scale metasurfaces. Ultimately, this work advances the development of reconfigurable and intelligent optical systems capable of adapting to diverse technological demands in a broad range of imaging, communication, and computing applications.

PUBLISHED CONTENT AND CONTRIBUTIONS

1. **Thureja**, P., Nyholm, A. W., Thomaschewski, M., Jahelka, P. R., Belleville, J. & Atwater, H. A. Spalled barium titanate single crystal thin films for functional device applications. *arXiv:2505.04045 [physics.app-ph]*. <https://doi.org/10.48550/arXiv.2505.04045> (2025).

P.T. participated in the conception of the original idea, performed spalls and thin film characterization, developed the thin film transfer technique, prepared samples for electro-optic testing and performed the corresponding measurements, and wrote the manuscript.

2. Kuznetsov*, A. I., Brongersma*, M. L., Yao, J., Chen, M. K., Levy, U., Tsai, D. P., Zheludev, N. I., Faraon, A., Arbabi, A., Yu, N., Chanda, D., Crozier, K. B., Kildishev, A. V., Wang, H., Yang, J. K. W., Valentine, J. G., Genevet, P., Fan, J. A., Miller, O. D., Majumdar, A., Fröch, J. E., Brady, D., Heide, F., Veeraraghavan, A., Engheta, N., Alù, A., Polman, A., Atwater, H. A., **Thureja**, P., Paniagua-Dominguez, R., Ha, S. T., Barreda, A. I., Schuller, J. A., Staude, I., Grinblat, G., Kivshar, Y., Peana, S., Yelin, S. F., Senichev, A., Shalaev, V. M., Saha, S., Boltasseva, A., Rho, J., Oh, D. K., Kim, J., Park, J., Devlin, R. & Pala, R. A. Roadmap for optical metasurfaces. *ACS Photonics* **11**, 816–865. ISSN: 2330-4022. <https://doi.org/10.1021/acsp Photonics.3c00457> (2024).

P.T. contributed to the writing of the manuscript.

3. Sisler*, J., **Thureja***, P., Grajower, M. Y., Sokhoyan, R., Huang, I. & Atwater, H. A. Electrically tunable space-time metasurfaces at optical frequencies. *Nature Nanotechnology*. <https://doi.org/10.1038/s41565-024-01728-9> (2024).

P.T. conceived the idea for this project, fabricated and characterized the active metasurfaces, performed quasi-static and time-modulated measurements, provided inputs for the real-time waveform optimization algorithm, designed the electrical PCB, and contributed to writing the manuscript.

4. **Thureja**, P., Sokhoyan, R., Hail, C. U., Sisler, J., Foley, M., Grajower, M. Y. & Atwater, H. A. Toward a universal metasurface for optical imaging, communication, and computation. *Nanophotonics* **11**, 3745–3768. ISSN: 2192-8614. <https://doi.org/10.1515/nanoph-2022-0155> (2022).

P.T. conceived the original idea, organized the content and wrote the manuscript.

5. **Thureja***, P., Shirmanesh*, G. K., Fountaine, K. T., Sokhoyan, R., Grajower, M. & Atwater, H. A. Array-level inverse design of beam steering active metasurfaces. *ACS Nano* **14**, 15042–15055. ISSN: 1936-086X. <https://doi.org/10.1021/acsnano.0c05026> (2020).

P.T. conceived the original idea, analyzed forward design methods, designed the iterative genetic optimization, performed several optimization studies, analyzed the experimental results, and wrote the manuscript.

TABLE OF CONTENTS

Acknowledgements	iii
Abstract	vii
Published Content and Contributions	ix
Table of Contents	x
List of Illustrations	xiii
List of Tables	xvi
Chapter I: Introduction	1
1.1 Optical wavefront engineering: Micro- and nanoscale platforms	1
1.2 Active metasurfaces	5
1.3 Goals of this thesis	7
Chapter II: Array-level inverse design of active metasurfaces for optimized spatial wavefronts	10
2.1 Beam steering with optical metasurfaces	10
2.2 Forward design of ideal antenna arrays	12
2.3 Nonideal active metasurfaces: Forward and array-level inverse design	15
2.4 Impact of phase and amplitude modulation	23
2.5 Experimental demonstration of array-level inverse design	27
2.6 Beam steering arrays with phase disorder	33
2.7 Realizing advanced metasurface functionalities	36
2.8 Outlook	41
2.9 Conclusions	43
Chapter III: Active multitasking metasurfaces using space-time modulation	45
3.1 Space- and time-varying media	46
3.2 Design principle for space-time metasurfaces	47
3.3 Time-modulated optical metasurfaces	50
3.4 Space-time modulation: Diffraction of frequency-shifted beam	55
3.5 Tunable diffraction of frequency-shifted beams	56
3.6 Active multitasking: Multi-frequency multi-beam steering	65
3.7 Outlook	68
3.8 Conclusions	71
Chapter IV: High-efficiency electro-optic metasurfaces using barium titanate	73
4.1 Electro-optic tuning based on Pockels effect	74
4.2 Barium titanate thin films	77
4.3 Electro-optic characterization	86
4.4 Design strategy for maximal electro-optic index change	97
4.5 Active transmissive metasurfaces: Unit cell design	103
4.6 Beam steering at red wavelengths	110
4.7 Extension to RGB wavelengths	114
4.8 Outlook	117

4.9 Conclusions	119
Chapter V: Toward universal active metasurfaces for optical imaging, communication and computation	122
5.1 Universal active metasurfaces	122
5.2 Metasurface design and promising material platforms	123
5.3 Two-dimensional metasurface control	131
5.4 Applications of universal active metasurfaces	137
5.5 Outlook and conclusions	143
Chapter VI: Conclusions	150
Appendix A: Array-level inverse design	153
A.1 Iterative genetic optimization	153
A.2 Metasurface fabrication	158
A.3 Experimental setup for phase and amplitude measurements	158
A.4 Analytical model accounting for experimental artifacts	160
Appendix B: Space-time modulated metasurfaces	162
B.1 Active metasurface phase measurements	162
B.2 Waveform optimization based on quasi-static metasurface response	162
Appendix C: Barium titanate-based active metasurfaces	165
C.1 XRD scans for bulk substrates and spalled film	165
C.2 Reusability of single-crystal BTO substrates through repolishing	165
C.3 Surface quality of (100) and (001)-oriented bulk substrates	166
Bibliography	169

LIST OF ILLUSTRATIONS

<i>Number</i>	<i>Page</i>
1.1 Schematic representation of optical phased array (OPA) for two-dimensional beam steering	2
1.2 Active metasurface modulation platforms	6
1.3 Quasi-static and time-modulated metasurfaces	7
2.1 Beam steering with ideal antenna array	14
2.2 Beam steering with nonideal plasmonic field-effect tunable metasurface.	17
2.3 Comparison of far-field radiation patterns obtained through full-wave simulations and analytical array factor calculations	19
2.4 Beam steering of nonideal active metasurface with array-level inverse design.	22
2.5 Optimized beam steering with reduced phase modulation	24
2.6 Impact of phase and amplitude modulation on beam steering performance	26
2.7 Array-level inverse design of amplitude-modulated array with Lorentzian modulation	28
2.8 Full wave simulations of experimentally realized metasurface	28
2.9 Experimentally realized metasurface and gate-tunable optical response	29
2.10 Forward-designed and optimized array profiles for experimental demonstration	31
2.11 Comparison of far-field radiation patterns with array-factor calculations and FDTD simulations	31
2.12 Experimental demonstration of beam steering with forward and array-level inverse design	32
2.13 Reduction in phase shift over consecutive measurements	34
2.14 Phase noise introduction in spatial phase profile.	35
2.15 Optimization for power efficiency	37
2.16 Variable FWHM of steered beam with ideal metasurface	39
2.17 Flat top beam with nonideal active metasurface	40
2.18 Simultaneous steering of two beams at independent angles	41
3.1 Momentum and frequency shift with space- and time-modulation	49

3.2	Calculated frequency spectrum of time-modulated metasurface with limited phase modulation	50
3.3	ITO-based plasmonic metasurface and tunable reflectance response .	52
3.4	Experimental setup for time-modulated metasurface operation and measurements	53
3.5	Tunable frequency spectra based on applied waveform	54
3.6	Tailored frequency spectrum using optimized waveform	55
3.7	Diffraction of a single harmonic with two-electrode metasurface . . .	57
3.8	Plasmonic ITO-based metasurface with 32 independently addressable electrodes	58
3.9	High-frequency PCB for control of 32-electrode metasurface	61
3.10	Experimentally measured bandwidth of metasurface and high-frequency PCB	62
3.11	Quasi-static beam switching and steering with 32-electrode metasurface	63
3.12	Tunable space-time diffraction with varying repetition numbers . . .	65
3.13	Spatial intensity profiles at harmonic frequencies	66
3.14	Harmonic frequency control with phase and amplitude modulation . .	69
4.1	Spalled barium titanate thin films	80
4.2	Control over thickness of c - and a -axis spalled BTO films	83
4.3	Correlation of thickness and roughness in spalled BTO films	85
4.4	Transfer of spalled film onto substrate.	86
4.5	Dispersion of electro-optic coefficient as function of modulation frequency	88
4.6	Electro-optic measurement of bulk BTO	91
4.7	Electro-optic measurement of spalled BTO thin film	93
4.8	BTO crystal orientation and resonator layout	99
4.9	Pockels coefficient and index change for a -axis BTO after principal axis transformation	101
4.10	Rotation of index ellipsoid and index change for c -axis BTO after principal axis transformation	103
4.11	Unit cell design of active transmissive metasurface based on BTO . .	106
4.12	Electric field distribution $ E_{xz} $ in metasurface unit cell for varying index changes	107
4.13	Electrostatic simulations of BTO metasurface unit cell	109
4.14	Angular dispersion of resonant mode	111
4.15	Beam steering at red wavelengths in transmission	112

4.16	Unit cell performance and beam steering at red, green, and blue wavelengths	115
4.17	BTO-based RGB modulator array	118
5.1	Universal active metasurface.	123
5.2	Promising material platforms for universal active metasurface	128
5.3	Two-dimensional metasurface control architectures	134
5.4	Multicasting and multiplexing schemes with space-time metasurfaces	141
A.1	Flowchart of iterative genetic optimization	154
A.2	Average computation time as function of optimization variables . . .	156
A.3	Robustness of optimization algorithm	157
A.4	Optical setup for amplitude, phase and beam steering measurements .	159
A.5	Comparison of simulated and experimentally measured optical response of ITO metasurface	160
A.6	Predicted and measured far-field radiation patterns with adapted model	161
B.1	Quasi-static phase shift of two-electrode active metasurface	163
B.2	Polynomial waveform optimization based on quasi-static response . .	164
C.1	XRD data for (001)-oriented bulk substrate and spalled thin film . . .	166
C.2	AFM scans of BTO substrate as-bought vs polished after spalling . .	167
C.3	Single crystal BTO substrates with domains	168

LIST OF TABLES

<i>Number</i>	<i>Page</i>
2.1 Analytically computed <i>vs</i> experimentally measured directivity D . . .	32
2.2 Optimized directivity D and efficiency η for steering at $\theta_r = 18.3^\circ$. .	37
4.1 Refractive index change Δn for experimentally reported values of electro-optic coefficients for various thin films.	76
4.2 Refractive index and electro-optic coefficient r_{42} for BTO synthesized using various techniques.	78
4.3 Pockels coefficients for bulk BTO in the unclamped and clamped case.	87
4.4 Transmission efficiency and angle of diffracted orders	113
4.5 Dimensions for metasurface unit cell at red, green, and blue wavelengths	114
4.6 Transmission efficiency and angle of diffracted orders for red, green, and blue wavelengths	116
5.1 Summary of experimentally demonstrated values for different mod- ulation mechanisms.	148
5.2 Challenges toward row-column tuning for various modulation mech- anisms relying on an electrical stimulus.	149

Chapter 1

INTRODUCTION

1.1 Optical wavefront engineering: Micro- and nanoscale platforms

The first reported optical lens, dating back to the Ancient Egyptian era (2620 BC), employed convex polished rock crystals to form the eyes of ornate statues [1]. The unique function of these lenses enabled the eyes to appear to track the viewer's movement around the statue [2]. Ever since, scientists have dedicated efforts to comprehend and manipulate the properties of light, leading to a variety of advanced technologies that are now integral to society. Notable examples include the invention of the telescope, enabling distant objects to be observed as if they were nearby, and the development of the first photographic camera, capable of capturing the visual information from a scene. In these constructs, optical wavefronts are controlled using bulky optical elements which have a thickness of several millimeters. However, with significant advances in micro- and nanofabrication in recent decades, researchers are now pioneering the development of next-generation micro- and nanoscale optical components. These components allow for precise manipulation of optical wavefronts, giving rise to versatile and unprecedented control over light. In the following, we provide an overview of three micro- and nanoscale technologies that have recently emerged as promising pathways for optical wavefront engineering: optical phased arrays (OPAs), spatial light modulators (SLMs), and (active) metasurfaces.

Optical phased arrays

Optical phased arrays (OPAs) function as the optical analog of radio-wave-based phased arrays and were first realized in the early 1970s [3]. In an OPA, a light source is divided into an array of individual optical emitters, typically facilitated by waveguides connected to antennas. The integration of independently addressable phase shifters enables precise manipulation of the emitted phase at each individual element, enabling applications such as dynamic beam steering. The primary methods employed for implementing phase shifters in OPAs include utilizing thermo-optic effects [4, 5] or p-i-n junctions [6]. Thermo-optic phase shifters offer minimal loss, but typically rely on higher power consumptions and operate at lower speeds. By contrast, p-i-n junctions induce phase delays through refractive index change

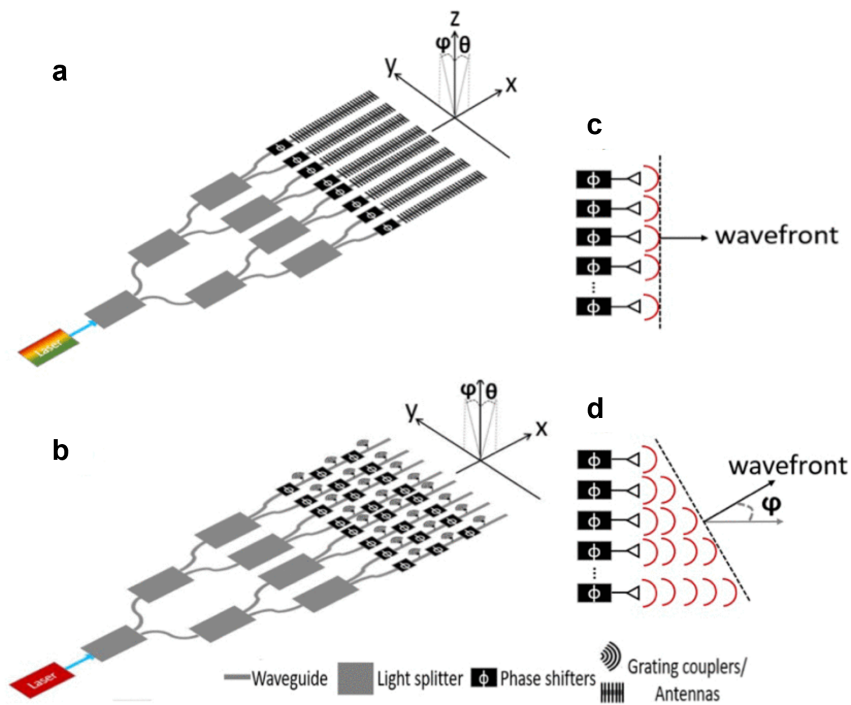


Figure 1.1: **Schematic representation of optical phased array (OPA) for two-dimensional beam steering.** (a) One-dimensional OPA with laser wavelength tuning for steering along longitudinal direction, (b) two-dimensional grating coupler array. (c) Emitted wavefront with no phase delay between emitters and (d) incremental phase delay for steering along transversal direction. © 2021 IEEE [8]

via dopants. Although electro-optic p-i-n phase shifters provide higher modulation frequencies (up to 200 MHz [7]) and lower power consumption compared to their thermo-optic counterparts, dopants typically introduce waveguide losses [8].

The performance and application scope of OPAs further depend on the type of antennas they employ. Typically, antennas in OPAs are constructed using either grating couplers or edge and end fire couplers [9, 10]. Edge emitters are primarily employed for one-dimensional beam steering, while two-dimensional steering has been achieved using grating couplers. One common strategy for achieving two-dimensional beam steering using this platform involves a one-dimensional array of grating couplers, where steering in the longitudinal direction, θ , is accomplished through laser wavelength tuning and steering along the transversal direction, ϕ , is achieved using phase shifters (Fig. 1.1a) [4]. In this configuration, researchers have demonstrated pixel sizes as small as $0.8 \mu\text{m}$ [11]. Alternatively, a two-dimensional array of individually addressable grating couplers can be employed (Fig. 1.1b) [5]. However, the spatial arrangement of waveguides in arrays typically necessitates

large inter-antenna spacings to prevent crosstalk between adjacent emitters. This spacing requirement is further compounded by the need for two-dimensional phase shifter arrays, leading to larger pixel sizes of up to $9\ \mu\text{m}$ [5] that ultimately limit the grating lobe-free steering range. Notably, researchers have demonstrated beam steering with large field of view (FOV) using non-uniform antenna arrangements in sparse arrays [12, 13]. Nonetheless, considerable amounts of background noise are reported in the measured far-field radiation patterns.

In summary, given the operation principle of OPAs, they excel primarily in beam steering and other applications reliant on spatial manipulation of the optical phase front, as schematically illustrated in Fig. 1.1c and d. However, their utility in controlling the properties of an electromagnetic wave beyond amplitude and phase is limited.

Spatial light modulators

Spatial light modulators (SLMs) enable precise control over the amplitude, phase, and polarization of optical wavefronts in response to electrical or optical stimuli [14]. Unlike OPAs, which comprise individual emitters within each unit cell, SLMs function by modulating light transmitted or reflected through a medium, with an individual unit cell, or *pixel*, defined by the control architecture employed in its implementation.

Among the diverse range of SLMs realized to date, the predominant platforms used in the commercial landscape are based on microelectromechanical systems (MEMS) [15] or liquid crystals [16]. MEMS-based SLMs, exemplified by digital micromirror devices (DMDs), utilize miniaturized mirrors that can be tilted to selectively reflect light, and therefore alter the scattered light amplitude. An individual pixel in this configuration is defined by the size of a micromirror and typically ranges around $10\ \mu\text{m}$ or larger [17]. Operating frequencies in such DMDs can reach several tens of kHz [14].

On the other hand, Liquid Crystal on Silicon (LCoS) technology offers smaller pixel sizes and thus precise phase mapping over a larger FOV. In LCoS SLMs, a liquid crystal cell containing electrodes controls the orientation of the naturally birefringent liquid crystal molecules, thus altering the refractive index of the medium. Typical pixel sizes in this configuration range between $3 - 4\ \mu\text{m}$ [18]. Further reduction in pixel size is limited by crosstalk resulting from the high driving voltages required to modulate a thick liquid crystal cell necessary for full phase control [19]. However,

recent advances in nanophotonic device design and microfabrication have allowed a reduction of the pixel size to $\sim 1 \mu\text{m}$ by modulating phase *via* resonance tuning rather than accumulation across the layer thickness [20]. While this advancement significantly enhances FOV capabilities, the pixel size remains a limiting factor for achieving diffraction-free steering within the visible spectrum. Furthermore, the limited response time of liquid crystal-based SLMs, ranging from hundreds of microseconds to milliseconds, hinders their application in high-frequency beam manipulation [21].

Metasurfaces

Metasurfaces represent a cutting-edge approach to optical manipulation utilizing two-dimensional (2D) arrays of resonant scatterers, typically on the nanoscale. These scatterers have the ability to locally and abruptly alter various properties of light impinging on an interface [22], including its amplitude, phase, polarization, spectrum, and momentum. The collective response from an array of scatterers results in constructive far-field effects that lead to a variety of phenomena like anomalous reflection [23], polarization control [24], or beam focusing [25]. Due to the subwavelength scale of each metasurface unit cell, metasurfaces enable higher diffraction angles and numerical apertures compared to conventional diffractive optical elements [21] and provide a promising alternative to optical phased arrays and spatial light modulators.

Metasurfaces have garnered significant interest from industries that greatly benefit from the availability of miniaturized and efficient optical components, which can easily be integrated in optoelectronic systems at low cost. Initial efforts focused on passive metasurfaces, where individual scatterers are geometrically designed to induce desired local changes in the electric field (*e.g.*, a phase offset) at the operating wavelength [22, 26–28]. Using this approach, researchers have demonstrated multifunctional passive metasurfaces capable of performing several tasks simultaneously [29], which would traditionally require a combination of multiple bulk optical components.

However, a fundamental limitation of passive metasurfaces is their static nature, lacking post-fabrication tunability. This restriction confines their use to specific, pre-defined functions. In contrast, many modern applications in the realms of optical imaging, communication, and computation require dynamically tunable components for on-demand wavefront shaping. This demand has led to the development of active

metasurfaces that can be reconfigured at frequencies up to several GHz, depending on the choice of the material platform. The subsequent section provides a summary of the current state-of-the-art on active metasurfaces.

1.2 Active metasurfaces

Active metasurfaces, in contrast to their passive counterparts, consist of an array of geometrically periodic, often identical, unit cells. Dynamic control over the optical response of the metasurface is obtained through application of an external stimulus. This external stimulus can modify the resonant properties of the subwavelength scatterers *via* actively inducing a refractive index change in an active material layer integrated into the metasurface. Alternatively, the application of an external stimulus can alter the metasurface unit cell dimensions or the relative position of individual scatterers, thereby enabling dynamic control of the wavefront of light reflected or transmitted from the array.

To date, active tuning of metasurfaces has leveraged mechanical deformation of nanophotonic structures [37, 38], field-effect tuning [30, 39], electro-optic [31], thermo-optic [32], electrochemical [33] and chemical effects [40], structural changes in phase change materials [34, 41] and liquid crystals [35], as well as all-optical modulation schemes [36] (Fig. 1.2). Moreover, recent experimental demonstrations have showcased multifunctional active metasurfaces capable of switching between multiple continuously tunable functions. The basis for such devices lies in implementing an active metasurface with individually addressable unit cells. Using this concept, Kafaie Shirmanesh *et al.* [42] demonstrated switching between diverse optically tunable functions, such as dynamic beam steering and varifocal lensing, by adjusting the spatial configuration of voltages applied to a single field-effect tunable metasurface. By using specifically tailored metasurface designs and varying the external stimulus applied onto each metasurface unit cell, researchers have further managed to dynamically generate desired changes in the amplitude, phase, and polarization of the scattered electric field.

The timescale of active reconfiguration of a metasurface is an important characteristic that determines its mode of operation. When the temporal rate of reconfiguration is significantly smaller than the optical frequency, the metasurface operates within what we term the *quasi-static* regime (Figure 1.3a). Conversely, when the metasurface elements are actuated with frequencies higher than the incident laser linewidth, typically a few tens of kHz for state-of-the-art lasers at optical wavelengths, the *time-*

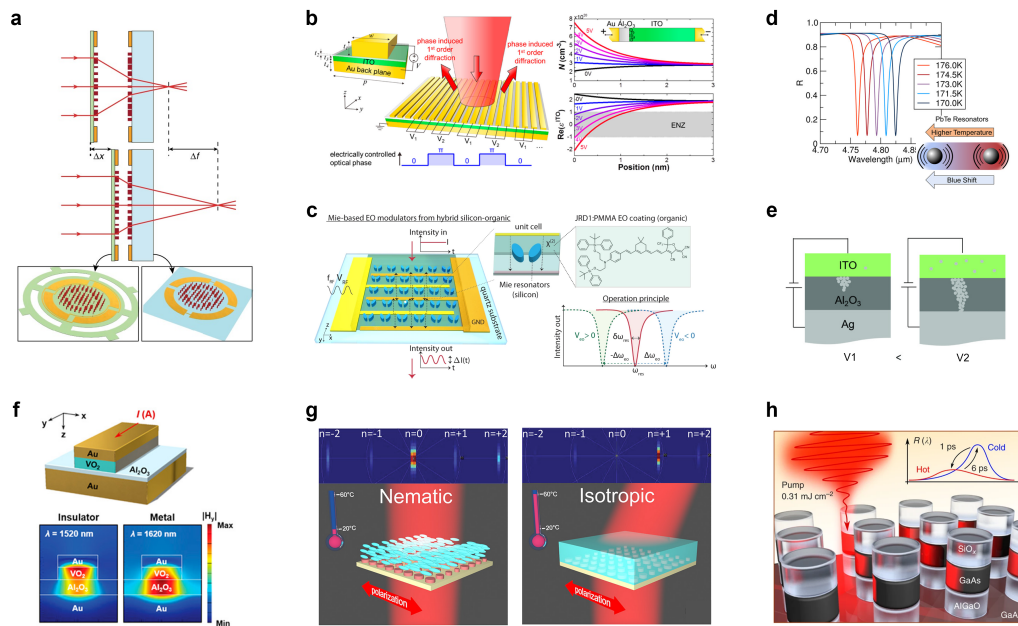


Figure 1.2: Active metasurface modulation platforms. (a) Schematic of MEMS-tunable metalens consisting of a moving lens on a membrane (left) and a stationary lens on a substrate; reprinted from [29]. (b) Schematic of field-effect tunable metasurface for beam switching. The tunable semiconductor layer (indium tin oxide, ITO) undergoes an epsilon-near-zero (ENZ) crossing upon carrier modulation. Reprinted with permission from [30]. Copyright 2016 American Chemical Society. (c) Schematic of Mie-resonance based electro-optic metasurface using JRD1 molecules and operation principle. The transmitted intensity undergoes a resonance shift upon voltage application; reprinted from [31]. (d) Thermo-optic tuning of the resonance in lead tellurium (PbTe) Mie resonators. Adapted with permission from [32]. Copyright 2017 American Chemical Society. (e) Schematic of electro-chemical modulation through formation of silver filaments in dielectric layer upon bias application; adapted from [33]. (f) Schematic of metasurface unit cell based on vanadium dioxide (VO₂) phase change material. VO₂ undergoes an insulator-to-metal phase transition in vanadium dioxide (VO₂) upon resistive heating. Reprinted with permission from [34]. Copyright 2019 American Chemical Society. (g) Schematic of beam switching metasurface infiltrated with liquid crystals. The liquid crystals transition from the nematic to isotropic phase upon heating. Adapted with permission from [35]. Copyright 2018 American Chemical Society. (h) Schematic illustration of all-optical resonance tuning in a gallium arsenide (GaAs) metasurface using femtosecond laser pulses. Free-carrier injection and subsequent recombination allow modulation on picosecond timescales; reprinted from [36].

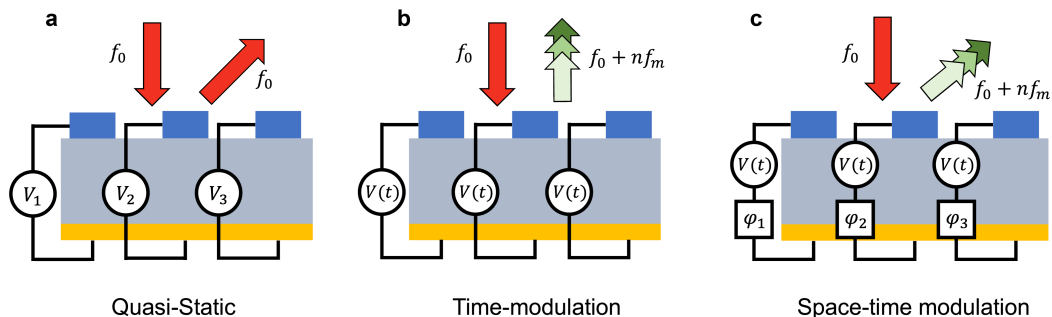


Figure 1.3: **Quasi-static and time-modulated metasurfaces.** Incident light of frequency f_0 is reflected from an electrically programmable metasurface. (a) In the quasi-static operation regime, the frequency of the reflected light remains unchanged and only the propagation direction is altered. (b) In the time-modulated regime, metasurface elements are collectively driven at a high frequency, f_m , allowing the generation of higher order harmonics in the reflected light with frequencies $f_0 + n f_m$. (c) In a space-time modulated metasurface, a phase offset φ_i is added between the time-modulated signals of individual metasurface elements using external phase shifters. This enables shaping of frequency-modulated reflected waves.

modulated operation regime is reached. In this regime, the metasurface gives rise to additional frequency harmonics that appear as sidebands, displaced in frequency relative to the incident laser frequency, as depicted in Figure 1.3b. These individual frequency harmonics can be independently controlled using *space-time modulated* metasurfaces (Figure 1.3c). Here, an additional phase offset is introduced between the high-frequency driving waveform of each metasurface element using external non-resonant phase shifters [43, 44]. This concept holds significant promise for optical communications applications, where high-frequency time modulation enables an increase in the number of communication channels, similar to wavelength division multiplexing (WDM) in optical fiber communications [45]. Furthermore, the ability to simultaneously control multiple frequency sidebands opens the door to increased processing speeds and parallelization capabilities in the realms of optical imaging and computation.

1.3 Goals of this thesis

The ability to dynamically control the optical response in both quasi-static and time-modulated regimes unlocks a vast design space that can be fully exploited by engineering suitable structures for the arbitrary control of light. Currently, researchers are increasingly working toward maximizing the information capacity that can be

controlled with an individual nanophotonic element by leveraging control over various input variables, such as modulation amplitude and frequency, to simultaneously alter multiple properties of the scattered light, *e.g.*, its propagation direction, frequency, and polarization. The practical implementation of such devices ultimately involves designing highly efficient optical elements capable of operating at specific optical wavelengths and modulation frequencies. Addressing these challenges requires a holistic approach that encompasses system-level problems, nanophotonic design optimization, and understanding of fundamental materials science. This thesis addresses multiple aspects of this broader objective.

Chapter 2 of this thesis focuses on the optimization of spatially varying wavefronts scattered from an active metasurface using an array-level inverse design approach. The optimization is numerically and experimentally demonstrated for a field-effect tunable indium tin oxide (ITO)-based metasurface with independently addressable metasurface unit cells. The tools developed in this chapter are applicable to a variety of active metasurfaces that are based on localized modes and provide a pathway for minimizing system-level losses in metasurfaces. We study the impact of nonideal phase and amplitude response and analyze the requirements for high-directivity beam steering metasurfaces.

In Chapter 3, we experimentally realize space-time modulated metasurfaces at optical frequencies, by driving ITO-based metasurfaces operating at telecommunication wavelengths with MHz voltage waveforms. By tailoring the phase offsets of applied waveforms, we engineer spatiotemporally varying configurations for targeted steering of frequency-shifted beams. This concept allows us to extend the information capacity of an individual metasurface, ultimately forming a path toward active *multitasking* metasurfaces, that allow simultaneous and independent dynamic control over multiple frequency channels.

Chapter 4 delves into the aspects of increased efficiency and operation at target wavelengths across the visible spectrum using the electro-optic response of barium titanate (BaTiO_3 , BTO). We demonstrate a novel synthesis approach for single-crystalline thin films that involves exfoliation from a stressed single crystal bulk substrate. We furthermore characterize the BTO thin films in terms of their physical properties as well as their electro-optic response. Finally, we design electrically tunable transmissive metasurfaces based on BTO for operation in the visible spectrum.

In Chapter 5, we provide an outlook toward the development of *universal* active metasurfaces, discussing the requirements to achieve this goal and identifying key

challenges that remain. This chapter synthesizes insights from the preceding chapters to outline the future of active metasurface research. We additionally delve into prospective use cases of universal active metasurfaces in the realms of optical imaging, communication, and computation. The dissertation is concluded with a summary of the key findings, highlighting significant advances and potential impacts on the field of nanophotonics, in Chapter 6.

ARRAY-LEVEL INVERSE DESIGN OF ACTIVE METASURFACES FOR OPTIMIZED SPATIAL WAVEFRONTS

The material in this chapter was in part presented in [46].

2.1 Beam steering with optical metasurfaces

Optical beam steering has become a major focus of global research owing to its significance in technologies such as light detection and ranging (LiDAR), free space optical communications, and holographic displays [47–50]. Operating at near-infrared (NIR) and visible wavelengths offers the potential to enable high-resolution beam steering with reduced footprints compared to radiofrequency (RF) phased arrays.

Beam steering is achieved by precisely controlling the phase and amplitude of light emitted or scattered from each antenna in an array, leading to constructive interference in a desired direction. In passive metasurfaces, this control is typically achieved by designing individual resonators that impart abrupt phase changes in light scattered at an interface while maintaining constant amplitude. By arranging these resonators to create constant spatial phase gradients, researchers have demonstrated effects such as anomalous refraction or reflection [23, 27, 51, 52]. The angles of refraction (θ_t) and reflection (θ_r) are determined by the design-specific phase gradient $\frac{d\Phi}{dx}$, as described by the generalized Snell's law [51]:

$$\begin{aligned} \sin(\theta_t)n_t - \sin(\theta_i)n_i &= \frac{\lambda_0}{2\pi} \frac{d\Phi}{dx} \\ \sin(\theta_r) - \sin(\theta_i) &= \frac{\lambda_0}{2\pi n_i} \frac{d\Phi}{dx}. \end{aligned} \tag{2.1}$$

Here, n_t and n_i are the refractive indices of the media in which light is transmitted and incident, respectively, and λ_0 is the vacuum wavelength. The design of these phase gradient arrays can be understood as a *forward* design process that results in anomalous refraction or reflection at a single, design-specific angle. However, the lack of post-fabrication tunability in passive metasurfaces limits their applicability in practical scenarios.

Active metasurfaces address the limitations of their passive counterparts by integrating a tunable permittivity layer that enables dynamic changes in the refractive index in response to an external stimulus, such as a bias voltage. To achieve a wide range of amplitude and phase values, reconfigurable optical frequency metasurfaces generally rely on intrinsic material and geometric resonances. This approach introduces nonidealities in the optical response. Unlike passive structures, active metasurfaces often exhibit a strongly covarying phase and amplitude as function of the applied bias. Additionally, it is challenging to design tunable permittivity antennas with a full phase modulation range of 360° [53, 54]. As a result, active beam steering metasurfaces with forward-designed array phase profiles result in decreased directivities due to significant power coupling into undesired sidelobes [42].

In this chapter, we introduce an array-level *inverse* design approach as a solution to optimize the spatial bias configuration across an array considering the nonideal antenna amplitude and phase response. Previously, inverse design techniques have been applied to shape and topology optimization of individual nanophotonic components, such as antennas in passive metasurfaces [55–59]. These methods involve iteratively adjusting the shape and size of each nanoantenna until the desired optical response is achieved. Various methods including the adjoint variable method [55, 60], genetic algorithms [58, 61], and machine learning [60, 62, 63] have been successfully used for this purpose.

For active metasurfaces, an analogous approach starts with designing an array of geometrically identical nanoantennas that exhibit optimal phase and amplitude tunability in response to an external control variable. Thus, the critical component-level inverse design objective shifts from optimizing the shape of a passive metasurface element to engineering nanoantennas with optimal functional characteristics, such as the range of achievable amplitude, phase, or polarization values in response to its inputs. Once an optimal active antenna design is developed, the scattering properties of the entire array can be co-optimized to meet a specific performance objective. Due to the added complexity of this process, the inverse design of active metasurfaces has remained largely unexplored until recently.

Chung *et al.* [64] demonstrated inverse design of an active beam switching metasurface. Notably, the liquid crystal-based metasurface considered in this work operated in only two states: voltage on and off. As a consequence, topology optimization of individual unit cells was required to facilitate beam switching between different

diffraction orders. In contrast, the array-level inverse design approach outlined here leverages the tunability of individual active nanoantennas that is made possible by applying an independent bias to each metasurface antenna. This approach results in an array of active antennas, each with continuously variable phase and amplitude, yielding a vast number of operational states that enable versatile metasurface function. Consequently, the phase and amplitude of scattered light can be optimized across a large array without any change in the geometric configuration of individual components.

In the following sections, we discuss conventional approaches for forward designs of ideal antenna arrays and the limitations encountered with nonideal, realistic active metasurface designs. We utilize a genetic algorithm for an iterative optimization of a figure of merit (FOM) that analytically models the desired function of a metasurface with uncoupled antennas. Further, we assess the robustness of the optimized designs through numerical studies, examining the effects of inaccuracies in the applied voltages and evaluating the impact of amplitude and phase modulation on the achievable performance. Finally, we experimentally validate our approach using a plasmonic indium tin oxide (ITO)-based field-effect tunable metasurface and discuss the realization of more advanced metasurface functions, such as the creation of flat-top beams, variable beam widths, and simultaneous steering of multiple beams.

2.2 Forward design of ideal antenna arrays

The electric far-field E_{ff} of an array of scatterers is calculated by pattern multiplication of the electric far-field of a unit cell E_{antenna} with the array factor. This calculation is based on antenna array theory [65, 66], which was initially developed for RF phased arrays. As RF phased arrays can maintain large interantenna spacings without the introduction of additional diffraction orders, their far-field response can be modeled as that of an array of independent scatterers with negligible near-field coupling. The far-field response is thus obtained by applying the Fraunhofer approximation to the superposition of individual electric field contributions from each scattering element.

This assumption becomes non-trivial in the case of optical metasurfaces with sub-wavelength antenna spacings, as the characteristic period d_x between neighboring antennas approaches the electromagnetic near-field regime given by $2d_x/\lambda^2$. Thus, coupling between neighboring elements can only be neglected for antennas that are spaced at large enough distances and/or possess strongly confined modes. The

validity of this assumption should be verified for each metasurface design through analysis of the electromagnetic near-field, or by comparing the calculated far-field profile to results obtained for full-wave simulations of an antenna array with spatially varying bias configurations.

For one-dimensional (1D) arrays, as the ones considered in the following study, the array factor is computed by taking into account the phase φ_n , amplitude A_n , as well as the period d_x that defines the position of the n -th antenna element (Fig. 2.1a). The scattered light phase and amplitude are determined by the external stimulus applied to each antenna, such as a bias voltage V_n . The electric far-field E_{ff} can then be written as

$$E_{\text{ff}}(\theta) = E_{\text{antenna}}(\theta) \cdot \sum_n [A_n(V_n) \exp(i\varphi_n(V_n)) \exp(ik(n-1)d_x \sin(\theta))]. \quad (2.2)$$

Here, θ is the polar angle, and $k = 2\pi/\lambda$ is the wavenumber associated with the operating wavelength λ . A 1D configuration of a square antenna array is realized by connecting antennas along one axis and enabling independent control of each element in the perpendicular direction (Fig. 2.1b). In a beam steering reflectarray, the incident light is normal to the metasurface, and the reflected beam is steered at a desired angle θ_r .

We define an ideal antenna response as one that yields a constant unit amplitude and a smoothly varying phase with a 360° phase modulation range (Fig. 2.1c). The respective ideal amplitude and phase properties are commonly reported in conventional phased array systems [5] as well as passive metasurfaces [51], and facilitate intuitively understandable forward design of phase gradient profiles for highly directive beam steering with minimal power loss in sidelobes. The additional manifestation of unit amplitude at each antenna element results in maximal power efficiency.

Figure 2.1d illustrates a forward-designed phase gradient profile with a constant phase shift φ_s between adjacent antennas in an ideal reflectarray. The array consists of 100 antennas that are uniformly arranged at a spacing of $d_x = 400$ nm. The operating wavelength is $\lambda = 1550$ nm. For an incident beam normal to the array, φ_s is computed as

$$\varphi_s = 360^\circ \cdot \frac{d_x \sin(\theta_r)}{\lambda}. \quad (2.3)$$

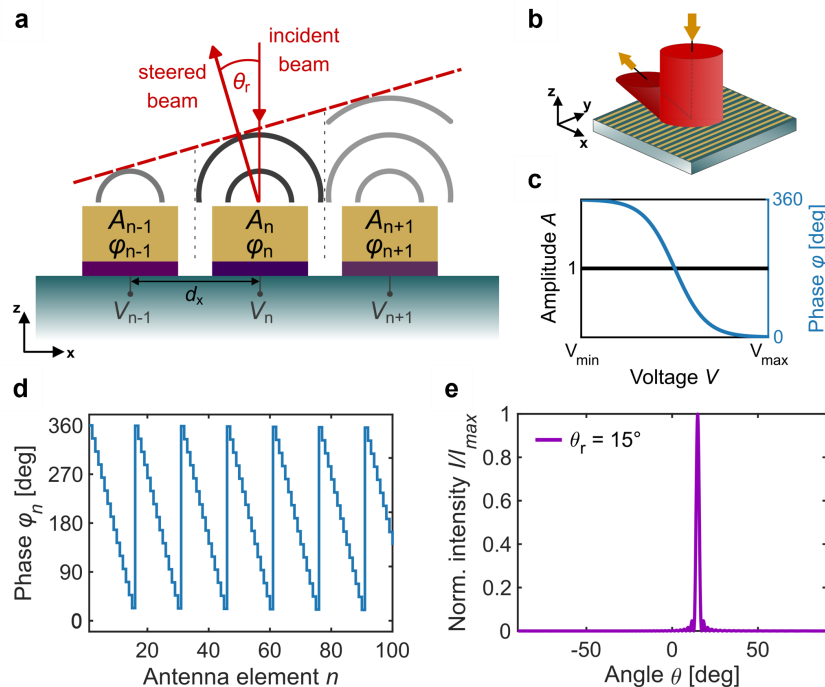


Figure 2.1: **Beam steering with ideal antenna array.** (a) Schematic of beam steering active metasurface: application of voltage stimulus V_n on antenna n (yellow) alters the complex dielectric permittivity of the active layer, indicated in shades of violet. As a consequence, the scattered light amplitude and phase of element n , A_n and ϕ_n , respectively, are varied. The antennas are arranged uniformly at a period d_x . We consider a reflectarray with incident light normal to the surface. Beam steering is achieved through constructive interference of the scattered light at the desired steering angle θ_r . (b) Schematic of a one-dimensional tunable metasurface. Antennas are connected in y -direction and allow independent control in x . (c) Representative scattered light amplitude and phase response on an ideal active antenna array for applied bias voltages from V_{\min} to V_{\max} . (d) Forward design of phase gradient profile for an ideal phased array consisting of 100 antennas arranged at a period of $d_x = 400$ nm. The operating wavelength is $\lambda = 1550$ nm and the target steering angle is $\theta_r = 15^\circ$. (e) Normalized far-field intensity I/I_{\max} vs polar angle θ for spatial phase profile shown in (d) with constant amplitude.

Wrapping of the phase profiles around 360° allows the design of blazed grating-like structures that steer the reflected beam in the desired direction. Due to a discrete sampling of the phases at fixed spatial increments d_x , the blazed grating of an antenna array comprises of discontinuous steps. The discrete sampling furthermore results in an aperiodicity of the phase profiles over the entire array, as a complete phase shift of 360° is not necessarily an integer multiple of φ_s . The phase profiles approach periodic blazed gratings for all steering angles as d_x approaches smaller values.

Assuming constant amplitude, the phase gradient profile shown in Fig. 2.1d results in a directive beam steered at $\theta_r = 15^\circ$ with minimal power scattered in other directions (Fig. 2.1e). The far-field radiation pattern is calculated as $I(\theta) = |E_{\text{ff}}(\theta)|^2$. Individual antennas are approximated as omnidirectional scattering elements with $E_{\text{antenna}}(\theta) = 1$. For the purpose of our study, we quantify the beam steering performance of the array by the directivity, defined as the ratio between the intensity at the desired angle θ_r to the power radiated in all directions normalized by the solid angle (Eq. 2.4). In contrast to efficiency, directivity remains unaffected by scaling of the far-field radiation pattern by a constant factor. For a one-dimensional reflectarray radiating into a half-space, the directivity $D(\theta_r)$ is formalized as [65]

$$D(\theta_r) = \frac{\pi \cdot I(\theta_r)}{\int_{-\pi/2}^{\pi/2} I(\theta) d\theta}. \quad (2.4)$$

For the ideal structure showcased in Fig. 2.1, equation 2.4 yields a directivity of $D_{\text{ideal}} = 78.2$. The sidelobe level SL is proportional to the ratio of the second largest to largest peak intensity, $I_{\text{max},2}$ and I_{max} , respectively,

$$\text{SL} = 10 \log_{10} \left(\frac{I_{\text{max},2}}{I_{\text{max}}} \right) \quad (2.5)$$

and corresponds to $\text{SL}_{\text{ideal}} = -13.3$ dB.

2.3 Nonideal active metasurfaces: Forward and array-level inverse design

Forward design

In contrast to ideal phased arrays, active metasurfaces typically exhibit a nonideal optical response due to the device-specific modulation mechanism. Here, we illustrate this behavior using the example of a field-effect tunable, plasmonic metasurface

introduced in [42]. Figure 2.2a shows a square unit cell with a characteristic period of $d_x = 400$ nm. It consists of a rectangular gold (Au) patch over a hafnium oxide/aluminum oxide laminated ($\text{HfO}_2/\text{Al}_2\text{O}_3$, or HAOL) gate dielectric and an active ITO layer. This composite structure is deposited on top of an Al_2O_3 dielectric spacer and an Au back reflector. Au electrodes intersecting the top metal patches in the y -direction enable the formation of equipotential rows, analogous to the 1D beam steering array shown in Fig. 2.1b. The entire metasurface consists of 96 independently addressable rows, referred to as metasurface antennas.

Active control is achieved by employing field-effect induced changes in refractive index to modulate the scattered light properties [67, 68]. Upon application of a bias voltage between the ITO and the top Au antenna, the reflectance and phase response are modulated as illustrated in Fig. 2.2b for an operating wavelength of $\lambda = 1510$ nm. This modulation occurs due to the Au-HAOL-ITO heterostructure, which functions as a metal-oxide-semiconductor (MOS) capacitor. Application of an electrical bias between the Au electrode and the ITO layer introduces a carrier density modulation in the ITO. Thus, a change in the complex dielectric permittivity of the ITO, ε_{ITO} , occurs in a thin layer at the interface to the gate dielectric [53], as described by the Drude model. Upon alteration of the applied electric field, $\text{Re}(\varepsilon_{\text{ITO}})$ switches its sign from positive to negative, undergoing an epsilon-near-zero (ENZ) transition, as highlighted in Fig. 2.2c with the gray shaded region. The continuity of the normal electric displacement component at the interface between two media requires

$$\varepsilon_1 \cdot E_{1\perp} = \varepsilon_2 \cdot E_{2\perp} \quad (2.6)$$

where ε_i is the complex dielectric permittivity and $E_{i\perp}$ is the normal electric field component in medium i . Hence, operation at an ENZ condition results in a strong field enhancement in the active ITO layer [30]. Spectral overlap of the ENZ transition with the magnetic dipole resonance of the antenna ensures a strong modulation of the scattered light response, allowing for reconfigurable device operation at telecommunication wavelengths. We note here that while $\text{Re}(\varepsilon_{\text{ITO}})$ is required to go to zero to satisfy the ENZ condition and ensure a large phase modulation, $\text{Im}(\varepsilon_{\text{ITO}})$ takes nonzero values (Fig. 2.2d). These losses, emerging from absorption in the active layer due to electron-electron collisions [69], result in reduced scattered light amplitudes.

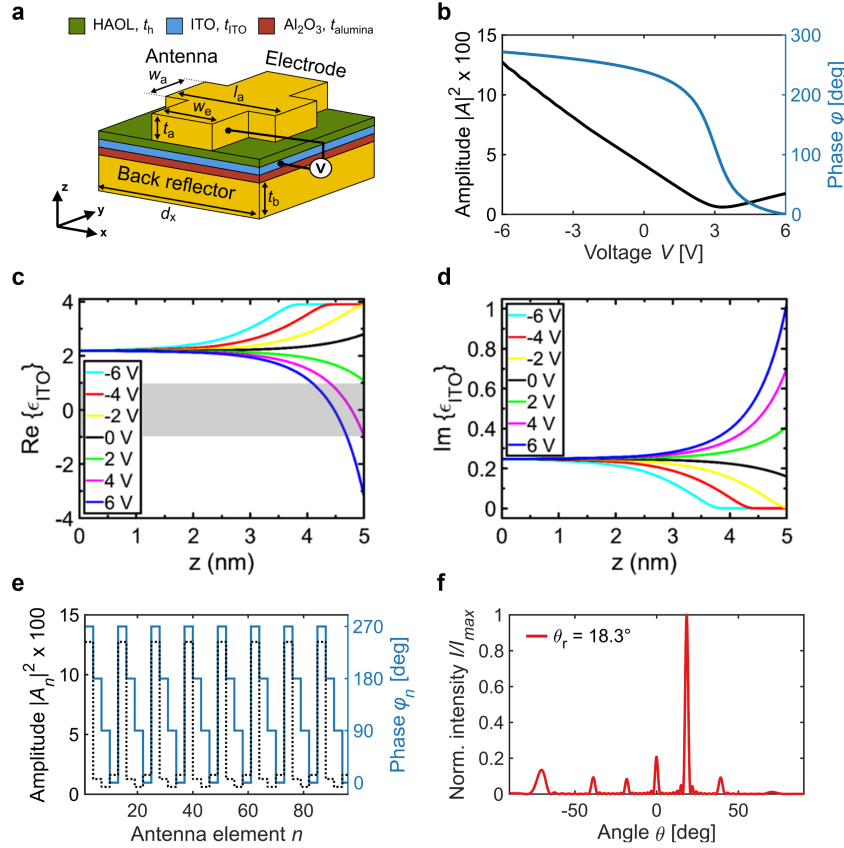


Figure 2.2: Beam steering with nonideal plasmonic field-effect tunable metasurface. (a) Square unit cell of active metasurface as introduced in [42]. Constitutive layers from top to bottom: Au rectangular patch ($t_a = 40$ nm, $w_a = 130$ nm, $l_a = 230$ nm) and electrode ($w_e = 150$ nm), HAOL dielectric spacer ($t_h = 9.5$ nm), active ITO layer ($t_{\text{ITO}} = 5$ nm), Al_2O_3 dielectric layer ($t_{\text{alumina}} = 9.5$ nm), and Au back reflector ($t_b = 80$ nm). The metasurface consists of individually addressable antennas in x which are periodically arranged at a spacing of $d_x = 400$ nm. (b) Scattered light amplitude (black) and acquired phase (blue) response as function of applied bias voltage at $\lambda = 1510$ nm. For clarity, the phase axis is set to 0° at its minimal value. The optical properties are obtained through full-wave simulations (Lumerical FDTD) of a periodic array of the unit cell with a given bias voltage across the entire array. (c) Real and (d) imaginary part of the ITO permittivity as function of z -position for different applied bias voltages at $\lambda = 1510$ nm. The gray-shaded region in (c) shows the ENZ regime where $-1 < \text{Re}\{\epsilon_{\text{ITO}}\} < +1$. $z = 5$ nm denotes the interface of the ITO and the HAOL gate dielectric, $z = 0$ nm represents the interface of the ITO and the Al_2O_3 dielectric layer, as indicated in the inset of (d). (e) Stairstep phase (blue) and amplitude (black dotted) profile for steering at $\theta_r = 18.3^\circ$. (f) Normalized far-field intensity I/I_{max} as function of polar angle θ for forward design shown in (e).

Generally, the operation wavelength is chosen so as to give rise to large phase modulation with a modest change in amplitude [42]. Nevertheless, the active metasurface exhibits a nonideal optical response (Fig. 2.2b) with (i) a nonunity amplitude, (ii) a limited phase modulation range of 272° , and (iii) covariation of the scattered light amplitude and phase properties with applied bias. These nonidealities significantly limit the beam steering performance of such a metasurface array designed using forward approach in the following ways: First, reduced phase modulation requires adjustment to ideal blazed grating designs. Stairstep phase profiles approximate the spatial phase gradients, as shown in Fig. 2.2e [42]. A dynamic change of the repetition number (*i.e.*, number of adjacent antennas with the same phase value) results in beam steering at a set of discrete angles. However, a reduced phase modulation introduces increased number of sidelobes in the far-field radiation pattern. Moreover, the additional covariance of the scattered light amplitude and phase rules out the design of pure phase gratings. Since an intuition-based forward design does not account for amplitude-phase covariation, substantial power is coupled into undesired sidelobes, as shown in Fig. 2.2f for steering at an angle of $\theta_r = 18.3^\circ$. As a result of these nonidealities, we observe a significant drop in directivity to $D_{\text{forward}} = 39.5$ with a sidelobe level of $\text{SL}_{\text{forward}} = -6.8$ dB.

The radiation pattern shown in Fig. 2.2f is obtained using the array factor calculation (Eq. 2.2) for an array of independent antennas. We verify the validity of this approach by comparing the analytically calculated radiation patterns to full-wave simulations [42] for forward-designed array profiles. Two apparent effects are observed in Fig. 2.3: Firstly, rather than an increase in the relative magnitude of the sidelobes, which would indicate interantenna coupling, Fig. 2.3a-c depict an attenuation of the sidelobes at broadside angles in the simulated radiation patterns. This effect increases the simulated directivity D_{sim} in comparison to its analytically computed counterpart D_{AF} that is based on array factor calculations. Secondly, a strong increase in the relative magnitude of the zero-order sidelobe and thus decrease in D_{sim} is reported for $\theta_r = 70.7^\circ$ (Fig. 2.3d). To understand the observed deviations, we remind ourselves that the analytical calculations are performed for omnidirectional scatterers with $E_{\text{antenna}} = 1$. While this assumption is valid for a broad range of steering angles with the current nanoantenna design, it breaks down at larger angles. Nonetheless, due to the validity of the analytically computed radiation pattern for a wide range of steering angles, no appearance of additional sidelobes, and a good match between the computed directivities for the simulated and analytically

obtained radiation patterns (Fig. 2.3), we can use the array factor calculation to develop new design strategies for optimized beam steering with nonideal antennas.

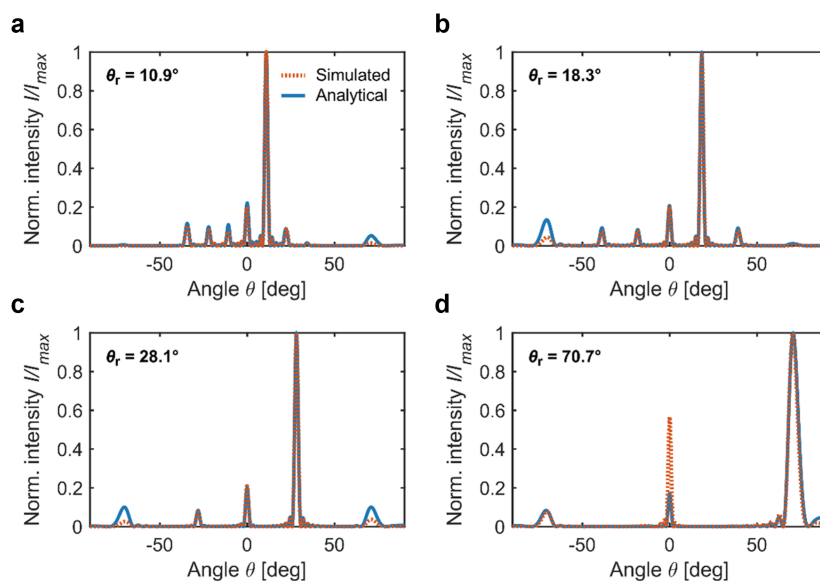


Figure 2.3: **Comparison of far-field radiation patterns obtained through full-wave simulations and analytical array factor calculations.** Normalized far-field intensity I/I_{\max} for full-wave simulations [42] (orange dashed) and analytical array factor calculations (blue). The results are obtained using forward-designed staircase array profiles for an array of 96 antennas arranged at a period of $d_x = 400$ nm and at a wavelength of $\lambda = 1510$ nm. The simulated (D_{sim}) and analytically calculated (D_{AF}) directivities at the respective steering angles θ_r are (a) $D_{\text{sim}} = 51.0$ and $D_{\text{AF}} = 43.5$, (b) $D_{\text{sim}} = 48.3$ and $D_{\text{AF}} = 39.5$, (c) $D_{\text{sim}} = 50.1$ and $D_{\text{AF}} = 39.1$, (d) $D_{\text{sim}} = 22.2$ and $D_{\text{AF}} = 23.0$.

Array-level inverse design

Here, we report an array-level inverse design algorithm that computes the bias voltage configuration for an electrically tunable metasurface to achieve optimized beam steering. Since each metasurface antenna is gated individually, the algorithm aims to optimize the covarying phase and amplitude value at each antenna. We address this multiparameter, global optimization problem using genetic algorithms (GA). In contrast to local search methods, genetic algorithms are based on stochastic optimizers that can escape local optima [70, 71]. In addition, they are highly suitable for discrete solution domains with discontinuous or nondifferentiable objective functions [59]. An inherently high-dimensional solution space arises due to simultaneous optimization of 96 metasurface antennas. This challenge is overcome by implementing an iterative genetic optimization that relies on a gradual

increase of the solution space. The algorithm initially runs an optimization for a reduced number of consecutive antennas, which are periodically repeated over the entire array. Once an optimal solution is found, it is provided to the next bigger solution domain as an initial solution. The final iteration simultaneously optimizes all variables. This approach enables the algorithm to effectively find near-optimal solutions in high-dimensional optimization spaces, while maintaining all degrees of freedom. Due to the stochastic nature of genetic optimization, the algorithm is run multiple times to obtain the optimal result in an extended data set. Further details on the implementation of the iterative genetic optimization algorithm, the distribution and robustness of the optimized results, and a comparison to alternative genetic optimization approaches are provided in Section A.1 of the Appendix. We would like to highlight that due to the high dimensionality of the nonconvex solution space given in this problem, the search for an absolute global optimum becomes infeasible. Thus, we compare the optimized FOM to the corresponding performance measure of an ideal antenna array in order to assess its proximity to a desired reference value. The beam steering optimization consists of maximizing the directivity at the desired steering angle θ_r . Thus, the objective function is defined as

$$\text{FOM}(\theta_r, \varphi_n(V_n), A_n(V_n)) = D(\theta_r). \quad (2.7)$$

The directivity accounts for the antenna-specific control variables (in this case, bias voltage) to maximize the intensity at θ_r , while minimizing power scattered in all other directions. The latter also simultaneously minimizes beam divergence, which is quantified by the full width at half-maximum (FWHM) of the steered beam. The inverse design algorithm outputs a highly nonintuitive array phase profile, as shown in Fig. 2.4a for the same steering angle of $\theta_r = 18.3^\circ$. The seemingly periodic nature of the spatial phase profile arises from the phase gradient required to steer a beam at a specified angle as well as the iterative design approach. Since the inverse design optimizes the covarying phase and amplitude values at each antenna, the algorithm aims to minimize the amplitude modulation A_{mod} over the entire antenna array.

$$A_{\text{mod}} = \frac{|A_{\text{max}}|^2 - |A_{\text{min}}|^2}{|A_{\text{min}}|^2}. \quad (2.8)$$

Here, A_{max} and A_{min} correspond to the maximal and minimal amplitudes, respectively. The amplitude modulation for the forward-designed array profile (Fig. 2.2e)

corresponds to $A_{\text{mod,forward}} = 19.7$. In comparison, the amplitude modulation using the inverse design approach (Fig. 2.4a) is $A_{\text{mod,inverse}} = 11.8$. As a result, by accounting for the antenna-specific scattered light properties, the co-optimization of phase and amplitude at each antenna results in significant sidelobe suppression, as shown in Fig. 2.4b. The optimized directivity for steering at $\theta_r = 18.3^\circ$ is $D_{\text{inverse}} = 72.7$, representing a substantial increase of 84% compared to the previously demonstrated forward design with $D_{\text{forward}} = 39.5$. Similarly, the sidelobe level obtained through inverse design amounts to $\text{SL}_{\text{inverse}} = -13.2$ dB.

These findings highlight the ability of the optimized radiation patterns to approach ideal beam steering. The approach was further generalized to the case of beam steering at angular increments of 0.5° . Figure 2.4c shows a comparison of the directivity values obtained with forward and inverse design, respectively. The results highlight the ability of optimized designs in a nonideal antenna array to approach the performance of an ideal phased array (dashed) at all steering angles. This contrasts with the results of forward design, where we evaluate the previously introduced staircase phase profiles for steering at a discrete set of angles as well as linear phase profiles. Linear phase profiles are those that are truncated symmetrically to remain within the restricted phase modulation range. This method offers an alternative approach to achieve continuous beam steering with limited phase modulation using forward design. As both approaches do not account for the nonideal optical response of the metasurface, reduced performance is observed using the forward design approach.

The cosine-like decrease of directivity with increasing steering angles can be understood by considering the two limiting factors defining beam directivity: the magnitude of the sidelobes relative to the peak intensity at θ_r (*i.e.*, the sidelobe level SL), and the FWHM of the main lobe. Notably, the prior does not change monotonically as the beam is scanned over the half space and remains around a constant value (inset of Fig. 2.4d). Thus, the decrease in directivity is attributed to the diminished effect of aperture size at oblique angles. That is, the antenna array aperture appears to be reduced in size at larger steering angles, leading to a broadening of the beam, as illustrated in Fig. 2.4d. Furthermore, since the reflectarray configuration does not allow for radiation to go beyond 90° , the main lobe is truncated for angles greater than 80° . Thus, an increase in directivity and a simultaneous decrease in FWHM is reported for the corresponding steering range.

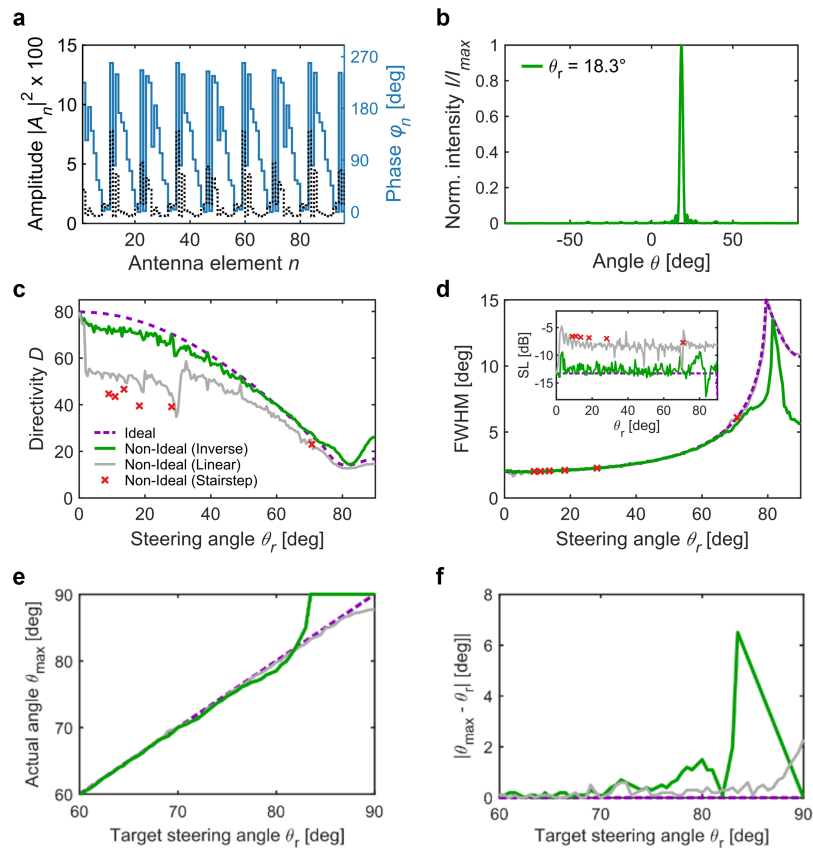


Figure 2.4: **Beam steering of nonideal active metasurface with array-level inverse design.** (a) Optimized phase profile (blue) with corresponding amplitude profile (black dotted) generated by inverse design for steering at $\theta_r = 18.3^\circ$. (b) Normalized far-field intensity I/I_{\max} vs polar angle θ for inverse-designed active metasurface. (c) Optimized directivity (green) for beam steering angles θ_r ranging from 0° to 90° at angular increments of 0.5° . The beam directivity (c) and sidelobe level (d) for ideal (dashed violet), forward designs consisting of linear truncated (gray), and stairstep (red crossed) phase profiles are shown for comparison. All results are obtained for the active metasurface introduced in Fig. 2.2. The aperture of the metasurface is $38.4 \mu\text{m}$.

An evaluation of the difference between the actual and target steering angle shows that the target steering angle is achieved with $\leq 0.2^\circ$ absolute deviation for steering angles up to 70° . For broadside angles, this value increases as steering in nonuniform angular increments is observed due to the limited phase modulation (Fig. 2.4e). Since a directivity optimization entails maximizing the intensity at θ_r while minimizing the beam divergence and sidelobes, inverse design can enhance the directivity at broadside angles by reducing the FWHM even when the actual steering angle θ_{\max} does not correspond to θ_r . Figures 2.4e and f illustrate how θ_{\max} and the absolute deviation from the desired steering angle $|\theta_{\max} - \theta_r|$ evolve for forward- and inverse-designed arrays. Additional constraints can be implemented in the algorithm to improve the accuracy of the steered beam across all desired steering angles.

2.4 Impact of phase and amplitude modulation

A seemingly fundamental drawback of active metasurfaces is access to a limited phase modulation range $\Delta\varphi = \varphi_{\max} - \varphi_{\min}$. In addition, for the active metasurface discussed here, Fig. 2.2 illustrates that a maximal phase shift of 272° is achieved with a bias application of ± 6 V. Since these levels approach values that are marginal to the breakdown field in the active ITO layer, it is desirable to operate at lower voltage and therefore a lower phase modulation range to increase device lifetime. Thus, for the purpose of this study, we limit the applied bias range to ± 4.5 V in the modeled active metasurface [42]. For further reduction in $\Delta\varphi$, the phase modulation is truncated symmetrically around the ENZ permittivity transition at 2.75 V. This simultaneously also ensures minimal amplitude modulation A_{mod} , which is desirable for enhanced performance.

Figure 2.5 illustrates the effect of a reduced $\Delta\varphi$ of the field-effect tunable metasurface on the performance of forward- and inverse-designed arrays steering at $\theta_r = 18.3^\circ$. The underlying design principle of forward-designed arrays with staircase phase profiles does not account for the covariation of phase with amplitude. Thus, decreased phase modulation ranges lead to significant power coupling into undesired sidelobes, as illustrated in the right column of Fig. 2.5 (gray). In contrast, inverse design facilitates highly directive beams even with a limited phase modulation range of 210° where directivity is enhanced by up to 55% compared to the respective staircase forward design (Fig. 2.5d). As the phase modulation range is reduced further, a decrease in the optimized directivity is observed, with increasing sidelobe amplitude at 0° and $-\theta_r$ (Fig. 2.5f, h). Nonetheless, the optimized directivity re-

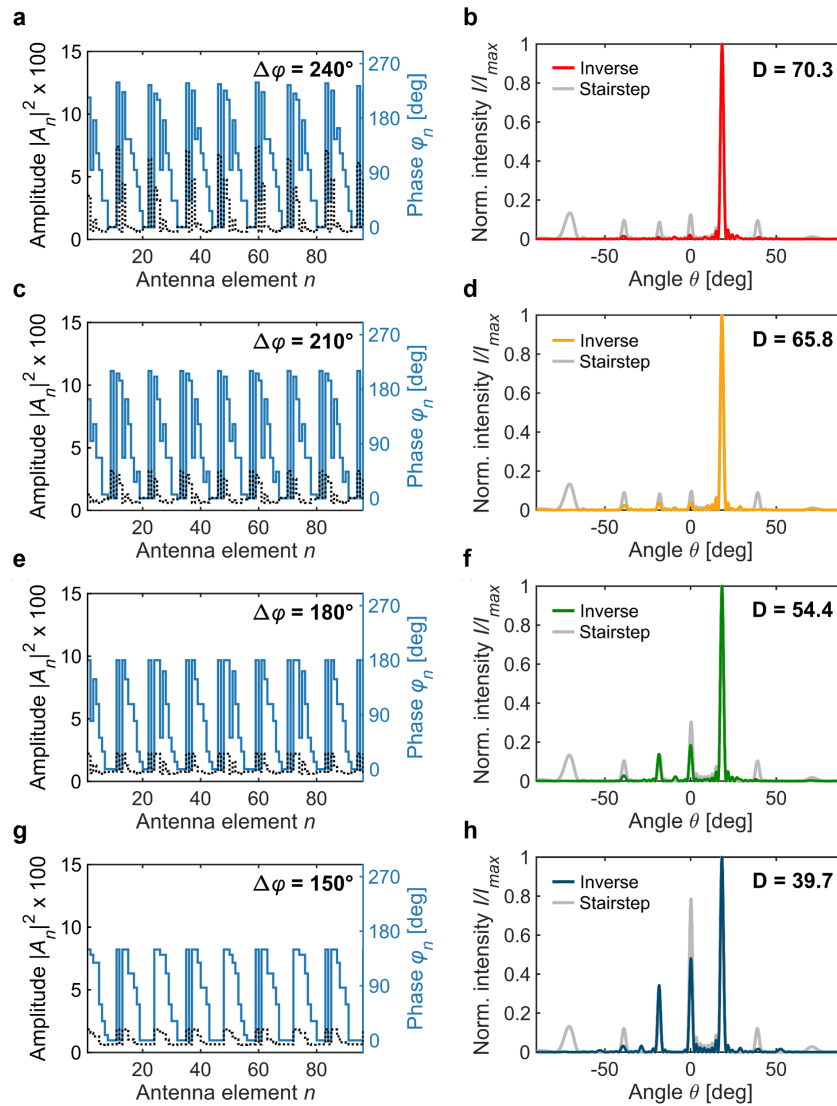


Figure 2.5: **Optimized beam steering with reduced phase modulation.** Optimized phase and amplitude designs for steering at $\theta_r = 18.3^\circ$ with reduced phase modulation ranges $\Delta\varphi$ of (a) 240° , (c) 210° , (e) 180° , and (g) 150° for the active metasurface shown in Fig. 2.2. Panels (b), (d), (f), and (h) illustrate the normalized far-field intensity I/I_{\max} as function of polar angle θ for the inverse-designed array phase and amplitude profiles as well as the forward-designed stairstep phase profile (gray). The optimized directivity with reduced $\Delta\varphi$ is labeled in the upper right corner of the figure.

ported with $\Delta\varphi = 150^\circ$ (Fig. 2.5h) is 41% higher than the corresponding forward design and comparable to the directivity of the staircase phase profile introduced with $\Delta\varphi = 270^\circ$ in Fig. 2.5d.

The results discussed here underscore the ability of array-level inverse design to create high-performing arrays despite covarying phase and amplitude. However, they do not allow for any decoupled conclusions on the independent effects of phase and amplitude modulation on the optimized performance. Hence, we studied a series of hypothetical metasurfaces with limited phase modulation, where amplitude was held at a constant value $A = 1$. In addition, we artificially generated representative trial values of the amplitude-voltage relation with modest amplitude modulation where the phase modulation range was held at a constant value of $\Delta\varphi = 360^\circ$. For generality, the arrays considered here consist of 100 antennas spaced at a period of 400 nm, with an operating wavelength of 1550 nm.

Figure 2.6a demonstrates the optimized directivities for active metasurfaces with constant, unit amplitude and varying phase modulation range $\Delta\varphi$. Phase is assumed to be a sigmoidal function of the applied bias. As $\Delta\varphi$ is reduced, directivity is maintained up to a threshold phase modulation range $\Delta\varphi_{\text{threshold}}$. With further distortion in the information carried by each element, destructive interference results in intensified sidelobes that reduce directivity. We define $\Delta\varphi_{\text{threshold}}$ as the phase modulation range required to obtain the threshold directivity of $0.9 \times D_{\text{ideal}}(\theta_r)$, where $D_{\text{ideal}}(\theta_r)$ corresponds to the directivity of an ideal, forward-designed antenna array. Figure 2.6b compares $\Delta\varphi_{\text{threshold}}$ for forward-designed antenna arrays with linear truncated phase profiles to those of the corresponding inverse designs. Our results indicate that inverse design lowers the required phase modulation range to obtain threshold performance by a considerable amount. By introducing disorder into the phase profile, inverse design succeeds in suppressing power coupled into undesired directions. Thus, the inverse design approach outperforms intuitively motivated forward design for reduced phase modulation range. The difference in $\Delta\varphi_{\text{threshold}}$ becomes particularly noticeable at large steering angles due to an additional reduction of the FWHM, as discussed in Fig. 2.4d.

In contrast, we consider antenna arrays exhibiting a phase modulation range of 360° but nonideal amplitude characteristics, as shown in Fig. 2.6c. The three different amplitude profiles represent distinct cases: constant amplitudes, linear functions, and Lorentzian line shapes. To obtain comparable results, the amplitude modulation of the two latter cases is chosen to be $A_{\text{mod}} = 20.0$. Figure 2.6d shows a comparison

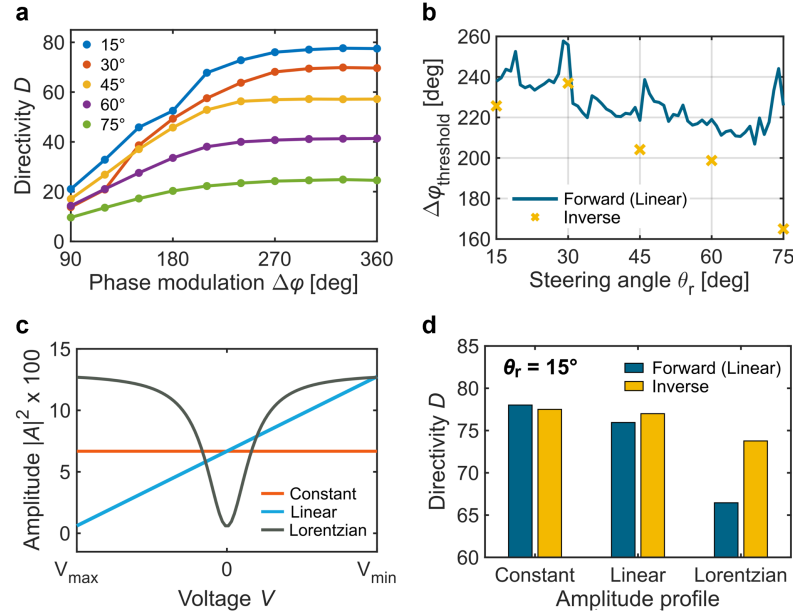


Figure 2.6: Impact of phase and amplitude modulation on beam steering performance. Analysis of a series of hypothetical structures consisting of a 1D array of 100 antennas uniformly spaced at 400 nm. The operating wavelength is $\lambda = 1550$ nm. (a) Optimized directivity D vs phase modulation range $\Delta\phi$ for a metasurface with constant amplitude $A = 1$. Optimized results are shown for steering at $\theta_r = 15^\circ$ (blue), 30° (orange), 45° (yellow), 60° (violet), 75° (green). (b) Required phase modulation $\Delta\phi_{\text{threshold}}$ for threshold directivity of $0.9 \times D_{\text{ideal}}(\theta_r)$ vs steering angle θ_r for forward (blue) and inverse designs (yellow). (c) Trial amplitude A as a function of bias voltage V for three distinct cases: constant (orange), linear (blue), Lorentzian (gray). V_{min} and V_{max} are the minimal and maximal applied voltages, respectively. (d) Directivity D of forward-designed, linear phase profiles and inverse-designed arrays using amplitude relations shown in (c). The phase modulation corresponds to $\Delta\phi = 360^\circ$ and the steering angle is $\theta_r = 15^\circ$.

of the directivity values obtained with forward and inverse designs for steering at $\theta_r = 15^\circ$. For constant amplitude, the directivity of both forward- and inverse-designed arrays is ideal. Minor variations in the optimized directivity are attributed to the stochastic nature of the algorithm. In comparison, linearly varying amplitude leads to lower directivities. However, due to the assumed sigmoidal variation of phase across the applied bias, amplitudes vary minimally over a large segment of the phase modulation range. As a result, near-ideal performance can be attained with both forward and inverse design. In the case of the Lorentzian amplitude profile, however, the largest change in phase occurs precisely in the low amplitude regime. This introduces a considerable difference in the performance of forward and inverse

designs. An analysis of the optimized amplitude profile (Fig. 2.7a) indicates that even though there is no significant difference in A_{mod} , inverse design can suppress undesired sidelobes, as shown in Fig. 2.7b. This can be attributed to a change in the distribution of phases across 360° in both designs. Since forward designs are based on constant phase shifts between adjacent antennas, the distribution of phases over the entire array is nearly uniform (Fig. 2.7c). As a consequence, forward designs are highly sensitive to the antenna-specific amplitude profile and the directivity is reduced to $D_{\text{Lorentz,forward}} = 0.85 \times D_{\text{const,forward}}$. Inverse design, on the other hand, aims to avoid low amplitude regimes. Due to the sigmoidal phase modulation, minimal amplitude is reported for an acquired phase of 180° . Therefore, our optimization approach results in a considerably smaller number of antennas with acquired phase in that regime (Fig. 2.7d), resulting in higher directivity with $D_{\text{Lorentz,inverse}} = 0.94 \times D_{\text{const,forward}}$.

This study illustrates that array-scale inverse design is most beneficial for highly nonideal active metasurfaces that exhibit low amplitude under conditions of large phase shift. It is to be noted that such cases are typically reported in tunable structures that rely on intrinsic resonances. The results generated using array-level inverse design approach the ideal performance obtained for constant amplitude and a given phase modulation.

2.5 Experimental demonstration of array-level inverse design

Here, we experimentally validate the array-level inverse design approach for an active beam steering metasurface. The previously introduced metasurface was redesigned to ensure an operating wavelength of the fabricated metasurface around 1550 nm. Figure 2.8 shows the full-wave simulation results obtained using finite difference time domain (Lumerical FDTD) for a metasurface with the following layer thicknesses: $t_b = 80$ nm, $t_{\text{alumina}} = 9.5$ nm, $t_{\text{ITO}} = 5$ nm, $t_h = 9.5$ nm, and $t_a = 40$ nm. The antenna and electrode dimensions are defined as $l_a = 210$ nm, $w_a = 160$ nm, and $w_e = 130$ nm, respectively, and the period is $d_x = 400$ nm. Additionally, we added a 60 nm thick silica (SiO_2 , t_c) capping layer to increase device durability (Fig. 2.9a). A scanning electron microscopy (SEM) image of the metasurface is shown in Fig. 2.9b. We would like to note that the period of the metasurface post-fabrication was measured to be $d_x = 430$ nm.

Once the metasurface was fabricated (as outlined in Section A.2 of the Appendix), we measured the spectra of the reflected light intensity (*i.e.*, reflectance) and phase in

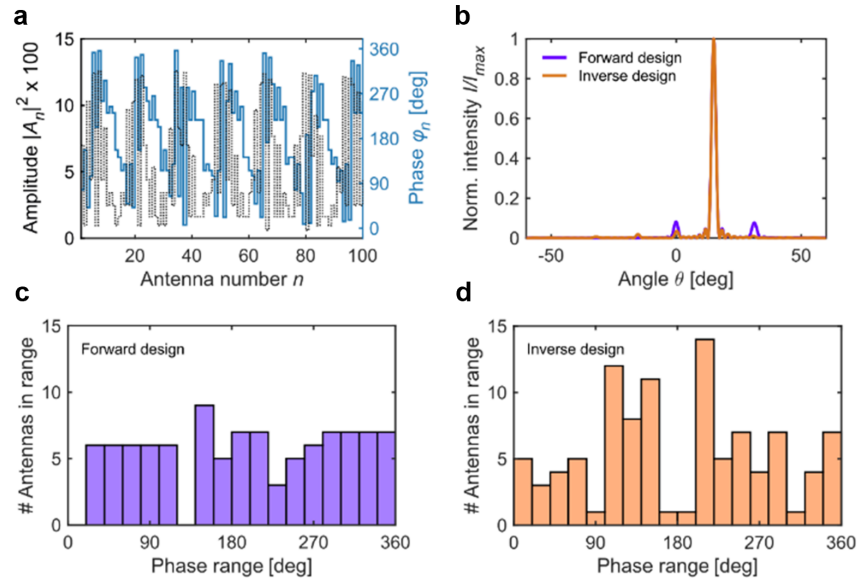


Figure 2.7: **Array-level inverse design of amplitude-modulated array with Lorentzian modulation.** (a) Optimized phase and amplitude profile over 100 antennas. The Lorentzian amplitude modulation shown in Fig. 2.6 is associated with a 360° sigmoidal phase modulation. (b) Normalized far-field intensity I/I_{\max} as function of polar angle θ for forward (linear truncated, violet) and inverse-designed (orange) arrays. The distribution of number of antennas in various phase ranges of 20° between 0° and 360° is displayed in (c) for forward design and (d) for inverse-designed array profiles.

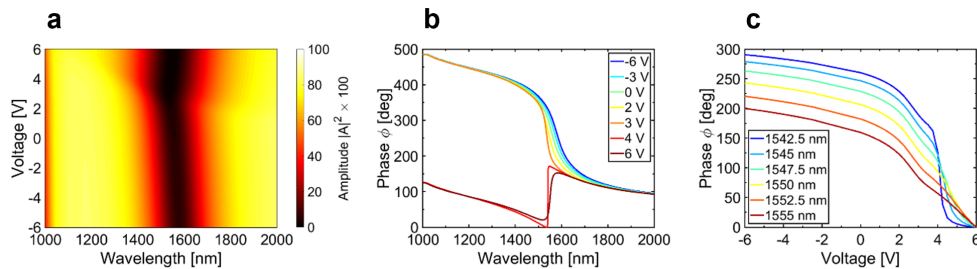


Figure 2.8: **Full wave simulations of experimentally realized metasurface.** (a) Reflectance as function of wavelength and applied bias voltage. (b) Acquired phase spectrum at different applied biases. (c) Acquired phase as function of applied bias at different wavelengths.

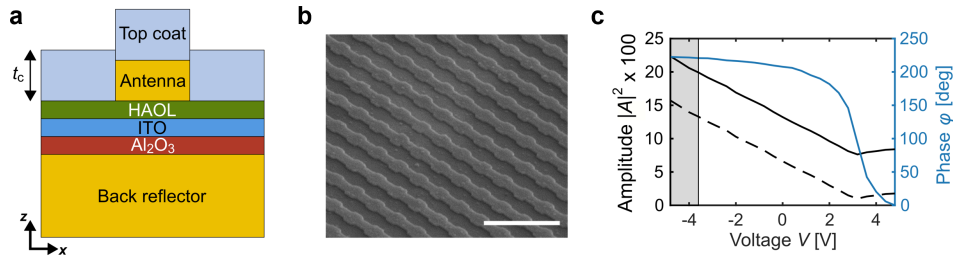


Figure 2.9: **Experimentally realized metasurface and gate-tunable optical response.** (a) Side-view schematic of the experimentally fabricated metasurface with a SiO₂ top-coat layer with thickness t_c . (b) SEM image of the fabricated nanoantennas with a scale bar of 1 μm . (c) Measured phase shift (blue) and reflectance (black) as function of the applied bias voltage. The dashed black line indicates the approximated reflectance contributing to the beam steering performance. Phase/amplitude values within the gray box were not used for optimization.

order to characterize the tunable optical response of the metasurface under different applied biases. To do so, we measured the amplitude and phase of the reflected light using a tunable NIR laser in the wavelength range of 1420 nm – 1575 nm. The phase shift of the reflected light was determined using a Michelson interferometer in which interference fringe patterns were generated by the superposition of the beam reflected from the metasurface and the incident reference beam. The acquired phase shift was then extracted by fitting the interference fringe patterns to sinusoidal functions. The experimental setup and the procedure for phase and reflectance measurements is described in Section A.3 of the Appendix. The voltage-tunable optical response of the metasurface was then characterized by measuring the amplitude and phase of the reflection from the nanoantenna array while changing a bias voltage that was collectively applied to all antennas, resulting in a uniform change in phase across the metasurface.

Figure 2.9c shows the experimentally measured reflectance as well as a total acquired phase shift of 223° for the light reflected from the fabricated metasurface. The operating wavelength was chosen to be $\lambda = 1548$ nm such that the phase shift provided by the metasurface could be maximized. Notably, considerably larger amplitudes than those reported in full-wave simulations are obtained. This phenomenon has been observed previously [42, 53] and is attributed to a misalignment in the incident polarization. As the misaligned component of the incident light does not interact with the antenna, this effect leads to increased reflected intensity normal to the metasurface. Furthermore, since the misaligned component does not contribute to the

accumulated phase shift, we assume reduced reflectance to approximate the actual amplitude contributing to the beam steering performance. Thus, a constant offset of $\Delta_r = 6.6\%$ is subtracted from the measured reflected light intensity (dashed line in Fig. 2.9c), leading to a minimum reflectance of 1%. The offset was accounted for in the array factor calculation by increasing the intensity at $\theta = 0^\circ$ by $\Delta_r = 6.6\%$. This approach was verified for previously measured far-field radiation patterns obtained using forward design [42], as discussed in Section A.4 of the Appendix. Finally, array-level optimization was performed using the measured phase shift and the actual approximated amplitude. Due to the difference between the work functions of Au and ITO, the ITO layer is slightly depleted at zero applied bias [30]. Thus, to avoid breakdown of the gate dielectric during beam steering measurements, we omit bias voltages below -3.6 V. Hence, a bias voltage range of [-3.6 V, +4.8 V] was used for the optimization, as indicated by the gray box in Fig. 2.9c. As a result, a phase shift of $\Delta\phi = 221^\circ$ was obtained.

The forward-designed and optimized array phase and amplitude profiles for experimental demonstration are shown in Fig. 2.10a and b, respectively. We confirmed through full-wave simulations of the forward- and inverse-designed array profiles that the fabricated reflectarray metasurface could be treated using the independent scatterer approximation, as shown in Fig. 2.11, vindicating our approach to an array-level inverse design.

Figure 2.12a illustrates the analytically obtained beam steering performances using forward-designed four-level staircase phase profiles with repetition numbers (RN) varying from RN = 3 to 6 (Fig. 2.10a). The far-field radiation patterns for forward design are illustrated in gray, and the corresponding results obtained using array-level inverse design are overlaid in color. As can be seen, even though sidelobes are not entirely removed due to a reduced phase modulation with covarying amplitudes, a considerable sidelobe suppression that increases beam directivity is achieved (Table 2.1). We note that while the optimization was performed for the entire half-space (*i.e.*, additional sidelobes at larger polar angles were suppressed to increase directivity), we only visualize and evaluate the directivity for the experimentally detectable range from -23° to $+23^\circ$.

As a comparison, the experimental measurements for the beam steering active metasurface using forward- and inverse-designed array profiles are illustrated in Fig. 2.12b. Increased sidelobes as well as increased relative intensities compared to the analytically computed case, in particular for the specularly reflected light, are

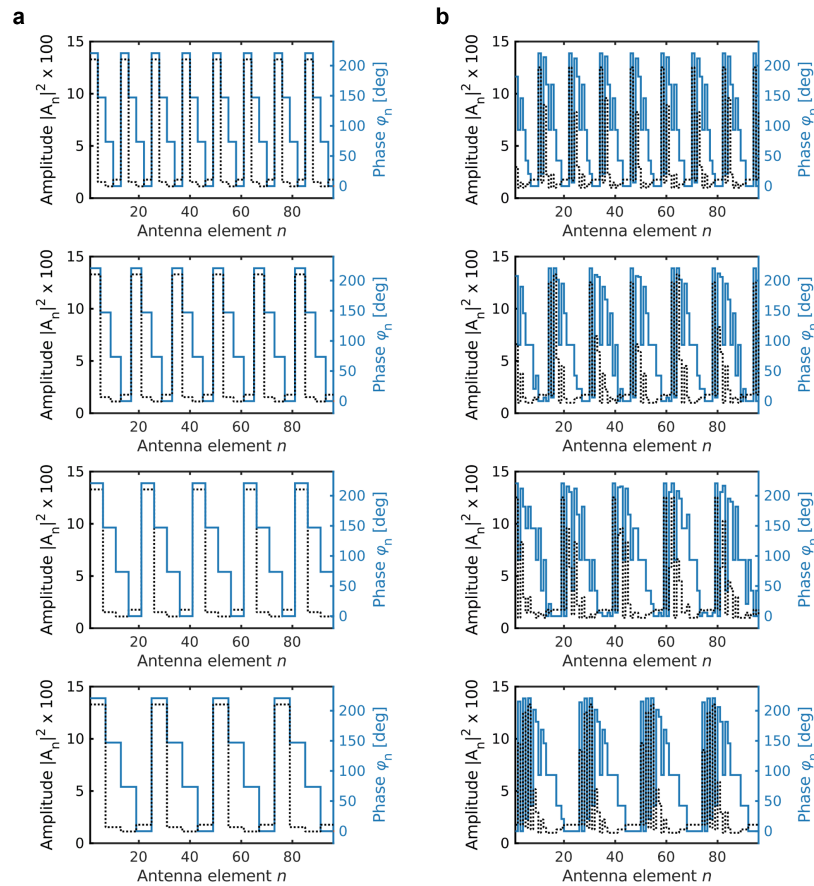


Figure 2.10: **Forward-designed and optimized array profiles for experimental demonstration.** Spatial array amplitude (black) and phase (blue) profiles for (a) forward and (b) inverse design used in experiments. In (a), the repetition number of the staircase phase profile is varied from $RN = 3$ (top) to 6 (bottom).

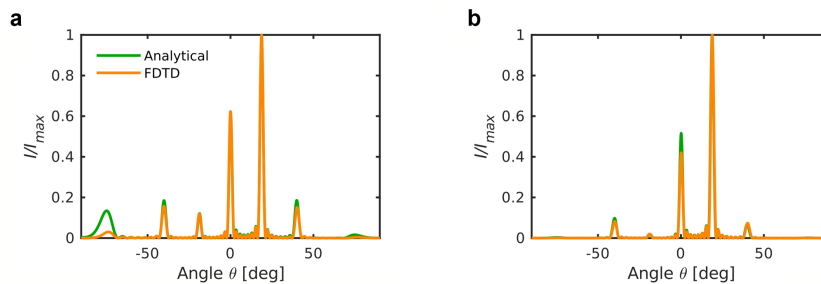


Figure 2.11: **Comparison of far-field radiation patterns with array-factor calculations (green) and FDTD simulations (orange).** Normalized intensity I/I_{\max} vs polar angle θ with (a) staircase forward design with a repetition number of $RN = 3$, and (b) array-level inverse design approach. The operating wavelength is $\lambda = 1545$ nm.

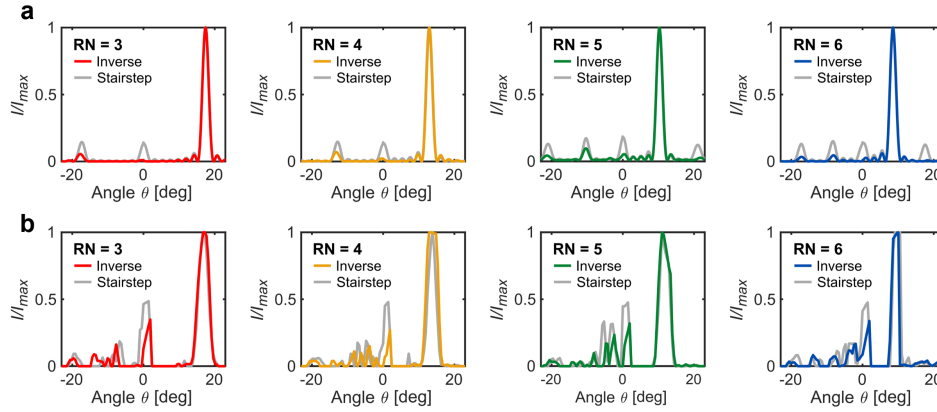


Figure 2.12: **Experimental demonstration of beam steering with forward and array-level inverse design.** (a) Analytically calculated and (b) experimentally measured far-field radiation patterns obtained using forward- (gray) and inverse-designed array profiles (colored). Forward designs are obtained using a four-level staircase phase profile with repetition number varying from $RN = 3$ to 6 (left to right). All figures are plotted for the experimentally detectable angular range from -23° to $+23^\circ$.

	analytical, forward	analytical, inverse	experimental, forward	experimental, inverse
$\theta_r = 17.4^\circ$ ($RN = 3$)	16.1	19.8 (+23%)	8.7	9.7 (+11%)
$\theta_r = 12.9^\circ$ ($RN = 4$)	16.2	19.6 (+21%)	10.2	9.8 (-5%)
$\theta_r = 10.3^\circ$ ($RN = 5$)	13.9	18.3 (+32%)	8.4	9.6 (+15%)
$\theta_r = 8.5^\circ$ ($RN = 6$)	13.8	19.7 (+43%)	9.6	12.0 (+25%)

Table 2.1: **Analytically computed vs experimentally measured directivity D** for $\theta = [-23^\circ, +23^\circ]$.

reported in both forward and inverse design. Notably, in the experiments conducted for staircase phase gradient profiles with repetition numbers varying from 3 to 6 (*i.e.*, $RN = 3, \dots, 6$), inverse design has resulted in an overall reduction in reflected optical power that is spuriously radiated outside the main steered beam, including specularly reflected power. The discrepancies in the amount of power radiated into undesired sidelobes between the analytical computations and experimental measurements are caused by the interplay of several effects, including antenna reflectances that are different from the assumed values, as well as a reduction in the available phase

modulation range. Reduction in the achievable phase modulation range is caused by extrinsic damage from application of large bias voltages which results in a change in the leakage current as well as the breakdown field of the gate dielectric. Figure 2.13 shows the phase reduction over three consecutive measurements for two different metasurfaces to illustrate this effect. Since the fabricated metasurface operates around phase modulation values that are near the previously reported values of $\Delta\varphi_{\text{threshold}}$ (Fig. 2.6b), further reduction in the phase modulation range can result in deviations of the beam steering performance from that analytically predicted using both forward- and inverse-designed array profiles. Furthermore, it should be noted that small variations in nanoantenna size can be introduced during metasurface fabrication. As a result, one can expect inconsistencies in amplitude and phase for individual scattering elements compared to the collectively measured optical response. Since the current experimental capabilities do not allow for an amplitude and phase measurement on a single-antenna basis, the notion of a phase/amplitude error becomes a crucial topic of discussion that is further investigated in the subsequent section. Notwithstanding the mentioned challenges, we were able to demonstrate that nonintuitive, inverse-designed array profiles can reduce spurious power coupled into sidelobes and thus enhance beam steering performance. For the measurements shown in Fig. 2.12b, a maximal increase in directivity of 25% was obtained in comparison to the respective forward design for $\theta_r = 8.5^\circ$ (Table 2.1). In addition, inverse design decreased specular reflection by an average of 33%. We note that a broadening of the main lobe due to experimental angular resolution errors resulted in lower beam directivity for $\theta_r = 12.9^\circ$ (RN = 4). Nonetheless, the peak sidelobe intensity was reduced by 43% in this case.

2.6 Beam steering arrays with phase disorder

The experimental realization of optimized, nonintuitive array designs is challenged by various sources of nonideality, error and noise, such as discrepancies in actual phase and amplitude as a result of inconsistent nanoantenna sizes post-fabrication, errors in bias application or interantenna coupling. The validity of the independent scatter model was verified *via* full wave electromagnetic simulation for both forward and inverse design in the case of the experimentally studied transparent conducting oxide metasurface (Fig. 2.11). However, this fundamental assumption becomes nontrivial for alternative metasurface platforms exhibiting leaky resonant modes. As a consequence, the resulting deviation from the optimized phase and amplitude

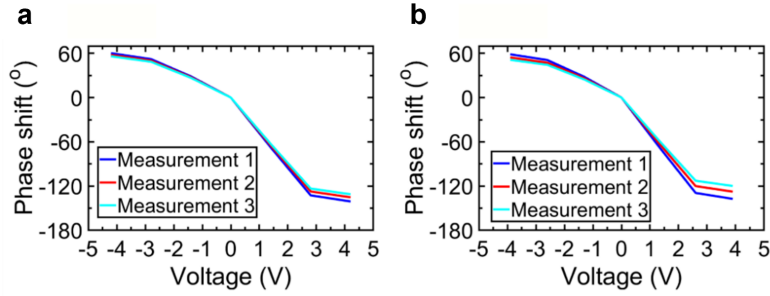


Figure 2.13: **Reduction in phase shift over consecutive measurements.** (a) A maximum phase shift of 201° , 193° , and 187° was obtained for the first test sample in the first, second, and third round of the phase measurement, respectively. (b) The phase modulation provided by the second test sample was measured to be 196° , 182° , and 171° in three consecutive measurements.

profiles are expected to cause additional scattering in undesired directions that lowers the directivity.

Here, we perform a sensitivity analysis of the optimized designs to error and noise. To do this, we systematically introduce random phase noise and identify threshold values beyond which a strong decrease in directivity is observed. We characterize f as the fraction of antennas in the array differing from their original phase value $\varphi_{\text{original}}$. The phase disorder range δ further quantifies the maximal amount of phase error at each deviating element (Fig. 2.14a). The disordered phase values $\varphi_{\text{disorder}}$ are calculated as

$$\varphi_{\text{disorder}} = \varphi_{\text{original}} + \text{rand} \left[-\frac{\delta}{2}, +\frac{\delta}{2} \right]. \quad (2.9)$$

Here, $\text{rand}[x, y]$ computes a uniformly distributed random value between x and y . Capping of $\varphi_{\text{disorder}}$ at the minimal and maximal phase values ensures that upon adding phase noise, the antenna phase stays within the available phase modulation range. To account for the covarying amplitude and phase, $\varphi_{\text{disorder}}$ is additionally mapped to the corresponding amplitude, which is obtained from the antenna-specific optical response.

Figure 2.14b illustrates the error tolerance of an inverse-designed array phase profile for our example field-effect tunable active metasurface steering at $\theta_r = 18.3^\circ$ (Fig. 2.4a). The optimized array design is insensitive to small phase errors corresponding to small f and/or small δ . In the limiting case of $f = 100\%$, phase error is introduced

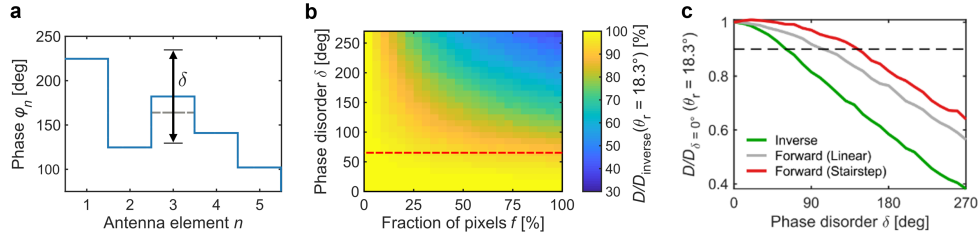


Figure 2.14: Phase noise introduction in spatial phase profile. The phase disorder range δ is defined such that it allows distortion of each antenna phase by a uniformly distributed random phase value between 0° and $\pm\delta/2$. The schematic illustrates a phase disorder range of $\delta = 100^\circ$. The gray dashed line represents the disordered phase value. (b) Phase disorder range δ vs fraction of antennas f that are changed from their original value for the optimized array design illustrated in Fig. 2.4a for $\theta_r = 18.3^\circ$. The red dashed line marks the threshold performance of $0.9 \times D_{\text{inverse}}$ in the limiting case of $f = 100\%$. (c) Relative change in directivity for increasing phase disorder δ for steering at $\theta_r = 18.3^\circ$ for inverse-designed arrays (green), forward-designed linear (gray) and stairstep (red) phase profiles. The black dashed line marks the threshold directivity. The data sets in (b) and (c) are averaged over 100 implementations.

into every antenna in the entire array. This case is characteristic of interantenna coupling that would lead to a distortion of the phase at each antenna due to its nearest neighbors. Our analysis shows that optimized designs can tolerate up to $\pm 30^\circ$ phase error ($\delta = 60^\circ$) before reaching the directivity threshold of $0.9 \times D_{\text{inverse}}$. In comparison, our analysis shows that the threshold performance of $0.9 \times D_{\delta=0^\circ}$ is obtained for larger amounts of phase disorder δ in the case of forward designs. As shown in Fig. 2.14c, $\delta_{\text{inverse}} = 60^\circ < \delta_{\text{forward,lin}} = 100^\circ < \delta_{\text{forward,step}} = 140^\circ$. Here, $D_{\delta=0^\circ}$ is the beam directivity of the respective array design without any introduction of phase noise. It is to be noted that directivities of stairstep profiles can surpass $D_{\delta=0^\circ}$ for $\delta \leq 40^\circ$. Since stairstep designs represent simplified gradient phase profiles, small amounts of phase disorder can lead to closer resemblances to higher-directivity linear array designs. The reduced error tolerance for inverse design is understandable, considering that the nonintuitive inverse-designed arrays typically exhibit more disordered phase profiles, even prior to any introduction of noise. As a result, they tolerate smaller errors before reaching substantial loss of information. Nonetheless, the findings reported in this analysis imply a considerable tolerance of phase noise for inverse-designed spatial array profiles.

2.7 Realizing advanced metasurface functionalities

Until now, our focus was on using array-level optimization for the demonstration of optimized beam directivity. Based on the target application, however, it might be desirable to realize alternative metasurface functions. In the following, we apply the iterative optimization approach introduced in Section 2.3 to optimize the spatial phase and amplitude configuration for (i) maximal power efficiency of the steered beam given a nonideal antenna response, (ii) the creation of flat top beams and beams with variable widths, and lastly (iii) simultaneous steering of beams in two desired directions.

Power efficiency of steered beams

The FOM quantifying the beam steering performance in this work was chosen to be the beam directivity D . It is a unitless quantity that depends on the ration of the intensity at the desired steering angle θ_r to the amount of power scattered into all directions normalized by the solid angle, as discussed in Eq. (2.4). Thus, it remains unaffected by scaling of the far-field radiation patterns by a constant (intensity) factor. Directivity is a common metric used to analyze the performance of RF phased arrays. An ideal metasurface array with $d_x = 400$ nm operating at $\lambda = 1550$ nm ($d_x/\lambda \sim 0.25$) approaches performances that are reported with an array of parallel short dipoles [72]. In addition, the optimized sidelobe level reported in this work corresponds to values that are generally obtained for phased arrays with a complete phase modulation over 360° [73].

The power efficiency η is determined by the absolute amount of power that is steered into the main lobe compared to the total input power. For an array profile with varying amplitudes, η is calculated as

$$\eta(\theta_r) = \frac{P_m(\theta_r)}{P_{\text{scat}}} \cdot A_{\text{eq}} \quad (2.10)$$

where P_m is the power scattered into the main lobe steering at θ_r and P_{scat} is the total scattered power. The ratio of P_m and P_{scat} is multiplied by the equivalent amplitude A_{eq} that would be required in an array of antennas with constant amplitude to generate an equivalent amount of scattered power. Thus, $A_{\text{eq}} = P_{\text{scat}}/P_{\text{input}}$ with P_{input} being the input power. Note that P_{input} can be determined by assuming an ideal reflectarray with constant, unit amplitude and a complete phase modulation over 360° .

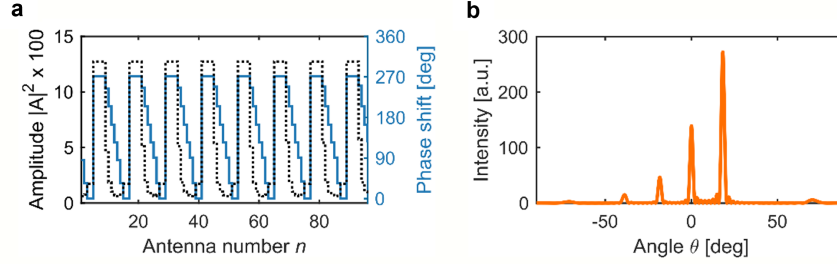


Figure 2.15: **Optimization for power efficiency.** (a) Inverse-designed array amplitude (black dotted) and phase (blue) profiles and (b) far-field radiation patterns for a power efficiency optimization. The optimization was performed based on the optical response of the field-effect tunable metasurface introduced in Fig. 2.2.

Due to the strong absorption in the active antenna element [42, 74], the power efficiency of the beam steering arrays studied in this work is strongly limited. Consequently, the optimized directivity discussed in Section 2.3 (Fig. 2.4a, b) results in a power efficiency of 0.9%, even though 86% of the total scattered power is directed into the main lobe. Here, we demonstrate as a proof-of-concept that the same inverse design algorithm can also be applied to a power efficiency optimization. For this purpose, the figure of merit is adapted to $\text{FOM} = \eta(\theta_r)$. Figure 2.15a shows the optimized array profile as well as the corresponding radiation pattern (Fig. 2.15b) for optimal power efficiency at $\theta_r = 18.3^\circ$. It is to be noted that the increase in power efficiency comes at the cost of beam directivity, as the algorithm aims to increase the occurrence of large amplitudes in the antenna array to enhance efficiency. Therefore, the amplitude modulation increases, leading to a reduction in beam directivity. Meanwhile, the opposite trend holds true for a directivity optimization: Inverse design aims to minimize amplitude modulation to reduce sidelobes. As the main phase shift occurs in a low amplitude regime, the minimization of amplitude modulation results in reduced power efficiencies. For reference, the corresponding directivity and efficiency values are tabulated in Table 2.2.

	Directivity D	Efficiency η
Forward design, stairstep	39.5	2.1%
Inverse design, directivity opt.	72.7	0.9%
Inverse design, efficiency opt.	41.9	2.7%

Table 2.2: **Optimized directivity D and efficiency η for steering at $\theta_r = 18.3^\circ$.**

As the scattered light amplitudes are the limiting factor for power efficiencies in beam steering metasurfaces, we would like to remark that they can be strongly enhanced with the use of active metasurfaces exhibiting higher reflectance or transmittance values, such as all-dielectric metasurfaces [20, 35, 75].

Variable beam widths and flat top beams

The beam width (or FWHM) is determined by the aperture size and varies as function of steering angle, as illustrated in Fig. 2.4. Based on the specific modality of optical imaging or sensing, it may be beneficial to control the beam width in addition to the steering angle to ensure uniform information collection from all directions. While the minimal beam width of light scattered from an array of antennas is fixed by the aperture size, we can use array-level inverse design to generate spatial phase and amplitude configurations that result in larger beam widths. This can be used in cases where, *e.g.*, coarse sampling of a scene is desired before finer details are imaged [76]. In the following, we illustrate first the generation of variable beam widths for a steered beam with an ideal metasurface and then demonstrate realization of flat top beams using the nonideal active metasurface introduced in Fig. 2.2.

Figure 2.16 shows the forward-designed and optimized spatial phase profiles for an ideal metasurface with 360° phase modulation and unity amplitude steering a beam at $\theta_r = 20^\circ$. Similar to the case studied in Fig. 2.1, we assume an aperture with 100 antennas arranged at a spacing of $d_x = 400$ nm operating at 1550 nm. Given the metasurface aperture, conventional forward design of the phase profile yields a beam with a FWHM of 2° (Fig. 2.1a, b). To design array profiles yielding a target FWHM, F_t , we write our objective function as a minimization problem with

$$\text{FOM}(F_t, \theta_r) = 50 \cdot |\text{FWHM}(\theta_r) - F_t| + 10 \cdot \frac{I_{\max,2}}{I(\theta_r)} + \frac{\text{avg}\left(I(\theta_r - \frac{F_t}{2}), I(\theta_r + \frac{F_t}{2})\right)}{\int I(\theta) d\theta}. \quad (2.11)$$

Here, the first term aims to minimize the difference between the FWHM of the beam steered at θ_r and the target FWHM, F_t , the second term aims to maximize the peak intensity at the target angle θ_r in comparison to the second largest peak, and the last term is an adapted directivity term which aims to maximize intensity across the FWHM while minimizing undesired sidelobes in all directions. The FOM is formulated as a weighted sum, where the weights are chosen such that they yield optimal radiation patterns for a range of target F_t values. The optimized spatial phase

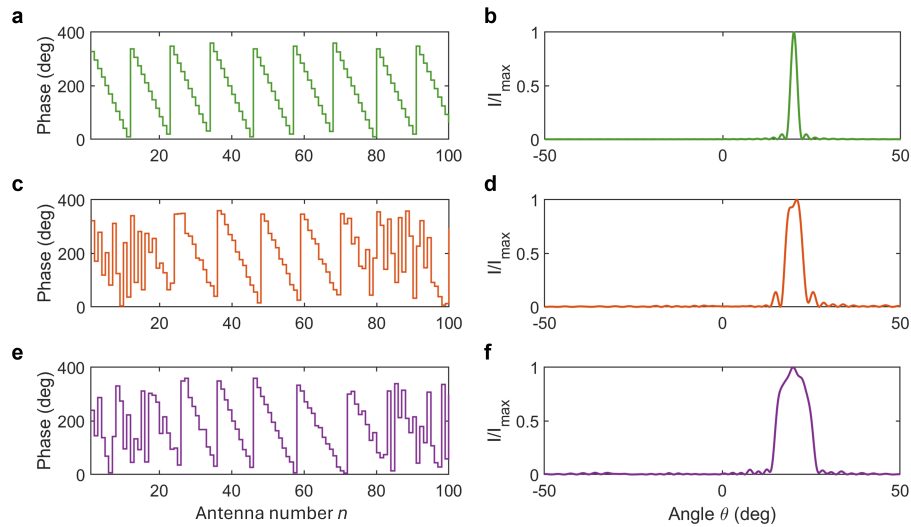


Figure 2.16: **Variable FWHM of steered beam with ideal metasurface.** Spatial phase profile over an array of 100 antennas spaced at $d_x = 400$ nm (left) and corresponding normalized intensity vs polar angle at $\lambda = 1550$ nm (right). The three cases illustrate forward design (green; a, b), optimization for a FWHM of 5° (orange; c, d), and optimization for a FWHM of 10° (violet; e, f). Ideal antenna properties, *i.e.*, unity amplitude and 360° phase modulation, are assumed for this optimization.

profiles and the corresponding radiation patterns for $F_t = 5^\circ$ (Fig. 2.16c, d) and $F_t = 10^\circ$ (Fig. 2.16e, f) are shown as exemplary cases. The optimization appears to artificially reduce the aperture of the metasurface by imposing a phase gradient over a smaller subset of antennas (‘steering aperture’) and setting noninutitive phase values outside (‘nonsteering aperture’). Similar approaches with forward design of the nonsteering aperture with constant phase values result in strong specular reflection. Therefore, further studies are needed to analyze the degree of phase randomness required in the nonsteering aperture to yield a tunable FWHM with low sidelobe levels. Nevertheless, for realistic active metasurface designs, the use of array-level inverse design is expected to yield improved results by additionally taking into account the device-specific optical response.

In applications that require a uniform illumination across a range of angles, the objective changes to generating flat top beams rather than having beams with a wider FWHM, as shown in the example above. For this, the FOM is chosen to be one that minimizes the difference of the actual radiation pattern from a target radiation pattern, where the target radiation pattern resembles an angular pass-band with zero and one normal intensity regimes. Figure 2.17 shows the optimized array

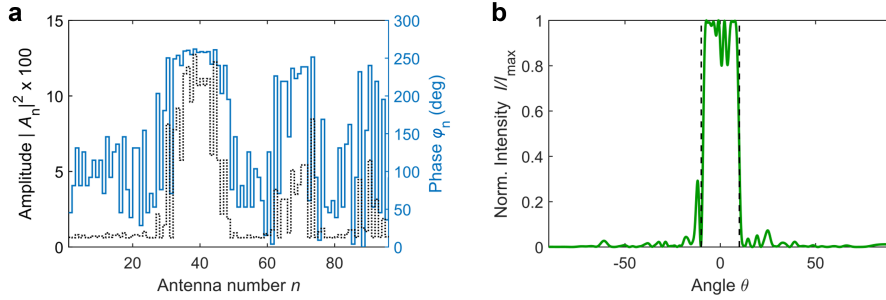


Figure 2.17: **Flat top beam with nonideal active metasurface.** (a) Inverse-designed array amplitude (black, dotted) and phase (blue) profiles and (b) corresponding normalized intensity as function of polar angle for nonideal active metasurface introduced in Fig. 2.3. The black dashed lines at $\pm 10^\circ$ indicate the target angular width of the flat top beam.

phase and amplitude profile as well as the corresponding radiation pattern for a flat top beam with an angular width of $\pm 10^\circ$. In this case, the optimization is performed for the nonideal active metasurface introduced in Section 2.3. Despite the nonideal optical response, the optimization algorithm is able to generate nearly uniform intensity across the target angular range with minimal undesired sidelobes. The uniformity of illumination can potentially be further improved by implementing constraints that limit the deviation of the actual normalized intensity from unity; however, this is likely to come at the cost of increased sidelobes.

Simultaneous steering of multiple beams

Until now, the focus of the optimization was to control the properties of one steered beam. However, the same array-level optimization can also be used to generate nonintuitive spatial amplitude and phase profiles that can simultaneously steer multiple beams in independent directions. This function could be used for increased scanning speeds in optical sensing applications, or for simultaneous detection of multiple objects. Here, we illustrate this principle based on the example of two independently steered beams with the nonideal active metasurface introduced above. The FOM that needs to be minimized for this purpose is chosen to be

$$\text{FOM}(\theta_{r,1}, \theta_{r,2}) = \frac{1}{I(\theta_{r,1})} + \frac{1}{I(\theta_{r,2})} + \int I(\theta) d\theta. \quad (2.12)$$

Here, the first two terms aim to maximize the intensity at the target steering angles $\theta_{r,1}$ and $\theta_{r,2}$, and the last term aims to minimize sidelobes. In addition to this

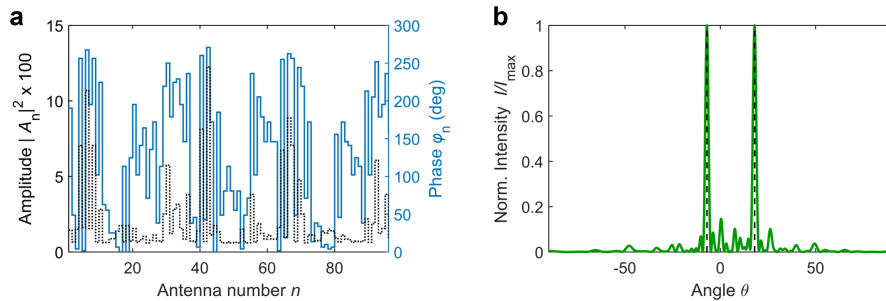


Figure 2.18: **Simultaneous steering of two beams at independent angles.** (a) Inverse-designed array amplitude (black, dotted) and phase (blue) profiles and (b) corresponding normalized intensity as function of polar angle for nonideal active metasurface introduced in Fig. 2.3. The black dashed lines indicate the target steering angles $\theta_{r,1} = -7^\circ$ and $\theta_{r,2} = +18^\circ$.

objective function, we implement constraints to fix the intensity of the two steered beams with respect to each other as well as the specularly reflected beam. For the results shown in Fig. 2.18 for two beams steered at -7° and $+18^\circ$, respectively, we also implemented two constraints requiring $I(\theta_{r,i}) \geq 8 \cdot I(\theta = 0^\circ)$ with $i = 1, 2$ corresponding to the two beams. The steering angles were arbitrarily chosen in this example and similar results were observed for different sets of angles. It can be seen that while the optimization yields two directive beams steering at the target angles, there are an increased number of sidelobes compared to the case of a single steered beam. Due to this, we anticipate that scaling of this approach to an increased number of steered beams will require tolerance for larger sidelobe levels. In addition, continuous scanning of multiple independent beams with array-level optimization is a computation heavy problem. In Chapter 3, we will present an alternative, scalable approach for multi-beam steering using spatio-temporal modulation.

2.8 Outlook

Real-time array-level optimization

The array-level inverse design approach presented in this chapter is based on a numerical framework which assumes independent scatterers with localized modes. However, many recent designs utilize delocalized modes in nonlocal metasurfaces [77–79]. For such structures, we need to develop more sophisticated analytical models, or we must shift to performing array-level optimization using full-wave simulations instead [80]. This method, however, is considerably more computation-

ally expensive and may restrict our abilities to compute the array configuration over a wide range of angles.

To address this challenge, one could perform real-time array-level optimization experimentally. For instance, in the case of beam steering metasurfaces, a camera could capture a Fourier space image at each iteration, which would then serve as an input for an optimization algorithm. The algorithm would extract the normalized intensity as a function of the polar angle and adjust the voltage configuration to optimize beam directivity. An iterative optimization similar to the one proposed in Section 2.3 could be adapted for this purpose. The primary source of time consumption would be image acquisition, rather than performing full-wave simulations for the entire array at each step. Ultimately, the computational time required would also depend on the number of antennas in the array that need to be configured to achieve a desired metasurface function. An additional benefit of this approach is that it could potentially account for experimental artifacts, such as nonuniform antenna widths, inhomogeneities in bias application, or slight misalignment, that may lead to spurious scattering in Fourier space.

Co-optimization framework for active metasurfaces

In many applications, it is necessary to not only optimize the directivity of steered beams but also maximize power efficiency. While the first part of Section 2.7 outlines a potential pathway for achieving this, power efficiency is ultimately constrained by the optical response of the antenna element, specifically, its scattered light amplitude and phase. In recent years, researchers have developed new design strategies to achieve higher efficiency active metasurfaces, including the use of various resonator designs yielding alternative electromagnetic modes [31, 80] and the exploration of new active materials [81–83].

Designing highly efficient active metasurfaces ultimately requires optimizing material choice, resonator design, and the overall system-level array design. In this context, the proposed array-level inverse design is crucial for the hierarchical co-design of both the array and the active antenna element in tunable metasurfaces. This approach aims to simultaneously optimize the array configuration *via* the external control variable, the nanoantenna shape, as well its complex dielectric function for a desired metasurface response. For practical implementation of hierarchical co-design, an incremental approach is most suitable. This would begin by combining array-level optimization with resonator design [84] and subsequently integrating res-

onator design with material choice, before developing a comprehensive optimization framework that addresses all three components simultaneously. Different optimization algorithms may be more suitable for different tasks. For example, resonator design (with a fixed material choice) could employ adjoint optimization [85–87] or machine learning [60, 88]. For optimizing and discovering new active materials, various data-driven strategies — such as machine learning, Bayesian optimization, density functional theory, and combinations thereof — could be pursued [89–92].

Enhancing control through space-time modulation

The final part of Section 2.7 proposes the use of array-level optimization for simultaneously controlling multiple independently steered beams. This approach enables control over both the angles and the relative intensities of the steered beams. While feasible for two beams, the optimization of the FOM becomes increasingly challenging as the number of beams increases, due to nonideal device characteristics. The complexity is further heightened when the beams are required to perform different dynamically tunable functions, such as steering and focusing.

In Chapter 3, we present a scalable approach for what we term *active multitasking* metasurfaces, which leverage space-time modulation [93–96]. In addition to the spatial modulation previously discussed, this approach utilizes high-frequency temporal modulation as an additional control variable. Temporal modulation of the metasurface at kHz to MHz frequencies allows for controlled frequency shifts in the scattered beam. By precisely tailoring the waveform applied to each metasurface electrode, we demonstrate the ability to independently control the spatial properties of beams with different frequency shifts. This method offers a scalable solution for controlling a large number of independent beams, theoretically limited only by the bandwidth of the experimental setup. We will discuss practical limitations and trade-offs between multiplexing and power efficiency in detail in the following chapter.

2.9 Conclusions

In conclusion, we have developed a versatile array-scale inverse design approach for active metasurface antenna arrays. Inverse design allows the array phase and amplitude profiles to be prescribed by change in the operating parameters of identical active antennas, rather than by geometrical shape optimization of individual antennas. We found that iterative optimization gives rise to nonintuitive array designs that enable high-directivity beam steering with nonideal antenna components.

Specifically, for the field-effect tunable metasurface analyzed here, directivities were enhanced by up to 84% compared to previously demonstrated forward designs, with sidelobe suppression approaching ideal values. Near-ideal performance was demonstrated for continuous beam steering by optimization at angular increments of 0.5° . Inverse design moreover reduced the required phase modulation range for high beam directivity. High-directivity beam steering was reported for a phase modulation range as small as 180° . Furthermore, enhanced beam directivities using nonintuitive, inverse-designed array profiles were reported for an experimentally fabricated metasurface exhibiting a phase modulation of approximately 220° . Finally, a sensitivity analysis to antenna phase noise indicated that optimized designs could tolerate approximately $\pm 30^\circ$ phase error at each antenna without significant performance losses.

While the current work illustrates the power of an array-level inverse design on the beam steering performance in active metasurfaces, the same optimization framework can also be applied to a variety of alternative objective functions and active metasurface platforms. Similarly, a system-level optimization can also be performed for passive metasurfaces that rely on nonideal antenna components [97].

The results presented in this work constitute a compelling design approach for high performance in nonideal active metasurfaces. As an outlook, we expect that by combining array-level inverse design with optimization protocols applied to materials selection [98, 99], a modern era for co-design of materials, device and system is arriving for nanophotonics. Ultimately, such an approach will enable the realization of highly efficient multifunctional metasurfaces capable of many functions beyond beam steering.

*Chapter 3*ACTIVE MULTITASKING METASURFACES USING
SPACE-TIME MODULATION

The material in this chapter was in part presented in [95].

Active metasurfaces, with their ability to dynamically control optical properties at the subwavelength scale, provide a versatile platform for advanced light manipulation. In the previous chapter, we demonstrated how this characteristic enables the realization of multiple tunable functions using a single metasurface. Example functions included beam steering, engineering of flat-top beams, and multi-beam steering, achieved through an array-level optimization approach [46]. We observed, however, that as the complexity of the target function increases — particularly when simultaneous optimization for multiple tasks is required — relying solely on spatial control of the array’s phase and amplitude properties becomes increasingly challenging.

In this chapter, we address this limitation by introducing an additional control variable into the system. Through high-frequency modulation of the applied voltage waveform, we create a *synthetic dimension* [100–102], which enables multiplexing of functionality in the frequency domain. This approach paves the way for metasurfaces capable of performing multiple, dynamically tunable tasks simultaneously by encoding them in distinct frequency channels. We refer to such devices as *active multitasking metasurfaces*.

The chapter begins with a review of the theoretical framework for time modulation and its role in engineering the frequency response from a metasurface. Following a brief review of previous experimental work, we present a proof of concept for electrically tunable space-time metasurfaces, utilizing field-effect tuning in indium tin oxide (ITO) with two interdigitated electrodes [95]. Building on this foundation, we extend the design to include 32 independently addressable electrodes, develop an electronic addressing scheme, and demonstrate active beam switching to tunable angles. Finally, we discuss potential multiplexing strategies for these metasurfaces in various applications and highlight remaining challenges and future directions.

3.1 Space- and time-varying media

Wave propagation at the interface between two isotropic media is governed by Snell’s law of reflection and refraction, a fundamental principle of optics that ensures conservation of transverse wave momentum across the interface [103]. Leveraging this principle, bulk optical elements are traditionally designed to introduce gradual, spatially varying changes in the accumulated phase shift of light beams propagating through the medium. In comparison, metasurfaces introduce subwavelength-scale spatial modulations of the refractive index. In passive metasurfaces, this is achieved by carefully designing resonator geometries, and in active metasurfaces by externally modulating the local permittivity. These spatial modulations impart momentum to incoming light, as described by the generalized form of Snell’s law [22], detailed in Section 2.1. This approach has enabled the development of various chip-scale optical components, including those for anomalous reflection [23, 104, 105], flat lenses [106–108], and polarization control [109–111].

While spatial structuring of metasurfaces imparts momentum discontinuities in the scattered light, the frequency of light is typically conserved. Although active metasurfaces can change their properties in time, their response is often slow. This characteristic limits their operation to the quasi-static regime (Fig. 1.3), where slow temporal modulations allow switching between different spatial phase gradient configurations while preserving the incident wavelength. In this regime, momentum can be imparted to light, enabling spatial wavefront shaping, but the optical wavelength remains unchanged.

To overcome this limitation, there is increasing interest in time-varying media, which exploit rapid modulations of optical properties (*e.g.*, refractive index) in response to external stimuli. These rapid modulations create a *temporal interface*, analogous to the previously discussed spatial interface, where light momentum is conserved, but its frequency is altered due to energy exchange with the medium [112]. Temporal control of electromagnetic waves has led to the demonstration of exotic optical phenomena such as frequency mixing [113], harmonic beam shaping [93], and the breaking of Lorentz reciprocity [44, 114, 115].

Metasurfaces provide a unique platform for integrating spatial and temporal modulation schemes, enabling the realization of space-time varying media [44, 116–120]. Spatiotemporal modulation of dielectric media has been studied for decades and has produced radio frequency (RF) devices with functionalities such as optical isolation [121], pure frequency mixing [122], and amplification of traveling waves

[123]. Recent advancements in digital coding architectures, in which biasing PIN diodes alters the phase response of the scattered light, have realized a more general spatiotemporal platform for frequency-multiplexed beam steering and shaping at microwave frequencies [93, 124, 125]. At optical frequencies, optical pumping of passive phase gradient metasurfaces consisting of nonlinear optical materials has been demonstrated [112, 126, 127]. However, such systems require the integration of high-power pump pulses, limiting their practicality for many applications.

In this work, we demonstrate electrically tunable metasurfaces that operate at telecommunication wavelengths and are modulated at radio frequencies to achieve spatiotemporal control over the scattered light wavefront and spectrum. Field-effect tunable metasurfaces are ideal candidates for the demonstration of space-time varying media, as they can be modulated with frequencies up to tens of MHz [30]. Our active metasurface employs ITO as an active semiconductor layer that undergoes a change in charge carrier modulation, and therefore dielectric permittivity. As described in Section 2.3, this modulation, combined with a geometrically resonant plasmonic stripe antenna [30, 42], results in a modulation of the reflected light intensity. The strong mode confinement achieved in this design enables localized control over the scattered light properties.

We present two implementations of this design. In the first, stripe antennas are connected to an interdigitated pair of electrodes, and in the second, the metasurface incorporates 32 independently addressable electrodes. These layouts enable uniform reflectance control through collective modulation of all antennas enabling control over the spectrum of light, or the design of two- or multi-level reflectance gratings that generate diffraction of frequency-shifted beams in space, as outlined in the following section.

3.2 Design principle for space-time metasurfaces

Active metasurfaces with individually addressable elements enable dynamic control over light propagation through spatial and temporal modulation schemes. These configurations are illustrated in Fig. 1.3 and include three key cases: (1) quasi-static spatial modulation, (2) purely temporal modulation, and (3) combined space-time modulation. Each case provides unique functionalities for tailoring the momentum and frequency of light.

In the quasi-static configuration (Fig. 3.1a), the metasurface exhibits a spatially varying but time-invariant refractive index profile. The far-field response is de-

scribed as the summation of electric fields reflected from n metasurface elements, with the response from each element described by

$$E(x, y) = A_n(x, y) \cdot e^{i\varphi_n(x, y)} \cdot e^{i(\mathbf{k} \cdot \mathbf{r} - \omega t)}. \quad (3.1)$$

Here, A_n and φ_n are the amplitude and phase response of each element as function of their spatial position in x and y , \mathbf{k} is the incident wave vector, \mathbf{r} represents the spatial observation point, ω is the frequency of light, and t the time variable. In the ideal case, where a uniform amplitude and 2π phase modulation are achievable through the refractive index modulation, the metasurface can be configured with a spatial phase gradient, as shown in the top row of Fig. 3.1a. This phase gradient imparts tangential momentum to the reflected light, steering it to a desired angle.

For time-modulated metasurfaces (Fig. 3.1b), the refractive index profile varies temporally but remains spatially invariant. In this case, the time-varying reflected electric field scattered from each element can be expressed as

$$E(t) = A(t) \cdot e^{i\varphi(t)} \cdot e^{i(\mathbf{k} \cdot \mathbf{r} - \omega t)}. \quad (3.2)$$

The frequency response of the scattered light is obtained *via* a Fourier transform of $A(t) \cdot e^{i\varphi(t)}$, revealing frequency sidebands offset from the central frequency by integer multiples of the modulation frequency. For ideal metasurfaces configured with a sawtooth phase profile, the primary frequency shift corresponds to the modulation frequency (*e.g.*, 1 MHz in the example shown in Fig. 3.1b), while higher-order harmonics may arise from non-ideal amplitude-phase relations.

Introducing a phase delay α to the driving waveform does not affect harmonic intensities but imparts a phase $l\alpha$ to each harmonic l . This behavior can be used to decouple phase and amplitude and engineer optical wavefronts in space and time. For example, two independent electrodes driven with the same waveform but $\alpha_1 = 0$ and $\alpha_2 = \pi$ produce a binary $0 - \pi$ phase grating that selectively diffracts odd harmonics.

In the general case of space-time modulation (Fig. 3.1c), the resulting scattered field from each element n is described as

$$E(x, y, t) = A_n(x, y, t) \cdot e^{i\varphi_n(x, y, t)} \cdot e^{i(\mathbf{k} \cdot \mathbf{r} - \omega t + \alpha_n)}. \quad (3.3)$$

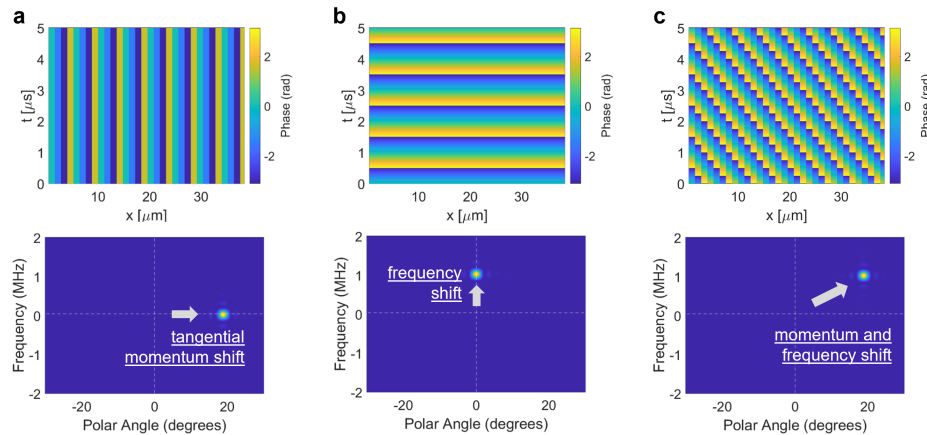


Figure 3.1: Momentum and frequency-shift with space- and time-modulation. Top row: Spatial and temporal configuration of phase response from ideal metasurface (2π phase modulation, uniform amplitude) under different modulation schemes. Bottom row: Corresponding frequency spectrum and scattering angle calculations obtained using Fourier transforms in space and time. Three operational regimes are illustrated: (a) quasi-static control with unit cell size of $1.2 \mu\text{m}$, (b) time-modulated operation with a 1 MHz sawtooth waveform, and (c) space-time modulation with a phase delay of $\pi/2$ between sawtooth waveforms applied to adjacent unit cells.

For a sawtooth waveform, which produces a single frequency-shifted harmonic with an ideal metasurface, this configuration allows precise steering of the frequency-shifted light. In more complex scenarios involving multiple frequency-shifted beams, tailored waveforms can be engineered for selective steering of target frequencies.

While the examples in Fig. 3.1 assume ideal metasurface arrays with 2π phase modulation and uniform amplitude, practical implementations often exhibit limitations such as reduced phase ranges and covarying amplitude, as discussed in the previous chapter. These limitations lead to the generation of multiple harmonics and variations in the ratios of unmodulated to modulated light. Figure 3.2 demonstrates the changes in the relative conversion efficiency of the 0^{th} and higher order harmonics for a metasurface modulated by a 100 Hz waveform generating a sawtooth phasefront, with varying degrees of phase modulation. The results show that while complete 360° phase modulation suppresses the 0^{th} harmonic and produces a clean $+1^{\text{st}}$ harmonic signal, smaller phase shifts lead to reduced conversion efficiency into the desired harmonic. The specific spectral distribution of a metasurface exhibiting covarying amplitude and phase ultimately depends on the applied time-varying signal and can be analyzed through the Fourier transform of the scattered field.

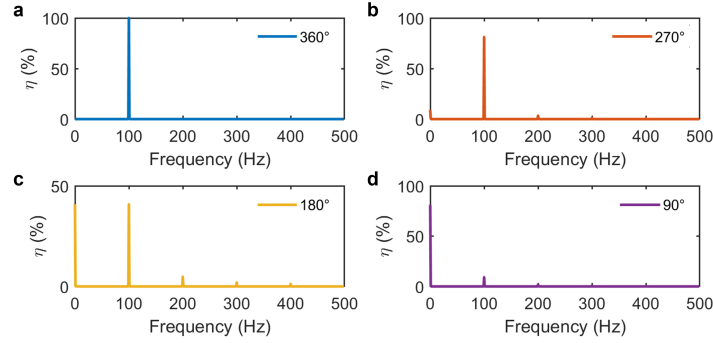


Figure 3.2: **Calculated frequency spectrum of time-modulated metasurface with limited phase modulation.** In all cases, the metasurface is driven with a 100 Hz sawtooth waveform, generating a linearly varying phasefront. The conversion efficiency, η , is presented for phase modulation depths of (a) 360°, (b) 270°, (c) 180°, and (d) 90°. The frequency spectra are obtained through a Fourier transform of the scattered time-modulated fields.

3.3 Time-modulated optical metasurfaces

To experimentally demonstrate time-modulated, and ultimately space-time modulated, metasurfaces, we employ an electrically addressable ITO-based plasmonic metasurface designed to operate in reflection [30]. The design and operational principle align closely with those previously discussed in Section 2.3. We first describe the unit cell design and its quasi-static reflectance properties under applied bias. Subsequently, we introduce the experimental setup for time-modulated measurements and demonstrate how the metasurface response enables tunable frequency shifts under time-modulated operation.

Metasurface design

Figure 3.3a illustrates a unit cell of the active metasurface used in this study. While the carrier modulation mechanism in this ITO-based metasurface mirrors the one described in Fig. 2.9, we adopt a simplified design in this study for ease of fabrication. Each metasurface unit cell comprises a plasmonic stripe antenna over a hafnium oxide/aluminum oxide laminated ($\text{HfO}_2/\text{Al}_2\text{O}_3$, HAOL) layer and an active ITO layer, forming a metal-oxide-semiconductor (MOS) capacitor heterostructure. This structure is patterned on a gold (Au) back reflector, which serves as the back gate, while the plasmonic gold antenna functions as the top gate. When illuminated with transverse electric (TE) polarized light, a gap plasmon resonance confines light within the ITO and HAOL layers, leading to enhanced optical modulation upon biasing.

In the first part of our study, we design a metasurface with two independent electrodes, each contacting alternating groups of 12 antennas. The entire metasurface measures $120 \times 120 \mu\text{m}^2$ (Fig. 2.9b). The two interdigitated electrodes are positioned on the right and left sides of the metasurface area.

Figure 2.9c presents the measured metasurface reflectance under applied bias. The plasmonic resonance, initially at 1475 nm at -4 V, shifts to 1460 nm at 4 V. The operation wavelength throughout this part of the study is 1530 nm. Figure 2.9d shows the voltage-dependent reflectance at this wavelength. The corresponding phase shift at 1530 nm is negligible, as detailed in Appendix B.1. Although the relative modulation is larger on resonance, the shortest wavelength accessible in our experimental setup is 1530 nm, which exhibits a limited relative reflectance modulation ($\sim 8\%$) and near-zero phase shift. Notably, even with these limitations, the device effectively demonstrates space-time diffraction with high directivity, as will be discussed in subsequent sections.

Experimental setup

To study the temporal response of the metasurface, we first modulate all antennas in-phase and measure the reflected frequency spectrum using the experimental setup in Fig. 3.4. The metasurface is illuminated with 1530 nm light which is amplified using an erbium-doped fiber amplifier to enhance the reflected signal strength and enable cleaner measurements. The metasurface is modulated at MHz frequencies using an arbitrary waveform generator (AWG). A fast photodiode connected to a spectrum analyzer captures the reflected light. The output of the spectrum analyzer is fed to a real-time optimization algorithm, which allows the applied waveform to be tailored for a target frequency spectrum. We note that while applied waveforms can be optimized analytically based on the quasi-static response from the metasurface (see Appendix B.2), real-time optimization can account for experimental artifacts, such as changes in the optical response at higher modulation frequencies, ensuring more accurate results, as discussed below.

Because the response times of the photodiode (~ 10 MHz) and spectrum analyzer (~ 1 GHz) are many orders of magnitude slower than the oscillation of the incident laser light (~ 200 THz), only the MHz frequency sidebands imparted on the 1530 nm light are measured. Therefore, the 1530 nm laser light serves as the carrier wave to study the modulation dynamics of the metasurface, while any unmodulated reflected light remains undetected. Since the device primarily operates *via* amplitude

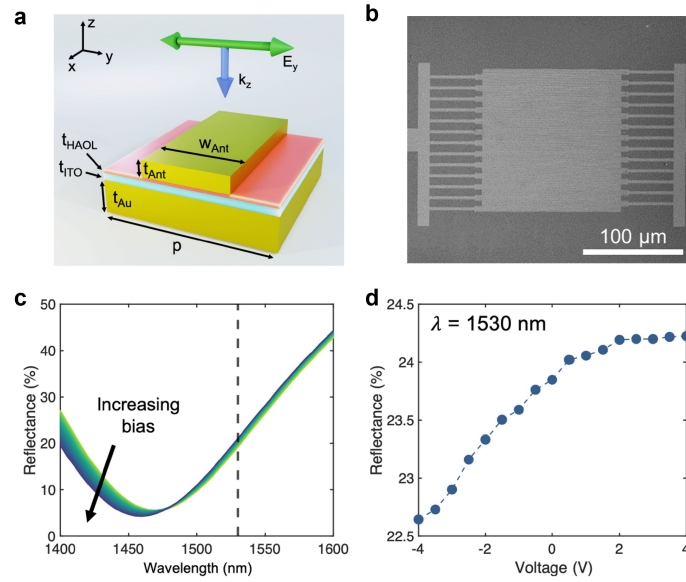


Figure 3.3: ITO-based plasmonic metasurface and tunable reflectance response. (a) Schematic of metasurface unit cell. The structure is periodic in the y -axis with a period, p , and extends $120 \mu\text{m}$ in the x -axis. The metasurface is illuminated from the top with a normally incident plane wave polarized along the y -axis. The dimensions labelled are $w_{\text{Ant}} = 220 \text{ nm}$, $t_{\text{Ant}} = 40 \text{ nm}$, $t_{\text{HAOL}} = 16 \text{ nm}$, $t_{\text{ITO}} = 17 \text{ nm}$, $t_{\text{Au}} = 80 \text{ nm}$, $p = 400 \text{ nm}$. (b) SEM image of metasurface. The center region creates a $120 \times 120 \mu\text{m}^2$ active area of nanoantennas which are contacted by the interconnects on either side of the metasurface. Scale bar: $100 \mu\text{m}$. (c) Measured reflectance spectra of metasurface under varying applied bias from -4 to 4 V . The dotted line corresponds to the operation wavelength of 1530 nm used throughout this work. (d) Measured reflectance modulation of the metasurface as a function of applied bias at an operation wavelength of 1530 nm .

modulation with minimal phase modulation, a significant portion of the reflected light is unmodulated compared to the frequency-shifted light. However, since only the modulated light is detected using the photodiode and spectrum analyzer, we can study the space-time response with excellent signal-to-noise ratio (SNR) without being limited by the modulation depth. It should also be noted that ITO-based modulators in principle are capable of achieving modulation frequencies up to GHz [128, 129]. Therefore, the MHz-frequency operation in this study is limited by the response time of the photodiode, and not by the metasurface itself.

Control of frequency spectrum

The reflected frequency spectrum of the metasurface can be controlled by applying standard time-varying waveforms to the metasurface (*e.g.*, sine, square, sawtooth).

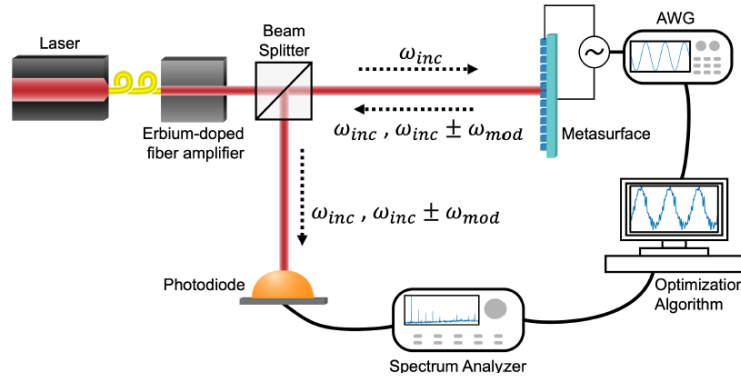


Figure 3.4: Experimental setup for time-modulated metasurface operation and measurements. The metasurface is illuminated with a laser at frequency ω_{inc} while being modulated by an arbitrary waveform generator (AWG) that produces a sine wave at frequency ω_{mod} . The reflected light contains both unmodulated components at ω_{inc} and frequency-shifted components at $\omega_{inc} \pm \omega_{mod}$. A photodiode connected to a spectrum analyzer detects the reflected signal, which is used as the input for a real-time optimization algorithm which enables optimization to tailor the applied waveform for a target spectrum.

At small applied voltages, the change in reflectance is linear to the applied voltage. As a result, the measured frequency response is directly proportional to the Fourier transform of the applied waveform. Figure 3.5 illustrates frequency spectra obtained using an ITO-based metasurface operating at 1530 nm with characteristics similar to the one depicted in Fig. 3.3. The primary difference is a thicker gate dielectric ($t_{HAOL} = 16$ nm instead of 8 nm), which necessitated larger voltages to achieve a comparable gate-tunable reflectance response. Measurements in the small-modulation-depth regime were conducted using waveforms with a 6 V peak-to-peak (p-p) amplitude.

Our results demonstrate that the frequency spectrum can be directly tailored by the applied waveform. This is evident from the observed changes when transitioning between sine (Fig. 3.5a, b), square (Fig. 3.5c), and sawtooth (Fig. 3.5d) waveforms. The measured spectra align closely with the frequency components of the applied waveforms, confirming that the metasurface operates primarily through amplitude modulation. Additionally, we note that the metasurface response was measurable up to 10 MHz (Fig. 3.5b), consistent with the bandwidth limitation of the photodiode used in the experimental setup.

At larger applied voltages, the metasurface enters a regime where its gate-tunable reflectance response becomes non-linear, as shown in Fig. 3.3d. In this regime, the

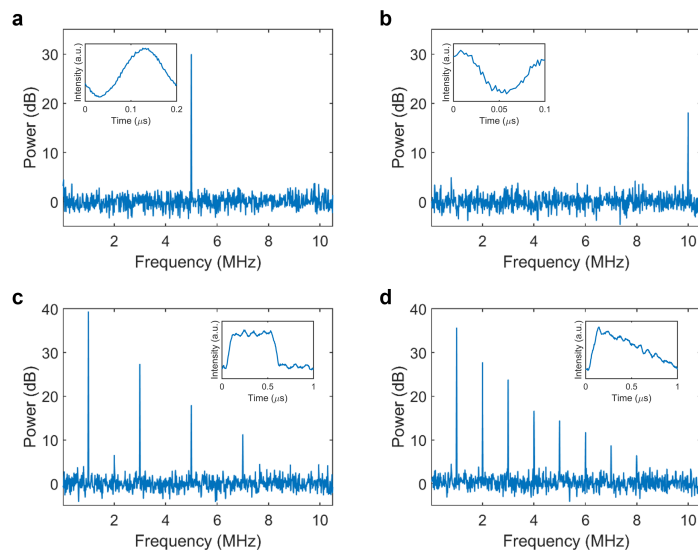


Figure 3.5: **Tunable frequency spectra based on applied waveform.** Frequency spectra of a metasurface illuminated with 1530 nm light and modulated using various waveforms: (a) sine waveform at 5 MHz, (b) sine waveform at 10 MHz, (c) square waveform at 1 MHz, and (d) sawtooth waveform at 1 MHz. The insets display the time-domain reflectance response of the metasurface over a single modulation period.

reflected frequency spectrum deviates from the spectrum of the driving electrical signal when voltages span the full modulation depth. To address this, we implemented an experimental feedback loop that iteratively updates the driving waveform until the desired frequency spectrum is achieved. This approach compensates for non-linearities of the metasurface response as well as other components, such as the metasurface interconnects, the printed circuit board (PCB), waveform generator, photodiode, *etc.* A genetic algorithm was employed to optimize the amplitude and phase of the first 20 terms in a Fourier series, generating the final driving waveform using 1 MHz as the fundamental harmonic.

For an initial demonstration, we optimized the applied waveform to generate only the 1 MHz signal. The top blue curve in Fig. 3.6a shows the initial sinusoidal waveform at 1 MHz, while the red curve represents the final optimized waveform. The corresponding frequency spectra are displayed in Fig. 3.6b. The initial sine wave produces a strong signal at 1 MHz but also generates unwanted power at 2 MHz. In contrast, the optimized waveform maximizes power at 1 MHz while suppressing all other frequencies. We refer the reader to Ref. [95] for details on the optimization algorithm and figure of merit (FOM) selection.

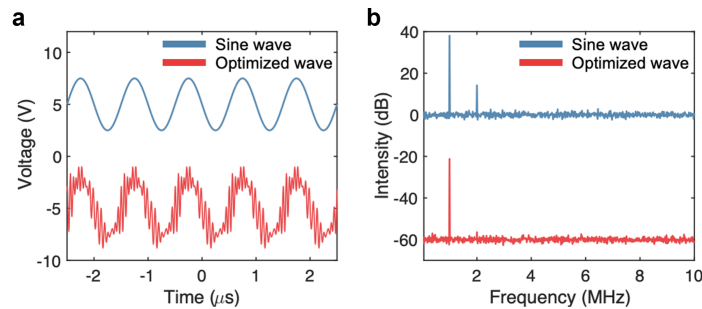


Figure 3.6: Tailored frequency spectrum using optimized waveform. (a) Driving voltage waveforms applied to the metasurface shown in Fig. 3.3: a 5 Vp-p sine wave (blue) and the optimized waveform (red). (b) Corresponding reflected frequency spectra for the sine wave (blue) and optimized waveform (red). Both the waveforms and frequency spectra are vertically offset for clarity in visualization.

The optimized waveform includes frequency components up to 20 MHz, exceeding the 3 dB cutoff of the photodiode at 10 MHz, and is therefore partially filtered during the experiment. However, it was found that incorporating these higher frequency components improved suppression of higher-order harmonics. The optimized waveform generates time-domain reflected signals that more closely approximate a sine wave, while the unoptimized sinusoidal input results in a distorted response due to the non-linear reflectance behavior from the metasurface [95]. In Ref. [95], we further illustrate how the FOM can be adapted to obtain tailored waveforms that yield desired harmonics with target relative amplitudes.

3.4 Space-time modulation: Diffraction of frequency-shifted beam

Space-time metasurfaces have the ability to spatially manipulate wavefronts across the generated spectrum, enabling distinct tasks to be encoded for individual harmonics. While detailed discussions on spatio-temporal configurations for controlling specific harmonics are presented in Section 3.6, this section focuses on the experimental demonstration of diffraction for a single frequency-shifted harmonic using the two-electrode metasurface layout introduced in Fig. 3.3b. Figures 3.7a and b illustrate two driving schemes under investigation. In both cases, the metasurface is driven with the optimized waveform from Fig. 3.6.

In the first driving scheme, the two antenna groups are modulated in-phase (Fig. 3.7a). Along with the previously presented frequency spectrum in Fig. 3.6b, we measure the frequency spectrum at both the 0th and +1st diffraction orders by positioning the photodiode accordingly. In this configuration, nearly all the

reflected 1 MHz signal is in the 0th order, with a small signal detected at 1 MHz in the +1st diffraction order. This minor signal is likely due to slight differences in the amplitude/voltage response between the two independent antenna groups.

In the second driving scheme, the two antenna groups are modulated out-of-phase, with the two waveforms phase-delayed by half a waveform period (π), as schematically depicted by the blue and orange colors in Fig. 3.7b. Under this scheme, our measurements reveal that the 1 MHz signal in the +1st diffraction order is approximately 12 times greater than the signal in the 0th order. The small residual signal at the 0th order is attributed to variations in the average reflectance of the entire metasurface in time, caused by the applied waveform as well as the aforementioned discrepancies in the amplitude/voltage response of the antenna groups.

To comprehensively evaluate the space-time performance of the metasurface, we employ the second driving scheme (Fig. 3.7b) and spatially scan the photodiode in Fourier space (Fig. 3.4). This approach allows us to measure the frequency spectrum at incremental positions, generating an intensity map of the reflected light as a function frequency and angle (Fig. 3.7c). The left panel displays the measured data, while the right panel shows spatial cross-sections of the measured intensity for each integer harmonic of the modulation frequency.

Despite the strong absorption in the metasurface and its reliance on amplitude modulation (which does not suppress unmodulated light), we observe that 94% of the modulated light power is in the $\pm 1^{\text{st}}$ diffraction orders at 1 MHz. This represents a significant improvement in performance compared to the quasi-static diffraction achievable with amplitude rather than phase modulation [95]. It is important to note that the limited absolute efficiency of the metasurface stems from the specific device design used in this study and does not present a fundamental limitation of the proposed method. In Section 3.7 and the subsequent chapter, we present pathways toward achieving higher efficiency metasurfaces.

3.5 Tunable diffraction of frequency-shifted beams

Until now, we have utilized a metasurface design based on a pair of interdigitated electrodes, which restricts spatial wavefront engineering to active switching of diffracted beams at a design specific angle that is fixed during fabrication. To enhance versatility in the spatial domain, we extended the design to a 32-electrode ITO-based metasurface. While active metasurfaces with an increased number of independently addressable electrodes have been demonstrated previously [42], time-

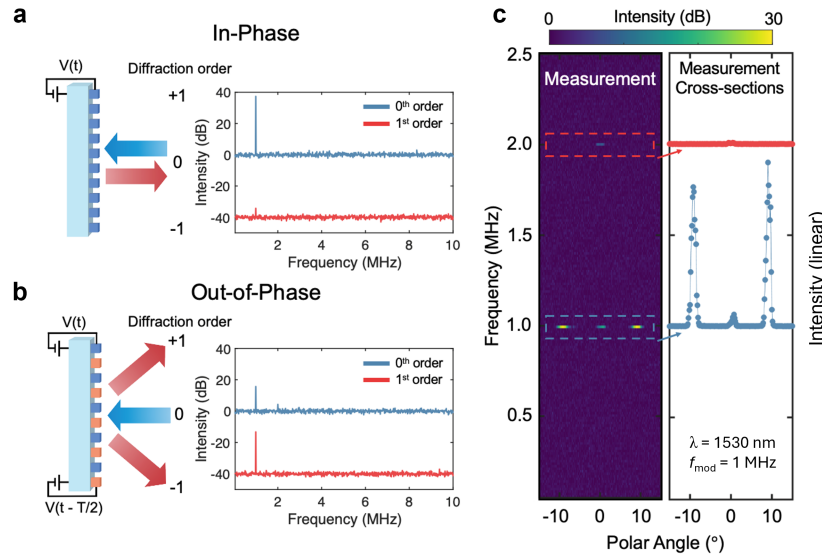


Figure 3.7: Diffraction of a single harmonic with two-electrode metasurface. Throughout this figure, the metasurface is modulated using the red optimized voltage waveform shown in Fig. 3.6a. (a) All metasurface antennas are modulated in-phase. Left: Schematic representation of the metasurface response. Right: Measured frequency spectra with the photodiode positioned at the 0th (blue) and +1st (red) spatial orders. (b) The driving waveform is applied to the metasurface antennas, with adjacent antenna groups modulated out-of-phase by half a period (π). Left: Schematic of metasurface response. Right: Measured frequency spectra with the photodiode positioned at the 0th (blue) and +1st (red) spatial orders. (c) The metasurface is driven under the out-of-phase condition from (b). Left: Measured intensity of reflected light as a function of frequency and angle, plotted in log scale. Right: Spatial intensity cross-sections from the left panel, plotted in linear scale at 1 MHz (blue) and 2 MHz (red).

modulation introduces the additional challenge of high-frequency electrical addressing of the metasurface, which necessitates sophisticated design of the control PCB.

In this section, we first present the layout of the 32-electrode metasurface and detail the high-frequency circuit board necessary for space-time modulation. We then demonstrate the integration of the metasurface with the PCB, showcasing its ability to achieve quasi-static diffraction and steering of beams to tunable angles. Finally, we analyze the spatio-temporal performance of this metasurface and conclude with a discussion on potential future improvements and measurements that could be applied to this design.

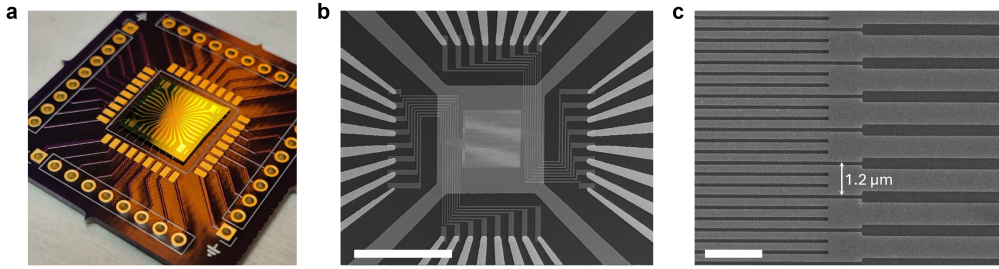


Figure 3.8: **Plasmonic ITO-based metasurface with 32 independently addressable electrodes.** (a) Metasurface chip integrated onto an adapter PCB *via* wire bonding. (b) SEM image of the metasurface showing 4×8 independent interconnects on each side and 4 common ground gates leading to each corner. The stripe antennas are oriented along the horizontal direction. The central $\sim 40 \times 120 \mu\text{m}^2$ region of the metasurface is connected to 32 independent electrodes, while the top and bottom thirds are shorted. Scale bar: $200 \mu\text{m}$. (c) Each electrode controls three stripe antennas, resulting in an effective period of $1.2 \mu\text{m}$. Scale bar: $2 \mu\text{m}$.

Metasurface layout and fabrication

A unit cell of the 32-electrode metasurface consists of the same stripe antenna design as shown in 3.3, with a period of $p = 400 \text{ nm}$. Similar designs with a 400 nm period have previously been used to realize multifunctional metasurfaces with 96 independently addressable electrodes [42, 46]. Here, we reduce the number of electrodes to 32 to realize a more compact chip that can be seamlessly integrated into the optical setup. Additionally, reducing the number of electrodes minimizes the risk of shorted interconnects through the formation of pinholes during the wire-bonding process.

Figure 3.8a depicts the 32-electrode chip integrated into an adapter PCB, which is subsequently mounted onto the driving PCB. Each chip measures $1 \times 1 \text{ cm}^2$ and features eight top electrodes and one ground electrode on each side. All ground electrodes are connected to the common back reflecting plane. A close-up of the metasurface with its top and bottom electrodes is shown in the SEM image in Fig. 3.8b. The central metasurface area, measuring $120 \times 120 \mu\text{m}^2$ contains horizontally oriented stripe antennas. Within this area, the central $\sim 40 \times 120 \mu\text{m}^2$ region is addressed with 32 independent electrodes, while the top and bottom thirds are shorted to the top- and bottommost electrodes, respectively. In the central tunable region, each electrode controls three stripe antennas, resulting in an effective period of $1.2 \mu\text{m}$, as shown in Fig. 3.8c.

The metasurfaces are fabricated on 2-inch Si wafers with a 1 μm thick thermally grown silica (SiO_2) layer for electrical isolation. The wafers are first cleaned using RCA 1 and RCA 2 cleaning procedures. The Au back layer and back contacts are patterned using photolithography with a bilayer photoresist (LOR7B and S1805). Following this, 5 nm titanium (Ti) and 80 nm Au are deposited using electron beam (e-beam) evaporation, and liftoff is performed in Remover PG. Next, the ITO layer is patterned using e-beam lithography with a bilayer polymethyl methacrylate resist (PMMA, 495 PMMA A2 and 950 PMMA A2). A 10 nm ITO is then deposited using RF sputtering with a 90/10 wt% indium oxide/tin oxide ($\text{In}_2\text{O}_3/\text{SnO}_2$) target at 3 mTorr and 100 W, while flowing 20 sccm argon (Ar) and 7 – 8.5 sccm of an argon/oxygen (Ar/O_2 , 90/10 wt%). The Ar/O_2 flow rate is adjusted to control the ITO carrier concentration, with higher carrier concentrations resulting in redshifted resonances. After liftoff in Remover PG, the HAOL layer is deposited through thermal atomic layer deposition (ALD) at 150 $^\circ\text{C}$ using a shadow mask. The deposition consists of two cycles of 1 nm Al_2O_3 /6 nm HfO_2 , without breaking vacuum, to achieve a total thickness of 14 nm. The stripe antennas and inner interconnects are then patterned using e-beam lithography with a bilayer PMMA resist (495 PMMA A4 and 950 PMMA A2). A 2 nm germanium (Ge) adhesion layer and 40 nm Au layer are e-beam evaporated, followed by liftoff in Remover PG. Finally, the top contact pads are patterned using photolithography (S1813 photoresist), deposited using e-beam evaporation of 20 nm Ti and 200 nm Au, and lifted off in Remover PG. The completed devices are diced into $1 \times 1 \text{ cm}^2$ chips and wire bonded into PCBs.

We note that the layer thicknesses, ITO carrier concentration, and stripe antenna widths were varied during each fabrication round to achieve strong phase modulation at target wavelengths between 1530–1560 nm. Although some devices successfully achieved this target, the experimental demonstrations of space-time metasurfaces below mostly relied on amplitude modulation.

Design of high-frequency circuit board

A straightforward control board design with 32 individual electrodes, each connected to multiple AWG inputs, can suffer from excessive spatial requirements and significant crosstalk when signals are applied at MHz frequencies. To address these challenges and enhance bandwidth, we developed a compact PCB design that eliminates the need for multiple ribbon cables. Signals from the AWG are delivered to the metasurface using controlled-impedance coaxial lines, which are properly

terminated at the board to ensure signal integrity. Additionally, high-bandwidth integrated circuit (IC) amplifiers are used to locally buffer the signals, further reducing crosstalk and ensuring stable signal operation.

The PCB incorporates two AD8113 multiplexers (MUXs), each capable of redirecting up to 16 inputs to 16 outputs. In our implementation, the two MUXs are configured to accept up to 8 inputs from a function generator and dynamically route them to any of the 32 metasurface electrodes. This routing is managed by an Arduino-compatible microcontroller unit (MCU, Teensy 4.1), enabling real-time programmable control. The MCU is powered by a 5 V bench top power supply, and commands are sent using the Arduino IDE.

To extend the functionality of the circuit board, we implemented full 32-channel support with both analog-to-digital converters (ADCs) and digital-to-analog converters (DACs) using the AD7616 (ADC) and LT2688 (DAC) chips. This design enables synchronous voltage control across all 32 channels with arbitrary waveforms at a sampling rate of approximately $40 \mu\text{s}$, corresponding to modulation frequencies of up to 25 kHz. By comparison, modulation frequencies for AWG-driven metasurface control are constrained by the AD8113 multiplexers, which have internal buffers limiting their usable bandwidth to the 3 – 10 MHz range.

Figure 3.9 illustrates the control board, which has a compact size of 3.6×4.6 inches. To maintain this compact footprint, the IC side of the board (Fig. 3.9a) is equipped with eight ultraminiature coax connectors (UMCCs) that interface with the AWG inputs *via* SubMiniature version A (SMA) and Bayonet Neill–Concelman (BNC) cables. This side also houses the two MUXs, along with the ADCs and DACs. The device side of the board (3.9b) includes the MCU and the input switches, which control whether the metasurface electrodes are driven by the ADC/DAC system or directly by the function generator. Metasurfaces can be easily connected to the board *via* an adapter PCB (Fig. 3.8a) that fits into the device socket, ensuring the board’s reusability for multiple metasurfaces.

The bandwidth of the metasurface integrated into the PCB is measured directly through optical readout using a photodiode, when a square wave is applied to the metasurface. The -3 dB cutoff frequency is determined to be 5.4 MHz, consistent with the bandwidth measured electrically at the device socket pins of the PCB (Fig. 3.10). This result indicates that the bandwidth is entirely electronically limited, with the primary constraint being the MUXs used in the PCB design, as discussed earlier.

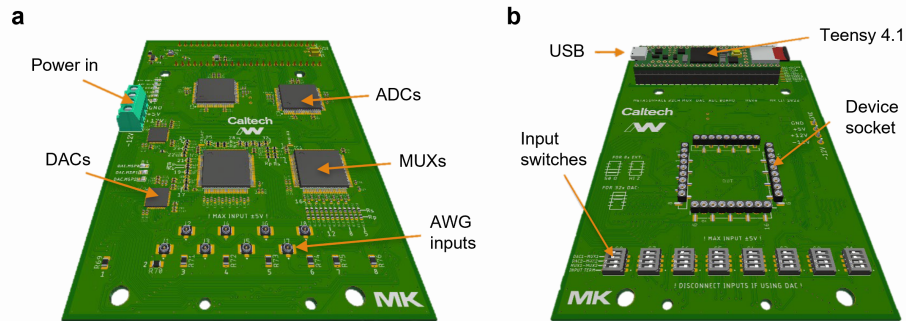


Figure 3.9: **High-frequency PCB for control of 32-electrode metasurface.** The PCB measures 3.6×4.6 inches. (a) IC side featuring the power source and eight ultraminiature coaxial connectors (UMCCs) that serve as inputs from the AWG. Key components include the analog-to-digital converter (ADC), digital-to-analog converter (DAC), and multiplexer (MUX). (b) Device side featuring the microcontroller unit (Teensy 4.1) with a USB interface. Input switches enable toggling between control *via* the AWG and the ADC/DAC system. The metasurface is connected to the board *via* a device socket using an adapter PCB.

Substituting the MUXs with higher-bandwidth components could enable the use of a similar PCB to probe the intrinsic frequency limit of the metasurface.

Quasi-static beam switching and steering

To demonstrate the added spatial versatility enabled by the increased number of electrodes and the PCB, we performed quasi-static beam switching and steering at various angles by modifying the spatial voltage profile applied to the metasurface. Figure 3.11a illustrates the two-level voltage profiles used to achieve beam switching at a wavelength of $\lambda = 1490$ nm. The repetition number (RN) is defined as the number of adjacent pixels with the same applied voltage. Experimental measurements (Fig. 3.11b) show tunable control over the diffraction angle, ranging from 17.9° (RN = 2) to 6.8° (RN = 5). When a uniform voltage is applied across the entire array (RN = 0), no diffraction is observed. By comparing the measured far-field intensity patterns to array factor calculations for metasurfaces with constant amplitude and varying amounts of phase modulation, we deduced that the metasurface exhibits a phase shift of approximately 80° . Considering the inherent coupling between phase and amplitude modulation in practical metasurface designs, the actual phase modulation might slightly exceed this value, compensating for some degree of amplitude modulation.

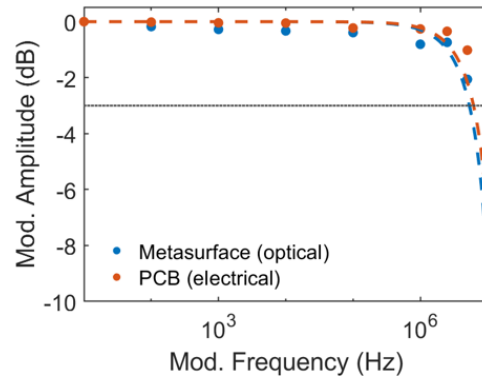


Figure 3.10: **Experimentally measured bandwidth of metasurface and high-frequency PCB.** Normalized modulation amplitude for metasurface integrated into PCB, driven by a square waveform. The metasurface modulation amplitude (blue) is measured through optical readout of the reflected signal using a photodiode, while the PCB modulation amplitude (orange) is measured electrically at the device socket pins. In both cases, the modulation amplitude is normalized to its value at 10 Hz. The gray dotted line indicates the -3 dB cutoff.

Despite the limited phase modulation, we demonstrated that asymmetric radiation patterns can be generated by applying distinct phase gradient profiles to the same metasurface (Fig. 3.11c). Calculated radiation patterns for these profiles (Fig. 3.11d) align well with the experimentally measured results (Fig. 3.11e).

These results confirm that, even with modest phase modulation, the metasurface and PCB setup can achieve tunable diffraction and steering, providing the desired spatial versatility. While quasi-static control cannot suppress the 0^{th} order diffraction with limited phase modulation, we will demonstrate in the next section that time-modulated control enables suppression of the 0^{th} spatial order of frequency-shifted light. This approach builds upon previous results with a two-electrode metasurface while incorporating enhanced tunability of the diffraction angle.

Tunable diffraction of frequency-shifted beams

To demonstrate tunable diffraction of frequency-shifted beams, we modulate the metasurface with a 12 V_{p-p} sinusoidal waveform at 1 MHz. We then drive the metasurface with two such waveforms, where one is phase-shifted by π , replicating the configuration previously shown in Fig. 3.7. By varying the repetition number, we achieve tunable diffraction of frequency-shifted beams, showcasing enhanced spatial versatility enabled by the increased number of electrodes. Unlike the earlier experiment performed with the two-electrode metasurface, this demonstration em-

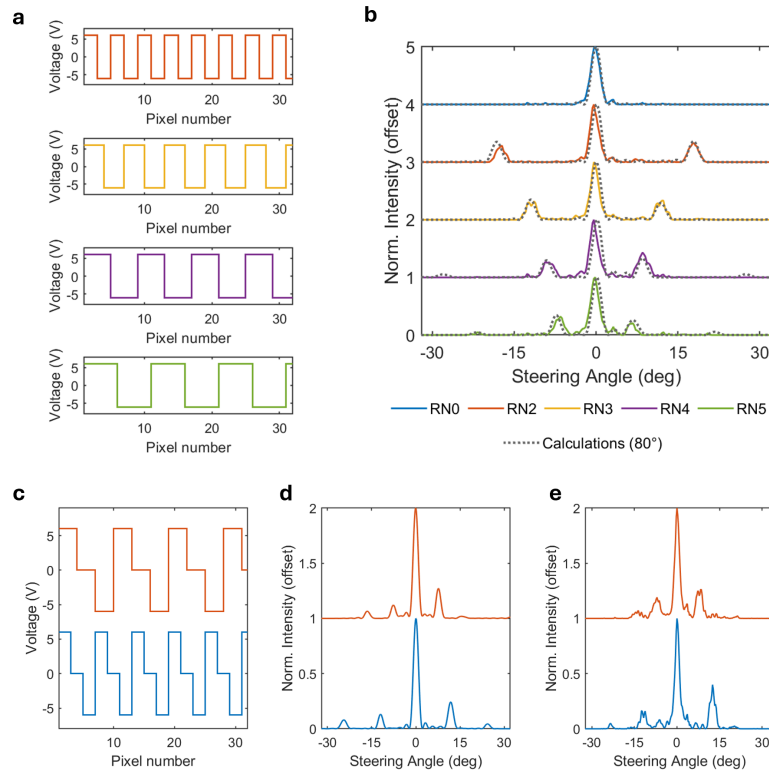


Figure 3.11: **Quasi-static beam switching and steering with 32-electrode metasurface.** (a) Two-level voltage profiles applied to the metasurface for tunable diffraction, with repetition numbers corresponding to $RN = 2$ (orange), 3 (yellow), 4 (violet), and 5 (green). Metasurface pixels are defined as unit cells addressable by individual electrodes (Fig. 3.8c). (b) Measured far-field intensity patterns associated with the voltage profiles shown in (a). For reference, we include the radiation pattern from the case where a uniform voltage is applied across all metasurface pixels ($RN = 0$). The dotted line represents the calculated far-field radiation pattern, assuming constant amplitude and a phase modulation of 80° between the two voltage levels. (c) Three-level voltage profile applied to metasurface, (d) calculated normalized far-field intensity pattern assuming phase values of 85° , 42.5° , and 0° for the three voltage levels, and (e) experimentally measured far-field radiation pattern. All intensity profiles are normalized to their maximal values and offset for visualization. Measurements and calculations were performed at a wavelength of $\lambda = 1490$ nm.

employs a standard, non-optimized waveform to probe the metasurface response across multiple frequency harmonics. The increased number of frequency harmonics arise from the non-linear relationship between the applied voltage and amplitude and phase response of the metasurface.

Figure 3.12 presents the measured intensity as a function of frequency and angle for different RNs, corresponding to varying number of electrodes driven by the same time-varying waveform. Adjacent sets of electrodes are offset by half a waveform (π) to achieve diffraction of individual frequency harmonics. An overview of the four cases analyzed in Fig. 3.12 reveals that varying the RN alters the the diffraction angle across the harmonics. In contrast, applying a uniform time-modulated waveform across the entire metasurface results in no significant diffraction for any harmonic (Fig. 3.12d). Minor signals observed at the diffracted orders at 1 MHz are attributed to slight variations in the electrode response, as elaborated in Ref. [95]. These differences can accumulate over time, particularly during repeated measurements using two-level time-modulated voltage profiles with voltages near the device's breakdown threshold. This accumulation may lead to buildup of charge carriers in the ITO layer, causing changes in the optical response of specific electrodes [46].

To better illustrate the spatial response from the metasurface and differentiate between the spatio-temporal configurations, we examine the spatial intensity profile at frequency harmonics up to 4 MHz for the four configurations shown in Fig. 3.12. Beyond this range, the signal-to-noise ratio becomes too low to provide reliable information. The intensity profiles, displayed in linear scale in Fig. 3.13, reveal that when a uniform time-varying waveform drives the entire metasurface (Fig. 3.13a, RN = 0), all frequency-shifted light remains confined to the 0th spatial order. However, for the metasurface driven by a a spatio-temporally varying waveform (Fig. 3.13b), selective diffraction is achieved at particular harmonic frequencies. Notably, the second harmonic at 2 MHz is selectively diffracted while the 0th order at this frequency is suppressed. Our results show that by varying the repetition number, the diffraction angle of the frequency-shifted light can be varied from 9° to approximately 14°.

The observed diffraction at only the second harmonic indicates that the metasurface achieves a selective phase shift of approximately 180° at this frequency. As discussed previously in Section 3.2, a phase delay α between two driving waveforms imparts a phase $l\alpha$ to each harmonic l [95]. In our prior study with the two-electrode metasurface which primarily relied on amplitude modulation, this behavior could

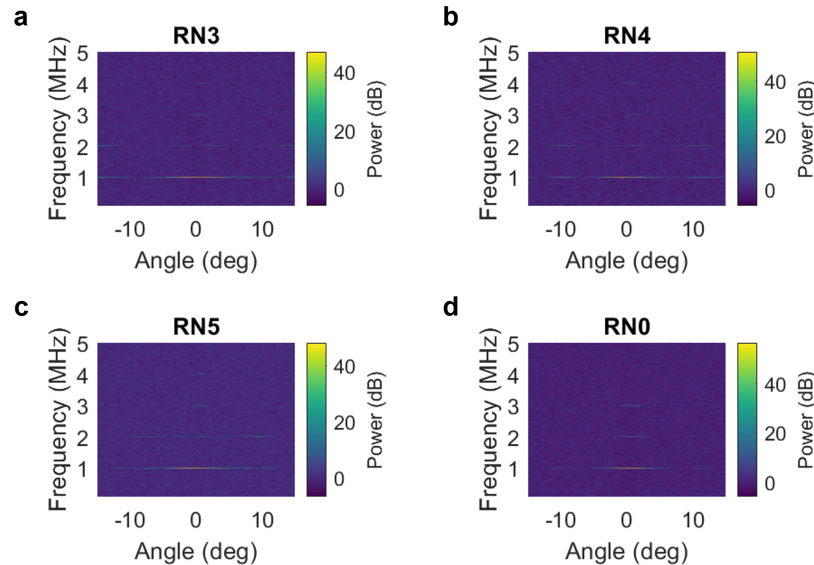


Figure 3.12: **Tunable space-time diffraction with varying repetition numbers.** Measured intensity of reflected light as a function of frequency and angle, plotted in log scale. A 12 V_{p-p} sinusoidal waveform is applied to the metasurface, with diffraction of frequency-shifted light achieved by offsetting the waveform applied to alternating sets of electrodes by half a period (π). Results are shown for (a) RN = 3, (b) RN = 4, (c) RN = 5, and (d) RN = 0, which represents the case where all antennas are modulated uniformly with the same waveform. The measurements are performed at a wavelength of $\lambda = 1510$ nm.

enable selective diffraction of odd harmonics based on the phase delay between adjacent electrodes [95]. For the 32-electrode metasurface studied here, the results suggest that the device exhibits covariation of amplitude and phase, leading to an effective phase delay of π at 2 MHz, enabling tunable diffraction for this harmonic.

3.6 Active multitasking: Multi-frequency multi-beam steering

One of the key benefits of spatio-temporal modulation in metasurfaces is the ability to encode information simultaneously in space and time, enabling multiplexing of channels using a single nanophotonic chip. In the previous experimental studies, we demonstrated how distinct frequency harmonics could be diffracted by configuring an active metasurface with phase-delayed driving waveforms. Specifically, in Ref. [95], we also showed that by phase-delaying individual fundamental frequencies of a Fourier series waveform across an interdigitated set of electrodes, we can achieve selective diffraction of desired harmonics. Building on this, we now explore general

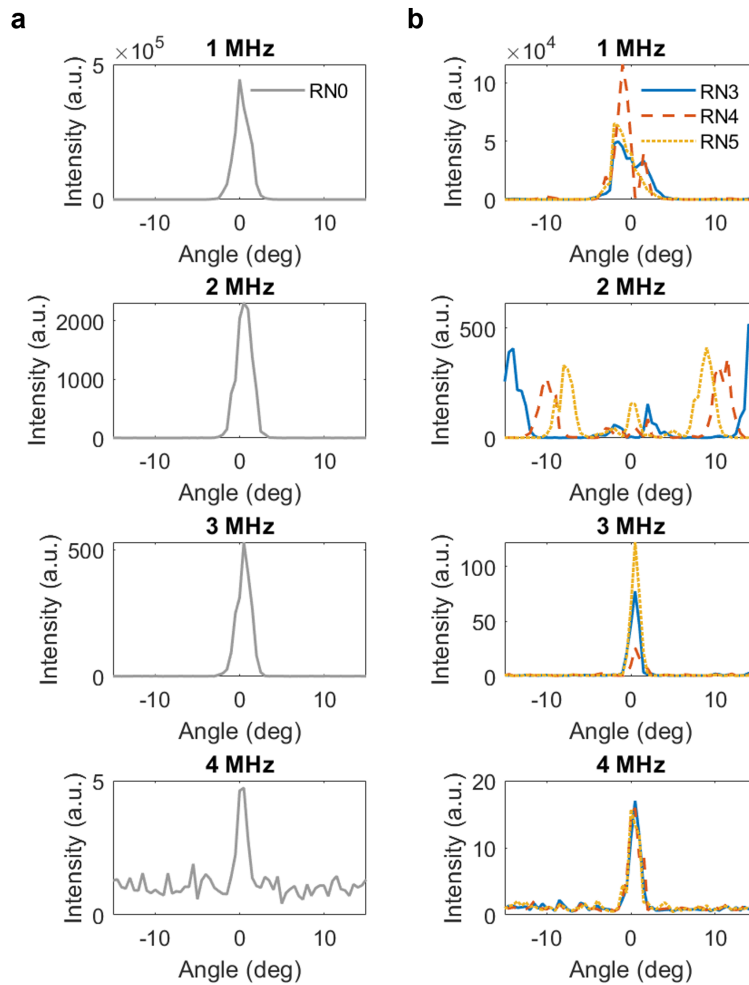


Figure 3.13: **Spatial intensity profiles at harmonic frequencies.** Intensity profiles at multiples of 1 MHz obtained from measurements shown in Fig. 3.12. (a) $RN = 0$ (gray) represents the case where the entire metasurface is uniformly modulated with a 1 MHz sinusoidal waveform. (b) $RN = 3$ (blue solid), 4 (orange dashed), and 5 (yellow dotted) correspond to the configurations where the metasurface is driven with two out-of-phase waveforms (π phase offset) applied across adjacent sets of electrodes, with RN defining the number of electrodes sharing the same waveform.

principles and strategies for adding frequency harmonics, multiplexing frequency channels, and steering different harmonics to different target angles.

When distinct waveforms with different fundamental frequencies are applied to metasurface elements in an interdigitated fashion, crosstalk between adjacent elements can produce undesired scattering at the generated frequency harmonics. One

approach to mitigate this issue is to divide the metasurface into subarrays, each driven by distinct waveforms at a different frequencies. While this method eliminates crosstalk, it reduces the effective aperture of each frequency channel, leading to lower spatial resolution. An alternative strategy involves driving all metasurface elements simultaneously with multiple waveforms, each at a different frequency. In this configuration, spatial information can be independently controlled within each frequency channel by introducing phase delays at specific fundamental frequencies.

To illustrate metasurface control across multiple frequency channels, we consider two operational regimes: one where external voltage biasing results in pure phase modulation, and another where biasing produces pure intensity modulation. For pure phase modulation (Fig. 3.14a), driving all elements in-phase with multiple fundamental frequencies results in a frequency shift that corresponds to the sum of the fundamental frequencies. For instance, as shown in Fig. 3.14b, driving a metasurface with the sum of two sawtooth waveforms at 1 MHz and 2 MHz, respectively, each resulting in sawtooth phase modulation from 0° to 360° , produces a frequency-shifted reflected beam with its strongest harmonic at 3 MHz. This behavior arises because phase is encoded in the exponential term of an electromagnetic wave, as described in Eq. (3.3). Moreover, we note that with complete 360° phase modulation, the 0^{th} harmonic can be suppressed, as illustrated in Figs. 3.1 and 3.2.

In contrast, pure amplitude modulation (Fig. 3.14c) more closely resembles the experimentally demonstrated cases discussed earlier. Here, the 0^{th} harmonic cannot be suppressed, even when the minimal reflectance reaches 0%. Nevertheless, distinct frequency harmonics can be generated by applying sinusoidal waveforms. For example, driving the metasurface with a Fourier series waveform comprising fundamental frequencies at 1 MHz and 2 MHz results in multiplexed frequency harmonics at f_0 , $f_0 + 1$ MHz, and $f_0 + 2$ MHz (Fig. 3.14d). The results shown here assume reflectance modulation ranging from 1% to 8%.

In this configuration, spatial information can independently be encoded into each harmonic without crosstalk between channels. For example, a metasurface modulated by a Fourier series waveform with fundamental harmonics at 1 MHz and 2 MHz can be programmed to leave the 1 MHz harmonic unchanged while incorporating a four-level spatial phase profile into the 2 MHz harmonic. This is achieved by introducing a phase offset of $\pi/2$ at 2 MHz between adjacent metasurface electrodes. Four distinct waveforms are required to modulate the metasurface in this case, resulting in the spatio-temporal reflectance profile shown in Fig. 3.14e. A

Fourier transform of this profile reveals the intensity distribution as function of frequency and polar angle (Fig. 3.14f), demonstrating selective steering of the second harmonic while maintaining specular reflection of the first harmonic. This method also enables encoding more complex spatio-temporal information across multiple harmonics, enabling a potential implementation of active multitasking metasurfaces for multi-frequency multi-beam steering or even simultaneous focusing and steering of beams using different frequency channels.

Implementing this concept experimentally faces two main challenges. First, the number of high-frequency waveforms that can be used to modulate the metasurface is inherently constrained by the capabilities of the driving electronics. In our current PCB setup, the metasurface can be driven with up to eight independent waveforms at MHz frequencies. Larger PCBs with increased number of channels could be implemented at the cost of a larger PCB form factor. Second, frequency multiplexing reduces intensity as energy is distributed across multiple channels. While space-time modulation increases the control and information densities, practical integration of frequency-multiplexed metasurfaces in applications will require high-efficiency to counteract intensity losses. Pathways to address this challenge are discussed in Section 3.7 as well as the subsequent chapters.

3.7 Outlook

Increasing the efficiency of frequency conversion

The conversion efficiency of the frequency harmonics reported in the experimental results discussed in this chapter was limited by two primary factors: (1) the reliance on amplitude modulation and (2) the inherent efficiency limitations in the plasmonic ITO-based metasurface used in this demonstration. We note that while, in principle, it would be possible to operate at a wavelength with higher phase modulation ($\lambda = 1470$ nm for the two-electrode metasurface discussed in Sections 3.3 and 3.4, see Appendix B.1), further experiments are necessary to confirm whether this level of phase modulation can be sustained at high frequencies. To date, phase measurements of metasurfaces have been reported only within the quasi-static operation regime. To evaluate the phase response at high frequencies, one approach would be to modulate the metasurface spatio-temporally and examine whether suppression of unmodulated specularly reflected light can be observed. By comparing the intensity of diffracted, frequency-shifted light to undiffracted, unmodulated light, it may be possible to approximate the effective phase modulation at that specific frequency. For greater accuracy, the associated reflectance modulation, which is measurable

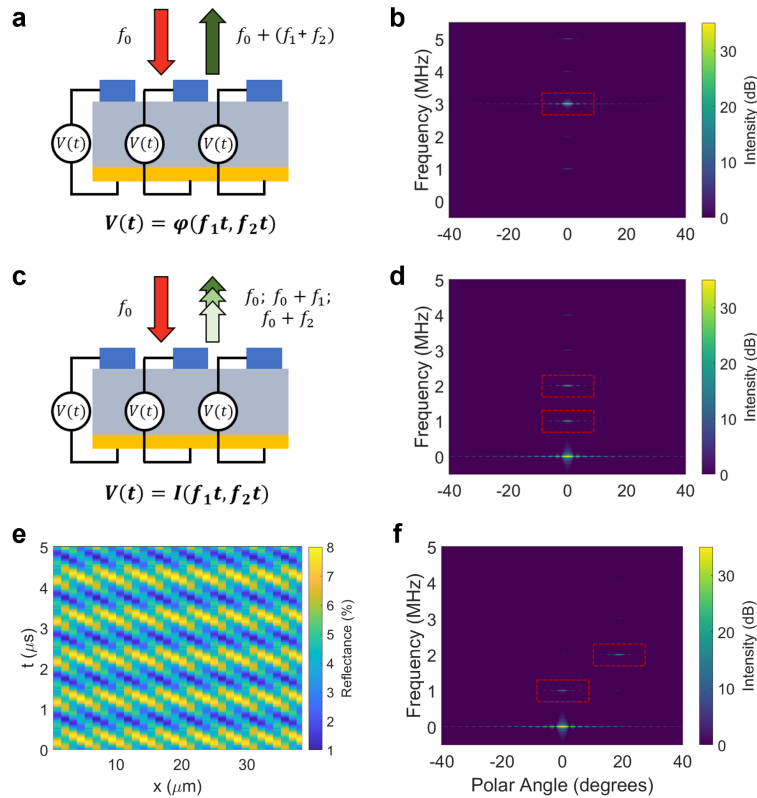


Figure 3.14: Harmonic frequency control with phase and amplitude modulation. (a) Schematic of metasurface driven with two time-varying waveforms, $f_1 t$ and $f_2 t$, producing pure phase modulation. The reflected beam is frequency-shifted by the sum of f_1 and f_2 . (b) Calculated intensity as function of frequency and polar angle for a metasurface driven by the sum of two sawtooth waveforms with fundamental frequencies $f_1 = 1$ MHz and $f_2 = 2$ MHz, resulting in pure phase modulation ranging from 0° to 360° . (c) Schematic of metasurface driven by two time-varying waveforms, $f_1 t$ and $f_2 t$, producing pure intensity modulation. The reflected beam contains multiple frequency-shifted harmonics determined by the applied waveform. (d) Calculated intensity as function of frequency and polar angle for a metasurface driven by a Fourier series voltage waveform with fundamental frequencies $f_1 = 1$ MHz and $f_2 = 2$ MHz, resulting in intensity modulation from 1% to 8%. (e) Spatio-temporally varying reflectance profile for a metasurface driven by a Fourier series waveform with $f_1 = 1$ MHz and $f_2 = 2$ MHz. The second harmonic incorporates a four-level spatial phase profile, introducing a $\pi/2$ phase offset at 2 MHz between adjacent elements spaced $1.2 \mu\text{m}$ apart. (f) Calculated intensity as function of frequency and polar angle for the metasurface configuration described in (e). All calculations are performed at $\lambda = 1550$ nm. Red boxes in (b), (d), and (f) highlight frequency-shifted harmonics.

at high frequencies using an oscilloscope, should also be incorporated into this analysis. Alternatively, it may be possible to use phase imaging cameras, such as the Phasics wavefront-sensing cameras which may enable real-time phase imaging [130].

While achieving higher phase modulation could significantly enhance conversion efficiency, the reflectance of plasmonic ITO-based metasurface remains a critical limiting factor. To improve the total reflectance or transmittance of space-time modulation, novel active metasurface designs are required. The transparent conducting oxide (TCO)-based plasmonic platform employed in this work offers several advantages, including potentially large phase shifts, ease of electrical modulation with high spatial resolution, and rapid modulation speeds. However, absorption in the gold and ITO layers limits the platform's overall efficiency. Alternative materials, such as cadmium oxide (CdO) [74], have been proposed to address this issue and achieve higher efficiency in TCO-based platforms. Alternative modulation schemes employing low loss active materials include the use of electro-optic materials and liquid crystals. We note that liquid crystals are generally not suitable for space-time modulation, as they generally support low modulation frequencies ranging up to hundreds of Hz to few kHz [131]. Electro-optic materials can be modulated at higher frequencies, but they typically exhibit lower index modulation and therefore require advanced resonator designs to achieve significant reflectance or phase modulation. While design strategies incorporating various electro-optic materials are currently being investigated by many research groups, we will explore the use of barium titanate as an active material for transmissive in the subsequent chapter.

High-frequency limits of experimental metasurfaces

The 32-electrode metasurface integrated into the high-frequency PCB developed in this project exhibits a -3 dB bandwidth of 5.4 MHz. In the current setup, the modulation bandwidth is constrained by the multiplexers used in the PCB (AD8113). Replacing these components with higher-frequency multiplexers, such as the AD8114 or AD8115, could enable testing of metasurfaces with multiple waveforms at frequencies approaching ~100 MHz or beyond. While the primary goal of this project was to demonstrate the proof-of-concept functionality of the PCB together with the metasurface, integrating these higher-performance components could be considered for future iterations now that the initial design has been validated.

Achieving higher modulation frequencies, however, is not solely dependent on the electronics. The design and material properties of the metasurface also play a crucial role. In principle, ITO-based metasurfaces could support larger modulation bandwidths through reduced metasurface footprints or through the implementation of two-dimensional antenna arrays that yield lower capacitance values [30]. Beyond ITO, alternative material platforms such as two-dimensional materials [132] or electro-optic materials [31] have been proposed to enable high-frequency modulation extending into the GHz regime. Together, advancements in both electronics and materials hold the potential to unlock higher-frequency capabilities for active metasurfaces.

Non-reciprocity using space-time modulation

The ability to independently control the spatial and spectral properties of light provides a promising pathway for designing nanophotonic elements that enable the violation of Lorentz reciprocity. Conventionally, nonreciprocity is achieved by applying a strong magnetic field, which necessitates bulky ferromagnetic materials and limits practicality for many applications. Spatiotemporal modulation, however, offers a more compact alternative by breaking time reversal symmetry without the need for large magnetic fields. To achieve significant spatial separation of light, which is a key requirement for optical isolation, the modulation frequency must approach the frequency of the incident light. As a result, most demonstrations of nonreciprocal space-time metasurfaces thus far have been in the RF domain [94, 121, 133, 134].

Recent advances in optical metasurfaces have achieved electrical modulation in the GHz regime [31] and could potentially be extended using the spatiotemporal modulation schemes outlined in this work to yield small spatial offsets. However, realizing larger spatial and spectral separations for applications like optical isolation would require novel optical designs. In this regard, optical pumping of space-time metasurfaces has emerged as an effective technique for achieving large spatial separation [115, 126].

3.8 Conclusions

In conclusion, we have demonstrated the experimental operation of near-infrared metasurfaces that are electrically modulated at MHz frequencies to generate desired harmonic spectra and independently diffract frequency harmonics in space. This result is made possible by recent advancements in the modulation frequency and

degree of spatial phase gradient control achievable in active metasurfaces operating at optical frequencies. Initially, we employed a two-electrode ITO-based plasmonic metasurface operating at 1530 nm and modulated it with tailored MHz waveforms to create time-varying wavefronts that selectively excite desired frequencies while suppressing unwanted harmonics. The generated frequency harmonics were then spatially manipulated by introducing a phase delay corresponding to half the waveform period between the signals applied to each electrode.

Building on this, we extended the concept of spatiotemporal modulation to a metasurface with 32 individually addressable electrodes, enabling tunable diffraction of frequency harmonics. We designed a high-frequency PCB capable of taking up to eight inputs from a function generator and routing them to any of the 32 metasurface electrodes, allowing for the creation of more complex spatiotemporal wavefronts. This platform opens the door to advanced functionalities beyond tunable diffraction, such as steering and focusing of frequency-shifted light. Additionally, we outlined theoretical approaches to leveraging phase- or amplitude-modulated metasurfaces for implementing mathematical operations, such as addition of frequency harmonics, or for obtaining frequency multiplexed operation, and active multitasking.

The ability to generate and spatially manipulate frequencies within a single chip-scale device significantly enhances the control and information density of nanophotonic elements. While fundamental challenges remain, such as the need to improve modulation bandwidth and the efficiency of metasurface platforms, the methods and designs presented here offer a pathway for many applications in optical communication, sensing, and information processing.

*Chapter 4***HIGH-EFFICIENCY ELECTRO-OPTIC METASURFACES
USING BARIUM TITANATE**

The material in this chapter was in part presented in [96, 135].

Rapid advances in information technology necessitate the development of functional devices that can meet the growing demands of modern data processing and communication systems. These devices must operate at ultrafast speeds, consume minimal power, and integrate seamlessly into compact architectures to keep pace with increasing data complexity and volume. Beyond conventional electronics, photonic platforms hold the promise to address these requirements, providing several benefits including high-speed operation, low energy dissipation, and high accuracy [136–139]. Achieving these capabilities hinges on the exploration of functional optical materials that are tailored for next-generation optical processing units.

The development of low-power photonic devices relies on materials with strong electro-optic responses in thin-film form. Silicon on insulator (SOI) technology is a widely adopted material platform for silicon photonic circuits due to its compatibility with CMOS processes [140–142]. However, its optical tunability is limited, as refractive index changes are primarily driven by thermo-optic effects [5, 80] or material doping [143], which typically result in longer response times or higher losses. Transition metal dichalcogenide (TMDC) monolayers have emerged as promising alternatives, offering gate tunability, strong light-matter interactions, tunable bandgaps, and short response times [132, 144, 145]. Despite these advantages, TMDC-based devices often exhibit narrow operational bandwidths, limiting their versatility in broadband applications, and require large interaction lengths due to their atomically thin active medium.

This chapter focuses on the use of electro-optic materials, specifically barium titanate, to overcome these challenges and realize high-efficiency active metasurfaces with low power consumption. We begin with an overview of the theory for electro-optic tuning. We will then introduce a novel synthesis technique for producing barium titanate thin films through spalling bulk single crystal substrates, followed by an experimental characterization of the physical and electro-optic thin film properties. As a first step toward realizing barium titanate-based active metasurfaces,

we include simulations of high-efficiency transmissive structures for beam steering at visible frequencies. This chapter concludes with an outlook on future device architectures incorporating barium titanate for enhanced functionality.

4.1 Electro-optic tuning based on Pockels effect

The optical properties of an anisotropic medium can be described by the index ellipsoid, which takes its simplest form in the principal coordinate system as

$$\frac{x^2}{n_x^2} + \frac{y^2}{n_y^2} + \frac{z^2}{n_z^2} = 1. \quad (4.1)$$

In this equation, x , y , and z represent the principal axes, along which the displacement field \mathbf{D} and the electric field \mathbf{E} are parallel. The terms n_i correspond to the refractive indices in direction i , and the values $1/n_i^2$ represent the principal values of the optical impermeability tensor $\boldsymbol{\eta} = \epsilon_0 \boldsymbol{\epsilon}^{-1}$, where ϵ_0 is the vacuum permittivity and $\boldsymbol{\epsilon}$ the dielectric permittivity tensor. In certain crystals, applying an electric field alters both the size and orientation of the index ellipsoid. These changes are caused by shifts in the distribution of bond charges within the crystal and, in some cases, small deformations of the ion lattice [146], leading to a change in the impermeability tensor. The resulting modification in the refractive index ellipsoid is characterized through the electro-optic coefficients r_{ijk} and s_{ijkl} , and is expressed as

$$\eta_{ij}(\mathbf{E}) - \eta_{ij}(0) = \Delta\eta_{ij} = r_{ijk}E_k + s_{ijkl}E_kE_l. \quad (4.2)$$

Here, r_{ijk} and s_{ijkl} represent the linear (Pockels) and quadratic (Kerr) electro-optic coefficients, respectively, both of which are material-dependent.

The Pockels effect occurs exclusively in non-centrosymmetric materials, which lack inversion symmetry. Among the 32 crystal point groups, 21 exhibit this property and can therefore display the Pockels electro-optic effect. These 21 groups are also piezoelectric. In contrast, the Kerr effect, a higher-order phenomenon, can occur in materials with any symmetry but it is typically much weaker. When the Pockels effect is present, the Kerr effect is generally negligible. The following discussion will focus on the Pockels effect and its application in active metasurfaces.

Given the symmetry of the dielectric permittivity tensor, the impermeability tensor is also symmetric. As a result, the indices i and j in equation (4.2) can be permuted, such that $r_{ijk} = r_{jik}$. This symmetry reduces the number of independent Pockels

coefficients from 27 to 18 and allows the use of a contracted notation for the electro-optic tensor [146] where

$$\begin{aligned}
 r_{1k} &= r_{11k} \\
 r_{2k} &= r_{22k} \\
 r_{3k} &= r_{33k} \\
 r_{4k} &= r_{23k} = r_{32k} \\
 r_{5k} &= r_{13k} = r_{31k} \\
 r_{6k} &= r_{12k} = r_{21k}.
 \end{aligned} \tag{4.3}$$

Under an applied electric field, the deformed index ellipsoid can then be written as

$$\begin{aligned}
 &\left(\frac{1}{n_x^2} + r_{1k}E_k\right)x^2 + \left(\frac{1}{n_y^2} + r_{2k}E_k\right)y^2 + \left(\frac{1}{n_z^2} + r_{3k}E_k\right)z^2 \\
 &+ 2yzr_{4k}E_k + 2xzr_{5k}E_k + 2xyr_{6k}E_k = 1.
 \end{aligned} \tag{4.4}$$

Here, E_k represents a component of the applied electric field with $k = 1, 2, 3$ (corresponding to x, y, z). Generally, the principal axes of the deformed ellipsoid do not coincide with the unperturbed axes, x, y, z , and must be determined through a principal axis transformation, through which one can extract the refractive index modulation.

The index modulation achieved through the electro-optic Pockels effect in dielectric materials is particularly advantageous for realizing low-loss metasurfaces capable of supporting ultra-fast modulation frequencies exceeding 100 GHz, as demonstrated in electro-optic modulators [147]. This makes them highly suitable for applications requiring spatiotemporal modulation of light, which was motivated in the previous chapter.

Lithium niobate (LiNbO_3 , LN), long regarded as the benchmark for bulk electro-optic telecommunication applications, has recently attracted renewed attention in its thin-film form. Thin film LN enables enhanced performance in nanophotonic devices through an increased integration density [148–150]. It exhibits a Pockels coefficient of $r_{33} = 30.8$ pm/V, leading to an index change of 0.0022 under an applied field strength of 0.15 MV/cm [151]. However, the relatively small index change necessitates the design of high quality factor resonators ($Q > 10,000$) to achieve

significant modulation of scattered light [152]. Additionally, many existing active modulator designs require large applied voltages (> 20 V), which are incompatible with standard CMOS backplane architectures. Table 4.1 summarizes the electro-optic refractive index changes achieved in various nanophotonic devices using thin film electro-optic materials. For completeness, we also include a comparison to multiple quantum wells based on the quantum confined Stark effect. In these structures, a refractive index change occurs as a result of a shift in the interband transition energy when biased with an electric field [153–155]. Along with the experimentally observed index changes, Table 4.1 also highlights the wavelength coverage of these electro-optic materials, indicating their transparency window and thus suitability for high-efficiency nanophotonic modulators and active metasurfaces across a broad spectrum.

Active electro-optic material	Electro-optic coefficient (pm/V)	Applied field strength (MV/cm)	Δn	Wavelength coverage
Aluminum nitride (AlN)	$r_{13} = 0.67$ [156]	1.8 [157]	0.0006	300 nm - 8 μm [158]
Lithium niobate (LN)	$r_{33} = 30.8$ [151]	0.15 [159]	0.0022	420 nm - 5.2 μm [160]
Organic electro-optic (OEO) chromophore JRD1	$r_{33} = 359$ [161, 162]	0.05 [163]	0.005	Above 1.2 μm^c [164]
Barium titanate (BTO)	$r_{42} = 923$ [165]	0.002 [165]	(0.0634) ^a	375 nm [166] - 7 μm [167]
Multiple quantum wells (MQW)	N/A	0.1 [75]	$\sim 0.002^b$ [168, 169]	915-960 nm [75], 1.41-1.44 μm [168], 1.53-1.57 μm [169]

Table 4.1: **Refractive index change Δn for experimentally reported values of electro-optic coefficients for various thin films.** ^a The observed effective refractive index change in the BTO film will differ from this value due to the specifics of the orientation of different ferroelectric domains. ^b We report the index change values in the spectral region where the extinction coefficient k is relatively small. ^c Additional studies are needed to identify the upper bound of the operating wavelength.

Barium titanate (BaTiO₃, BTO) stands out as a versatile perovskite material with exceptional dielectric, ferroelectric, piezoelectric, and electro-optic properties [170–

173]. Between 5°C and 120°C, BTO adopts a non-centrosymmetric tetragonal phase ($a = b \neq c$ -axis) with its central titanium (Ti) ion displaced along one of the principal axes. This structural configuration gives rise to spontaneous polarization and a pronounced electro-optic response. The Pockels coefficients of bulk BTO ($r_{42} = 1300 \pm 10$ pm/V, $r_{33} = 105 \pm 10$ pm/V, $r_{13} = 10.2 \pm 0.6$ pm/V) [139] far exceed those of widely used LN. Like other electro-optic materials, BTO supports ultrafast modulation frequencies ranging up to several hundred GHz [174, 175]. It furthermore exhibits a broad transparency window, spanning from 0.4 – 7 μm , as well as high refractive index values [139, 167], which facilitate the design of efficient resonators and waveguides across visible and near-infrared wavelengths. These properties make BTO an ideal material for next-generation photonic and optoelectronic devices. However, photonic integration often requires transitioning from bulk crystals to thin films, which presents several challenges.

4.2 Barium titanate thin films

Materials grown in thin film form are often polycrystalline or amorphous, and therefore typically exhibit lower electro-optic coefficients and reduced refractive index modulation compared to their single-crystal counterparts. The extent of this reduction is highly dependent on the growth method. For instance, BTO thin films grown using metalorganic deposition techniques are often 3-4 times lower than those of bulk materials [96, 173]. Table 4.2 provides an overview of the r_{42} coefficient reported for BTO prepared using various growth techniques. Currently, the highest quality BTO thin films have been achieved through molecular beam epitaxy with an electro-optic coefficient of $r_{42} = 923$ pm/V [165]. However, epitaxial growth process remains slow and expensive, limiting its scalability for large-area applications and it still does not match the electro-optic performance of bulk BTO.

To overcome the challenges associated with thin-film fabrication, we propose spalling to produce large-area, single-crystalline BTO thin films from bulk substrates. This low-cost, scalable technique has the potential to achieve large electro-optic coefficients, comparable to those obtained through epitaxial growth. Spalling is a recently developed kerfless method for separating layers from their host substrates, and was initially applied to III-V semiconductors [182]. In this process, a metal stressor layer is deposited on a bulk crystalline substrate, introducing compressive stress within the substrate. When the residual stress surpasses a critical

Synthesis method	Refractive index ($\lambda = 1550$ nm)	Electro-optic coefficient r_{42} (pm/V)	Modulation frequency
Bulk (top-seeded solution growth)	2.286 [176]	1300 [139]	< 0.1 GHz [177]
MBE [165]	2.286	923	65 GHz
PLD [178]	2.27	390	70 GHz
RF sputtering [179]	2.278	89	419 kHz
CVD [180]	2.13	4.5	17.3 kHz
CSD (sol-gel) [181]	(1.94 at $\lambda = 633$ nm)	($r_{\text{eff}} = 27$ pm/V)*	5 MHz

Table 4.2: **Refractive index and electro-optic coefficient r_{42} for BTO synthesized using various techniques.** The reported refractive index values represent the average of the ordinary and extraordinary indices. The electro-optic coefficients correspond to measurements performed at the modulation frequencies specified in the adjacent column. *For sol-gel BTO, an effective electro-optic coefficient is reported due to the polycrystalline nature of the material.

threshold, a crack can be initiated with an external pulling force, such as exfoliation with tape.

There are two common approaches for creating spalled films. The first involves electroplating a tensile-stressed metal layer, such as nickel (Ni), to generate the stress required for crack propagation. The second relies on crystallization-induced stress in amorphous Si thin films deposited directly on the bulk substrate [183]. During annealing, the Si film undergoes crystallization and shrinkage, and thus generates sufficient stress for crack initiation. In this work, we adopt the first method, which utilizes electroplated Ni to create single-crystalline BTO thin films with controlled thickness and retained material properties.

Spalling single-crystal barium titanate

Figure 4.1a illustrates a schematic of our approach, which begins with the deposition of a 30 nm Ti and 30 nm gold (Au) seed layer on a single-crystal BTO substrate. This seed layer provides a strongly adhesive, conductive base for electroplating, as BTO itself is an insulating material. We then use a heated nickel chloride solution to electroplate 1-4 μm of Ni. The Ni thickness is primarily controlled by varying the plating time, while the solution temperature, plating current, and area are kept constant. The thickness of the spalled film, also referred to as the spall depth t , is determined by a force balance between the tensile force in the electroplated Ni, the

resulting compressive force in the BTO substrate, and the opening mode fracture along the crack introduced through the external pull force [182, 184]. In our setup, this external pull force is applied using a tape attached to a roller, which enables the exfoliation of continuous, single-crystalline BTO thin films. The resulting BTO spall is single-crystalline in nature, as confirmed through x-ray diffraction (XRD) scans shown in Appendix C.1.

The lateral dimensions of spalled BTO films currently range up to a few millimeters, as dictated by the 4.5 mm diameter of the plating aperture. However, prior studies on III-V semiconductors have demonstrated that spalling can be scaled to produce wafer-sized thin films [185, 186]. Additionally, bulk single-crystal BTO substrates can be reused for multiple spalling cycles by introducing repolishing techniques such as vibration polishing or chemical-mechanical polishing between cycles (see Appendix C.2). This reusability further enhances the cost-effectiveness of the proposed approach compared to alternative growth methods.

Figure 4.1b shows a spalled *c*-axis oriented (001), single-crystalline BTO thin film obtained through this procedure. The spalled BTO film rests on top of the Ti/Au seed layer, followed by the Ni layer and Kapton tape (from top to bottom). Optical microscopy reveals a large, continuous BTO area with lateral dimensions of approximately $1.5 \times 3 \text{ mm}^2$, alongside smaller spalled regions. Discontinuities in the spalled film are attributed to nonuniform Ni plating and inconsistencies in the manual pull force. While Kapton tape was used in this demonstration, alternative tapes, such as polyvinyl alcohol (PVA) or heat-release tape, could enable easier transfer of spalled films to other substrates and will be explored in the subsequent discussion. A profilometer scan of the spalled substrate (Fig. 4.1c) along the dotted black line in Fig. 4.1b measures the spall depth, which ranges from $15 \text{ }\mu\text{m}$ (middle inset) to less than $1 \text{ }\mu\text{m}$ (right inset). The insets in Fig. 4.1c highlight surface corrugations, which vary from hundreds of nanometers in thicker regions (left inset) to tens of nanometers in thinner films (right inset). Areas with film thicknesses around $1 \text{ }\mu\text{m}$ or less exhibit bright color variations under white light, indicative of thin-film interference effects. These observations are consistent across both (001) and (100) films spalled from single-crystal bulk substrates, as shown in Fig. 4.1d.

Thin film characterization

The brightly colored thin-film regions shown in Fig. 4.1, often obtained at the edges of spalled films, highlight the potential for producing larger-area films with

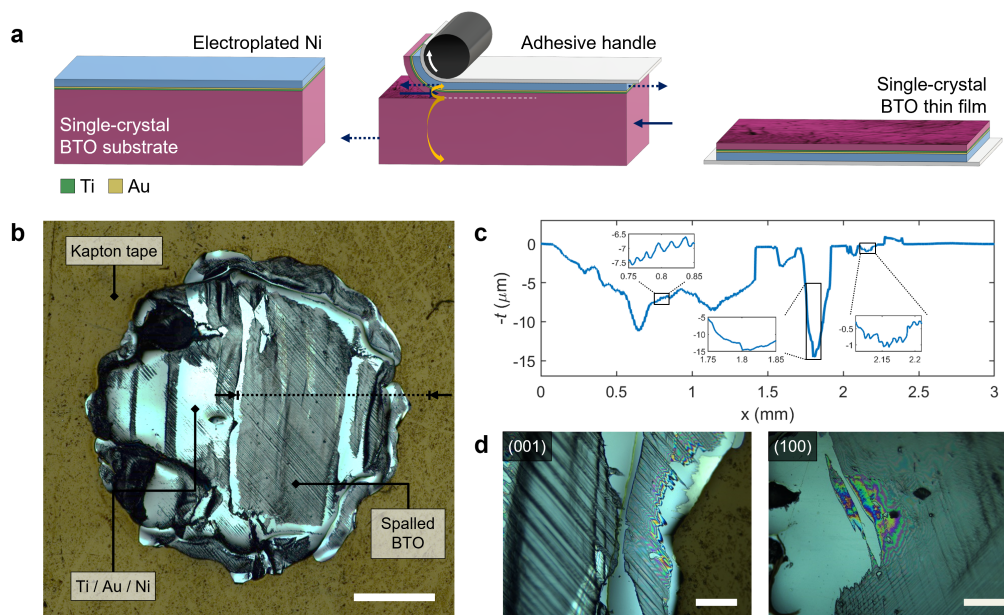


Figure 4.1: **Spalled barium titanate thin films.** (a) Schematic representation of procedure for spalling BTO. Left: A seed layer of Ti (green) and Au (yellow) is deposited on a bulk single-crystal BTO substrate. Ni (blue) is electroplated on top of the seed layer to induce compressive stress in the substrate. Middle: An adhesive handle (light grey) is stuck onto the substrate and can be peeled off with a roller (black). A force balance between the tensile (dotted, black) and compressive forces (solid, black) as well as the bending moment (orange) dictates the spall depth (white dashed). Right: The spalled single-crystalline BTO thin film is attached to the metal back layer and an adhesive handle. (b) Optical microscope image of spalled (001)-oriented BTO film. Scale bar: 1 mm. (c) Profilometer scan along black dotted line in (b), performed on the spalled substrate. The vertical axis indicates the negative of the spall depth $-t$, with zero corresponding to the level of the unspalled substrate. Insets show magnified height profiles corresponding to the square boxes, highlighting variations in spall depth and surface roughness. (d) Optical microscope images with spalled regions indicating thin film interference effects for (001)- and (100)-oriented films on the left and right, respectively. Scale bars: $100 \mu\text{m}$.

sub-micron thicknesses that are suitable for photonic device integration. Achieving such films requires precise control over both thickness and surface roughness, which can be manipulated by adjusting the electroplated Ni thickness and thus the corresponding compressive stress induced in the bulk substrate. To further explore this for single-crystalline BTO, we electroplated two partially overlapping Ni layers onto a *c*-axis oriented single-crystal bulk BTO substrate, creating three distinct thickness regions, as shown in the inset of Fig. 4.2a. The first layer consisted of approximately $1.35\ \mu\text{m}$ of Ni, followed by a partially offset second layer of $1\ \mu\text{m}$ thickness. This configuration allowed us to spall BTO simultaneously from three regions, each subjected to a different stress state (from left to right: intermediate, high, and low). Performing all spalls simultaneously minimized variations caused by inconsistencies in the manual pull force.

Figure 4.2a shows an optical microscope image of the spall performed using PVA tape. The highest stress state (central area, blue box) yielded the largest spalled area, spanning millimeter-scale lateral dimensions and spall depths ranging from $5 - 7\ \mu\text{m}$. The intermediate (orange box) and low-stress states (green box) yielded continuous BTO areas extending several hundred micrometers, with film thicknesses between $0.4 - 2.5\ \mu\text{m}$ and $0.1 - 1.8\ \mu\text{m}$, respectively. Notably, the lowest stress state resulted in the thinnest and smoothest films, characterized by brightly colored areas exceeding $100 \times 100\ \mu\text{m}^2$ and minimal surface features (Fig. 4.2b). To quantify surface roughness across different film thicknesses, we use atomic force microscopy (AFM). The scans shown in Fig. 4.2c correspond to the stress regime outlined in Fig. 4.2b (blue, orange, and green boxes) and reveal a decreasing root mean square (RMS) roughness r with decreasing thickness. Specifically, r corresponds to 125 nm in the high-stress region, 66 nm in the intermediate-stress region, and 27 nm in the low-stress region. RMS roughness was evaluated over the areas marked by white dashed boxes in Fig. 4.2c.

A similar analysis was performed for spalls obtained from (100)-oriented bulk crystals and is shown in Fig. 4.2d-f. For the spall shown in Fig. 4.2d, the three stress states were created by first electroplating approximately $2\ \mu\text{m}$ of Ni, followed by a second layer with a thickness of $600 - 800\ \text{nm}$. Due to the small difference in the Ni stressor layer thickness between the intermediate and high-stress regimes, only minimal differences in roughness are observed in the spalled films from these two regions. The spall depth t , measured via profilometry, ranges around $6 - 11\ \mu\text{m}$

in most regions of the intermediate stress regime, while values between $t = 10 - 12 \mu\text{m}$ are obtained for the high-stress regime.

Notably, finer features on the spalled films, such as horizontally or vertically oriented domain lines, extend across both the intermediate and high-stress regions, as seen in the blue box in image 4.2e. These features correspond to those found on the bulk substrate used for spalling, suggesting that the surface quality and domain structure of the bulk substrates are critical factors influencing spalled thin films (see Appendix C.3 for further discussion). While the surface quality is comparable between most parts of the high and intermediate-stress spalls, the second panel (orange box) in Fig. 4.2e reveals that small regions exhibiting thin-film interference can also be observed in the (100)-oriented films under intermediate stress conditions.

These thin film interference regions can be achieved more controllably by electroplating a thinner Ni layer, as shown in the low-stress regime. Because the Ni stressor thickness used in this case was smaller than that used for the (001)-oriented substrate, we obtain smaller spalled areas in this case. Nevertheless, we can identify thin film areas spanning up to tens of microns laterally, identified through the thin-film interference effect, as shown in the optical microscope image (green box, Fig. 4.2e). Due to the inherently lower surface quality of the (100)-oriented bulk BTO substrate, we observe some film breakage within the thin-film regions.

Figure 4.2f provides AFM scans of three different regions within the corresponding panels in Fig. 4.2e. The RMS roughness was evaluated over the white dashed regions in Fig. 4.2f and corresponds to approximately 235 nm in the high-stress state (top), 56 nm in the intermediate-stress regime (middle), and 47 nm for the low-stress regime (bottom).

AFM scans across a range of spalled film thicknesses allowed us to establish a relationship between roughness r and thickness t (Fig. 4.3a). Films spalled from both (001)- and (100)-oriented single-crystal substrates followed similar trends, with roughness approximating a square root function $r(t) \approx C \cdot t^{0.5}$, where C is a constant prefactor. For the fits shown in Fig. 4.3a, $C = 55.8$ and $C = 74.1$ for films obtained from (001) and (100) substrates, respectively, while the exponents are 0.45 and 0.40. Roughness was generally higher for (100)-orientated films, likely due to a more inhomogeneous domain structure in the bulk substrate, which contributed to greater initial surface roughness. Potential causes for this increased surface roughness in a -axis oriented substrates are discussed in Appendix C.3.

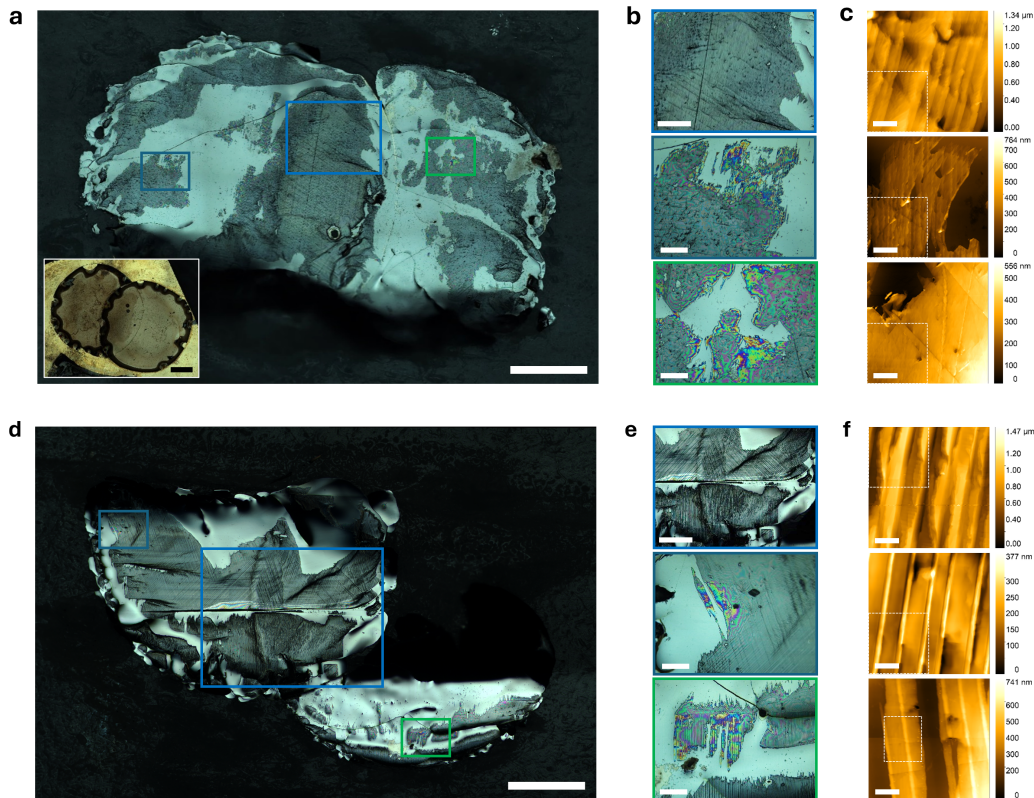


Figure 4.2: **Control over thickness of *c*- and *a*-axis spalled BTO films.** (a, d) Optical microscope image of (a) spalled (001) and (d) spalled (100) BTO thin film. The orange, blue, and green boxes indicate regions obtained through spalling with an intermediate, thick, and thin Ni stressor layer, respectively. Inset in (a) shows two overlaid circular electroplated Ni layers on top of a Ti/Au seed layer on the corresponding BTO substrate. Scale bars: 1 mm. (b, e) Optical microscope images of the area in the blue, orange, and green boxes in (a) and (d), respectively. (b) Scale bars (from top to bottom): 250 μm , 100 μm , 100 μm . (e) Scale bars (from top to bottom): 500 μm , 100 μm , 100 μm . (c, f) AFM images of (c) spalled (001) and (f) spalled (100) thin films within the areas shown in (b) and (e), respectively. The dashed white area in each image corresponds to the region over which the RMS roughness was evaluated. Scale bars: 10 μm .

Previous studies have reported a linear correlation between the spall depth and Ni stressor thickness when the stressor is significantly thinner than the substrate [182, 187]. This relation is due to greater compressive strain energy that is introduced into the substrate with increasing stressor thicknesses [182, 188, 189]. In ferroelectric materials such as BTO, such compressive strain can induce domain switching [190, 191]. To investigate this phenomenon further, we employed electron back scatter diffraction (EBSD) to map the crystal orientation across a thin film spalled from a (100) bulk crystal (a -axis). Figure 4.3b shows the band contrast image of the scanned area, reflecting the film's topography, alongside a crystal orientation map of a $60 \times 60 \mu\text{m}^2$ area. The crystal orientation map reveals a large single-domain area (approximately $40 \times 15 \mu\text{m}^2$) with (100) orientation in the upper half of the scanned region. A comparison of the band contrast image and the crystal orientation map indicates that regions with differing domain orientations correspond to topographical features in the scanned area.

These observations, combined with prior studies, suggest a strong correlation between the Ni stressor thickness, film thickness, and roughness in spalled BTO thin films. However, further studies are necessary to map the depth profile of the strain field in the substrate and understand the relation between film thickness, roughness, and domain switching. If domain switching in spalled BTO thin films occurs as a result of spalling, understanding whether it is a static process that occurs during electroplating of the stressor layer, or a dynamic process occurring as strain energy is released during exfoliation is crucial. Such insights will enable better control over spalled film properties, leading to targeted improvements in surface roughness and domain uniformity.

We also note that the initial quality of the bulk substrate, particularly its domain configuration, plays a critical role in determining the final domain structure and surface roughness of the spalled film. Using high-quality, single-crystalline (ideally single-domain) bulk substrates is therefore essential for producing smooth, spalled thin films of ferroelectric materials.

Thin film transfer

To fabricate functional devices from spalled films, it is necessary to transfer the films from the tape used for exfoliation onto a hard substrate. To facilitate this process, we perform the spall using water-soluble PVA tape for easy removal. The spalled film, adhered to PVA tape, is initially secured on a glass substrate.

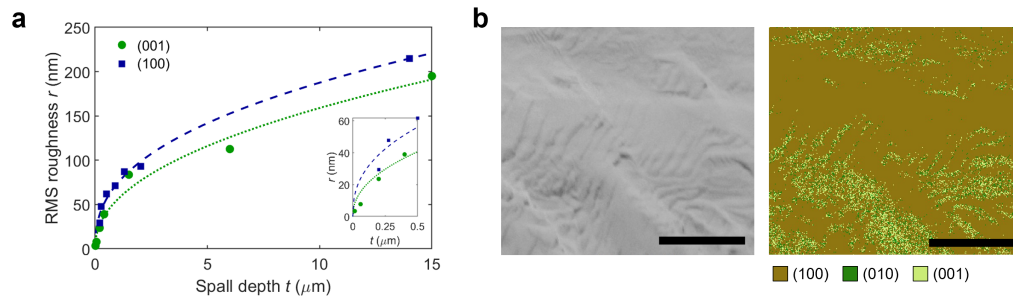


Figure 4.3: **Correlation of thickness and roughness in spalled BTO films.** (a) RMS roughness r of spalled (001) and (100) BTO films as function of the spall depth t . The inset highlights the roughness for spall depths below 500 nm. (b) Band contrast image (left) and corresponding crystal orientation map (right) obtained through electron backscatter diffraction. Scale bars: 20 μm .

Polypropylene carbonate (PPC) is then spin-coated over the entire sample to ensure uniform adhesion of the entire heterostructure to a polydimethylsiloxane (PDMS) stamp (Fig. 4.4a, d). The desired region is carefully cut out with a blade and picked up using the PDMS stamp, which is subsequently immersed in water to dissolve the PVA tape.

For substrate transfer, we use a resin that curable under ultraviolet (UV) light and semi-resistant to solvents. The PDMS stamp, now holding the spalled film, is positioned onto a drop of UV resin on the target substrate (Fig. 4.4b, e), with the Ni layer (Fig. 4.4b, blue) facing down. For this demonstration, we employ a silicon (Si) wafer with a 1 μm thick thermal oxide (silicon dioxide, SiO_2) layer. After curing the resin under UV light, the PDMS stamp is peeled off, and the sample is cleaned with acetone and isopropyl alcohol (IPA) to remove PPC residues on the spalled BTO film (Fig. 4.4c, f). Although some minor pitting is observed around the spalled area, likely due to the interaction between the solvent and the PPC residue adhering to UV resin, the spalled region itself remains clean and free from similar patterns. Importantly, the absence of gaps between the spall and the UV resin ensures that the surface roughness of the spalled remains unaffected during this process.

We use the transferred film shown in Fig. 4.4f to fabricate an electro-optically tunable device for characterizing the Pockels coefficient of spalled BTO thin films. In this device configuration, the electroplated Ni serves as both a metal back reflector and electrical contact. For applications requiring the removal of Ni, a two-step tape transfer process can be employed. In this approach, the spall is initially performed

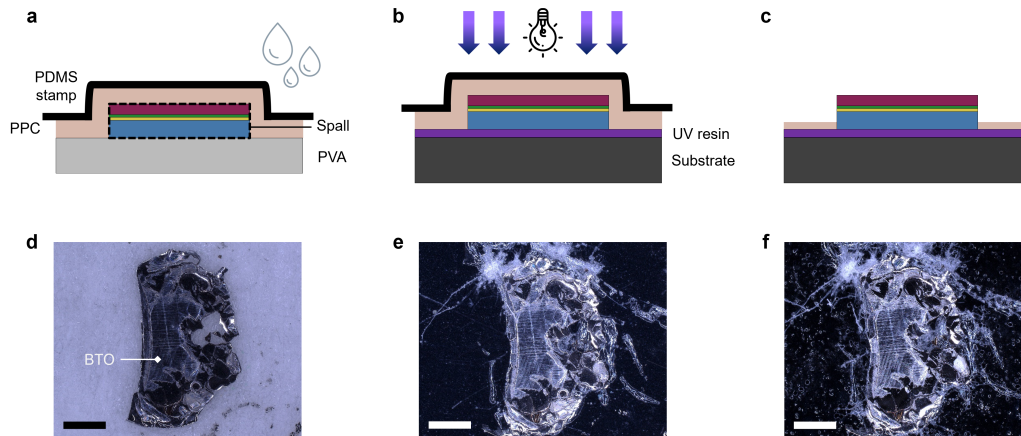


Figure 4.4: Transfer of spalled film onto substrate. (a) The spalled heterostructure (outlined by dashed black lines), consisting of Ni (blue), Au (yellow), Ti (green), and BTO (magenta), and adhered to PVA tape (gray), is spin-coated with PPC (tan) and picked up with a PDMS stamp (black). The PVA tape is then dissolved in water. (b) The spall is picked up with PPC/PDMS and adhered to a substrate (dark gray) with UV-curable resin (purple). The resin is cured under UV light (purple arrows). (c) After curing, the sample is cleaned with acetone/IPA to remove PPC from the spalled BTO. (d)-(f) Dark field optical microscope images of (d) spalled BTO film adhered to PVA and covered with PPC and PDMS, (e) spalled film adhered to PPC/PDMS on Si/SiO₂ wafer with UV resin, and (f) the transferred film after cleaning in acetone/IPA. Scale bars: 1 mm.

using a heat release tape, followed by a transfer to PVA tape with the BTO film facing downward. Once the spalled heterostructure is flipped, the procedure illustrated in Fig. 4.4 can be followed with the Ni layer exposed on top. The Ni layer can then be removed by immersing the stack in a Ni etchant, though this approach relies on the resistance of the UV-curable resin to the etchant.

For applications that require organic-free bonding, alternative methods such as wafer bonding may offer a viable solutions. However, applying heat and pressure to spalled BTO thin films could result in additional ferroelectric domain reorientation or even film breakage. Further research is needed to optimize bonding methods while preserving their structural and functional integrity.

4.3 Electro-optic characterization

To evaluate the functional properties of the spalled BTO thin films, we focus on characterizing their Pockels coefficient, a key parameter for electro-optic applica-

tions. As discussed in Section 4.1, noncentrosymmetric crystal groups, including BTO in its tetragonal phase, exhibit both electro-optic and piezoelectric effects. These effects are inherently coupled: The direct piezoelectric effect generates electric polarization in response to applied stress, while the converse piezoelectric effect induces strain under an applied electric field. This strain alters the refractive index through the photoelastic effect, which must be considered alongside the electro-optic effect to fully understand the material's behavior.

The Pockels tensor, which characterizes the electro-optic response, therefore includes contributions from three components: the piezoelectric, electronic, and ionic effects [192]. At low frequencies, from DC up to approximately 1 MHz, the photoelastic response dominates, as mechanical lattice deformations can follow the modulation signal. In this range, acoustic phonons also contribute to the modulation [193]. Above the acoustic phonon frequency, typically between 1 to 100 MHz, a crystal is considered to be 'clamped' because the mechanical deformations are too slow to respond to the modulation signal. At these frequencies, nonlinearities associated with optical phonons contribute to the Pockels effect and are referred to as ionic contributions. For frequencies exceeding the optical phonon range (around a few THz), these ionic contributions become negligible, and the electro-optic effect is primarily governed by electronic resonances, which have characteristic frequencies in the PHz regime.

To account for this frequency dependence, the Pockels tensor is typically divided into two parts: the unclamped tensor, which includes contributions from all three components and is observed up to few MHz, and the clamped tensor, which only reflects the higher frequency contributions [177]. Table 4.3 provides an overview of the unclamped and clamped electro-optic coefficients in bulk BTO.

Pockels coefficient	unclamped (pm/V)	clamped (pm/V)
$r_{13} = r_{23}$	10.2 ± 0.6	8 ± 2
r_{33}	105 ± 10	40.6 ± 2.5
$r_{42} = r_{51}$	1300 ± 100	730 ± 100

Table 4.3: **Pockels coefficients for bulk BTO in the unclamped and clamped case.** [139]

Given the frequency-dependent nature of electro-optic coefficients, it is crucial to characterize bulk BTO and spalled thin films across a range of modulation frequencies. Various techniques have been developed for this purpose, typically combining

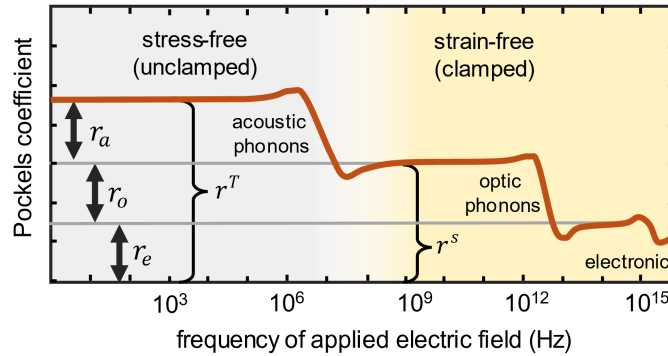


Figure 4.5: **Dispersion of electro-optic coefficient as function of modulation frequency.** Adapted from [194].

high-frequency electric fields with lock-in detection schemes for enhanced precision. These methods include interferometric approaches [195–197], transmission-based measurements [198, 199], as well as measurements leveraging integrated devices [200, 201]. Each approach offers unique advantages, such as increased sensitivity to small Pockels coefficients, the ability to resolve individual components of the Pockels tensor *vs* effective coefficients, and the varying levels of sample preparation [202].

In the following, we employ a Teng-Man reflectometry setup to characterize the Pockels coefficients of both bulk BTO substrates and spalled thin films. This method was selected for its high sensitivity and minimal sample preparation requirements, making it particularly well-suited for assessing electro-optic properties across different material forms. Below, we first outline the measurement procedure and subsequently present the experimental results for the characterization of bulk BTO and spalled thin films.

Teng-Man reflectometry

The Teng-Man measurement technique was originally developed for measuring the electro-optic coefficient r_{33} of poled polymer films [195, 196]. The experimental setup is shown in Fig. 4.6a, with the inset providing a schematic of the bulk BTO sample used for calibration. The incident laser beam is linearly polarized at 45° , ensuring equal amplitude for the *s*- and *p*-polarized components. Upon reflection from the sample, the beam propagates through a Soleil-Babinet compensator (SBC), an analyzer, and into a detector. The SBC functions as a continuously variable wave

plate, allowing precise control of the phase retardance through positional adjustment. A lock-in amplifier is used to modulate the sample.

The setup is used in two configurations: (1) with two irises before and after the sample, respectively, ensuring a probing diameter of less than 300 μm and signal collection from the reflected beam after a single pass through the sample (as shown in the inset of Fig. 4.6a), and (2) with two lenses in place of the irises to probe smaller areas with tens of microns diameter. In the first configuration, the reflected intensity is measured with the lock-in amplifier, while in the second, an oscilloscope can be used due to a stronger signal. For this study, configuration (1) is employed for measurements of the bulk sample, while both configurations (1) and (2) are used to evaluate spalled films for comparative analysis.

The working principle of Teng-Man reflectometry involves modulating the phase retardance between the s - and p -waves, denoted as Ψ_{sp} , using the SBC. The averaged output intensity is given by

$$I_{\text{DC}} = I_0 + 2I_c \cdot \sin^2\left(\frac{\Psi_{\text{sp}} + \Psi_c}{2}\right) = C_0 + C_1 \cdot \sin^2\left(\frac{\Psi_{\text{sp}} + \Psi_c}{2}\right). \quad (4.5)$$

Here, I_0 represents the background intensity, and I_c corresponds to half the maximum intensity. The compensator phase Ψ_c is controlled by adjusting the retardation setting and can be written as $\Psi_c = C_2 \cdot x$, where x is the SBC position in millimeters. By fitting the DC intensity measurements at various SBC positions to equation (4.5), we can extract C_0 , C_1 , Ψ_{sp} , and C_2 .

Next, a modulating voltage $V = V_m \cdot \sin(\omega_m t)$ at frequency $\omega_m = 2\pi f_m$ is applied across the sample. This induces a phase change $\delta\Psi$ in both the s - and p -waves due to changes in the refractive index, δn , and path length, δs , which are caused by the electro-optic effect. As a result, the phase change is given by $\delta\Psi = (2\pi/\lambda)(s\delta n + n\delta s)$, with λ corresponding to the optical wavelength. The modulated intensity, I_m , is obtained by differentiating I_{DC} by using a first-order approximation for V_m [203], and can be written as

$$I_m = \delta C_0 + \delta C_1 \cdot \sin^2\left(\frac{\Psi_{\text{sp}} + \Psi_c}{2}\right) + \frac{C_1}{2} \sin(\Psi_{\text{sp}} + \Psi_c) \delta\Psi_{\text{sp}}. \quad (4.6)$$

The second term corresponds to reflectivity changes due to refractive index variation, while the third term reflects contributions from the phase difference change $\delta\Psi_{\text{sp}}$.

In the measurement, we record the absolute value of the modulated intensity $|I_m|$ at several positions and fit to equation (4.6) to obtain δC_0 , δC_1 , and $\delta\Psi_{\text{sp}}$.

The Pockels coefficients are derived using $\delta\Psi_{\text{sp}} = \Gamma_m \sin(\omega_m t)$, where Γ_m is expressed as

$$\Gamma_m = \left(\frac{2\pi r_{33} V_m}{\lambda} \right) \left[\frac{n_o n_e \sin^2 \theta}{(n_e^2 - \sin^2 \theta)^{1/2}} + \frac{r_{13}}{r_{33}} \left(\frac{n_o^3}{n_e} (n_e^2 - \sin^2 \theta)^{1/2} - \frac{n_o^4}{(n_o^2 - \sin^2 \theta)^{1/2}} \right) \right]. \quad (4.7)$$

Here, θ is the incident angle of light on the sample. When the output beam intensity is biased at the half-intensity I_c , the modulated intensity is in its most linear region. At this point, $I_m/I_c \approx \delta\Psi_{\text{sp}}$. Substituting this relation into the equations above yields

$$r_{33} = \left(\frac{\lambda}{2\pi} \right) \left(\frac{I_m}{I_c V_m} \right) \left[\frac{n_o n_e \sin^2 \theta}{(n_e^2 - \sin^2 \theta)^{1/2}} + \zeta \left(\frac{n_o^3}{n_e} (n_e^2 - \sin^2 \theta)^{1/2} - \frac{n_o^4}{(n_o^2 - \sin^2 \theta)^{1/2}} \right) \right]^{-1}. \quad (4.8)$$

Here, we define $\zeta \equiv r_{13}/r_{33}$. For BTO, we assume $\zeta = 1/10$ based on the electro-optic coefficients reported in bulk BTO [139]. Under the approximation $n_o \approx n_e \approx n$, Eq. (4.8) simplifies to

$$r_{33} = \left(\frac{\lambda}{2\pi} \right) \left(\frac{I_m}{I_c V_m} \right) \cdot \frac{10(n^2 - \sin^2 \theta)^{1/2}}{9n^2 \sin^2 \theta}. \quad (4.9)$$

In our measurement, light is incident on the sample at $\theta = 45^\circ$.

Bulk electro-optic characterization

To calibrate the Teng-Man setup and obtain reference values for the electro-optic coefficients of bulk BTO substrates used for spalling, we pattern (100)-oriented bulk substrates (a -axis) with top and bottom electrodes. The bottom electrode consists of a 5 nm Ti adhesion layer followed by a 100 nm Au layer and is contacted from the edge of the substrate using silver paste. For the top electrodes, we pattern three 50 nm thick ITO contacts, as shown in Fig. 4.6b. These top contacts are designed to enable probing of the electro-optic coefficients with both in-plane and out-of-plane electric fields. Each ITO top electrode also includes an Au bond pad (5 nm Ti / 80 nm Au) for electrical addressing. The choice of crystal orientation for bulk testing

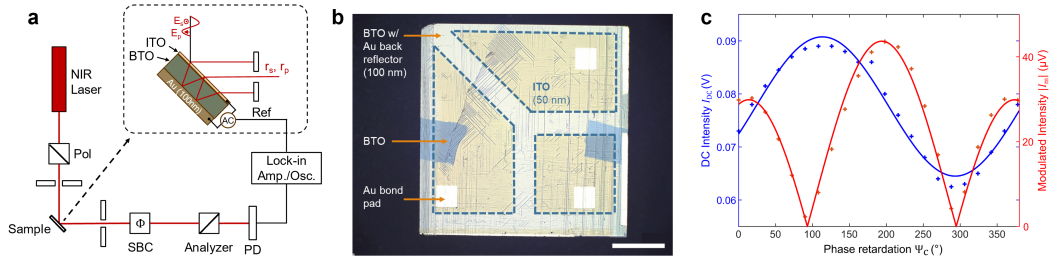


Figure 4.6: Electro-optic measurement of bulk BTO. (a) Schematic of Teng-Man measurement setup. The setup was verified using bulk BTO samples, consisting of a 100 nm thick Au back electrode and a 50 nm thick ITO top electrode (inset). Configuration (1) uses irises before and after the sample. In configuration (2), each iris is replaced with a lens with a focal length of $f = 3.5$ cm. Pol: Polarizer. PD: Photodetector. Lock-in Amp./Osc.: Lock-in amplifier. Osc.: Oscilloscope. Ref: Reference signal. (b) 0.5 mm thick (100)-oriented bulk BTO substrate with 100 nm thick Au back reflector and top electrodes consisting of 50 nm thick ITO (area inside gray dashed lines) and 1 mm^2 sized bond pads consisting of 5 nm Ti and 100 nm Au. Scale bar: 2.5 mm. (c) DC intensity I_{DC} (blue) and modulated intensity $|I_m|$ (red) obtained for bulk substrate shown in (b).

allows us to potentially probe both r_{33} and r_{42} coefficients, unlike (001)-oriented substrates (c -axis), which primarily facilitate r_{33} measurements.

Importantly, while the a -axis orientation allows measurement of additional electro-optic coefficients, it introduces in-plane birefringence. This birefringence causes the E_x and E_y components of the $+45^\circ$ linearly polarized incident plane wave to experience different refractive indices, resulting in a rotation of the polarization of the reflected beam. To account for this effect, the Teng-Man setup for a -axis samples requires the polarizer to be oriented at $+45^\circ$, the SBC at $+45^\circ$ and the analyzer at approximately 0° . In contrast, c -axis films conventionally use a configuration with the polarizer, SBC and analyzer oriented at $+45^\circ$, $+90^\circ$ and -45° , respectively. The measurement configurations are selected based on the expected shape of the I_{DC} and $|I_m|$ curves, with I_{DC} resulting in a single peak around a phase retardation of 180° and $|I_m|$ resulting in two maxima at the quadrature points of the DC curve. We refer to the first configuration as a -axis configuration while the second is referred to as c -axis configuration. All measurements on bulk substrates are performed at a wavelength of $\lambda = 1520$ nm.

In a first step, we probe the electro-optic coefficient on top of the ITO electrode area with an out-of-plane modulating field and the Teng-Man setup in the a -axis

configuration. Initial measurements yield an electro-optic coefficient of 4.1 pm/V. We then pole the bulk BTO substrate out-of-plane with a voltage of 200 V across a thickness of 0.5 mm (poling field of 4 kV/cm) for 1 hour. After poling, the Teng-Man setup is switched to the c -axis configuration to obtain clean measurements, yielding an electro-optic coefficient of 11.4 pm/V. We attribute this increase in the electro-optic coefficient to a reorientation of the domains from a -axis to c -axis in the probing region. However, due to a preferential (100) orientation of the substrate and a relatively small poling field, only partial reorientation occurs, resulting in an electro-optic coefficient smaller than the literature value for r_{33} .

To probe r_{33} more accurately with a (100)-oriented bulk substrate, we move the probing spot to an area between two ITO top electrodes in the bottom half of the substrate shown in Fig. 4.6b. This position allows application of an in-plane modulating field in a preferentially a -axis oriented region. We perform the measurements using an a -axis configuration of the Teng-Man setup and obtain an electro-optic coefficient of 22.3 pm/V. We then apply a voltage of 200 V between the two in-plane electrodes spaced 1 mm apart (poling field of 2 kV/cm), leading to a drastic increase in the measured electro-optic coefficient, which reaches 96.4 pm/V. This value is in good agreement with literature values for bulk BTO ($r_{33,\text{lit}} = 105 \pm 10$ pm/V [139]). The corresponding measurements for I_{DC} and $|I_m|$ are shown in Fig. 4.6c, indicating clear peaks in the modulated intensity curve (red) at the quadrature points of the DC curve (blue).

Thin film electro-optic characterization

The Pockels coefficient of spalled BTO films is evaluated using the film shown in Fig. 4.4f. The spalled film, obtained from a c -axis bulk crystal, has a thickness of approximately 20 μm and lateral dimensions greater than 0.5×1.5 mm² (Fig. 4.7a). The Ni stressor layer beneath the BTO serves a dual purpose of a metal back contact and reflective surface. A transparent top electrode is patterned on top of the spalled BTO using shadow masks. This electrode consists of a 50 nm thick ITO layer (light green dashed region in Fig. 4.7a) that facilitates optical probing. The ITO layer is partially overlaid with a 5 nm Ti and 100 nm Au layer (brown dotted region in Fig. 4.7a) for wire bonding. This electrode configuration allows direct characterization of the r_{33} coefficient under an out-of-plane modulating field, given the c -axis orientation of the spalled BTO film.

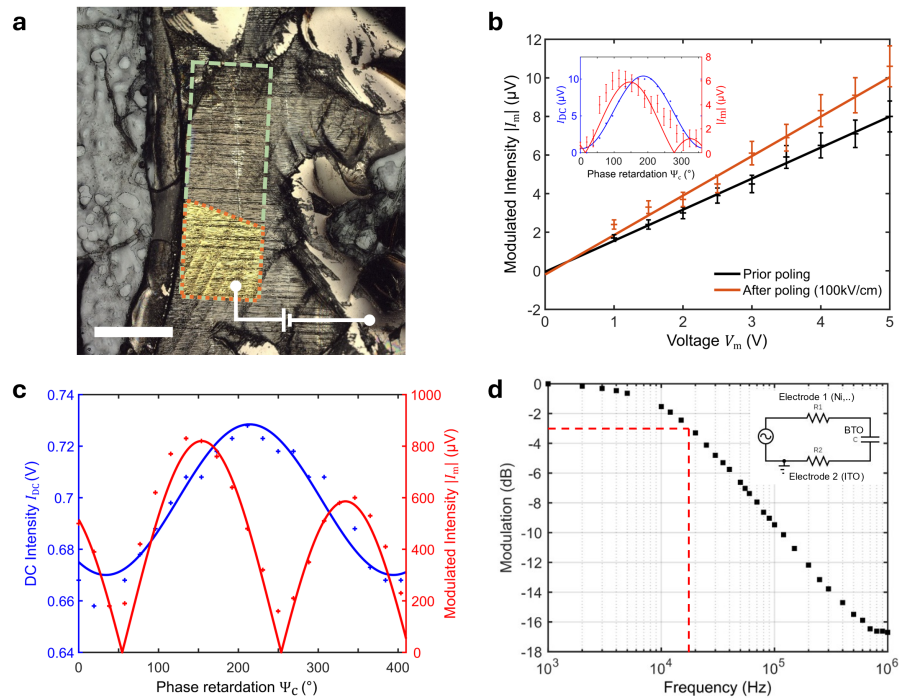


Figure 4.7: **Electro-optic measurement of spalled BTO thin film.** (a) Optical microscope image of BTO spall from Fig. 4.4f with ITO/Au top electrode. The light green dashed region indicates the area with transparent ITO for optical probing, the brown dotted region represents the area with Au on top of ITO. Wires are bonded to the Au top contact and Ni back layer, enabling probing of the electro-optic coefficients with an out-of-plane electric field. Scale bar: 500 μm . (b) Modulated intensity $|I_m|$ as a function of applied voltage V_m using configuration (1) of the Teng-Man setup. Inset: DC intensity I_{DC} (blue) and modulated intensity $|I_m|$ (red) as function of phase retardation Ψ_c for the sample shown in (a). Crosses represent measurement points, and the lines are the fits used to extract the Pockels coefficient. Error bars correspond to standard deviations and are deduced from repeated measurements. (c) DC intensity I_{DC} (blue) and modulated intensity $|I_m|$ (red) as function of phase retardation Ψ_c with configuration (2) of Teng-Man setup. (d) Normalized modulation intensity as a function of modulation frequency. The red dashed line indicates the -3 dB cutoff frequency at approximately 18 kHz. The inset illustrates the equivalent circuit of the device, with R1 and R2 representing the resistances of the top and bottom electrodes, and C representing the capacitance of the BTO layer.

We first perform measurements on the spalled film shown in Fig. 4.7a using configuration (1) of the Teng-Man setup with an iris before and after the sample. As outlined in the preceding sections, we begin by measuring the DC intensity as function of the phase retardation Ψ_c to calibrate the SBC, and then measure the modulated intensity curve. The inset of Fig. 4.7b shows a representative measurement for this case with I_{DC} plotted in blue and $|I_m|$ in red. As expected, I_{DC} reaches a minimum at $\Psi_c \approx 0^\circ$ and 360° due to the cross-polarization of the polarizer and analyzer (Fig. 4.6a). Next, we apply a modulating voltage across the sample with $V_m = 5$ V at a frequency $f_m = 10$ kHz, which enables a measurement of the unclamped electro-optic coefficient [177, 193]. The modulated intensity $|I_m|$ is measured using a lock-in amplifier, with the red points in the inset of Fig. 4.7b representing averaged data over repeated measurements. Error bars denote standard deviations across these measurements. The values for I_{DC} and $|I_m|$ are then fitted to equations (4.5) and (4.6), respectively, and r_{33} is evaluated using equation (4.9) at the operating wavelength $\lambda = 1500$ nm. Using refractive index values for BTO from Ref. [173], we determine an electro-optic coefficient of $r_{33} = 42 \pm 3$ pm/V. To confirm that the measured response is governed by the electro-optic Pockels effect, we demonstrate a linear relationship between the applied voltage V_m and the modulated intensity $|I_m|$ in Fig. 4.7b (black line), validating the fitted r_{33} value. The values for $|I_m|$ in Fig. 4.7b are recorded at $\Psi_c \approx 115^\circ$, where the response is maximized.

We observe an asymmetry in the two peaks of the modulated intensity in the inset of Fig. 4.7b, which is attributed to surface roughness leading to scattering in the reflected signal, as well as partial polarization rotation due to domain switching during spalling. To limit the impact of these effects, we repeat the measurement after poling the spalled thin film with an out-of-plane field by applying a constant voltage of 20 V for one hour. This procedure increases the measured electro-optic coefficient to 55 ± 5 pm/V. Assuming the same ratio of r_{42}/r_{33} as in bulk BTO, we can project a value of $r_{42} = 680$ pm/V based on the measured r_{33} after poling. Although this value is lower than that of bulk BTO, it significantly exceeds those achieved using alternative bottom-up growth techniques such as sputtering or pulsed laser deposition (see Table 4.2).

Furthermore, based on the EBSD scans previously shown in Fig. 4.3b, we know that there is a correlation between domain orientation and surface roughness and that single-domain regions are tens of microns in size. To investigate the effect of

domain structure on the measured electro-optic coefficient, we perform a secondary measurement using configuration (2) of the Teng-Man setup, where the irises before and after the sample are replaced with lenses. With this change, we can reduce the optical probing diameter from several $100\ \mu\text{m}$ to $\sim 50\ \mu\text{m}$ and achieve a cleaner signal readout. As a result, the DC intensity and modulated intensity can be measured with an oscilloscope and are shown in Fig. 4.7c in blue and red, respectively. After fitting the data from a series of measurements, we obtain an electro-optic coefficient of $r_{33} = 160 \pm 40\ \text{pm/V}$, leading to a projected value of $r_{42} = 1980\ \text{pm/V}$. Despite the nonideal roughness and domain structure of spalled BTO, these results suggest that bulk properties are preserved locally, particularly in potentially single-domain regions. We anticipate that future improvements to the electro-optic properties of spalled films will involve obtaining large-area thin films with low roughness or polishing thin films after spalling to get cleaner reflected signals. Moreover, poling thin films at elevated electric fields and temperatures may enable complete restructuring and stabilization of domains in the desired configuration.

All electro-optic measurements discussed until now were performed using a modulation frequency of 10 kHz. Figure 4.7d illustrates the frequency dependence of the modulated signal up to 1 MHz, showing a -3 dB cutoff frequency, $f_{-3\text{dB}}$, at approximately 18 kHz. The decrease in modulation intensity is attributed to the RC time constant of the device, rather than a transition from unclamped to clamped Pockels coefficients. The circuit model for the spalled BTO film measured for electro-optic characterization is shown in the inset of Fig. 4.7d.

In the ideal case, $f_{-3\text{dB}}$ can be approximated using the resistance of the ITO layer ($\rho_{\text{ITO}} \approx 10^{-4}\ \Omega\cdot\text{cm}$), the relative permittivity of BTO along the c -axis ($\epsilon_{\text{BTO},c} \approx 135$), the dimensions of the ITO top electrode ($w_{\text{ITO}} = 0.5\ \text{mm}$, $L_{\text{ITO}} = 1\ \text{mm}$), as well as the film thicknesses ($t_{\text{ITO}} = 50\ \text{nm}$, $t_{\text{BTO}} = 20\ \mu\text{m}$). However, the surface roughness of the spalled BTO film will introduce deviations from these values. Based on the results shown in Fig. 4.3a, we expect greater than 200 nm surface roughness for a $20\ \mu\text{m}$ thick spalled BTO film. Since the ITO thickness is much smaller than the RMS roughness of the BTO film, current flow paths will be disrupted, increasing ITO resistivity as described by the Fuchs-Sondheimer model [204, 205]. Assuming an increase in ITO resistivity by two orders of magnitude ($\rho_{\text{ITO,rough}} \approx 10^{-2}\ \Omega\cdot\text{cm}$), the theoretical modulation bandwidth of the spalled film can be calculated as

$$f_{-3\text{dB}} = \frac{1}{2\pi RC} = \frac{1}{2\pi} \times \frac{w_{\text{ITO}} \cdot t_{\text{ITO}}}{\rho_{\text{ITO,rough}} \cdot L_{\text{ITO}}} \times \frac{t_{\text{BTO}}}{\epsilon_0 \cdot \epsilon_{\text{BTO,c}} \cdot L_{\text{ITO}} \cdot w_{\text{ITO}}} \approx 592 \text{ kHz}. \quad (4.10)$$

Here, the conductivities of Ni and Au are neglected. R represents the resistance of the ITO electrode, C is the capacitance of the spalled BTO film, and ϵ_0 is the vacuum permittivity. Our calculations indicate that the upper limit of the frequency bandwidth for the current device is in the range of hundreds of kHz. Empirical data shows an even lower RC time constant for the measured device, which could be attributed to an even lower ITO resistivity and increased relative permittivity of BTO due to local variations in the domain structure. To accurately capture the transition from unclamped to clamped electro-optic coefficients, alternative device geometries will need to be explored.

Measurement procedure for characterization of r_{42}

Thus far, we have focused on an electro-optic characterization that relies on the same electrodes for both poling and probing, resulting in parallel poling and modulating fields. However, in the characterization of bulk BTO substrates, we noted that the in-plane birefringence of a -axis BTO substrates provides an opportunity to additionally probe the r_{42} coefficient with the Teng-Man setup.

To achieve this, an a -axis substrate or spalled film must first be poled using an in-plane field. Following this step, instead of applying a modulating field that is parallel to the poling field, electro-optic coefficients would be probed at an angle to the poling field. This requires patterning individual probing electrodes that are integrated within the gap between the poling electrodes. These electrodes can be oriented at various angles to the poling field to enable angle-dependent characterization of the electro-optic coefficients. With this configuration, it becomes possible to probe a linear combination of r_{33} and r_{42} . This approach is analogous to phase modulator designs utilizing an a -axis oriented BTO film with lateral electrodes positioned at approximately 45° , which maximize the effective electro-optic coefficient [204, 205].

Building on this understanding, we now shift the focus to design considerations aimed at maximizing the electro-optic index change. Specifically, we analyze the requirements for achieving high-performance active metasurfaces using BTO thin

films and explore designs for active transmissive metasurfaces optimized for operation at visible wavelengths.

4.4 Design strategy for maximal electro-optic index change

To maximize the electro-optic index change under an applied field, it is crucial to identify the optimal crystal orientation, the polarization of the electric field relative to the applied electric field \mathbf{E} , and the wavevector \mathbf{k} . The subsequent calculations assume a single-domain BTO thin film and use electro-optic coefficients reported for bulk barium titanate. Such properties can be realized over areas spanning tens of microns using the spalling procedure described above. For an analysis of the achievable index changes in the achievable index in multi-domain configurations of BTO thin films in comparison to single-domain regions, we refer the reader to Ref. [193].

As discussed in Section 4.1, the polarity of BTO in its tetragonal phase gives rise to a strong electro-optic response at room temperature and is defined by the following Pockels tensor

$$\mathbf{r} = \begin{pmatrix} 0 & 0 & r_{13} \\ 0 & 0 & r_{23} \\ 0 & 0 & r_{33} \\ 0 & r_{42} & 0 \\ r_{51} & 0 & 0 \\ 0 & 0 & 0 \end{pmatrix}. \quad (4.11)$$

In this tensor, the dominant electro-optic contributions arise from $r_{42} = r_{51} = 1300$ pm/V in bulk crystals [139]. Based on this tensor, the modified index ellipsoid can be formulated as

$$\left(\frac{1}{n_o^2} + r_{13}E_z\right)x^2 + \left(\frac{1}{n_o^2} + r_{23}E_z\right)y^2 + \left(\frac{1}{n_e^2} + r_{33}E_z\right)z^2 + 2yze_{42}E_y + 2xze_{51}E_x = 1. \quad (4.12)$$

Here, n_o and n_e represent the ordinary and extraordinary refractive indices, respectively. We consider the case where the a -, b -, and c -axis of the crystal are aligned with the x , y , and z coordinate axis, respectively (Fig. 4.8a). To determine the conditions for maximizing the index change, we need to perform a principal axis transformation. Our calculations follow the methodology outlined in Ref. [206], and show achievable index changes using the Pockels coefficients of bulk BTO.

***a*-axis oriented BTO**

We first consider the case of *a*-axis oriented BTO, where the *x*-axis of our coordinate system is oriented out-of-plane. For a resonator or waveguide structure on an *a*-axis oriented BTO film, an example of which is shown in Fig. 4.8b, we can identify two methods of optical excitation. In a TM mode (Fig. 4.8c), the primary direction of the optical electric field is out-of-plane (along the *x*-axis). In contrast, in a TE mode (Fig. 4.8d), the primary component of the optical electric field is in-plane, either along the *y*- or *z*-axis [206, 207]. In a waveguide structure such as the one shown in [206], the specific in-plane direction depends on the waveguide orientation, with the optical electric field being perpendicular to it.

We can now qualitatively determine which electro-optic coefficients primarily contribute to the index change using Eq. (4.12) and the orientation of the applied field:

1. **Applied external field along E_z** (waveguide oriented along *y*, Fig. 4.8e): For a TE mode, the optical electric field is primarily along the *z*-axis, leading to a dominant contribution from r_{33} . For a TM mode, the optical electric field is along the *x*-axis and modulation arises primarily from r_{13} .
2. **Applied external field along E_y** (waveguide oriented along *z*, Fig. 4.8f): Significant refractive index modulation simultaneously requires nonzero *y*- and *z*-components of the optical electric field. However, in a TE mode, the optical electric field is along the *y*-axis, while a field along the *x*-axis is obtained for a TM mode.
3. **Applied external field along E_x** : A similar argument as in the case of an applied field along E_y holds in this case. The condition of having an electric field simultaneously along the *x*- and *z*-axes cannot be satisfied.

While r_{33} can effectively create index modulation in one of the configurations discussed above, the highest Pockels coefficient, r_{42} , offers a pathway to more versatile modulators by relaxing certain design constraints. To utilize r_{42} , the resonator (or waveguide) needs to be oriented at an angle ϕ relative to the optical axis, as illustrated in Fig. 4.9a. This configuration allows us to introduce a rotated coordinate system (x' , y' , z') which is defined as

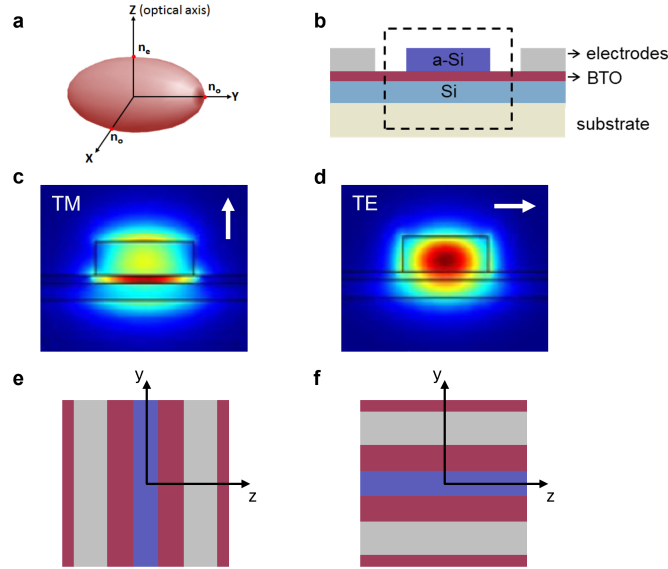


Figure 4.8: **BTO crystal orientation and resonator layout.** (a) Orientation of the index ellipsoid relative to coordinate system, with the optical axis (c -axis) aligned along z . The intersections of the index ellipsoid with the principal axes define the ordinary and extraordinary refractive indices, n_o and n_e , respectively. (b) Cross-section of waveguide structure studied in Ref. [206], featuring an a -axis oriented BTO thin film (magenta). Electric field profile of (c) TM and (d) TE modes, respectively. Arrow in the upper right indicates the orientation of the optical electric field within the BTO film. In-plane waveguide configurations are shown for (e) a waveguide along y (purple) with an applied field along z (between gray electrodes), and (f) a waveguide along z and applied field along y . Figures adapted from Ref. [206].

$$\begin{aligned}
 x &= x' \\
 y &= y' \cos \phi + z' \sin \phi \\
 z &= -y' \sin \phi + z' \cos \phi.
 \end{aligned} \tag{4.13}$$

When an external field $E_{z'}$ is applied, the field components transform as $E_y = E_{z'} \sin \phi$ and $E_z = E_{z'} \cos \phi$. We can then substitute these into Eq. (4.12) and analyze separately for TE and TM modes. For the TE mode, the optical electric field is nonzero only along the z' -axis ($x' = y' = 0$). This simplifies the expression to

$$\left[\frac{1}{n_o^2} \sin^2 \phi + \frac{1}{n_e^2} \cos^2 \phi + [(r_{13} + 2r_{42}) \cos \phi \sin^2 \phi + r_{33} \cos^3 \phi] E_{z'} \right] z'^2 =$$

$$\left[\frac{1}{n_{z'}^2} + r_{z'} E_{z'} \right] z'^2 = 1. \quad (4.14)$$

Here, $n_{z'}$ and $r_{z'}$ are the effective refractive index and Pockels coefficients along the z' -direction, given by

$$n_{z'} = \frac{n_o n_e}{\sqrt{n_e^2 \sin^2 \phi + n_o^2 \cos^2 \phi}} \quad (4.15)$$

$$r_{z'} = r_{33} \cos^3 \phi + (r_{13} + 2r_{42}) \cos \phi \sin^2 \phi.$$

Figure 4.9b illustrates the variation in $n_{z'}$ with ϕ for wavelengths between 400 to 700 nm. As the rotation angle increases from 0° to 90° , $n_{z'}$ transitions from n_e to n_o , reconnecting with the configurations discussed in Fig. 4.8e and f. The corresponding variation in $r_{z'}$ is shown in Fig. 4.9c, and reaches a maximum of $r_{z',\max} = 1025$ pm/V for $\phi = 54^\circ$. In multi-domain BTO films, this optimal angle shifts closer to 45° [165, 193].

Finally, assuming $r_{z'} E_{z'} \ll n_{z'}^{-2}$, we can use the differential relation $dn = -\frac{1}{2} n^3 d\left(\frac{1}{n^2}\right)$ [146] to approximate the refractive index under an applied field, $n_{z',\text{field}}$, at the optimal angle as

$$n_{z',\text{field}} = n_{z'} - \frac{1}{2} n_{z'}^3 r_{z',\max} E_{z'}. \quad (4.16)$$

Figure 4.9d presents the effective index change, $|\Delta n_{z'}| = |n_{z'} - n_{z',\text{field}}|$, across the visible spectrum for an applied field of 0.1 MV/cm within BTO. For the calculations above, we use the refractive index values for BTO found in Ref. [208] and the unclamped Pockels coefficients summarized in Table 4.3.

We can repeat a similar analysis for the TM mode, where the optical electric field is only nonzero along the x' -axis and $y' = z' = 0$. Applying the principal axis transformation in this case results in the following equation

$$\left[\frac{1}{n_o^2} + r_{13} \cos \phi E_{z'} \right] x'^2 = \left[\frac{1}{n_{x'}^2} + r_{x'} E_{z'} \right] x'^2 = 1. \quad (4.17)$$

Here, the effective refractive index and Pockels coefficient along x' , $n_{x'}$ and $r_{x'}$, are defined as

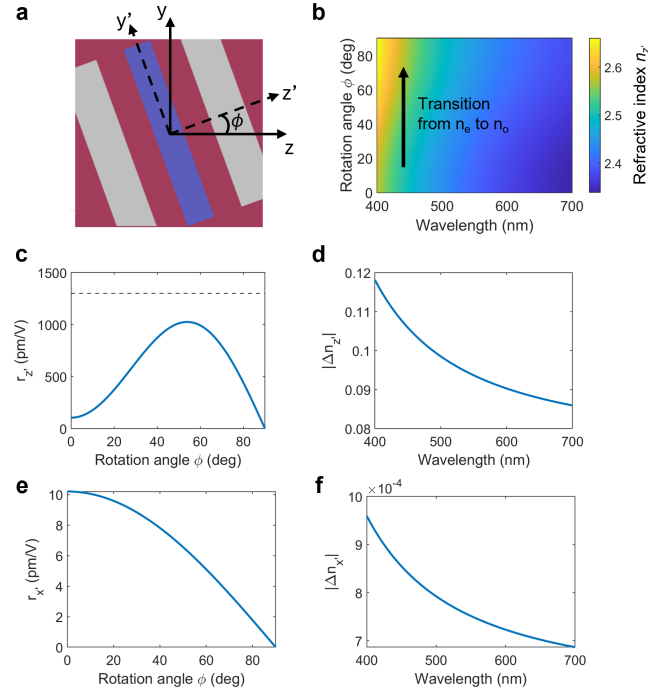


Figure 4.9: Pockels coefficient and index change for a -axis BTO after principal axis transformation. (a) In-plane rotation of principal axes by angle ϕ around the $x = x'$ rotation axis, resulting in new in-plane principal axes y' and z' . (b) Effective refractive index n'_z as function of rotation angle ϕ and wavelength. (c) Effective Pockels coefficient $r'_{z'}$ for the TE mode as function of ϕ . The dashed gray line indicates the unclamped bulk value of r_{42} for reference. (d) Effective index change $|\Delta n'_{z'}|$ as function of wavelength, calculated using the maximum $r'_{z'}$ from (c) and an applied field of 0.1 MV/cm. (e) Effective Pockels coefficient $r'_{x'}$ for the TM mode as function of ϕ . (f) Effective index modulation $|\Delta n'_{x'}|$ as function of wavelength based on the maximal achievable value for $r'_{x'}$ shown in (e) and an applied field of 0.1 MV/cm. All calculations assume a single-domain, a -axis oriented BTO film.

$$\begin{aligned} n_{x'} &= n_o \\ r_{x'} &= r_{13} \cos \phi. \end{aligned} \quad (4.18)$$

As shown in Fig. 4.9e, this configuration yields a significantly smaller Pockels coefficients with a maximum of $r'_{x',\max} = r_{13} = 10.2$ pm/V at $\phi = 0$. This value is two orders of magnitude lower than the maximum effective Pockels coefficient, $r'_{z',\max}$, discussed earlier. Consequently, the resulting refractive index change, $|\Delta n'_{x'}|$, is also two orders of magnitude smaller, as depicted in Fig. 4.9f for the same applied field.

***c*-axis oriented BTO**

In *c*-axis oriented BTO, the optical axis is aligned with the *z*-axis of the coordinate system, as shown in Fig. 4.8a. From Eq. (4.12), it is evident that leveraging r_{42} in this configuration requires an in-plane field (E_x , E_y , or a linear combination thereof). However, applying such fields to *c*-axis BTO films inevitably rotates the index ellipsoid, leading to a polarization rotation that complicates the design of pure phase or amplitude modulators.

The polarization rotation can be understood by considering a representative case of a field applied along the *x*-axis ($E_x \neq 0$) while $E_y = E_z = 0$. Under these conditions, equation (4.12) simplifies to

$$\frac{x^2}{n_x^2} + \frac{y^2}{n_y^2} + \frac{z^2}{n_z^2} + 2xzr_{42}E_x = 1. \quad (4.19)$$

The resulting principal axis transformation corresponds to a rotation around the *y*-axis by an angle θ , and is given by

$$\begin{aligned} x &= x' \cos \theta + z' \sin \theta \\ y &= y' \\ z &= -x' \sin \theta + z' \cos \theta. \end{aligned} \quad (4.20)$$

After this transformation, the index ellipsoid along the new principal axes (x' , y' , z') becomes

$$\left(\frac{1}{n_x^2} - r_{42}E_x \tan \theta \right) x'^2 + \frac{y'^2}{n_y^2} + \left(\frac{1}{n_z^2} + r_{42}E_x \tan \theta \right) z'^2 = \frac{x'^2}{n_{x'}^2} + \frac{y'^2}{n_{y'}^2} + \frac{z'^2}{n_{z'}^2} = 1. \quad (4.21)$$

Under the assumption that $r_{42}E_x \tan \theta \ll \frac{1}{n_x^2}$, we can write the effective refractive indices as

$$\begin{aligned} n_{x'} &= n_x + \frac{1}{2}n_x^3 r_{42}E_x \tan \theta \\ n_{y'} &= n_y \\ n_{z'} &= n_z - \frac{1}{2}n_z^3 r_{42}E_x \tan \theta \end{aligned} \quad (4.22)$$

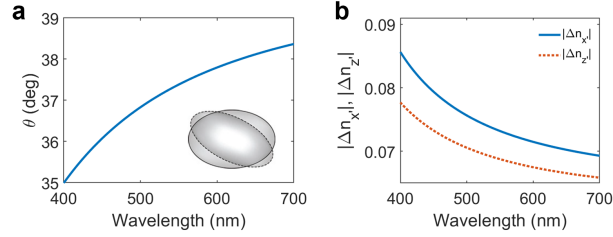


Figure 4.10: **Rotation of index ellipsoid and index change for c -axis BTO after principal axis transformation.** (a) Rotation angle θ as function of wavelength for an applied field of 0.1 MV/cm. The inset illustrates a schematic of an index ellipsoid rotated around the out-of-plane y -axis (dashed). (b) Effective refractive index modulation $|\Delta n_{x'}|$ (solid blue) and $|\Delta n_{z'}|$ (dotted orange) along the transformed principal axes (x' , z') based on the rotation angle in (a) and an applied field of 0.1 MV/cm.

and the rotation angle is determined by

$$\tan 2\theta = -\frac{2r_{42}E_x}{\frac{1}{n_x^2} - \frac{1}{n_z^2}}. \quad (4.23)$$

Figure 4.10 shows the rotation angle θ and the change in effective refractive indices $|\Delta n_{x'}|$ and $|\Delta n_{z'}|$ as function of wavelength for an applied field of 0.1 MV/cm. Here, we used $n_x = n_o$ and $n_z = n_e$. While the achievable index changes in c -axis BTO are smaller than those attainable with a -axis BTO for a TE mode, they are comparable in magnitude and could enable the design of active polarization modulators (discussed further in Section 4.8).

4.5 Active transmissive metasurfaces: Unit cell design

BTO is an especially attractive material for active metasurfaces due to its superior electro-optic properties, short response times, high refractive index, and broad transparency window spanning visible to near-infrared wavelengths. These characteristics make it highly suitable for dynamic phase and amplitude modulation. This study focuses on active metasurfaces operating at red, green, and blue wavelengths ($\lambda = 630, 532, \text{ and } 460 \text{ nm}$, respectively), with a particular focus on transmissive designs. Unlike reflective metasurfaces, transmissive metasurfaces enable seamless integration with chip-scale light sources to create monolithic, ultra-compact optical devices capable of dynamic wavefront shaping. However, the shorter interaction length in transmissive metasurfaces typically necessitates more sophisticated designs with higher quality factors, making both their design and experimental

realization considerably more challenging. As a result, the majority of active metasurface research to date has focused on reflective devices.

Previous studies have shown that nanoblock resonators made from amorphous silicon (a-Si) can achieve active beam steering in transmission [80]. These resonators leverage higher-order Mie resonances to attain high quality factors [209], enabling precise wavefront manipulation. Building on these principles, nanoblock resonators composed of BTO can offer comparable functionality across multiple wavelengths while simultaneously achieving shorter response times. As detailed in Section 4.4, refractive index changes of approximately 0.1 or higher are achievable in a -axis BTO under applied fields of 0.1 MV/cm, with further increases possible at higher fields. This index modulation, combined with negligible optical losses and high-quality resonances, has the potential to support large phase modulation ranges potentially extending up to 2π .

Although BTO has a lower refractive index ($n_{\text{BTO}} \sim 2.4 - 2.6$) compared to amorphous silicon ($n_{\text{a-Si}} = 3.45$), comparable quality factors can be attained by increasing the nanoblock dimensions relative to the operation wavelength. These BTO resonators can be gated laterally using electrodes made from a variety of materials, including metals (Au, Ag, Cu, *etc.*), dielectrics (ITO, AZO, PEDOT, *etc.*), or doped BTO itself (*via* diffusion, implantation, thermal reduction, *etc.*). The lateral gating configuration ensures that the external electric field is parallel to the in-plane optical field, thereby leveraging the high r_{42} Pockels coefficient of BTO.

Active nanoantenna design using avoided crossing

Our transmissive metasurface design incorporates an array of BTO nanoblock resonators with lateral ITO electrodes, positioned on a SiO₂ dielectric spacer and a silicon nitride (Si₃N₄) membrane. The resonators are composed of a -axis BTO and oriented at the optimal angle of $\phi = 54^\circ$ from the in-plane optical axis to maximize the effective Pockels coefficient, as illustrated in Fig. 4.9c. The effective refractive indices of BTO in this configuration are given by

$$\begin{aligned}
n_x^T = n_{z'} &= \frac{n_o n_e}{\sqrt{n_e^2 \sin^2 \phi + n_o^2 \cos^2 \phi}} \\
n_y^T = n_{y'} &= \frac{n_o n_e}{\sqrt{n_e^2 \sin^2(\phi + \pi/2) + n_o^2 \cos^2(\phi + \pi/2)}} \\
n_z^T = n_{x'} &= n_o
\end{aligned} \tag{4.24}$$

where the notation x^T , y^T , and z^T is adopted for consistency with conventional coordinate systems. These axes correspond to the z' , y' , and x' axes, respectively (Fig. 4.9a).

Using a Si_3N_4 membrane as the underlying substrate reduces refractive index mismatch and minimizes optical mode perturbations in the BTO resonator. Furthermore, Si_3N_4 exhibits low optical losses at visible wavelengths [210], making it well-suited for operation at red, green, and blue wavelengths. We opt for a membrane thickness of 200 nm to balance optical compatibility with mechanical stability and robustness for future device fabrication. The reduced substrate thickness also facilitates the realization of ultra-thin functional optical elements that seamlessly integrate into advanced optical systems.

In transmissive metasurfaces, achieving a phase shift greater than π is often challenging due to shorter interaction lengths compared to reflective designs. One approach is to operate at points where two resonances merge, leveraging the combined phase shift at critical coupling. However, this often results in significant absorption, thus compromising absolute transmittance and efficiency. To overcome this limitation, we incorporate a thin SiO_2 spacer layer, which allows us to manipulate the coupling of modes. By optimizing the spacer thickness, we engineer an avoided crossing, which facilitates large and slowly varying phase shifts alongside high transmittance values [211], as detailed below.

Figure 4.11a shows the optimized layout of the metasurface unit cell for operation at red ($\lambda = 630 \pm 10$ nm). The nanoblock resonator has lateral dimensions of $w_x = 160$ nm, $w_y = 300$ nm, and a height of $h = 180$ nm. A larger width along the y^T axis was chosen due to a lower effective refractive index of BTO along that axis ($n_x^T = 2.69$, $n_y^T = 2.38$ at $\lambda = 630$ nm). The SiO_2 spacer thickness is $d = 40$ nm, and the membrane thickness is $t = 200$ nm. The BTO resonator is gated laterally in equipotential rows along the y^T axis for one-dimensional wavefront shaping. For the electrodes, we use ITO modeled as a Drude material with a carrier concentration

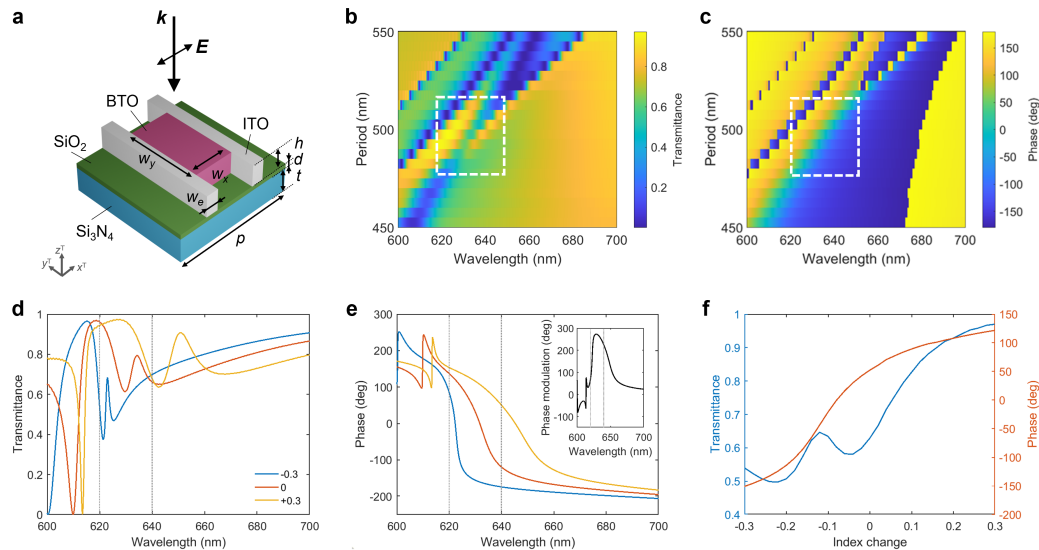


Figure 4.11: Unit cell design of active transmissive metasurface based on BTO.

(a) The unit cell consists of an a -axis oriented BTO nanoblock resonator with dimensions $w_x = 160$ nm, $w_y = 300$ nm, and height $h = 180$ nm. The resonator is placed on top of a SiO_2 spacer layer of thickness $d = 40$ nm, and a Si_3N_4 membrane with thickness $t = 200$ nm. Lateral gating of the resonator is achieved with ITO electrodes having a width $w_e = 50$ nm and height $h = 180$ nm. The unit cell period is $p = 490$ nm, which is equal in both x^T and y^T direction. The metasurface is illuminated with a normally incident plane wave that is linearly polarized along the x^T direction. (b) Transmittance and (c) phase response as functions of period and wavelength. The white dashed boxes highlight an avoided crossing with high transmittance and large associated phase shift. (d) Transmittance and (e) phase response for a unit cell period of $p = 490$ nm, shown for three different values of refractive index change (Δn) in the BTO resonator along the x^T direction: $\Delta n = -0.3$ (blue), $\Delta n = 0$ (orange), $\Delta n = +0.3$ (yellow). The gray dotted lines in both plots indicate the target operation regime of $\lambda = 630 \pm 10$ nm. The inset in (e) shows the phase modulation resulting from a change in Δn from $+0.3$ to -0.3 . (f) Transmittance (left, blue) and acquired phase (right, orange) as a function of refractive index change at a wavelength of $\lambda = 628.7$ nm, where the phase modulation is maximized.

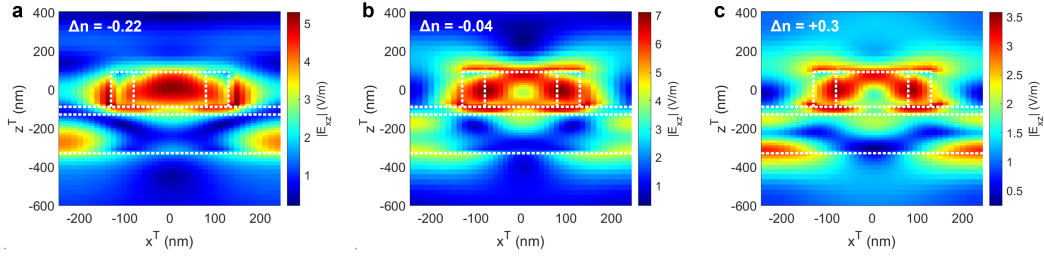


Figure 4.12: **Electric field distribution $|E_{xz}|$ in metasurface unit cell for varying index changes.** Magnitude of electric field in $x^T - z^T$ plane across the center of the BTO resonator for refractive index changes of (a) $\Delta n = -0.22$, (b) $\Delta n = -0.04$, and (c) $\Delta n = +0.3$ at $\lambda = 628.7$ nm.

of $N = 3 \cdot 10^{20} \text{ cm}^{-3}$ and a mobility of $\mu = 40 \text{ cm}^2/(\text{Vs})$. The ITO electrodes match the height of the BTO resonators to ensure a uniform field within the resonator.

All parameters, including the period p , were determined using a parameter sweep. As shown in Fig. 4.11b, an avoided crossing was identified at the target wavelength through a sweep of the period, as highlighted with the white dashed box. This region features high transmittance values that are simultaneously associated with a large, smoothly varying phase shift, as depicted in Fig. 4.11c. The maximal transmittance with large phase modulation is achieved for a period of $p = 490$ nm.

Based on a uniform index change in BTO along the x^T axis (applied field between the ITO electrodes), we simulated the transmittance and phase as functions of index change and wavelength. Figures 4.11d and e illustrate the transmittance and phase response for index changes of $\Delta n = -0.3$ (blue), 0 (orange), and $+0.3$ (yellow). The gray dashed lines denote the target operation window of $\lambda = 630 \pm 10$ nm. Our results show that transmittance above $\sim 37 - 68\%$ is maintained across these wavelengths, with higher minimum transmittance observed at redshifted wavelengths. The inset of Fig. 4.11e highlights the phase modulation attainable with an index change from $\Delta n = +0.3$ to -0.3 , achieving a maximum phase modulation of 272.7° at a wavelength of $\lambda = 628.7$ nm. The associated transmittance modulation as a function of index change is shown in Fig. 4.11f, with the transmittance varying between $50 - 97\%$ at this wavelength.

Figure 4.12 depicts the electric field distribution across the center of the metasurface unit cell in the $x^T - z^T$ plane. We show the field profiles for the two transmittance dips in Fig. 4.11e at $\Delta n = -0.22$ (a) and $\Delta n = -0.04$ (b), which correspond to

distinct resonant modes. For $\Delta n = -0.22$, the mode is strongly confined within the resonator, whereas for $\Delta n = -0.04$, the electric field redistributes and shifts toward the edges of the resonator and the ITO electrodes. This redistribution highlights the need to investigate the sensitivity of the metasurface response to variations in ITO properties in future work. By contrast, for an index change of $\Delta n = +0.3$ (Fig. 4.12c), where we obtain highest transmittance, the electric field coupling to the resonator is significantly weaker. The weak coupling is evident from the low field strength and broader field distribution extending beyond the resonator, resulting in high transmittance. We note that in all three cases, a considerable portion of the electric field resides in the Si_3N_4 membrane. This behavior has implications for the design and implementation of beam steering metasurfaces, and will be further explored in Section 4.6.

Electrostatic simulations

The electromagnetic simulations described above are complemented by electrostatic simulations (Fig. 4.13), confirming that the desired index changes can be achieved with modest applied voltages. Specifically, we find that a refractive index change of 0.2 at $\lambda = 632$ nm is attainable with an applied voltage of 6 V across a BTO resonator with a width of $w_x = 180$ nm. Scaling these results to the unit cell design shown in Fig. 4.11a, an applied voltage of 8 V between the ITO electrodes will be sufficient to induce an index change of 0.3.

We note that this index change can only be achieved by patterning of lateral ITO electrodes that are directly adjacent to the BTO resonator and fully cover its side-walls. Due to the high relative permittivity of BTO, there is a strong sensitivity of the refractive index change Δn to the presence of air gaps between the resonator and the ITO electrode. We characterize this air gap by the distance w_{air} between the resonator and the electrode. Our simulations indicate that an air gap as small as 5 nm will cause a nearly two-order-of-magnitude reduction in Δn (Fig. 4.13b).

These numerical findings are corroborated by analytical calculations, assuming a BTO relative permittivity of $\epsilon_{\text{BTO}} = \epsilon_x^T = 2400 \cdot \sin \phi + 60 \cdot \cos \phi$ with $\phi = 54^\circ$, reflecting values in the clamped case. The electric field, E_x , is calculated as

$$E_x = \frac{\epsilon_{\text{air}} \cdot w_{x,\text{BTO}}}{\epsilon_{\text{BTO}} \cdot w_{\text{air}} + \epsilon_{\text{air}} \cdot w_{x,\text{BTO}}} \cdot \frac{V_{\text{applied}}}{w_{x,\text{BTO}}} \quad (4.25)$$

where $\epsilon_{\text{air}} = 1$, $w_{x,\text{BTO}}$ is the lateral dimension of the BTO resonator along the x^T direction, and V_{applied} is the applied voltage. The refractive index change within the

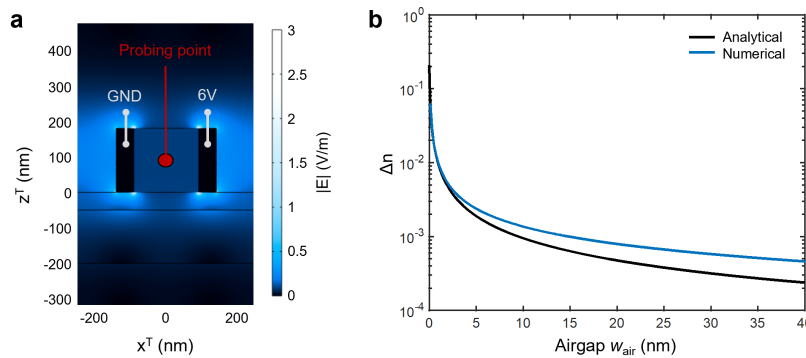


Figure 4.13: **Electrostatic simulations of BTO metasurface unit cell.** (a) Magnitude of electric field in $x^T - z^T$ plane across the center of the BTO resonator assuming an applied voltage of 6 V between the two ITO electrodes. The refractive index change Δn is probed at the center of the nanoblock, marked with the red spot. (b) Analytical (dark blue) and numerically obtained (light blue) refractive index change Δn as function of a distance, characterized by the width w_{air} introduced between the nanoblock and the ITO electrode on each side.

BTO resonator is then approximated using $\Delta n = 0.5 \cdot n_{\text{BTO}}^3 r_{\text{eff},54^\circ} E_x$ and is shown using the dark blue curve in Fig. 4.13b. Here, $r_{\text{eff},54^\circ} = 1025 \text{ pm/V}$ and $n_{\text{BTO}} = 2.45$ around $\lambda = 630 \text{ nm}$.

To fabricate a BTO resonator with fully covered sidewalls forming ITO electrodes, two approaches are viable: angled sputtering to coat the sidewalls, or uniform ITO deposition over the entire metasurface followed by selective etching between the electrodes. Future work will focus on realizing designs with simplified fabrication processes, such as using lateral ITO electrodes with a shorter height, partially etching the BTO layer to replace the spacer layer with unetched BTO, or integrating the electro-optic BTO layer with higher-order Huygens metasurface structures composed of other low-loss dielectrics (such as silicon, amorphous silicon, gallium arsenide). Such designs could simultaneously benefit from high quality factors and the electro-optic tunability of BTO.

Angular dispersion

In addition to discussing the sensitivity of the observed mode to fabrication errors, it is essential to evaluate the system-level sensitivity. Specifically, this pertains to the incident angle of the illuminating plane wave, which can introduce perturbations to the optical mode and thereby affect the reported transmittance and phase modulation. Here, we examine the case where the metasurface is illuminated by a plane incident at

an angle θ relative to the z^T -axis within the $x^T - z^T$ plane, as illustrated in Fig. 4.14a. Our simulations of the transmitted intensity and phase reveal that features similar to those observed at the avoided crossing under normal incidence – characterized by high transmittance and a large, smoothly varying phase shift – can be observed up to an incident angle of approximately 2° , as indicated by the black dashed boxes in Fig. 4.14b and c, respectively. While these results demonstrate some tolerance to the incident angle, the stronger angular selectivity of this design compared to alternative metasurface designs [209], suggests the presence of a degree of nonlocality in the optical mode which contributes to achieving this performance.

An analysis of the transmittance and phase curves as function of refractive index changes indicates that as the incident angle increases from $\theta = 0^\circ$ to 2° (Fig. 4.14d-f), additional higher-Q modes begin to emerge. At the wavelength corresponding to peak phase modulation at normal incidence ($\lambda = 628.7$ nm), a phase modulation of up to 251° is still maintained at $\theta = 2^\circ$ (Fig. 4.14f). However, this is accompanied by a significant increase in transmittance modulation, evident from the appearance of additional modes with refractive index variation (blue and yellow curves). The heightened transmittance modulation will likely reduce performance in applications such as beam steering at these larger incident angles, as previously discussed in Section 2.4. Nonetheless, such metasurface designs may find greater utility in alternative applications, such as optical filters or angularly selective sensors, where strong angular sensitivity is advantageous.

4.6 Beam steering at red wavelengths

To demonstrate a specific application of the proposed BTO-based metasurface design, we analyze its beam steering efficiency in transmission and compare it to previously reported values for the reflective field-effect tunable plasmonic metasurfaces discussed earlier in this thesis [42, 46]. For this analysis, we consider the case of a normally incident plane wave, as shown in Fig. 4.11.

Since the proposed design incorporates lateral ITO electrodes that fully cover the sidewalls of the BTO resonator, we can assume an array configuration with spatially varying, periodic refractive index changes, where the index change is uniform throughout the BTO resonator, as schematically depicted in Fig. 4.15a-c. To simplify the analysis, we adopt a forward design approach, assuming equidistant index variations between adjacent metasurface unit cells within a supercell period. This configuration could be further refined by selecting index variations based on

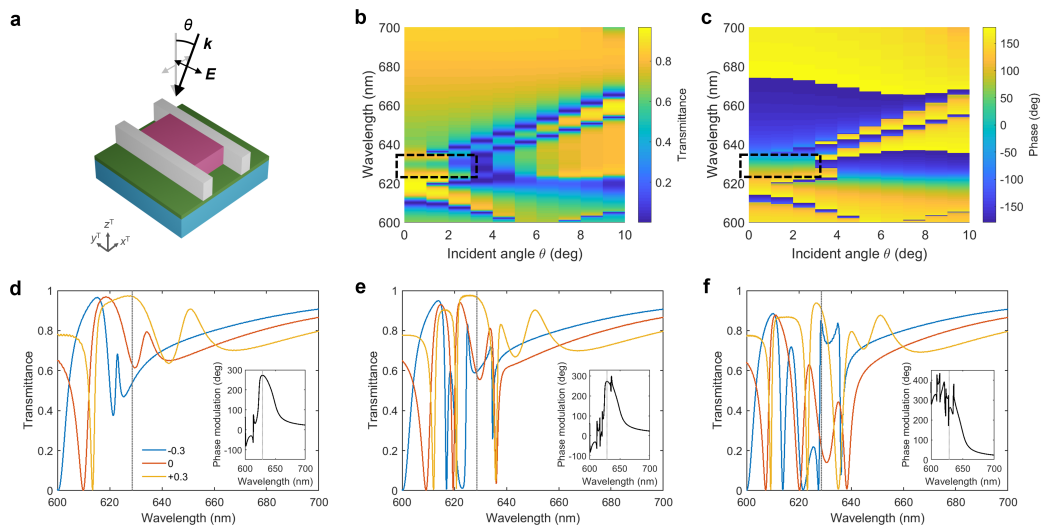


Figure 4.14: Angular dispersion of resonant mode. (a) Schematic illustration of metasurface unit cell illuminated by a plane wave incident at an angle θ relative to the surface normal (z^T -axis). The electric field E lies perpendicular to the incident wave vector k in the $x^T - z^T$ plane. (b) Transmittance and (c) phase as function of the incident angle θ and wavelength. The black dashed boxes mark regions displaying features similar to those observed at the avoided crossing under normal incidence (high transmittance and large, smoothly varying phase shift). (d)-(f) Transmittance as function of wavelength for refractive index changes of $\Delta n = -0.3$ (blue), $\Delta n = 0$ (orange), $\Delta n = +0.3$ (yellow) for incident angles of (d) $\theta = 0^\circ$, (e) $\theta = 1^\circ$, and (f) $\theta = 2^\circ$. Insets in each panel show the associated phase modulation as a function of wavelength for refractive index changes from $\Delta n = -0.3$ to $+0.3$. The gray dotted line indicates the wavelength of peak phase modulation at normal incidence, located at $\lambda = 628.7$ nm.

equidistant phase modulation or, more effectively, through an array-level inverse design strategy that optimizes the index value at each unit cell to account for both phase and transmittance modulation [46].

As demonstrated by the mode profiles of the metasurface unit cell (Fig. 4.12) and its angular dispersion characteristics (Fig. 4.14), the design exhibits a degree of nonlocality. Consequently, array-level optimization in this case requires a numerical optimization approach. This process needs to be performed using numerical solvers, such as Lumerical FDTD, to accurately account for interantenna coupling effects and evaluate the true performance of the metasurface. Despite employing a simplified forward design methodology in this study, tunable diffraction is achieved with effective suppression of the specularly transmitted beam.

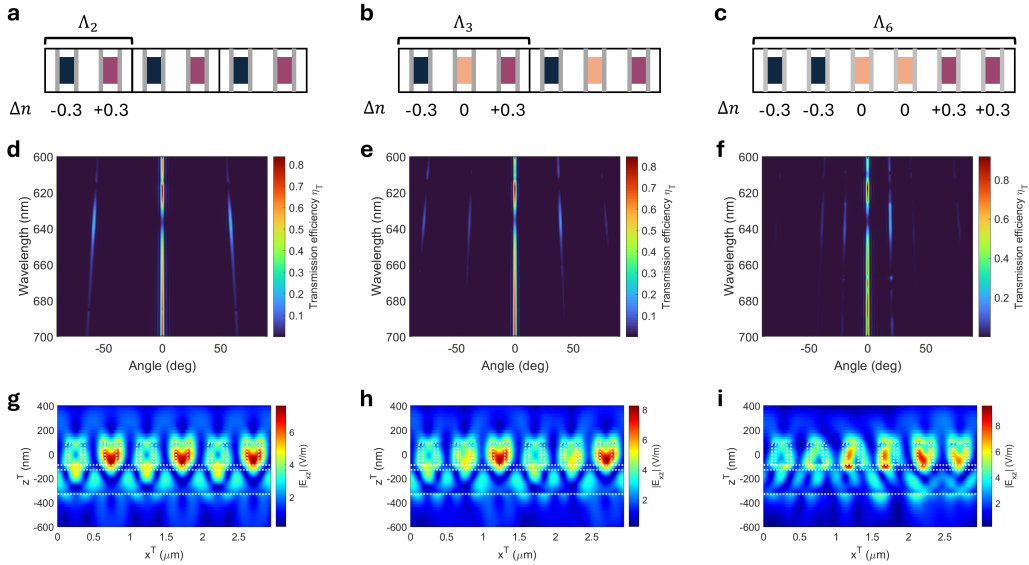


Figure 4.15: **Beam steering at red wavelengths in transmission.** (a-c) Top view schematic of metasurface array configuration for three different supercells consisting of (a) two unit cells (Λ_2), (b) three unit cells (Λ_3), and (c) six unit cells (Λ_6). The BTO resonators are modeled with uniform refractive index variations $\Delta n = -0.3$ (dark blue), $\Delta n = 0$ (light orange), and $\Delta n = +0.3$ (magenta). (d-f) Simulated transmission efficiency η_T as function of wavelength and angle for the corresponding configurations shown in (a-c). The total array sizes are (d) 50×50 , (e) 51×51 , and (f) 54×54 unit cells, respectively. (g-i) Magnitude of electric field $|E_{xz}|$ in $x^T - z^T$ plane across the center of the BTO resonator for the configurations in (a-c), shown at the wavelength corresponding to maximal suppression of the zeroth diffraction order, with (g) $\lambda_{\max} = 636.4$ nm, (h) $\lambda_{\max} = 635.3$ nm, and (i) $\lambda_{\max} = 635.8$ nm, respectively.

Figure 4.15 illustrates the transmission efficiency as function of wavelength and angle for three different metasurface array configurations. These configurations consist of supercells with period Λ containing two unit cells (Fig. 4.15a, Λ_2), three unit cells (Fig. 4.15b, Λ_3), and six unit cells (Fig. 4.15c, Λ_6). While the first two configurations assign a distinct index variation to each unit cell, the third configuration (Λ_6) utilizes three index variation values, each repeated twice. Figures 4.15d-f show beam steering as a function of angle for the three different cases, assuming square metasurface arrays with 50×50 , 51×51 , and 54×54 elements, respectively. The transmission efficiency, η_T , of the diffracted orders was evaluated by normalizing the transmitted intensity with the far-field intensity at 0° without a metasurface. The results are summarized in Table 4.4.

Supercell	λ_{\max} (nm)	θ_{+1} ($^{\circ}$)	$\eta_{T,+1}$	$\eta_{T,0}$
Λ_2	636.4	58.4 $^{\circ}$	24.2%	6.5%
Λ_3	635.3	38.9 $^{\circ}$	17.0%	10.8%
Λ_6	635.8	19.4 $^{\circ}$	22.7%	3.9%

Table 4.4: **Transmission efficiency and angle of diffracted orders.** For each supercell configuration shown in Fig. 4.15, we report the wavelength with maximal suppression of the zeroth diffraction order, λ_{\max} , the angle of the first diffracted order, θ_{+1} , the transmission efficiency of the first order, $\eta_{T,+1}$, and the transmission efficiency of the zeroth order $\eta_{T,0}$.

The metasurface is capable of steering light to a maximal diffraction angle of $\theta = \pm 58.4^{\circ}$ using a supercell period consisting of two unit cells (Λ_2). As summarized in Table 4.4, suppression of the zeroth-order specularly transmitted beam is achieved in all three cases, with the highest suppression ratio between the first and zeroth orders observed for Λ_6 . This increased suppression ratio for Λ_6 , particularly compared to Λ_3 , can be attributed to the repeated configuration of index variations, which limits the effect of crosstalk between adjacent unit cells caused by abrupt changes. We additionally note that the peak suppression ratio in all cases occurs at wavelengths that are slightly redshifted from the wavelength of peak phase modulation ($\lambda = 628.7$ nm). This redshift is linked to a reduced transmittance modulation at these wavelengths, with minimal transmittance modulation observed at $\lambda = 638.4$ nm (Fig. 4.11d).

Despite achieving a phase modulation greater than 250° , we cannot obtain complete suppression of the specularly transmitted light due to the nonlocality of the optical modes. This effect is most apparent when comparing the electric field distributions for Λ_3 and Λ_6 , shown in Figs. 4.15h and i, respectively. For Λ_3 , the optical mode is most evidently distorted within the BTO resonator for $\Delta n = 0$, whereas for Λ_6 , a distortion is observed within the Si_3N_4 membrane. Despite this crosstalk, we are able to successfully demonstrate tunable beam steering using conventional forward design methods. Notably, in comparison to previously realized plasmonic field-effect tunable metasurfaces [46], where the maximal efficiency of the diffracted order *after* an array-level inverse design approach was 2.7%, the current all-dielectric metasurface design achieves a nearly tenfold increase, with transmission efficiencies approaching 25% for Λ_2 . Future enhancements in the transmission efficiency of the diffracted order could be realized through an optimization of the unit cell design with the objective to minimize crosstalk between adjacent elements or to reduce

transmittance modulation while maximizing phase modulation, as well as through system-level improvements leveraging array-level inverse design strategies.

4.7 Extension to RGB wavelengths

Electro-optically tunable metasurfaces based on barium titanate offer the distinct advantage of a broad transmission window that spans from the visible to the mid-infrared spectrum. This characteristic makes BTO particularly attractive for the realization of metasurfaces that operate at multiple wavelengths, relying on similar optical modes with slightly modified designs. In this section, we demonstrate a proof of concept for metasurface designs capable of operating at red, green, and blue (RGB) wavelengths, specifically $\lambda = 630 \pm 10$ nm, 532 ± 10 nm, and 460 ± 10 nm, respectively. To model the refractive index values of BTO across the visible spectrum, we use the dispersion relations provided by Wemple *et al.* [208]:

$$\begin{aligned} n_o^2 - 1 &= \frac{4.064\lambda^2}{\lambda^2 - 0.211^2} \\ n_e^2 - 1 &= \frac{4.187\lambda^2}{\lambda^2 - 0.223^2}. \end{aligned} \quad (4.26)$$

To facilitate future integration of RGB resonators in a single metasurface array, we designed all structures with consistent layer thicknesses. For this purpose, we first blueshift the design shown in 4.11 to enable operation at $\lambda = 532$ nm, and find comparable performance with nanoblock dimensions of $w_x = 120$ nm, $w_y = 250$ nm, and $h = 150$ nm, and a period of $p = 380$ nm. Building on this, we then extended the design to $\lambda = 630$ nm and $\lambda = 460$ nm. The optimized dimensions for all three designs are summarized in Table 4.5.

$\lambda_{\max \text{ phase}}$ (nm)	w_x (nm)	w_y (nm)	p (nm)
632.7	220	280	490
531	120	250	380
459.4	100	200	400

Table 4.5: **Dimensions for metasurface unit cell at red, green, and blue wavelengths.** The wavelength yielding maximal phase modulation $\lambda_{\max \text{ phase}}$ is reported together with the lateral resonator dimensions w_x and w_y , respectively, and the unit cell period p . All resonators are designed with a uniform height of $h = 150$ nm, a dielectric spacer thickness $d = 40$ nm, and a membrane thickness $t = 200$ nm.

Figures 4.16a-c illustrate the transmittance and phase modulation as function of index change for each resonator at the wavelength of maximal phase modulation,

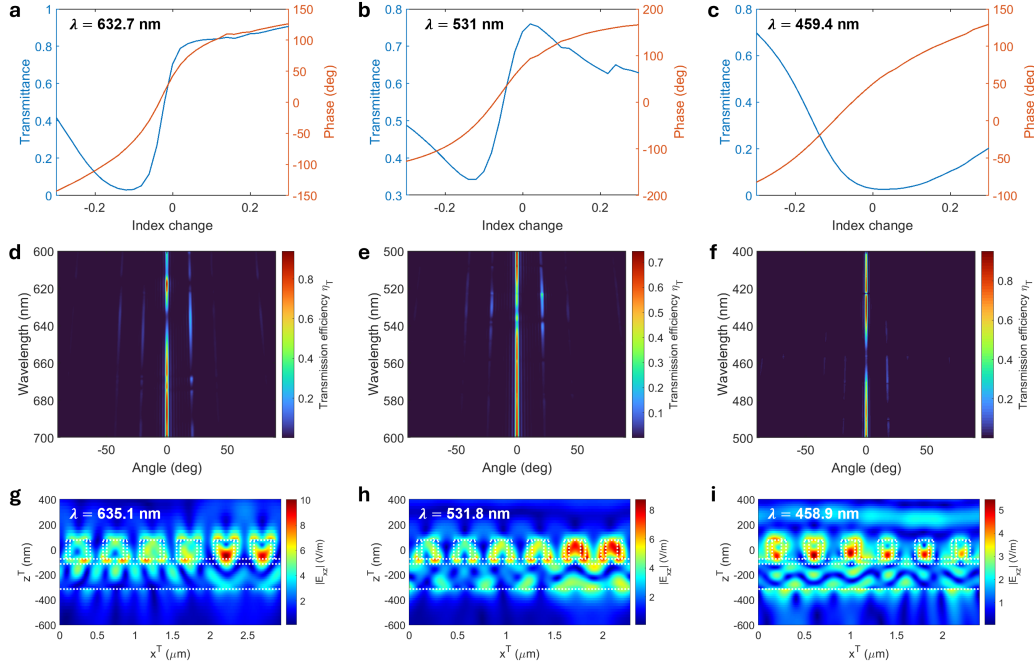


Figure 4.16: Unit cell performance and beam steering at red, green, and blue wavelengths. (a-c) Transmittance and phase modulation as function of a refractive index change from -0.3 to $+0.3$ shown at the wavelength of peak phase modulation (a) $\lambda_{\text{max phase}} = 632.7$ nm, (b) $\lambda_{\text{max phase}} = 531$ nm, and (c) $\lambda_{\text{max phase}} = 459.4$ nm. (d-f) Transmission efficiency η_T as function of wavelength and angle for the three resonator designs specified in Table 4.5. (g-i) Electric field distribution E_{xz} across the center of the BTO resonator in the $x^T - z^T$ plane at the wavelength of maximal suppression of the zeroth transmitted order.

$\lambda_{\text{max phase}}$. The average transmittance is highest for the green-wavelength resonator, as this design was specifically optimized for its performance, whereas the red and blue designs were subject to additional constraints to maintain a consistent resonator height. For the red wavelength (Fig. 4.16a), the average transmittance is 54%, accompanied by a phase modulation of 269° at $\lambda = 632.7$ nm. At the green wavelength (Fig. 4.16b), we achieve an average transmittance of 56% with a phase modulation of 293° at $\lambda = 531$ nm. Finally, for operation at the blue wavelength (Fig. 4.16c), an average transmittance of 21% is achieved together with a phase modulation of 212° . These variations in transmittance and phase modulation can be attributed to different optical modes given a fixed height across all three designs, as well as differences in the refractive index at the respective wavelengths. We note that all three resonators were analyzed under an index modulation of $\Delta n = \pm 0.3$ which

corresponds to different applied voltages for each case. Based on the resonator width w_x specified in Table 4.5, the required applied voltages are 11 V, 6 V, and 5 V for red, green, and blue, respectively.

Next, we analyzed the beam steering performance by evaluating the transmission efficiency η_T as function of wavelength and angle for each design. For all three designs, we consider the configuration schematically depicted in Fig. 4.15c with the supercell Λ_6 , consisting of two repetitions of three equidistant refractive index variations. The transmission efficiency results for the diffracted order and zeroth order are summarized in Table 4.6.

λ_{\max} (nm)	θ_{+1} ($^\circ$)	$\eta_{T,+1}$	$\eta_{T,0}$
635.3	19.4 $^\circ$	24.0%	5.1%
531.8	21.0 $^\circ$	12.4%	18.9%
458.9	17.2 $^\circ$	7.2%	5.3%

Table 4.6: **Transmission efficiency and angle of diffracted orders for red, green, and blue wavelengths.** Reported are the wavelength of maximal suppression of the zeroth diffraction order, λ_{\max} , the angle of the first diffracted order, θ_{+1} , the transmission efficiency of the first order, $\eta_{T,+1}$, and the transmission efficiency of the zeroth order $\eta_{T,0}$.

Interestingly, the green-wavelength design achieves maximal phase modulation with minimal transmittance modulation across these designs, however, it exhibits limited suppression of the zeroth order in the analyzed beam steering configuration. This limitation likely arises from its small unit cell period ($p = 380$ nm), resulting in increased coupling between adjacent resonators, as shown by the electric field distributions in Fig. 4.16h. Similarly, the blue-wavelength design shows hybridization of modes (Fig. 4.6i), however, a stronger zeroth-order suppression can be achieved in this case. In contrast, the red-wavelength design shows the least mode coupling (Fig. 4.6i), resulting in improved diffraction efficiency.

Further studies of the optical modes are required to fully understand these differences and optimize designs for higher suppression ratios between the first diffracted and zeroth orders. Despite these challenges, this study successfully demonstrates the feasibility of developing metasurfaces capable of operating at RGB wavelengths. Our findings provide a strong foundation for future optimization efforts aimed at integrating of these resonators into an RGB modulator array.

4.8 Outlook

In this chapter, we introduced a new synthesis method alongside designs for achieving high-efficiency transmissive metasurfaces for beam steering at visible wavelengths. While significant progress was made, several challenges remain for the experimental realization of these metasurfaces and their integration into practical applications. In the following, we outline key tasks that can build upon the insights gained in this work.

Spalling large-area single-domain BTO films

A critical requirement for integrating spalled BTO films in active metasurfaces is the production of large-area films that are both single-crystal and single-domain. Such films maximize the electro-optic response, enabling their use in diverse photonic applications. Our earlier studies demonstrated that the thickness of spalled films can be controlled through the thickness of electroplated Ni, which also influences the RMS roughness of the films. Specifically, we noted that thinner films exhibited smoother surfaces and likely experienced reduced domain switching caused by mechanical forces.

Extending this process to larger areas requires a deeper understanding of how mechanical stresses affect both roughness and thickness. Key questions include whether domain switching occurs as a static effect during electroplating or a dynamic process during spalling. Automating the spalling process rather than relying on manual exfoliation could ensure greater consistency and control, facilitating the fabrication of large spalled areas suitable for device integration.

Integration into RGB array

Optimizing individual metasurface resonators for distinct wavelengths (red, green, and blue) is the first step toward integrating them into a modulating element capable of multi-wavelength operation. Achieving this goal requires careful consideration of the resonator arrangement to maximize color accuracy and contrast while minimizing interelement crosstalk.

Configurations such as fully interdigitated arrays, such as the one shown in Fig. 4.17, may provide a solution for large fields of view. However, segmenting the array into subarrays of RGB pixels could reduce crosstalk and improve the color contrast [212]. Alternatively, stacking transmissive metasurfaces for each wavelength could facilitate multi-wavelength control. This approach, though promising, requires detailed analysis of losses introduced by non-resonant layers. Interestingly, stacked

configurations could also enable two-dimensional wavefront shaping by rotating each layer in-plane by 90° .

For arbitrary wavefront shaping, a two-dimensional interconnect scheme may be necessary. This would likely involve redesigning resonators, possibly with different crystal orientations, to allow for electric gating along both dimensions. While this approach could simplify wavefront shaping, it introduces additional design and fabrication complexities

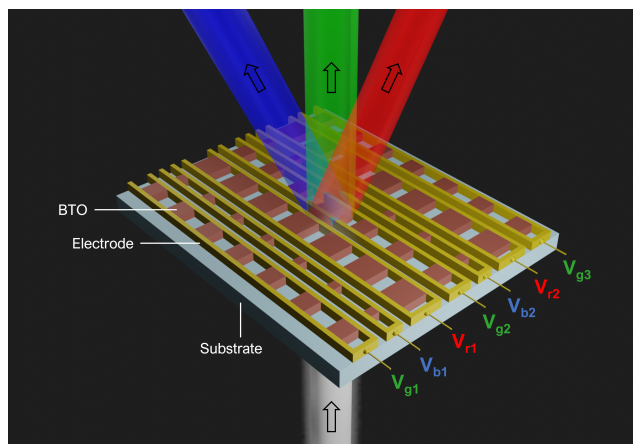


Figure 4.17: **BTO-based RGB modulator array.** Broadband (white) light is incident on an active transmissive metasurface consisting of resonators designed for RGB control. By applying individual gate voltages to each resonator n , $V_{\{r,g,b\},n}$, the transmitted beams can be split in distinct wavelengths and perform different operations at distinct wavelengths.

Fabrication and alternative design strategies

The experimental realization of transmissive metasurfaces based on the proposed designs requires precise fabrication of BTO nanoblock resonators with vertical sidewalls. If BTO exhibits etching behavior similar to titanium dioxide (TiO_2), such precision may be feasible [213]. However, if its etch characteristics align more closely with other electro-optic materials such as lithium niobate, which typically etches with a sidewall angle [214], further studies will be needed to evaluate the impact of sidewall angles on optical performance.

An alternative approach for resonator design could involve relaxing etching requirements by including an underetched BTO layer to partially or fully replace the dielectric spacer. Alternatively, etching could be avoided entirely by using high-index materials such as Si or gallium arsenide (GaAs) for the resonators, while leveraging the electro-optic tunability of an underlying unetched BTO layer.

Additionally, adopting an out-of-plane electrode configuration instead of lateral gating may help mitigate crosstalk between metasurface elements by increasing the spacing between resonators. Such designs would likely benefit from c -axis BTO thin films, leveraging the r_{33} electro-optic coefficient. Although r_{33} is ten times smaller than r_{42} in BTO, it is three times higher than r_{33} in LN and may therefore relax the requirements for the resonator quality factor in comparison to LN.

Polarization tunability

In Section 4.4, we discussed the contributions from the electro-optic coefficients for various electrode configurations in a - and c -axis thin films. In c -axis BTO, applying an in-plane electric field rotates the index ellipsoid. In this case, when the incident wave vector is misaligned with the principal axes, the polarization state becomes a linear combination of normal modes dictated by the transformed index ellipsoid.

This electrically controllable rotation of the index ellipsoid, as defined in equation (4.23), could be exploited for realizing polarization-tunable elements. However, achieving this requires a comprehensive understanding of the BTO anisotropy, resonator optical modes, and the interplay between the electro-optic effect, crystal orientation, and applied electric field. Advanced numerical modeling and experimental validation will be crucial for realizing these devices.

Realization of high-frequency modulators

The instantaneous electro-optic response of BTO makes it an ideal candidate for high-frequency modulators capable of spatiotemporal light manipulation. Previous studies have demonstrated modulation frequencies in the GHz range for BTO-based devices [193]. Developing such active metasurfaces will require optimizing resonator geometry, electrical addressing schemes, and overall interconnect layouts to minimize RC time constants. By incorporating these capabilities, metasurfaces could achieve precise control not only over amplitude, phase, polarization, and wavevector, but also frequency of light.

4.9 Conclusions

In summary, we have developed a scalable and cost-effective method for fabricating high-quality single-crystal BTO thin films suitable for integration in advanced functional devices. Spalled films can be obtained with desired crystal orientations, as demonstrated for (100) and (001) bulk crystals, with film thicknesses ranging from 100 nm to 15 μm and lateral dimensions spanning several hundred micrometers to

millimeters. The film thickness is controlled by the electroplated Ni layer, which dictates the stress state of the underlying BTO substrate. While stress-induced domain switching during spalling introduces surface roughness, the intrinsic properties of bulk BTO are preserved. We characterized the electro-optic Pockels coefficient of spalled BTO films after transfer to a rigid substrate and measured an electro-optic coefficient of $r_{33} = 55 \pm 5$ pm/V in multi-domain regions and $r_{33} = 160 \pm 40$ pm/V in smaller, likely single-domain regions. Our results indicate that spalled BTO films can exceed the performance of commercially available thin-film lithium niobate. Future work should focus on improving surface quality, controlling domain structures, and developing techniques for transferring isolated BTO thin membranes, broadening their applicability in scalable photonic device integration.

From a design perspective, we explored how BTO thin films that retain bulk electro-optic properties can be integrated into transmissive active metasurfaces. Using a -axis oriented films allows for a maximization of the effective electro-optic coefficient, which can be harnessed in resonant active metasurfaces. By applying an in-plane electric field at 54° to the optical axis, and using an incident plane wave polarized parallel to this field, an effective electro-optic coefficient of $r_{\text{eff}} = 1025$ pm/V can be achieved. This enables index changes of up to 0.3 at visible wavelengths with applied fields around 0.3 MV/cm. Such fields can be induced in BTO nanoblock resonators through lateral gating along the resonator sidewalls. Through careful engineering of the resonator geometry and underlying layers, we demonstrated an avoided crossing of optical modes, enabling high transmittance alongside a large, smoothly varying phase shift. Specifically, our transmissive metasurface design achieved a phase modulation of 272.7° with transmittance varying from 50-97% at $\lambda = 628.7$ nm assuming an index change of ± 0.3 . This design was also shown to enable active beam steering up to $\pm 58^\circ$, with partial suppression of the zeroth-order transmitted beam due to resonator crosstalk. Using conventional forward design methods, we obtained a transmission efficiency of the diffracted beam ranges of around 17 – 24%, with further improvements anticipated through array-level inverse design approaches. Additionally, leveraging the broad transparency window of BTO, we showed that similar designs can be adapted for active beam steering at RGB wavelengths.

While significant efforts remain for the experimental realization of BTO-based transmissive metasurfaces, the advances outlined here establish a strong foundation for next-generation metasurfaces capable of comprehensive light control across multi-

ple dimensions. These developments mark a critical step toward active metasurfaces for universal light manipulation, paving the way for transformative applications in optical communication, computation, and imaging.

*Chapter 5***TOWARD UNIVERSAL ACTIVE METASURFACES FOR
OPTICAL IMAGING, COMMUNICATION AND
COMPUTATION**

The material in this chapter was in part presented in [21, 96].

5.1 Universal active metasurfaces

The ability to dynamically control the optical response in the quasi-static and time-modulated regimes opens a multidimensional design space that can be fully harnessed by developing appropriate nanophotonic structures for arbitrary manipulation of light. In the previous chapters, we explored how these capabilities can enhance the information density of metasurfaces while utilizing high-performance materials that can be seamlessly integrated into designs for both reflection and transmission. Building on this foundation, we now address the fundamental question: What does it take to realize a universal optical element (Fig. 5.1) which enables dynamic, independent, and comprehensive control over all constitutive properties of light in both reflection and transmission? State-of-the-art wavefront shaping metasurfaces generally encompass active and continuous control over the amplitude and phase of light scattered from each nanostructured element. A universal active metasurface, in comparison, should additionally provide complete control over the polarization, spectrum and momentum, the orbital angular momentum as well as the shape of optical pulses. Such a universal active metasurface would have the potential to serve as a programmable transfer element that can encode arbitrary functions and perform a variety of complex tasks using a single dynamically tunable component. As such, it could be integrated into a wide range of applications, including free-space communications, analog computing, and holographic displays to name a few.

In this chapter, we focus on the pathways toward achieving a universal active metasurface for independent and comprehensive, real-time control over all properties of light, including its amplitude, phase, polarization, momentum, spectrum, orbital angular momentum, and pulse shape. We identify key challenges and highlight the respective recent developments in three areas that will drive the realization and unlock the potential of a universal active metasurface: metasurface design, control architecture, and advanced operation modes. We outline the target performance

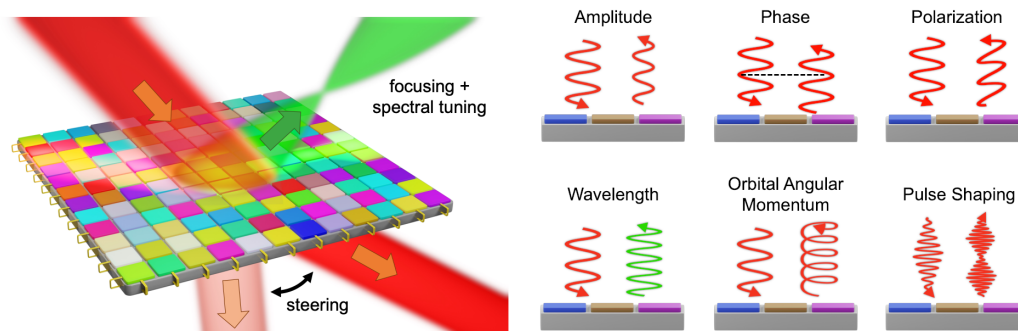


Figure 5.1: **Universal active metasurface.** Schematic of a universal active metasurface enabling dynamic wavefront shaping in reflection and transmission. This metasurface should allow for dynamic and independent control of the amplitude, phase, polarization, wavelength, the orbital angular momentum, and pulse shape of an electromagnetic wave.

characteristics with regards to a high-performance active metasurface design and discuss potential pathways for their realization. We further examine challenges toward realizing a two-dimensional control architecture and discuss strategies to overcome currently existing limitations. We then explore uncharted operation modes that could be attained with a universal metasurface, providing inspiration for future applications in the realms of optical imaging, communication, and computation. Finally, we give a perspective and point toward key technological problems that will require further research from the nanophotonics community to bring us closer to the realization of a truly universal active metasurface.

5.2 Metasurface design and promising material platforms

The design of a universal active metasurface forms a convoluted problem involving several parameters. Passive metasurfaces generally rely on shape- and orientation-dependent phase retardation introduced by resonant scatterers to create desired changes in the scattered electric field. In comparison, the performance of an active structure is determined by its geometrical parameters as well as the choice of the active material and/or the corresponding modulation scheme. In the following, we review active metasurface design strategies that hold the potential to realize a universal active metasurface. The desired objectives can be summarized as follows: First, a large dynamic range of tuning is desired for deterministic wavefront shaping. Here, the objective is to obtain complete and independent control over the characteristic properties of light. This includes a 0-to- 2π phase shift upon actuation

(while maintaining constant amplitude) and 100% intensity modulation efficiency (with constant phase). We define the latter as $\eta = 1 - I_{\min}/I_{\max}$, where I_{\min} and I_{\max} are the minimal and maximal electric field intensity at a given wavelength, respectively. In addition, low loss structures are required to ensure high output efficiencies. To access the time-modulated operation regime, active metasurfaces further need to support large modulation frequencies. Additional performance metrics include broadband operation, allowing for a tunable excitation wavelength and achromaticity. While these criteria do not form an exhaustive list of requirements for a high-performance universal metasurface, they determine critical design choices for the architecture and materials employed in a metasurface unit cell as well as its modulation mechanism.

Field-effect tuning based on carrier index modulation (discussed in detail in Chapters 2 and 3) has attracted significant attention over the past decade, as it has been used to experimentally demonstrate a large dynamic range of tuning of amplitude, phase, and polarization. Individual studies have reported up to 96% reflectance modulation efficiency [215], greater than 1.5π phase modulation [42, 53, 54, 216], as well as a linear to circular and cross-polarization conversion [217]. Field effect tuning relies on the charge carrier dependent optical properties in semiconductors, often transparent conductive oxides (TCOs), or in graphene. In semiconductor-based tuning, a metal (or semiconductor)-insulator-semiconductor heterostructure [30, 69] is integrated into a resonant unit cell. Upon gating, a local charge carrier accumulation or depletion zone is created at the insulator-semiconductor interface (Fig. 5.2a), causing a change in the complex dielectric permittivity, ε [218, 219]. Additionally tuning the dielectric permittivity into the epsilon-near-zero (ENZ) regime leads to an extreme localization of the electric field in this zone, which perturbs the optical resonant mode of the unit cell [220]. This ability to transition the active material through the ENZ region, and hence dynamically modify the scattering of a resonant unit cell has led to the development of electronically programmable active metasurfaces with independently addressable metasurface elements [42, 221]. Moreover, modulation frequencies of up to 10 MHz have been demonstrated using TCO-based metasurfaces [30, 95], with the potential of accessing GHz frequencies with optimized design of device electrical interconnects and driver circuits.

The operating wavelength of TCO metasurfaces is chosen based on the bulk carrier density of the active semiconductor during fabrication. Indium tin oxide (ITO) is a commonly used active material for operation in the near-infrared. A recent study,

however, showed that over 70% of the incident light is absorbed in the ITO layer at its ENZ transition and only 2.7% of the light is reflected [74]. Cadmium oxide (CdO) was proposed as an alternative transparent conducting oxide with enhanced optical properties, leading to reflectance values above 22% [74]. For operation in the mid-infrared (3 – 10 μm), several materials including graphene, and doped semiconductors such as indium arsenide (InAs) [222] have been proposed. Phononic materials, such as silicon carbide (SiC) [223], indium phosphide (InP) [224] and gallium arsenide (GaAs) [225], may provide a promising pathway to realize field-effect tunable metasurfaces operating beyond 10 μm [226]. This class of materials supports a phonon-polariton mode that undergoes an ENZ transition in the far-infrared while maintaining a low extinction coefficient. For operation in the visible, transition metal nitrides stand out as an emerging class of materials that undergo an ENZ transition between 400 nm – 800 nm [226, 227].

Atomically thin polar van der Waals (vdW) materials and transition metal dichalcogenides (TMDCs) offer an alternative pathway to extend the operation wavelength of active metasurfaces to the visible spectrum. These materials support strong excitonic resonances at wavelengths determined by the dielectric properties of the TMDC material. By integrating the 2D semiconductor material into a capacitive structure and biasing the gate electrode, charges can be injected into the active layer. Due to the exciton-charge interaction, a modification of the excitonic resonance is observed [228–230]. As a result, a large change in refractive index can be achieved [231, 232]. The index changes at excitonic resonances manifest themselves in phase and amplitude modulation even without explicit optical resonators. An integration into planar heterostructures forming resonant cavities further enhances the observed dynamic range of tuning [233–235]. Recently, black phosphorus (BP) was proposed as an excitonic material suitable for active metasurfaces. The intrinsic anisotropy along the crystal axes [236] of BP allows for dynamic polarization control [237]. Currently, patterning of 2D materials and integration into metasurface building blocks is being pursued to further enhance light-matter interactions and enable advanced optical functions [83]. Recent experimental demonstrations of this include a tunable zone plate lens allowing for a modulation of the focal intensity [238] as well as a nanostructured array for dynamic control of the scattering pattern, supporting modulation frequencies of up to 625 MHz [132].

Despite the progress on the dynamic modulation achieved using field-effect tunable metasurfaces, there are several limitations that need to be overcome for use in ap-

plications. One of the challenges with metasurfaces based on thin films of excitonic materials is the scalability of devices to large areas (greater than $500 \mu\text{m}^2$). The highest quality 2D semiconductor films are obtained through mechanical exfoliation. This approach becomes especially challenging when multiple layers need to be stacked on top of each other. Recent advances with robotically assisted thin film transfer [239, 240] may provide a potential pathway toward realizing scalable active heterostructures. Nevertheless, current TMDC-based active structures require cryogenic temperatures to realize their full dynamic range of tuning [132]. Additionally, while the operating wavelength of TCO-based metasurfaces can be changed to some degree *via* an appropriate choice of material doping, the operating wavelength range for TMDC-based structures is intrinsically fixed by the excitonic transition of the material. Field-effect tunable metasurfaces further require a high electric field confinement and mode overlap of their active media with resonant nanocavity structures to obtain strong light-matter interactions. This can be achieved *via* plasmonic resonators and cavities, which, however, contribute to high absorption and thus lower device efficiencies. Alternatively, a double distributed Bragg reflector cavity was proposed to enhance light-matter interactions in a BP-based planar heterostructure [241]. Using this design, a phase modulation of 300° was predicted along with a minimum reflectance above 50% at an operating wavelength of $2.9 \mu\text{m}$, where BP exhibits lower losses. Further research is required to explore a potential extension of this platform to an active metasurface with independently addressable unit cells.

Electro-optic tuning of metasurfaces offers a promising approach to low-loss metasurfaces. As discussed in Chapter 4, the Pockels effect relies on a linear variation of refractive index in response to an applied electric field (Fig. 5.2b) [242]. This is a broadband phenomenon which appears in non-centrosymmetric crystals, such as lithium niobate (LN) [243], barium titanate (BTO) [173], and aluminum nitride (AlN) [157] amongst others. Electro-optically tunable materials further support ultrafast modulation frequencies (>100 GHz in electro-optic modulators [244]). While polycrystalline or amorphous thin film materials typically exhibit smaller electro-optic coefficients compared to single crystal materials (see Table 4.2), commercially available high-quality LN thin films have recently propelled the integration of electro-optic materials into active metasurfaces [105, 245]. Another significant advance entailed a recent demonstration of epitaxially grown thin-film BTO with an approximately $30\times$ larger electro-optic coefficient compared to LN [165]. Reports of active metasurfaces integrating BTO as a tunable layer, however, have thus far been limited to lower electro-optic coefficients [139]. In Chapter 4, we propose spalling

BTO thin films from bulk single crystals to overcome this challenge. While our measurements indicate that spalled thin films retain bulk electro-optic properties, further research is needed to realize seamless integration of spalled films into active structures. Organic electro-optic (OEO) chromophores, in comparison, provide a promising pathway for low-cost, high-throughput integration using methods such as spin-coating, micro-dispensing or ink-jet printing [161, 246, 247]. They have additionally enabled a strong modulation of the transmitted intensity at frequencies up to 5 GHz [31]. However, we note that high electric field intensities may cause photo degradation of the chromophores due to the presence of oxygen in the active material [248]. Besides the Pockels effect, the quantum confined Stark effect offers an alternative route to obtain a fast, electro-optically tunable response. In this case, a change in refractive index is induced upon an applied electric field, which causes a shift in the interband transition energy [153–155]. Based on this principle, Wu *et al.* [75] recently proposed an all-dielectric active metasurface based on multiple quantum wells (MQWs). In this work, active beam switching was realized with a phase shift of 70° and a simultaneous reflectance modulation efficiency of $\eta \sim 73\%$.

We refer the reader to Table 4.1 for a summary of the electro-optic refractive index change obtained in various nanophotonic devices using the active dielectric materials highlighted here. Due to a modest index change, the active electro-optic layer generally needs to be coupled to a high-quality (Q) resonant mode to obtain a strong modulation of the scattered wavefront using active metasurfaces. To this end, several metasurface designs relying on guided mode resonances have been realized [75, 152]. However, in this case, the extended mode along one dimension complicates the design of compact resonant elements for two-dimensional metasurface arrays with independently addressable unit cells. Active metasurfaces governed by optical bound states in the continuum (BICs) or quasi-BICs [249–251] may offer another promising pathway to incorporate electro-optic materials into high-Q resonant structures [252] and thus represent one approach to the design of non-local active metasurfaces [77]. Non-local metasurfaces rely on a collective mode generated by an array or subset of metasurface elements. Similarly, Weiss *et al.* [245] proposed a design strategy relying on the mode overlap of a Fabry-Pérot resonance, a localized surface plasmon resonance, and a surface lattice resonance. Notably, the surface lattice resonance only appears when the array periodicity coincides with the localized surface plasmon resonance of the metasurface elements. Therefore, further investigations are required to analyze whether this modulation scheme can be extended to gain active control on an individual unit cell level.

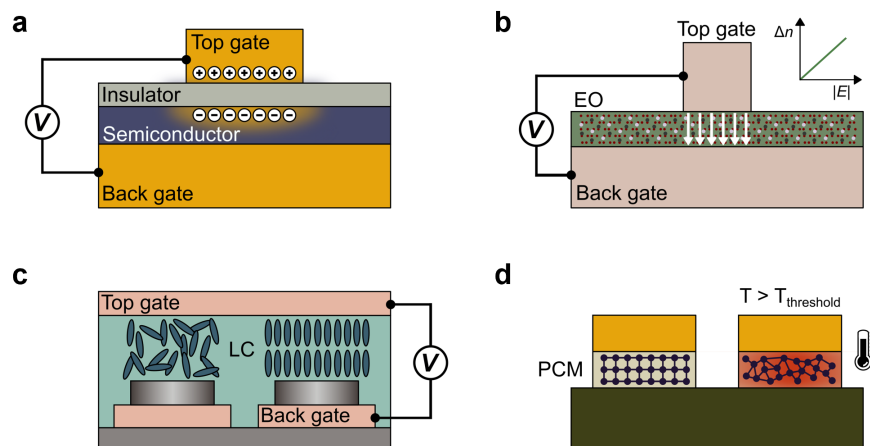


Figure 5.2: **Promising material platforms for universal active metasurface.** (a) Field-effect tunable metasurface. When the active semiconductor is integrated into a metal (or semiconductor)-oxide-semiconductor layer, a charge accumulation layer is formed upon application of a gate voltage. (b) Electro-optically tunable metasurface relying on Pockels effect. An electric field E (white arrows) applied across an electro-optic (EO) thin film of a non-centrosymmetric crystal leads to a linear change in refractive index Δn . (c) Liquid crystal-based metasurface. The liquid crystal molecules (LC) reorient in an external electric field. (d) Active metasurface based on phase change materials (PCM). The active material undergoes a phase transition from crystalline to amorphous when heated above a threshold temperature $T_{\text{threshold}}$.

Liquid crystals are well understood materials that have been widely deployed in display applications, and thus offer another active medium for realizing active metasurfaces with individually addressable unit cells. Here, a tunable optical response is obtained due to the optical birefringence of the liquid crystal molecules, which reorient upon application of a thermal [35, 253] or electrical stimulus (Fig. 5.2c) [20, 254]. The corresponding large refractive index change ranges from $\Delta n = 0.15 - 0.4$ across the visible and infrared spectrum ($\sim 460 \text{ nm} - 80 \mu\text{m}$) [20, 255]. A commonly used active metasurface design approach relies on Huygens' scatterers which are based on the spectral overlap of electric and magnetic dipoles. By actuating individual unit cells using an electrical bias, the liquid crystal orientation can be locally modified, as shown by Li *et al.* [108] in a transmissive liquid crystal-based metasurface. Alternatively, an active reflective liquid-crystal structure was recently realized based on Fabry-Pérot nanocavities that support multiple resonances across the visible spectrum [19]. Here, a continuously tunable phase shift across 2π is obtained while maintaining a high reflectance above 40%. It is worth noting that as

the metasurface pitch is reduced to values below $1\ \mu\text{m}$, crosstalk between unit cells arises due to the elastic motion of liquid crystals [20, 256]. Furthermore, due to the response time of the molecules, the modulation frequencies are limited to several kHz, with currently fastest rates of 40 kHz reported in commercial light detection and ranging (LiDAR) devices [131].

Phase change or phase transition materials, by contrast, produce structural changes in the active layer upon Joule heating (Fig. 5.2d), and take advantage of the large difference in complex refractive index achievable in different phases of the same material. Phase change materials, such as germanium-antimony-telluride (GST) and its derivatives [41, 257], undergo a non-volatile transition from an amorphous state to a crystalline state. Phase transition materials, on the other hand, rely on a volatile insulator-to-metal transition in materials such as vanadium dioxide (VO_2) [34, 258]. Both material categories have been integrated into active structures exhibiting multi-level phase tuning. Experimental realizations of active metasurfaces using an electrical stimulus, however, have thus far been limited to modulation frequencies of 3 kHz [258]. Optical control has enabled significantly faster modulation rates, with amorphization in GST induced upon 50 fs long laser pulses [259]. (Notably, the recrystallization required repetitive pulsing of the fs laser for 1 s at 960 Hz.) Furthermore, several metasurface designs realizing tunable functions, such as active beam switching [258, 260] and bifocal lensing [260], have been demonstrated using phase change and phase transition materials. Nevertheless, the implementation of a metasurface with independently addressable elements requires further investigations on thermal heat management. In a preliminary study, Kim *et al.* [261] theoretically showed that thermal crosstalk between adjacent elements in a VO_2 -based metasurface could potentially be mitigated by incorporating heat conduction layers into the design.

High-performance active metasurfaces comprise structures that allow independent and comprehensive control over all properties of light. A full 2π phase coverage with close to unity amplitude has previously been obtained through strategies such as coupling of a resonator to a back reflector [152]. Additional independent control over the amplitude was attained using dual-gated structures [53], which can cover the entire complex amplitude space based on distinct voltage configurations [54, 216]. Notably, however, the design of compact and efficient active metasurfaces becomes increasingly challenging with the addition of each degree of freedom. At each step, the design problem constitutes of a thorough co-optimization of the

active material, the geometrical parameters of the metasurface element, as well as the external control variable. Furthermore, it becomes crucial to weigh trade-offs between different objectives for a desired application. As such, the task of finding an optimally functioning universal active metasurface is ideally formulated as an inverse design problem.

While inverse design has been widely explored for the geometrical optimization of unit cells in passive metasurfaces [57, 60, 62], active metasurfaces present a unique challenge in which the performance of a device must be optimized at multiple states simultaneously [262]. This concept of multi-state optimization has been theoretically demonstrated to optimize the function of active metasurfaces based on phase change materials [262, 263] or liquid crystals [64], which can switch between two states. In these studies, a shape or topology optimization was conducted on a single unit cell level using multi-objective optimization algorithms. For the design of a continuously tunable metasurface, however, the number of operation states of a metasurface dramatically increases. This challenge is further amplified with the independent addressability of metasurface elements. Several groups have thus employed a so-called array-level inverse design (see Chapter 2) [46, 264]. Here, the value of the external bias is optimized at each element to overcome the limitations posed by a forward-designed active unit cell, which exhibits co-varying phase and amplitude and smaller than 2π phase shift upon actuation. We would like to note here that a common challenge in obtaining high-performance active metasurfaces is the degraded array performance despite working with structures that exhibit a large phase modulation and high reflectance. While some of these discrepancies can be attributed to fabrication imperfections, an important aspect that needs to be addressed is mutual coupling between neighboring metasurface elements [265].

Table 5.1 provides an overview of the performance of different modulation mechanisms in terms of the initially defined objectives. Field-effect tunable metasurfaces relying on carrier modulation and liquid crystal-based active structures stand out in terms of the achievable intensity modulation efficiency and the phase modulation. While field-effect tunable metasurfaces outperform in terms of the modulation frequency, liquid crystal-based architectures enable higher efficiency designs in both reflection and transmission. However, a drawback of current liquid-crystal based structures is the lack of subwavelength control in the visible due to mutual crosstalk. Meanwhile, metasurfaces relying on electro-optic tuning seem promising in terms of their efficiency and the accessible modulation frequencies. The operation wave-

length can additionally be chosen from a broadband regime. However, the small index changes in the active material pose additional challenges to the realization of high-Q resonant metasurface unit cells at small dimensions needed for full two-dimensional control. Metasurfaces based on 2D materials or phase change/phase transition materials may provide an effective alternative to satisfy the desired objectives, however, several challenges need to be surmounted before these technologies can be used in applications, including the design of low-loss broadband structures with individual unit cell control. Ultimately, the realization of an optimal universal metasurface will rely on inverse design which is part of an overall hierarchical co-design of the active metasurface components: from the desired dielectric function of an active layer to an optimization of the unit cell shape as well as the configuration of the external stimuli. Multi-objective optimization algorithms could further support the design of metasurface unit cells that are robust to fabrication imperfections. To this end, an active area of research will consist of the development of computationally efficient algorithms. Supplementing the algorithms with physics-based models and constraints will enable efficient search and optimization of experimentally feasible design spaces [266].

5.3 Two-dimensional metasurface control

To shape arbitrary wavefronts in space, a universal active metasurface needs to be fully reconfigurable in two dimensions. This is of particular interest for many imaging and communication applications, which may require directional scanning of beams across a scene. Two-dimensional control further enhances the information processing capability of an optical computing metasurface by dramatically increasing the number of independently addressable unit cells. However, this increased number demands sophisticated control architectures that allow for compact chip packaging with subwavelength unit cell spacings. Additionally, the control architecture should have minimal interference with the optical response of an active metasurface, *i.e.*, ideally the control system should not cause any degradation in the dynamic range of tuning or the attainable efficiency. Most demonstrations of active metasurfaces to date have consisted of a collective modulation of an entire array of scatterers [77, 244, 258] or addressing of individual unit cells along one dimension of the array (while connecting the scatterers along the perpendicular direction) [42, 216]. In the following, we highlight the active modulation schemes most suitable for achieving two-dimensional control based on the photonic modes and the nature of the external stimulus. We then discuss several pathways of designing an appropriate

control architecture and evaluate the impact the respective approaches may have on the performance of an active metasurface.

To achieve an active metasurface that can be controlled in two dimensions, the resonant photonic mode needs to be confined along the lateral, longitudinal, and vertical dimension of the metasurface. This has been achieved in various active metasurface platforms using geometrically resonant scatterers in field-effect tunable metasurfaces [42] or liquid crystal-based structures [20]. In the case of a guided mode resonance [75], an extended mode is formed. Thus, independent control of metasurface elements can only be performed along the direction perpendicular to the guided mode, limiting this approach to one-dimensional spatial modulation. Similarly, active non-local metasurfaces [77] rely on phase modulation over length scales that are larger than the wavelength (and thus an individual metasurface element), but potentially smaller than the metasurface aperture. While this does not necessarily exclude two-dimensional control, additional research efforts are required to evaluate how non-local metasurfaces can be used for arbitrary wavefront shaping.

Additional constraints toward the realization of a two-dimensional control architecture are imposed by the nature of the external stimulus, which can be electrical, thermal, optical, chemical, or mechanical. Mechanical deformations, that are caused by, for example, stretching of an elastic substrate [274, 275], have previously been used to demonstrate two-dimensional beam focusing. However, prior research relied on changes that are introduced over the entire array configuration. As a result, the realized devices are restricted in terms of achieving different functions using a single chip. Similarly, it is challenging to confine changes induced using external chemical sources (such as the hydrogen or oxygen flow in hydrogenation metasurfaces [40]) or thermal sources [35, 276] to subwavelength spaces. Advanced schemes to inhibit the interference of neighboring unit cells would be necessary, requiring extensive multiphysics analysis and design. In comparison to these concepts, all-optical modulation relies on a pump-probe experiment, in which an intense pump pulse generates free carriers in the active medium and thus alters the properties of the scattered probe pulse [277]. Alternatively, interference of the two beams [278] or optical pumping of metasurface elements [279] can introduce structural and refractive index changes in the active medium. In either case, the resolution of the spatial pattern generated on the metasurface is given by the diffraction-limited spot of the pump laser. The requirement of additional pump lasers and beam scanners to write individual elements, however, inhibits a compact integration.

Over recent years, electrical biasing of metasurface elements has emerged as a promising pathway to enable two-dimensional control on a single unit cell level. The introduction of localized effects using an electrical stimulus has led to the development of several technologies ranging from electrically induced structural changes in phase change materials [118, 257] or liquid crystals [20] to mechanical deformations of scattering elements [37]. Due to its versatility in being able to be integrated with several modulation schemes, the following discussion aims to highlight potential pathways toward realizing a two-dimensional electrical biasing network and their respective challenges.

One route to designing an interconnect architecture for a two-dimensional active metasurface is to create individual biasing lines for each metasurface element. Kim *et al.* [221] recently experimentally demonstrated two-dimensional wavefront control using a plasmonic, field-effect tunable metasurface. In this work, fan-outs were used to electrically address each individual unit cell (Fig. 5.3a). The gate electrodes were designed orthogonal to the scatterer orientation, as illustrated in Fig. 5.3a. This configuration results in minimal perturbation of the resonance when the scatterers are excited with linearly polarized light in the y -direction. A common challenge with a biasing architecture like this, however, is its scalability. For metasurfaces with thousands or even millions of scattering elements, larger spacings between unit cells are required due to routing complexities. To overcome this limitation without sacrificing the metasurface aperture, multiple scatterers can be connected to one electrode, as shown in [221]. Notably, as the unit cell size approaches the incident wavelength, the field-of-view of the metasurface is strongly reduced. Additionally, an increased amount of undesired scattering is expected for coarsely resolved phase profiles, as previously shown for gradient beam steering metasurfaces [42].

An alternative strategy relies on row-column or perimeter tuning of individual unit cells. This approach involves connecting the metasurface elements in individual rows and columns (Fig. 5.3b), respectively, allowing for a dramatic reduction of biasing lines from N^2 (for individual unit cell control) to $2N$ for an array consisting of $N \times N$ unit cells. Row-column tuning is commonly used in commercial spatial light modulators consisting of large arrays of pixels (more than 1000×1000 elements). Spatial light modulators comprise non-resonant pixels relying on a phase accumulation in thick liquid crystal layers [280]. Arbitrary wavefront shaping is achieved using either a dynamic random-access memory (DRAM) or a static random-access

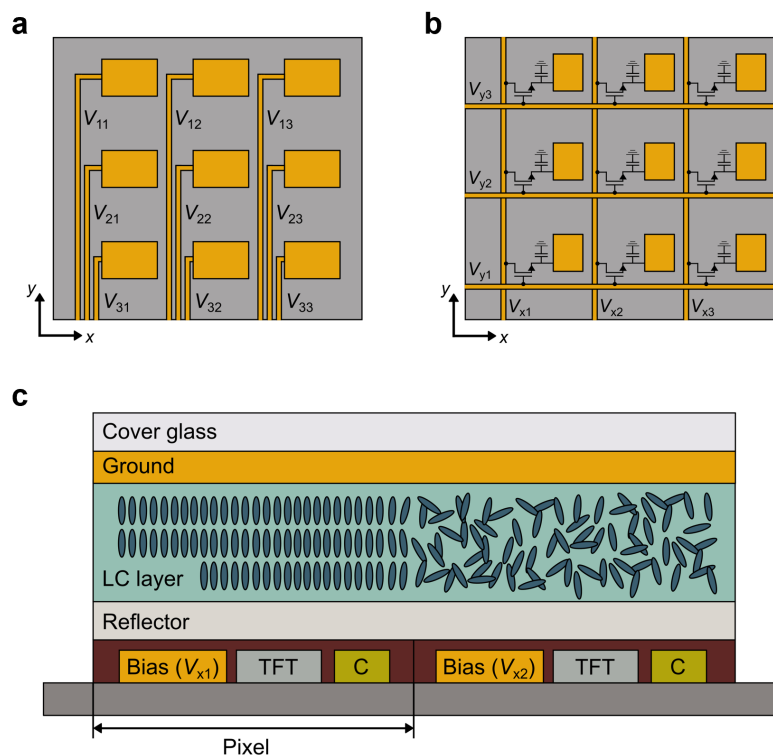


Figure 5.3: **Two-dimensional metasurface control architectures.** (a) Biasing of individual elements with voltage V_{mn} in a $m \times n$ array, where m and n are the number of rows and columns, respectively. (b) Row-column tuning of elements using biasing lines V_{xn} and V_{ym} . A switching transistor and storage capacitor are built in at each element. (c) Cross-section across two pixels of a liquid crystal-based spatial light modulator relying on DRAM. The backplane consists of the biasing line, a thin film transistor (TFT) and a capacitor (C). These elements are covered by a reflector, the liquid crystal (LC) layer, the ground electrode, and the cover glass.

memory (SRAM) circuit [280, 281]. The backplane of a DRAM unit cell consists of the biasing line, a single thin film transistor (TFT) and a capacitor to switch and store the state of an element, respectively. Figure 5.3c illustrates a schematic cross section across two pixels of a liquid crystal-based spatial light modulator in a DRAM architecture. By periodically scanning the biasing line in each row and column, respectively, the capacitor at each pixel is charged with the required voltage. SRAM circuits, in comparison, are purely digital and built using multiple logic gates per element to encode the desired voltage. Consequently, DRAM architectures allow for smaller pixel sizes that are usually in the range of $2 - 10 \mu\text{m}$ [281, 282].

To achieve high resolution wavefront control with a wide field-of-view, researchers are pursuing strategies to further downscale the pixel size in spatial light modulators.

Conventionally, the biasing line, the switching TFT, and the storage capacitor are arranged laterally in one plane, as schematically shown in Fig. 5.3c. The TFT channel length cannot be further reduced in this configuration, as a concentration of large currents into small regions causes an increase in temperature that leads to channel degradation [256]. To overcome this limitation, vertically stacked thin film transistors (VSTs) and vertical channel thin film transistors (VTFTs) have been proposed [256, 283–285]. A VST architecture relies on an overlap of the biasing line and the TFT/capacitor elements to reduce the pixel area. Using this approach, Choi *et al.* [283] realized spatial light modulators with pixels as small as $1\ \mu\text{m}$ in the lateral direction. VTFTs allow additional downscaling of the pixel in the longitudinal direction by forming the channel along the sidewall of the vertical structure [256, 284, 285]. The main challenge of using this approach is the patterning and material deposition required to obtain the vertical structure [256].

In comparison to spatial light modulators, metasurfaces consist of resonant scattering elements. As a result, the phase accumulation occurs due to the scatterer rather than the liquid crystal layer thickness. Liquid crystal-based metasurfaces therefore support reduced cell thicknesses that allow operation under smaller applied voltages. The smaller liquid crystal layer thickness additionally allows for shorter response times. Li *et al.* [286] recently realized a two-dimensional liquid crystal-based metasurface based on row-column tuning with a pixel size of $1 \times 1\ \mu\text{m}^2$. It is to be noted that the reduced liquid crystal layer thickness in metasurfaces limits the effects of fringing electric fields, which degrade device performance due to smeared out phase profiles [287, 288]. Nevertheless, the elastic motion of the molecules, which leads to crosstalk between adjacent unit cells, limits further reductions in pixel size [256]. In comparison, active materials that are used in field-effect or electro-optically tunable metasurfaces do not face this limitation (with the appropriate design of a localized resonant mode). The advancements in downscaling pixels using vertically stacked or vertically oriented TFTs could provide a potential pathway for the integration of subwavelength DRAM circuits into active metasurfaces. Rather than having a continuous ground plane, the back reflector of an active metasurface would need to be transformed into a ground gate electrode oriented perpendicular to the top electrode (Fig. 5.3b). In addition, a transistor and capacitor need to be integrated to enable sequential scanning of rows/columns. Non-volatile phase change memory materials [289, 290] could provide a promising platform to introduce the required latency into the interconnect architecture without the need of an additional capacitor. However,

elaborate thermal analyses need to be performed to ensure that there is no thermal crosstalk between adjacent elements.

A crucial aspect in the design of electrical circuits for row-column tuning is the dwell time required to configure or change the state of each metasurface element. The added dwell time is expected to have a direct impact on the accessible modulation frequencies of active metasurfaces. Fast scanning of biasing lines would, in principle, enable applications such as holographic displays, where our eyes receive an image that is averaged over fractions of a second. However, the additional time required to scan all row/column elements across large two-dimensional arrays may potentially limit access to the time-modulated operation regime of an active metasurface. This becomes particularly relevant for modulation mechanisms that support frequencies beyond the MHz regime. An alternative approach suggested row-column tuning without a capacitive element [291]. This would, in principle, allow driving frequencies of several MHz to GHz based on the modulation mechanism. In this design, however, the attainable functions of an active metasurface are restricted to those that can be represented as a convolution of two linearly independent responses associated with the orthogonal directions of the array. As a consequence, this approach inhibits arbitrary wavefront shaping.

In summary, while there are existing interconnect architectures for biasing of individual unit cells, the designs implemented in active metasurfaces to date are not scalable. Row-column tuning using a capacitive element offers an alternative approach with a drastic reduction in biasing lines. Existing TFT technologies for spatial light modulators have been downscaled to a pixel size of $\sim 1 \mu\text{m}^2$. For operation in the visible, however, further reductions in size are required to increase the field-of-view. Thus, careful redesign of the biasing network and analysis of interelement crosstalk is required to develop an appropriate interconnect architecture for two-dimensional control. Additional studies are needed to understand the impact of dwell time reconfiguration on time-modulated operation. Table 5.2 provides a summary of challenges toward the realization of a two-dimensional active metasurface based on row-column tuning (with latency). Further, we would like to note that most reported works on active metasurfaces and spatial light modulators in this section have relied on operation in reflection only. Therefore, we need to explore alternative materials and biasing architectures that have a minimal impact on the output efficiency and thus enable metasurface operation both in reflection and in transmission. An important consideration for the realization of two-dimensional

active metasurfaces is its CMOS-compatibility, which would be required to utilize existing fabrication techniques in commercial semiconductor foundries. Finally, we note that as we move to large-scale active metasurfaces, we need to rely on low-cost, high-throughput fabrication techniques, such as immersion lithography [142], nanoimprint lithography [292], or rolling mask lithography [293].

5.4 Applications of universal active metasurfaces

Successfully realizing a universal active metasurface would have significant impacts upon many research directions currently being pursued within the field of optics. In the following, we discuss the limitations of existing technologies in the fields of optical imaging, communication, and computation, and explore novel applications that could be realized with the added capabilities of a universal active metasurface.

Optical imaging

Optical imaging is a crucial component of realizing many next-generation technologies, including autonomous vehicles, machine vision for drones, biomedical and diagnostic techniques, holography, and quantum information technologies. One of the most important building blocks of optical techniques is the lens. Whilst conventional lenses have been able to demonstrate desirable optical imaging techniques, they are bulky, heavy, and expensive, preventing them from being integrated into wearable and lightweight devices. Metalenses, on the other hand, exhibit a significantly reduced form factor, allowing for their integration into these devices. While the current cost of fabrication for metalenses is considerably higher than their bulky counterparts, metalenses have the potential to exhibit exotic functionalities, such as achromatic or 3D imaging, through precise engineering of their subwavelength elements.

Unlike conventional lenses, the resonant scatterers of passive metalenses are generally highly dispersive in nature. This leads to strong chromatic aberration away from a particular wavelength, and hence they have usually been designed for single-wavelength operation [106, 294, 295]. Recently, several metalenses capable of focusing a set of discrete wavelengths without chromatic aberration [296, 297] and over a finite continuous wavelength range [28, 107, 297–301] have been demonstrated. One approach that has been adopted to realize this extended achromaticity is to use integrated-resonant unit elements (IRUEs), in which coupled metallic nanorods supporting multiple plasmonic resonances provide a linear phase profile with $1/\lambda$ [301]. However, the diameters of these passive metalenses are limited to the

order of $100\ \mu\text{m}$ by the requirement for large group delays [300], restricting their spatial resolution and performance. Furthermore, as these are passive systems, the focal lengths are fixed and cannot be varied post-fabrication. Varifocal metalenses using active metasurfaces have been demonstrated through field-effect tuning [42], integrating phase-change materials [302] and mechanical modulation with elastic substrates [303]. However, these metalenses are typically single-wavelength operation, as they suffer from chromatic aberrations. This is due to a non-linear relationship between the phase of the scatterers and wavelength, stemming from insufficient control over their phase profiles. Thus, a universal metasurface with arbitrary phase control of its elements could potentially exhibit dynamic focal-length tuning whilst potentially replicating the appropriate phase profiles of the passive metasurface elements, leading to the realization of a tunable achromatic metalens.

One optical technique that has been realized with passive metalenses is three-dimensional (3D) imaging. To date, depth-sensing has been realized using two main approaches: light-field imaging [304, 305] typically uses multiple metalenses, either interleaved or off-set from each other. Alternatively, engineering of point spread functions (PSFs) [306–309] relies on metasurfaces with complimentary PSFs to achieve both axial and lateral sensitivity. However, these approaches tend to suffer from a combination of poor spatial resolution, poor axial resolution, limited field of view, limited depth of focus and/or limited wavelength range, depending upon the device. Importing the universal metalens discussed in the previous paragraph into 3D optical imaging systems would offer several advantages over current devices. First, reconfigurable metalenses could be programmed to perform functions sequentially in time that are currently performed by spatially separated distinct components. Examples of this are taking several snapshots in different imaging planes or redefining the PSF. Thus, the entire aperture of the device could be utilized for each function, resulting in improved spatial lateral resolution. Furthermore, continuous tuning of the focal length would offer higher axial resolution than passive devices with a set of discrete focal lengths. A universal active metasurface could also allow some degree of tuning over the depth-of-focus and wavelength operations ranges, so that a single device could be used for multiple applications.

Another sought-after technique in optical imaging is holography. Passive and active metasurfaces have been used to demonstrate static [295, 310, 311] and dynamic [40, 312, 313] holography. However, many of the previous demonstrations of dynamic holography involve switching part of the hologram on or off, often through chemical

reactions. To the best of our knowledge, there has yet to be a demonstration of a truly reconfigurable hologram metasurface at optical wavelengths, in which any arbitrary two-dimensional image could be displayed. To achieve this feat, precise dynamic control over each individual unit cell would be required. Moreover, a metasurface capable of displaying three-dimensional holographic images would need to exhibit control over both amplitude and phase independently [314]. Thus, the universal metasurface would be an ideal platform for demonstrating two- and three-dimensional holograms that could be dynamically and arbitrarily changed. Furthermore, the universal metasurface could potentially remove anomalous speckles from images and demonstrate sophisticated holographic techniques such as rendering surface textures of 3D holographic objects through its independent control of phase and amplitude, realizing a quality of holographic display not achievable with current technology.

Optical communication

Space-time or time-modulated metasurfaces are a class of active metasurfaces that simultaneously impart a spatial and temporal phase gradient to incoming light [94, 116, 119]. Their control over the spectral content of the scattered light has made them an exciting candidate for many applications in optical communications from LiDAR to deep space communications. While the concept of time-modulated metasurfaces has previously been demonstrated in the radio frequency (RF) domain, it has only recently become feasible in optical frequencies with the realization of active metasurfaces with decreased response times, allowing for higher modulation frequencies [44, 94, 95, 117, 118]. Recently, there has been a surge of interest in the photonics community to realize time-modulated metasurfaces in the optical domain because of their ability to: 1) create a dispersionless spatial phase gradient with constant amplitude, 2) enable multi-channel communication in a single aperture, and 3) exhibit nonreciprocal behavior.

As discussed in Section 5.2, many active metasurfaces suffer from the coupling of phase and amplitude which limits the efficiency of a given optical function and creates unwanted scattering of light, especially if 2π phase span is not achieved in the quasi-static domain. In space-time metasurfaces, the conversion efficiency from the fundamental frequency to the harmonic of interest is still limited by amplitude-phase coupling [119]. However, the spatial phase can be tuned across a 2π range by shifting the phase of the applied waveform at each metasurface element using a series of external phase shifters. This allows for the creation of a nonresonant,

dispersionless phase shift with constant amplitude, which can effectively overcome the challenges associated with coupled phase and amplitude in quasi-static active metasurfaces.

Another capability that is realized by space-time metasurfaces is multicasting and multiplexing of information [94, 118, 119, 315]. Multicasting refers to sending a single input to multiple outputs, separated either in space or frequency. Multiplexing encodes multiple inputs into a single output wave that can be demultiplexed back into the original signals at the receiver. Figure 5.4 illustrates possible multicasting and multiplexing schemes achievable with a time-modulated metasurface operating at optical frequencies and modulated with RF signals. It is important to note that, in general, the frequency harmonics generated by a space-time metasurface will be steered to different angles, regardless of the spatial phase-gradient. However, because the attainable modulation frequencies in state-of-the-art active metasurfaces are multiple orders of magnitude smaller than optical frequencies, the angular separation between generated harmonics will be negligible and for the purpose of this discussion, we will ignore this angular separation. Figure 5.4a shows a simple frequency multicasting device that accepts one input frequency, generates new harmonic sidebands, and uses a subwavelength spatial phase-gradient to direct the output light to a given angle. For such a device, all metasurface elements are identical and modulated with the same RF waveform, phase-shifted in space. Extending this concept, one can apply two alternating waveforms to every other metasurface element to achieve a more complex multicasting functionality, depicted in Fig. 5.4b. Here, the temporal and spatial phase-gradients of each modulating waveform can be altered to tune the angle and spectral content of the two scattered wavefronts. Finally, by using metasurface elements with different resonance wavelengths [316], multiple input frequencies can be accepted and multiplexed to multiple independently tunable output channels, as depicted in Fig. 5.4c. While the spatial phase gradients depicted in Figure 5.4 are assumed to be subwavelength blazed gratings, alternative optical functions can be realized for each wavefront by designing appropriate spatial phase configurations. The ability to control multiple channels simultaneously increases the amount of information that can be sent and received with optical frequencies in a single aperture.

Lastly, another exciting capability of space-time metasurfaces is their ability to violate Lorentz reciprocity by breaking time-reversal symmetry [44, 94, 116, 317]. The spatio-temporal modulation of refractive index creates an effective motion of

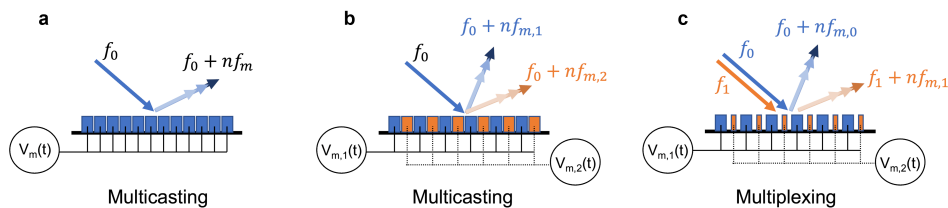


Figure 5.4: **Multicasting and multiplexing schemes with space-time metasurfaces.** Metasurfaces are illuminated with optical frequencies and modulated with RF signals. In all schematics, $V_m(t)$ denotes a time-varying voltage of frequency f_m applied to the metasurface, f_0 is the frequency of light incident on the metasurface, and the output light is a sum of the incident frequency with integer multiples of the modulating frequency. (a) A single input is converted to multiple frequencies and steered to a given angle. (b) A single input frequency incident on a space-time metasurface driven with two waveforms of differing frequency and spatial phase gradient. This results in two spatially tunable beams, each consisting of a different spectrum of harmonics. (c) A space-time metasurface consisting of two alternating elements with different resonant frequencies. This allows two input frequencies to be individually steered, while controlling the harmonic content of each beam.

phase within the device, causing incoming light to see a direction-dependent phase gradient. This effect is commonly demonstrated by applying a large in-plane magnetic field, requiring a bulky ferromagnetic magnet. Space-time metasurfaces can break time-reversal symmetry in a compact and lightweight device, increasing the range of possible applications. A simple device that is enabled by this functionality is a unidirectional beam splitter which acts as a conventional beam splitter when illuminated from one side and allows light to pass normally when illuminated from the other. Additionally, the nonreciprocal separation of angles between incident and transmitted signals can allow for full-duplex communication: a communication network consisting of devices that can simultaneously send and receive information. Interference between received and transmitted signals is a common problem that limits full-duplex communication. This is solved by designating one frequency to receive signals and another to transmit, increasing the complexity and cost of the overall device.

Space-time metasurfaces allow for full 2π coverage with constant amplitude, multicasting and multiplexing functionalities, and nonreciprocal behavior, enabling various complex communication functionalities in a single aperture. Such compact devices are highly desirable in applications such as LiFi, LiDAR, space communication.

Optical computation

Due to their control over phase and amplitude in space and time, a great amount of research has been dedicated to metasurfaces for optical computing. The field of optical computing has been an active research topic for many decades but the reliance on nonlinear phenomena to create logic gates (requiring high power densities and long propagation distances) has prevented optical processors from surpassing the performance of their electronic counterparts [318]. Despite its limited use in industrial applications, optical computing has many inherent advantages over electrical computing such as capability for highly parallelized processing, high rate of data transfer, and low power requirements [319, 320].

Recently, metasurfaces have been used as tools for optical signal processing to perform functions such as edge detection, differentiation, and solving differential equations [321–325]. In these devices, one of two techniques is commonly employed to process input information: the use of spatial Fourier transforms or Green's function [319]. In the spatial Fourier transform approach, a $4f$ lens system is used with a precisely designed metasurface spatial filter at the Fourier plane of the two lenses. In contrast, demonstrations using Green's function devices directly encode the desired transform to a single metasurface layer, without using lenses to take the Fourier and inverse Fourier transforms. In their pioneering demonstration, Silva *et al.* [322] implement both techniques to take spatial derivatives of an input waveform. Their first device uses a metasurface sandwiched between two gradient index (GRIN) lenses. The GRIN lenses take Fourier and inverse Fourier transforms and the metasurface is specially designed to take the first derivative of the input signal. In contrast, the authors also used a multilayered metamaterial slab to create the Green's function associated with a second derivative. By directly implementing this function, the device does not need to work in the Fourier space and removes the requirement of the GRIN lenses. Many variations of these techniques have been demonstrated recently, further illustrating the computational capabilities of metasurfaces [326–329].

In all works discussed thus far, a passive metasurface or metamaterial is designed for a single functionality. A universal tunable metasurface would provide the freedom to control the transfer function of a device even after fabrication. A single metasurface could be used as an effective 'optical calculator' to, for example, impart a spatially dependent multiplicative factor on an input waveform, then be reconfigured to take the derivative of a different waveform. This freedom greatly increases the

applications of a single metasurface. In addition, arbitrary control over all properties of light allows for a general transfer function in a single metasurface layer. A recent study by Kulce *et al.* [320] investigated the fundamental information limits of a single layer metasurface consisting of individually controllable complex valued transmission coefficients. This work considered a signal from an input aperture, sent through a series of linear transforms, and received at an output aperture. The authors showed this system could be reproduced by a single universal metasurface consisting of at least $N_i \times N_o$ individually addressable elements, where N_i and N_o are the pixels of the input and output apertures, respectively. Thus, for a universal active metasurface with a sufficiently large aperture and density of individually addressable elements, any series of linear transfer functions can be implemented and changed in time, in a single layer. While implementing a finite number of linear transforms in series is useful, many scientific problems require a feedback loop and iterate toward a solution. For example, solving differential equations without an analytic solution and machine learning algorithms that typically start with an initial guess, adapt this guess, and repeat until a solution is obtained which meets certain accuracy criteria. To implement such algorithms optically, we envision integrating a universal metasurface in a cavity and adapting its amplitude/phase profile over time until a solution is achieved. An alternative to this approach could be to cascade a finite number of metasurfaces in space. While this arrangement has a limit on the number of times an input signal interacts with a metasurface layer, interesting functionalities could be explored by designing the device to create near-field coupling between the metasurface layers. Such a highly connected system could potentially be used to reproduce neural networks where each metasurface element represents a neuron and connections between neurons could be controlled via manipulation of the near-field coupling. These proposed devices represent forward-looking perspective of possible uses for a universal metasurface and illustrate the wide range of applications for metasurfaces in digital and analog optical computation.

5.5 Outlook and conclusions

Over the last few years, there has been remarkable progress toward dynamic manipulation of light using active metasurfaces. In this chapter, we highlighted several technologies that are particularly promising for the realization of a universal active metasurface for arbitrary, on-demand wavefront shaping. Table 5.1 provides a summary of the performance of state-of-the-art active metasurfaces in terms of their dynamic range of tuning, the attainable output efficiencies, the modulation fre-

quency, and the wavelength coverage. While none of the current designs meets all target performance characteristics, ITO-based field-effect tunable multifunctional metasurfaces [42, 217, 221] currently most closely resemble the conceptual universal active metasurface. These metasurfaces have been used to demonstrate a diverse set of functions based on individual unit cell control. High modulation frequencies of field-effect tunable metasurfaces (in the range of several MHz [30]) further give access to advanced operation modes, which rely on the concept of space-time modulated metasurfaces [95]. However, the large absorption observed in these gate-tunable plasmonic metasurfaces is a major drawback of this approach.

Active metasurfaces, which use electrically controlled reorientation of liquid crystal molecules, are also a promising pathway toward the realization of the universal metasurface. Liquid crystals offer an advantage of active tuning with low losses and are thus widely used in applications. Researchers have realized both reflective [19] and transmissive [20, 35] liquid crystal-based structures exhibiting a large dynamic range of tuning. Furthermore, multi-resonant designs have been proposed for operation across the visible spectrum [19]. A significant limitation, however, arises due to the slow response times of liquid crystal molecules, restricting the operation of such metasurfaces to the quasi-static regime. Electro-optic materials could therefore be an effective alternative for active metasurfaces supporting high modulation frequencies along with low losses. Current leading designs, however, are based on high quality extended modes [75] which, in principle, inhibit the perspective of two-dimensional control of the wavefront shape. Thus, novel designs of subwavelength high-Q metasurface elements need to be developed, which will localize the mode in three dimensions.

Another challenge which needs to be surmounted for the realization of a universal active metasurface is the design of an appropriate two-dimensional control network. Electrical biasing of metasurface unit cells has emerged as a promising pathway for individual unit cell control in a variety of modulation schemes. Here, the main challenge lies in developing electrical circuits that allow for subwavelength unit cell control in large arrays with thousands to millions of elements. The design of individual biasing lines for each metasurface element [221] provides an intuitive approach to realizing two-dimensional control in the near future. However, it is challenging to integrate this control architecture into compact subwavelength spacings. Thus, row-column tuning may provide an effective alternative to dramatically reduce the number of biasing lines. The latency required to scan and configure each element

demands an integration of additional transistors and capacitors in the biasing network. In this aspect, continuous efforts made toward miniaturizing existing thin film transistor technology used in spatial light modulators [256, 283] may have a direct impact on the mechanisms in which next-generation active metasurfaces are configured.

Based on current challenges toward the realization of a universal metasurface, we anticipate the following areas to play a critical role in the development of versatile active metasurfaces:

1. *Advanced fabrication techniques and new materials:* Low-loss active materials supporting high modulation frequencies form a crucial component of a high performance universal metasurface. The current leading material platform in this aspect constitutes of electro-optic materials. Commercially available lithium niobate thin films have allowed for considerable progress toward achieving a large dynamic range of tuning. However, the corresponding metasurface designs rely on extended or non-local high-quality resonant modes to capitalize on the modest electro-optic refractive index changes. Further progress in the fabrication of thin crystalline films of electro-optic materials may enable their integration with alternative unit cell designs for individual element control. An example of this was discussed in Chapter 4 through the integration of spalled single-crystal barium titanate thin films in active metasurfaces. Alternatively, the search for new low loss materials and material compounds for integration into field-effect tunable metasurfaces may provide an effective pathway to obtaining power efficient active metasurfaces that support high modulation frequencies. In this context, machine learning-assisted materials discovery will play a critical role to find materials or material compounds that exhibit optimal complex dielectric functions for low loss operation [330–332].
2. *New metasurface design concepts:* On a unit cell level, a universal metasurface requires individual unit cell control, independent manipulation of all characteristic properties of light, and a tunable operation wavelength. Metasurfaces based on electro-optic materials require novel design strategies for developing subwavelength metasurface unit cells which can both exhibit high quality factors and localize the optical mode in three dimensions. Notably, resonant operation of active metasurfaces results in a coupled response of mul-

multiple properties of the scattered electric field, such as its amplitude and phase. This creates undesired effects in the wavefront of scattered light. Dual-gated metasurfaces, enabling the application of two independent voltages to a single unit cell, have therefore been proposed to demonstrate independent control over the amplitude and phase of the reflected light [53, 54, 216]. An extension of this concept to multi-gated structures could provide independent control over more than two characteristic properties of the scattered light. Alternatively, independent control over the scattered light properties may be realized by stacking metasurfaces, where each surface controls a different property of light [333]. Further advances in the design of efficient transmissive active metasurfaces would be instrumental for the realization of compact optical components consisting of metasurface stacks. Finally, further advances in the design of multi-spectral active metasurfaces are needed to obtain a tunable operation wavelength. This may involve designs of geometrically multi-resonant structures [19, 316], or an integration of different active materials into one unit cell.

3. *Multiphysics modeling for two-dimensional electrical control architectures:* Two-dimensional control of active metasurfaces is necessary to move active metasurfaces into the realm of practical applications and harness their full potential. In this regard, further efforts toward multiphysics modeling of the metasurface together with its electrical control network are required to evaluate the feasibility of different designs. In the case of a two-dimensional biasing network, the gate electrodes pass through the area where light is directly interacting with the resonant scatterer. This is different from the case of one-dimensional control, where metasurface unit cells are electrically biased from the side. Therefore, it is critical to analyze the impact of the control circuit on the optical response of a resonant metasurface element. This includes analyzing the impact of biasing lines on the overall dynamic range of tuning and device efficiency as well as potential crosstalk between high-frequency signals across closely spaced biasing lines. Additional studies addressing the electrical response times are required to determine inherent limits to the modulation frequencies arising from the employed interconnect architectures. Finally, a thermal analysis is needed to evaluate heat damage thresholds upon downscaling electrical components as well as thermal crosstalk effects between adjacent unit cells.

4. *Miniaturization of electrical control components and integration into metasurfaces*: In order to obtain high-resolution beam shaping with a large field-of-view, we need to develop large scale metasurfaces with subwavelength unit cells. Row-column tuning of a two-dimensional array provides an effective pathway to limit the number of biasing lines. However, the row- / column-wise reconfiguration requires a latency that is achieved through the integration of additional transistors and capacitors in the circuit. Further research is required to realize sub-micron scale electrical circuits that allow to switch and store the state of an individual element. Current metasurface designs then need to be adapted to incorporate the biasing network into each individual unit cell. A grand challenge in this aspect also lies in the realization of two-dimensional transmissive metasurfaces, which experience minimal loss in efficiency due to the biasing network.

With the realization of a universal active metasurface, we expect an explosion of novel applications in the realms of optical imaging, communication, and computation, some of which have been discussed in this chapter. An integration of the active metasurface with nanophotonic light sources, such as vertical cavity surface emitting lasers (VCSELs) [334, 335], may further lead to the emergence of chip-scale light sources that allow for arbitrary beam shaping in real-time. Moreover, coupling of the universal metasurface to quantum emitters will enable the realization of novel quantum devices that could be used to capture and manipulate the state of single photons [336, 337]. For efficient use in applications, we ultimately foresee using deep learning approaches to identify the optimal control sequences applied to the metasurface, resulting in the desired optical response. The ability to encode active metasurfaces using advanced computational methods will thus enable the creation of a universal optical processing unit that can function independently and reprogram itself based on the desired task at hand.

Modulation mechanism	Intensity mod. efficiency η	Phase mod. (with corresponding η)	Refl. R or Transm. T at largest phase shift	Mod. freq.	Operation wavelength
Field-effect (carrier modulation)	96% [215]	360° ($\eta = 48\%$) [216]	8% Refl. [42], 4% Refl. [216]	30 MHz [267]	1510 nm [42] – THz [39]
Field-effect (excitonic transition)	50%, * [234]	42° ($\eta = 29\%$), * [132]	45% Refl., * [132]	625 MHz, * [132]	620 nm [238] – 755 nm [156]
Electro-optic tuning	37% Chromophores (Transm.) [268], 40% LN [245], 73% MQW [75]	70° ($\eta = 73\%$) MQW [75]	5% MQW Refl. [75]	5 GHz [31]	915 nm [75] – 1550 nm [245]
Liquid crystals	80% (Transm.) [35]	180° Transm. ($\eta = 75\%$) [269], 360° Refl. ($\eta = 38\%$) [19]	36% Transm. [20]	40 kHz [131]	460 nm [19] – GHz (Transm.) [270]
Phase change and phase transition	82% GST [271], 88% GSST [259], 78% VO ₂ [34]	180° ($\eta = 78\%$) [34]	20 % Refl. [34]	20 THz [259]	0.38 μ m [272] – THz (Transm.) [273]

Table 5.1: Summary of experimentally demonstrated values for different modulation mechanisms. Intensity modulation efficiency η , phase modulation, and the corresponding reflectance (R) or transmittance (T) at the largest phase shift, as well as the modulation frequencies and the operation wavelength regime. The modulation frequency refers to the highest frequency at which the amplitude response of an active metasurface resembles the applied signal. All reported values are for nanophotonic structures operating in reflection unless otherwise noted. *Values obtained using either a heterostructure or a spatial light modulator.

Modulation mechanism	Challenges toward row-column tuning (with latency)
Liquid crystals	crosstalk in subwavelength pixels due to elastic motion of molecules
Field-effect tuning	potential reduction in modulation frequency based on dwell time
Electro-optic tuning	potential reduction in modulation frequency based on dwell time
Electro-mechanical deformations (MEMS/NEMS)	interference of mechanical motion with biasing lines, potential reduction in modulation frequency based on dwell time
Phase change materials	thermal crosstalk in subwavelength pixels, potential reduction in modulation frequency based on dwell time
Phase transition materials	thermal crosstalk in subwavelength pixels

Table 5.2: Challenges toward row-column tuning for various modulation mechanisms relying on an electrical stimulus.

Chapter 6

CONCLUSIONS

In this thesis, we explored and developed new pathways toward realizing an electrically programmable, universal active metasurface for dynamic, independent, and comprehensive control over the properties of light. The work outlined here encompasses multiple facets, including the investigation of system-level metasurface operation modes, optimized array configurations, unit cell design, and integration of novel materials. The findings presented here establish a comprehensive framework for next-generation nanophotonic platforms with enhanced information processing capabilities.

We first leveraged plasmonic, field-effect tunable metasurfaces using indium tin oxide (ITO) as a platform to develop an array-level inverse design approach which co-optimizes the array phase and amplitude profiles for a desired objective function. Through iterative optimization methods, we demonstrated that nonintuitive array configurations could enhance the directivity of beam steering metasurfaces by up to 84% compared to conventional forward designs, despite nonideal amplitude and phase response from the antenna components of a previously realized ITO-based metasurface [42]. Experimental validation for a metasurface with approximately 220° phase modulation further confirmed that inverse-designed metasurfaces yield improved beam steering performance. We extended this optimization framework to alternative objective functions, including the design of metasurface arrays for flat top beams, tunable full-width at half-maximum, and multi-beam steering configurations. These results establish array-level inverse design as a powerful tool for overcoming antenna-level nonidealities in practical metasurface applications.

While array-level inverse design enhances the capability of active metasurfaces to perform a variety of functions with improved performance, optimization becomes increasingly challenging as the complexity of the target function increases, particularly when simultaneous optimization of multiple tasks is required. To address this challenge, we extended the operational regime of optical metasurfaces to space-time modulation using the previously introduced ITO-based metasurface. In this regime, a near-infrared metasurface is modulated with tailored waveforms at MHz frequencies to generate frequency harmonics offset from the incident laser

frequency by integer multiples of the modulation frequency. By introducing phase offsets between the waveforms applied to adjacent electrodes, we experimentally demonstrated tunable diffraction of desired frequency harmonics up to an angle of 14° . We then extended this concept theoretically, demonstrating spatiotemporal wavefront configurations that enable multi-frequency, multi-beam steering, realizing an example of active multitasking metasurfaces with increased channel capacity. While challenges remain in experimentally enhancing the modulation bandwidth and efficiency of the generated frequency harmonics, our results highlight the potential of space-time modulated metasurfaces in enhancing the channel capacity in next-generation active metasurfaces and enabling advanced components such as nonreciprocal optical elements.

To enhance device efficiency and extend the operation wavelength range, we shifted our focus to electro-optically tunable metasurfaces based on the Pockels effect in barium titanate (BTO). Conventional bottom-up growth techniques typically result in BTO thin films with reduced electro-optic coefficients. To overcome this limitation, we developed a scalable and cost-effective fabrication method that relies on spalling single-crystal thin films from bulk substrates using a metal stressor layer. Using this approach, we successfully obtained mm-scale *a*-axis and *c*-axis thin films with thicknesses ranging from 100 nm to 15 μm . While stress-induced domain switching during spalling introduces surface roughness, we verified that the spalled thin films retain their bulk electro-optic properties. Ellipsometric Teng-Man measurements revealed a Pockels coefficient of $r_{33} = 55 \pm 5$ pm/V in multi-domain regions and $r_{33} = 160 \pm 40$ pm/V in smaller, likely single-domain regions, exceeding the performance of commercially available thin film lithium niobate.

Buidling on these material advancements, we then designed transmissive metasurfaces leveraging the bulk electro-optic properties of BTO. Our calculations indicate that, with an optimal crystal orientation and applied field configuration, index changes of up to 0.3 are attainable with applied fields around 0.3 MV/cm at visible wavelengths. Using this response, we simulated a transmissive metasurface operating at $\lambda = 628.7$ nm, achieving a phase modulation of 272.7° with an associated transmittance modulation from 50 – 97%. Using this design, we simulated beam steering up to $\pm 58^\circ$ with diffracted transmission efficiencies between 17 – 24%. Finally, leveraging the broad transparency window of BTO, we adapted this design for beam steering in transmission at RGB wavelengths.

To conclude, we outlined pathways toward the realization of a universal active metasurface, highlighting the need for advancements in materials, design methodologies, and scalable control architectures for two-dimensional wavefront shaping. We envision key research directions that include the discovery of low-loss, high-speed tunable materials, the development of unit cell designs that enable independent control over multiple properties of light, and the miniaturization of electrical control networks for large-scale metasurfaces. Addressing these challenges will require a multidisciplinary approach integrating nanophotonics, materials science, and computational design. Ultimately, the results presented in this thesis provide a foundation for realizing reprogrammable, intelligent optical systems that dynamically adapt to diverse technological demands in transformative applications.

ARRAY-LEVEL INVERSE DESIGN

A.1 Iterative genetic optimization

The following pages provide further details on the implementation and robustness of the results obtained with the iterative genetic optimization approach introduced in Chapter 2. We would like to note here that a variety of global optimization algorithms, including particle swarm optimization, simulated annealing, and others can be used for the purpose of array-level optimization.

Numerical framework

Figure A.1 shows a flowchart of the optimization approach implemented in our study using the global optimization toolbox on MATLAB R2018b. For beam steering, the input of the algorithm comprises of the steering angle θ_r , as well as the objective function $FOM(x, \varphi(V), A(V))$ that takes into account the tunable scattered light properties of the metasurface. Here, x is the 1D vector representing the array configuration that needs to be optimized. In addition, we define the following global variables: the total number of antennas N_{tot} , the number of optimization rounds r_{tot} , as well as an array containing the number of possible variables $nvars$ which are to be optimized in each iteration. For the active metasurface with 96 tunable antennas, $nvars$ is defined as [4, 8, 24, 48, 96] such that the optimal solution is found within a maximal number of five iterations.

The concept of iterative genetic optimization relies on an initially reduced search space. The algorithm aims to optimize for a sequence of small number of variables that are periodically repeated over the entire array. Once an optimal solution x_{opt} is found, $nvars$ is incrementally increased to the next value. An initialization with $k = nvars(i + 1)/nvars(i)$ repetitions of the current optimized solution x_{opt} guides the algorithm in larger solution domains. This procedure is repeated until all N_{tot} antennas are considered as free variables in the final iteration. Once $nvars(i) = N_{\text{tot}}$, the current optimization round is terminated and x_{opt} is stored along with its corresponding function value in an array. This iterative optimization process is repeated for r_{tot} rounds, after which the solution with the maximal f_{opt} is given as output. This step is necessary due to the stochastic nature of genetic optimization. Note that prior knowledge from blazed grating design allows us to make the algorithm

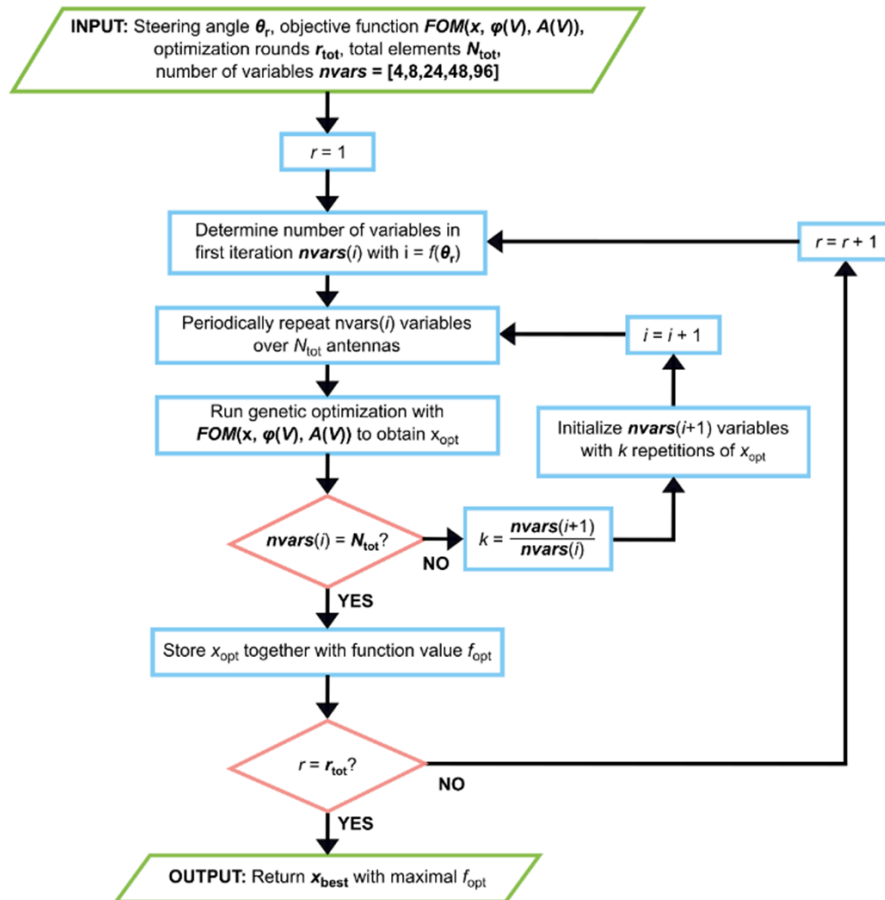


Figure A.1: **Flowchart of iterative genetic optimization for an array of $N_{tot} = 96$ antennas.** The inner loop represents the iterative genetic optimization with increasing number of optimization variables to approach the high dimensionality of the underlying optimization problem. The outer loop describes a series of optimization rounds that allow to take the optimal solution over multiple repetitions.

more efficient. The number of variables that are to be optimized in the first iteration can be determined as a function of the steering angle θ_r , using the grating equation defined in Eq. (2.3).

Optimization parameters

A matrix containing the metasurface-specific tunable phase-amplitude relation is provided as an input to the algorithm. Then, a discrete integer optimization is performed including the matrix rows (that define the scattered light response for various voltages). The lower and upper bounds are variable and define the first and last row of the matrix, respectively. The default creation, crossover, and mutation functions of discrete genetic optimization enforce each variable to be an integer, as

discussed in [338]. To accommodate for the large number of parameters that are to be optimized, the population size is increased to 200. The optimized results are obtained with a crossover fraction of 0.95 and an elite count of 20. Each iteration stops when the average change in the best function value over 250 generations is less than 10^{-6} .

Computational cost

In contrast to forward-designed array profiles that rely on an analytical equation (Eq. 2.3), the inverse design approach comes with enhanced computational cost due to a consideration of the antenna-specific functional response. For the problems analyzed in this work, the optimal solution in each iteration is reached within 200-600 generations. A single computation ($r_{\text{tot}} = 1$) for an iterative optimization of 96 variables performed on our workgroup computer (Intel Xeon E5-2687W processor, 20 cores) takes approximately 12 min.

The required computation time highly depends on the total number of variables that are to be optimized. Figure A.2 shows the average computation time with TOC_{avg} for a single iterative optimization round as a function of N_{tot} . The average time was evaluated over $r_{\text{tot}} = 10$ optimization rounds for six different angles ($\theta_r = 9.0^\circ, 10.9^\circ, 13.6^\circ, 18.3^\circ, 28.1^\circ, 70.7^\circ$). Notably, the computation time scales linearly as $O(N_{\text{tot}})$ in the investigated regimes while the solution space scales exponentially as $O(s^{N_{\text{tot}}})$ where s is the number of sampling points. For our study, the antenna-specific scattered light response was sampled at $s = 65$ discrete voltage points through full-wave simulations [42]. The difference in scaling is attributed to the stopping criteria: In the current implementation, the algorithm stops once the average change in best function value over 250 generations is less than 10^{-6} . As the most significant contribution of the directivity enhancement occurs for the initial optimization in a reduced solution domain, each subsequent iteration adds approximately 250 generations to the optimization process that result in minor performance enhancements. Therefore, a linear increase in computation time is observed. In future work, the stopping criteria can be optimized such that the computational cost is reduced without a significant loss in best performance.

Robustness of optimization algorithm

Genetic algorithms rely on a random initial population that contains possible solutions to a given problem. Selection procedures only permit survival of the best solutions to the next generation. Operators inspired by natural genetic variation

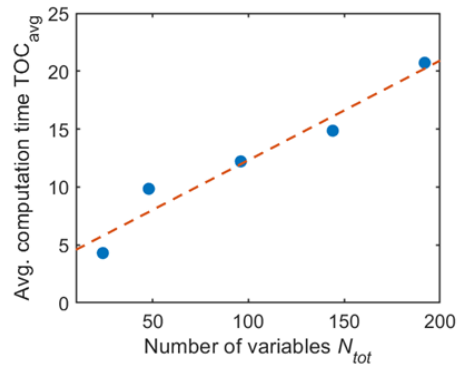


Figure A.2: **Average computation time TOC_{avg} as function of optimization variables N_{tot} .** Data points TOC_{avg} (blue) are obtained as a mean over $r_{tot} = 10$ optimization rounds and six different steering angles ($\theta_r = 9.0^\circ, 10.9^\circ, 13.6^\circ, 18.3^\circ, 28.1^\circ, 70.7^\circ$). The linear relation between TOC_{avg} and N_{tot} is illustrated with an orange dashed line.

(crossover and mutation) further introduce variability into population members. Due to the stochastic operations in genetic optimization, convergence characteristics differ between individual optimization rounds [71]. Thus, it is common practice to report the optimal solution as the one with maximal FOM over an extended dataset obtained over r_{tot} optimization rounds. To verify the robustness of the best result, we analyzed the distribution of the optimized directivity over $r_{tot} = 20$ optimization rounds. In addition, we perform a comparison of the distribution to two alternative optimization methods: a direct, non-iterative optimization of the entire antenna array with an initial guess based on linear phase profiles and a direct optimization without a user-defined initial guess. In the latter case, the algorithm generates a random initial solution to seed the algorithm. Figure A.3a shows the range of optimized directivities for the three analyzed methods for a steering angle of $\theta_r = 18.3^\circ$. In all three cases the beam directivity is strongly enhanced in comparison to forward designs. Direct optimization of 96 variables with an initial guess based on forward-designed linear phase profiles results in a maximal increase in directivity of 77% compared to the previously demonstrated stairstep forward design with $D_{forward} = 39.5$. Meanwhile, an increase of up to 80% is reported with a direct optimization using a randomly generated initial guess. In comparison, the iterative optimization approach which relies on an incremental increase of the solution space facilitates a maximal increase in directivity of up to 84%, as reported in Section 2.3. While the optimized directivity approaches similar values in all three cases, there is a distinct difference in the robustness of the final result. The direct optimization with an initial

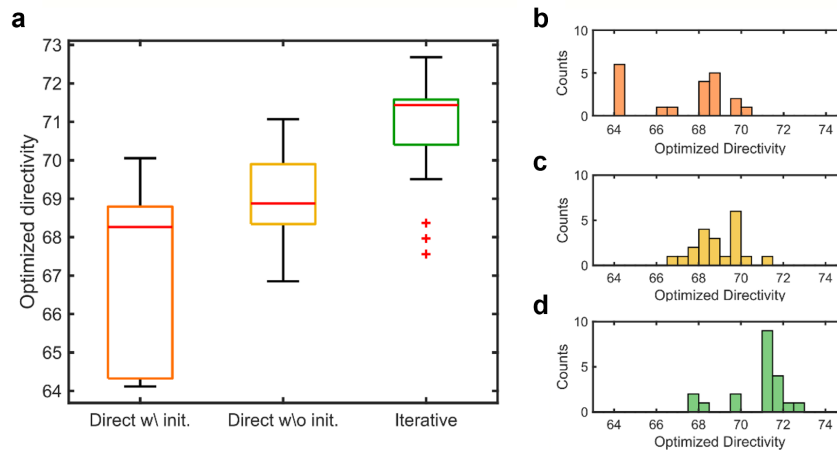


Figure A.3: **Robustness of optimization algorithm.** (a) Distribution of the optimized directivity over $r_{\text{tot}} = 20$ optimization rounds for a steering angle of $\theta_r = 18.3^\circ$. The results are illustrated for three different optimization methods: a direct, non-iterative optimization approach of the entire array with an initial guess based on forward-designed linear phase profiles (orange), a direct optimization without a user-defined initial guess (yellow), and an iterative optimization approach with an incremental increase of the solution space (green). The red horizontal line in the boxplot marks the median of the distribution, while the upper and lower edges of the box indicate the 25th and 75th percentile. The whiskers extend to the most extreme optimized directivity points that are not considered outliers and are marked in red crosses. Histograms of the optimized directivity distributions with a bin width of 0.5 are illustrated in (b), (c), and (d), respectively.

guess based on forward design drives the algorithm to similar local minima, as the forward designs do not account for the antenna-specific amplitude-phase correlation (Fig. A.3b). A subset of the solutions that can escape these local minima results in marginally higher directivities. By contrast, the direct optimization with a random initial guess (Fig. A.3c) leads to stronger directivity enhancements due to an unbiased and thus more extensive exploration space. Finally, the iterative approach relies on an optimization of the array profile in a reduced solution domain before passing the optimized result from the prior iteration as an initial guess to the next iteration. By doing so, this method ensures that the antenna-specific scattered light response is accounted for when supplying the algorithm with an initial solution in each iteration. As a result, higher directivities are obtained with increased robustness, as illustrated by the strongly increased median in the corresponding boxplot in Fig. A.3a. For the case studied here, 75% of the optimized performances lie within 3% of the maximal directivity $D_{\text{opt,iter}} = 72.7$ (Fig. A.3d).

A.2 Metasurface fabrication

To fabricate the metasurfaces used in Chapter 2 of this thesis, we followed the fabrication procedure for the ITO-based field-effect tunable metasurface by Kafaie Shirmanesh *et al.* [42]. First, we clean silicon (Si) substrates with a 1 μm thick silica (SiO_2) layer on top using standard cleaning processes. Then the outermost parts of the connection pads are patterned using photolithography. After developing the exposed photoresist, we deposit a 20 nm thick titanium (Ti) layer followed by a 200 nm thick gold (Au) layer *via* e-beam evaporation. The excess resist and the Ti/Au film are removed through a lift-off process in acetone. Then the Au back reflector is patterned using electron-beam lithography (EBL) [VISTEC EBPG 5000+] at an acceleration voltage of 100 keV after spinning an e-beam resist layer. The exposed e-beam resist layer is then developed and 3 nm of chromium (Cr) followed by an 80 nm-thick Au layer are deposited using an e-beam evaporator. In a next step, a 9.5 nm-thick alumina (Al_2O_3) layer is deposited on the samples through shadow mask *via* EBL. Once the exposed resist is developed, we sputter a 5 nm thick ITO layer *via* room-temperature RF magnetron sputtering. The deposition pressure is 3 mTorr and the applied RF power is 48 W. The plasma is struck by using argon (Ar) gas with a flow rate of 20 sccm, and argon/oxygen gas (Ar/O_2 :90/10) with a tunable flow rate is used to control the carrier concentration of the deposited layer [53]. After lifting off the excess e-beam resist and films, the contact pads of the ITO layer are patterned *via* EBL followed by a deposition of a Ti/Au film (20 nm/200 nm) using an e-beam evaporator. We then deposit the hafnium oxide/aluminum oxide laminate (HAOL) gate dielectric layer through shadow masks by ALD [53]. In the next step, the nanoantennas as well as the inner contact lines are patterned on the sample using EBL. After developing the exposed e-beam resist, a 2 nm-thick germanium (Ge) layer followed by a 40 nm thick Au layer is deposited on the sample using an e-beam evaporator. Once the lift-off process is done, a 60 nm thick SiO_2 layer is deposited as the top coat through shadow mask *via* e-beam evaporation. Finally, 96 metasurface element pads and 4 ITO pads are wire-bonded from the sample to 100 conducting pads on a sample mounting printed circuit board (PCB) which itself is controlled by using a voltage-driving PCB [42].

A.3 Experimental setup for phase and amplitude measurements

To characterize the tunable optical response of the fabricated beam steering metasurface, we measured the spectra of the reflected light amplitude (reflectance) and phase under different applied biases. Figure A.4 shows the optical setup used to

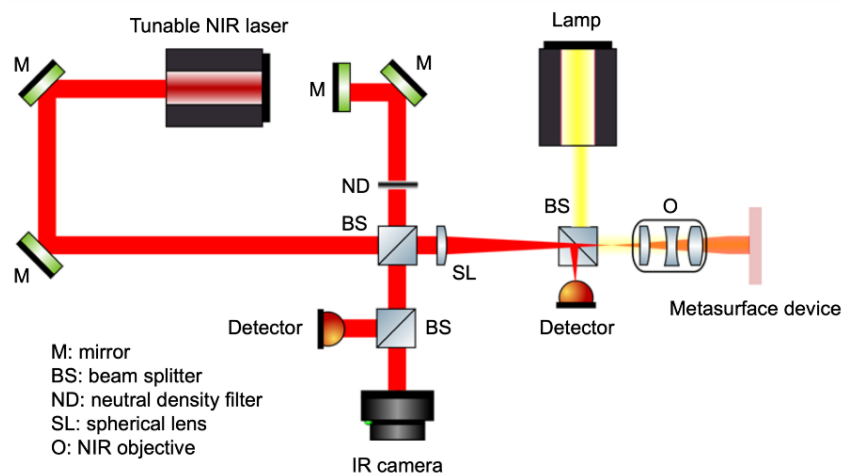


Figure A.4: **Optical setup for amplitude, phase and beam steering measurements.** The metasurface sample is illuminated by a tunable NIR laser. The reflected beam from the metasurface is directed to a detector (amplitude measurement) and an IR camera (phase and beam steering measurements). The incident beam is also guided to the IR camera to be used as a reference for generation of the interference fringe patterns.

measure the phase shift as well as the reflectance modulation provided by the metasurface. In order to measure the phase of the light reflected from the metasurface, the metasurface is illuminated by a tunable NIR laser which is focused on the sample by an objective with a long working distance (Mitutoyo M Plan Apo 20x, NA = 0.40, WD = 20 mm) after passing through a polarizer. The reflection from the metasurface as well as the incident laser beam (to serve as a reference beam) are then directed to an infrared (IR) camera, creating interference fringe patterns. The incident laser beam is focused on the edge of the metasurface nanoantenna array. As a result, the scattered beam is reflected partly from the metasurface and partly from the Au backplane. This results in a lateral shift in the interference fringe patterns of the metasurface and the backplane when the applied bias is changed. We then fit these two cross-sections to sinusoidal functions and obtain the relative delay between the fitted sinusoidal curves when changing the applied voltage. The phase shift acquired due to the applied bias is then retrieved [53]. In the next step, to measure the reflectance, the surface of the metasurface is illuminated by the NIR laser beam. Then, the beam reflected from the metasurface is guided to a spectrometer and the reflectance is calculated as

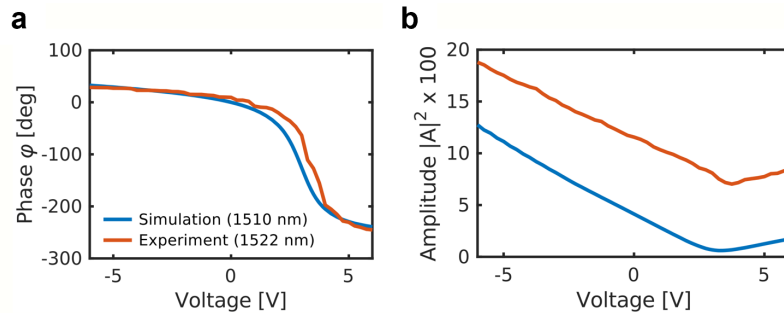


Figure A.5: **Comparison of simulated and experimentally measured optical response of ITO metasurface.** (a) Phase shift and (b) reflectance for field-effect tunable metasurface introduced in [42] obtained through full-wave simulations ($\lambda = 1510$ nm) and experiments ($\lambda = 1522$ nm).

$$\text{Reflectance [\%]} = 100 \times \frac{R_{\text{MTS}} - R_{\text{dark}}}{R_{\text{reference}} - R_{\text{dark}}} \quad (\text{A.1})$$

where R_{MTS} , $R_{\text{reference}}$, and R_{dark} are the raw reflectance from the metasurface sample, a mirror and the background, respectively.

A.4 Analytical model accounting for experimental artifacts

Here, we discuss the changes that are made to the analytical model to reproduce experimentally measured beam steering radiation patterns. The data is based on simulations and experiments performed by Kafaie Shirmanesh *et al.* [42]. Figure A.5 shows a comparison of the simulated and experimentally measured phase and reflectance data. While the measured phase shift closely matches the simulated response, the experimentally measured reflectance R_{meas} is increased by an offset of approximately 7%. This increase is attributed to a misalignment between the incident light polarization and the antenna, leading to enhanced specular reflection. In addition, the misaligned component of the incident light does not contribute to the phase accumulation and hence cannot be considered for optimization of the beam directivity. Therefore, we model the actual reflectance of the metasurface R_{actual} as $R_{\text{meas}} - \Delta_r$ with Δ_r being a constant value that is determined as an average difference in reflectance over the applied bias range. To account for this change, the intensity at 0° is increased by Δ_r .

Using the approximated reflectance of the metasurface, we computed the far-field radiation patterns for forward-designed four-level stairstep phase profiles. Figure A.6 shows a comparison of the analytically predicted far-field radiation pattern to the

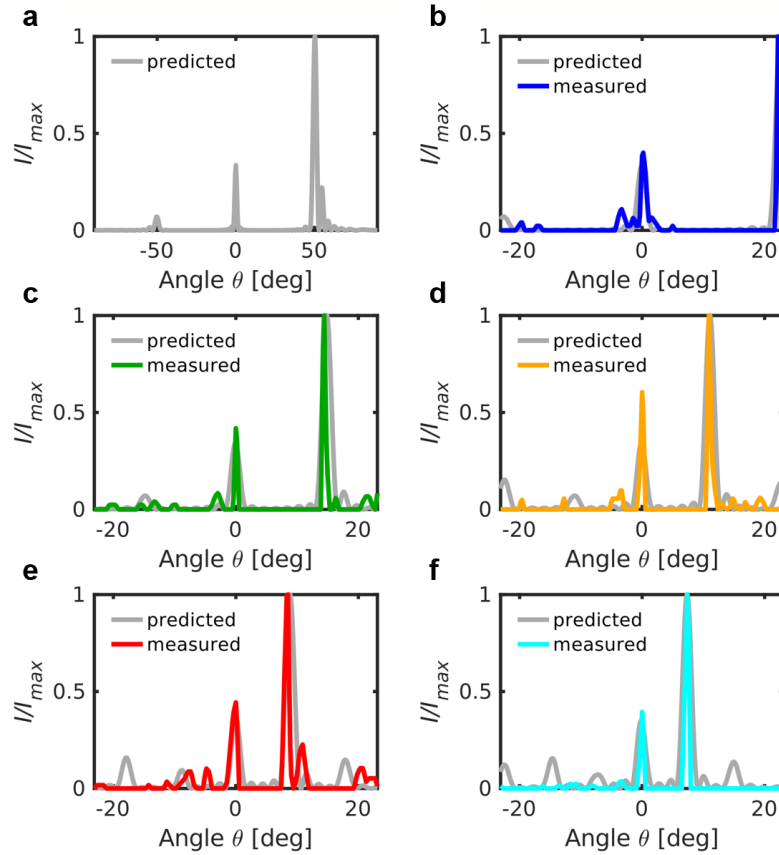


Figure A.6: **Predicted and measured far-field radiation patterns with adapted model.** Analytically computed (gray) and experimentally measured (colored) normalized intensity I/I_{\max} vs polar angle θ for forward-designed staircase phase profiles with repetition numbers of (a) RN = 1, (b) RN = 2, (c) RN = 3, (d) RN = 4, (e), RN = 5, (f) RN = 6. The operational wavelength is $\lambda = 1522\text{nm}$.

experimentally measured beam steering performance for repetition numbers varying from RN = 1 to 6. We would like to note that in addition to the altered reflectance values, we also consider a continuously varying change in the characteristic pitch size of the metasurface from 490 nm – 510 nm, with the largest pitch size being at the center of the metasurface. By doing so, we are able to obtain an excellent match between the analytically predicted and experimentally measured beam steering performance. Small discrepancies in the sidelobe intensity are attributed to the fact that the adapted model is purely based on an approximate reflectance response of the metasurface. We further remark that due to the limited detectable angular range in our experimental setup, beam steering measurements could not be performed for RN = 1.

Appendix B

SPACE-TIME MODULATED METASURFACES

B.1 Active metasurface phase measurements

Figure B.1 plots the maximum phase shift achieved by our active metasurface as a function of wavelength. The largest phase shift occurs between 1465 nm and 1470 nm, corresponding to the minimum reflectance measured in Fig. 3.3d. The phase shift of this device at the design wavelength for this work (1530 nm) is near-zero ($< 20^\circ$). While there is larger amplitude and phase modulation at shorter wavelengths (~ 1470 nm), we chose to work at 1530 nm because it is the shortest wavelength we could access with sufficient power in our experimental setup. This work could be repeated closer to resonance using the same principles discussed here and the final results would be identical, but the overall efficiency of the device would be higher. Specifically, there would be a higher ratio of total modulated light to unmodulated light. However, since our measurement technique already filters out unmodulated light, in this work we are still able to show the same principles of space-time modulation and engineer the power sent to each modulated frequency with good signal-to-noise ratio (SNR).

It is noteworthy that this work demonstrates space-time diffraction with excellent directivity at each modulated frequency using a device with such limited reflectance and phase modulation. If this device was modulated in the quasi-static regime, it would exhibit very low diffraction efficiency. By using space-time modulation, roughly the same total amount of light is diffracted as in the quasi-static case, but the light sent to the $\pm 1^{\text{st}}$ orders are separated in frequency from the 0^{th} order (normally reflected light) which allows for easier detection with high SNR. This is a major benefit of space-time metasurfaces.

B.2 Waveform optimization based on quasi-static metasurface response

In Section 3.3, we discussed how a real-time optimized waveform can be used to generate desired frequency spectra. An alternative approach would be to use the quasi-static metasurface response and perform an analytical optimization to design tailored waveforms. This method follows a similar principal to the optimization techniques introduced in Chapter 2, but instead of optimizing in the spatial domain, we optimize the covarying amplitude and phase in time.

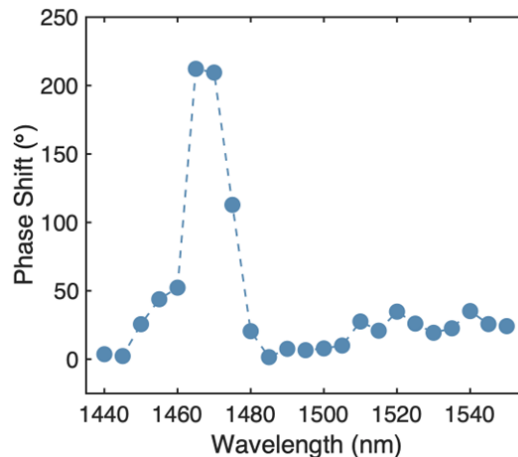


Figure B.1: **Quasi-static phase shift of two-electrode active metasurface.** The plotted phase shift is the absolute value of the change in phase between an applied bias of -6 V and 6 V.

To formulate the waveform, we express it as a polynomial function $V(t) = \sum_n a_n \cdot t^{n-1}$ where $n - 1$ represents the degree of the polynomial. The optimization minimizes a figure of merit (FOM) defined as $2 \cdot \sum_i p_i / p_1 + \text{mean}(V(t))$, where p_i is the power at the i -th harmonic. Initial optimizations with varying polynomial degrees indicate that a 7-th degree polynomial results in the highest ratio between the +1st and 0th harmonic while maintaining minimal mean voltage. It is desirable to maintain a mean voltage close to 0 V to avoid accumulation of charge carriers in the ITO layer over time. We additionally impose a constraint to have equal values at the beginning and end of a waveform period, preventing sudden voltage jumps that would be challenging to realize at high frequencies.

For illustration, we performed an optimization for a metasurface operating at 1555 nm using its quasi-static reflectance and phase response (Fig. B.2a). The resulting optimized waveform is given by

$$V(t) = 1.6 + 1.4 \cdot t - 8.4 \cdot t^2 - 2.3 \cdot t^3 + 3.4 \cdot t^4 - 9.9 \cdot t^5 + 6.4 \cdot t^6 + 9.4 \cdot t^7. \quad (\text{B.1})$$

The mean voltage of this waveform (Fig. B.2b) is 0.1176 V, while the suppression ratio of p_1/p_0 is 19.96 (Fig. B.2c).

Despite the high suppression ratio predicted in calculations, experimental results using a 10 kHz waveform did not exhibit suppression of the unmodulated, specularly

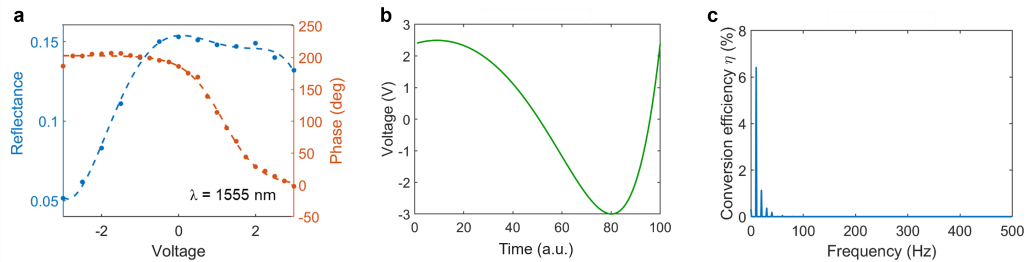


Figure B.2: Polynomial waveform optimization based on quasi-static response. (a) Experimentally measured quasi-static reflectance and phase response (points) and fits to experimental data (dashed) used for optimization. (b) Optimized polynomial voltage waveform as function of time. The time-axis is labeled in arbitrary units as the 100 points can be spaced apart at desired increments to obtain target frequencies. (c) Conversion efficiency as function of frequency for optimized waveform at 10 Hz.

reflected light. This discrepancy suggests that the reflectance and phase response of the metasurface in the quasi-static regime differ from those attainable at high frequencies. While high-frequency reflectance can be measured using an oscilloscope, alternative techniques are required to accurately characterize the phase response at target modulation frequencies. To address this limitation, we integrated a real-time optimization algorithm in our experimental setup, as shown in Fig. 3.4. Although real-time optimization requires longer processing times due to iterative measurements, it enables significantly improved performance for a variety of target frequency spectra [95].

BARIUM TITANATE-BASED ACTIVE METASURFACES

C.1 XRD scans for bulk substrates and spalled film

Commercially bought BTO substrates [339] were produced via top-seeded solution growth and were single-crystalline with multiple domains. We confirmed the single-crystallinity of bulk substrates and spalled films through $\theta - 2\theta$ x-ray diffraction (XRD) scans. As shown in Fig. C.1, the prominent peaks for both the bulk substrate and spalled thin film correspond to the (001) and (100) orientations, along with their higher-order diffractions. These peaks arise due to the multi-domain nature of the substrates and films, combined with the millimeter-scale x-ray probing spot. To probe the domain structure at a finer scale, we employed electron backscatter diffraction (EBSD), as discussed in Fig. 4.3. Similar results were obtained for (100)-oriented crystals.

Figure C.1b shows the $\theta - 2\theta$ scan for a thin film spalled from a (001)-oriented single-crystal. The reduced intensity observed for the thin film is primarily attributed to its surface roughness and reduced thickness. In addition to the signal from BTO, we also measure a minimal contribution from the underlying Ni layer due to the size and position of the x-ray probing spot relative to the spalled film area.

C.2 Reusability of single-crystal BTO substrates through repolishing

One major advantage of spalling compared to alternative growth techniques is the ability to reuse bulk substrates by introducing a polishing step between spalls. Considering that the substrates are typically 0.5 – 1 mm thick, and each iteration removes less than 50 μm of material thickness, the effective cost of a spall can be lowered up to 20-fold, bringing the expense down to tens of dollars per square centimeter.

In this study, various polishing procedures were tested and the RMS roughness r of each was compared to that of as-bought substrates. Figure C.2a shows an AFM scan of an as-bought substrate with $r = 5.9$ nm. Hand polishing of BTO substrates yields planarized surfaces but results in a significantly higher RMS roughness of $r = 66.4$ nm. While spalls can still be performed with this level of roughness, it is insufficient for many applications.

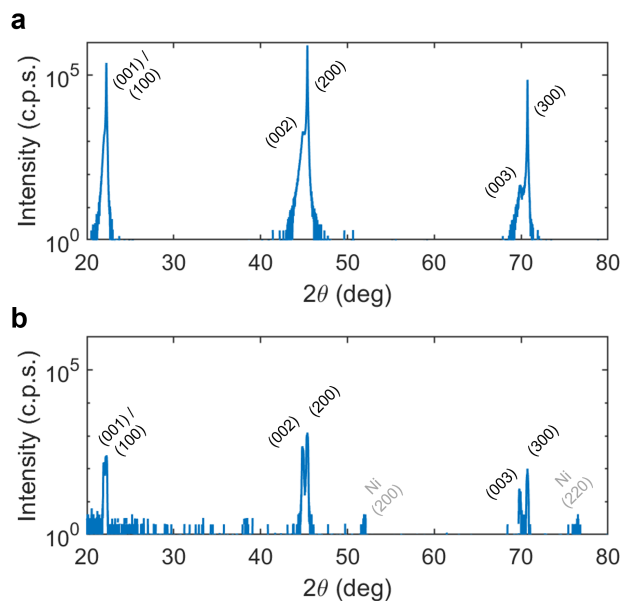


Figure C.1: **XRD data for (001)-oriented bulk substrate and spalled thin film.** $\theta - 2\theta$ scan for (a) bare bulk substrate and (b) spalled thin film on a Ti/Au seed layer and electroplated Ni. BTO diffraction orders corresponding to various crystal orientations are labeled in both figures, Ni diffraction orders are indicated in gray in (b).

To address this, we explored vibration polishing using a slurry of silica (SiO_2) or alumina (Al_2O_3) nanoparticles, which significantly reduce surface roughness. Figures C.2b and c show AFM scans of the BTO substrate after vibration polishing with 60 nm-sized SiO_2 particles for 7 hours and 50 nm-sized Al_2O_3 particles for 3 hours, respectively. The resulting RMS roughness values were $r = 27.2$ nm and $r = 9.4$ nm. The stronger reduction in surface roughness achieved with Al_2O_3 particles is attributed to their higher material hardness relative to BTO.

It is important to note that while vibration polishing does not planarize the substrate, it effectively restores surface roughness to near-initial levels, enabling large-scale spalls suitable for device integration, as shown in Fig. 4.1b.

C.3 Surface quality of (100) and (001)-oriented bulk substrates

Commercially bought single crystal BTO substrates [339] are produced using top-seeded solution growth (TSSG). This process involves growing boules from molten solutions at elevated temperatures. During this process, the controlled cooling and crystallization of the molten material enable the formation of high-quality

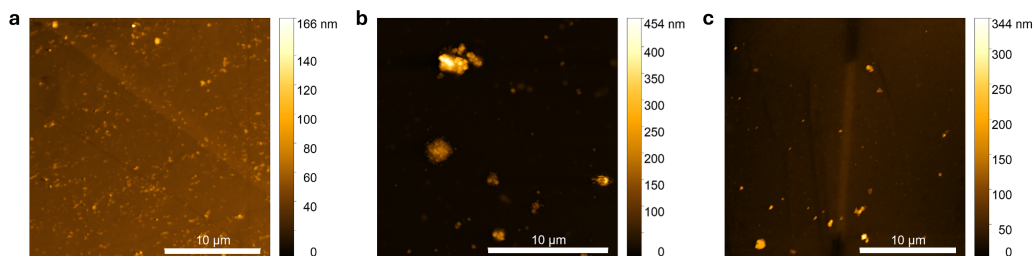


Figure C.2: **AFM scans of BTO substrate as-bought vs polished after spalling.** (a) As-bought BTO substrate, (b) as-bought BTO substrate, vibration polished with 60 nm-sized SiO_2 particles for 7 hours, (c) BTO substrate post-spall, vibration polished with 50 nm-sized Al_2O_3 particles for 3 hours. Scale bars: 10 μm .

single crystals [340]. After the boule is formed, sections of it are cut and polished to create substrates. These substrates are typically multidomain in nature, with distinct regions corresponding to different orientations of the polar axis (spontaneous polarization).

This multidomain structure forms as BTO undergoes a structural phase transition from the cubic to tetragonal phase upon cooling below its Curie temperature. This transition generates spontaneous polarization, with the formation of domains being influenced by various factors such as the cooling rate, internal and external stresses, and thermal gradients during TSSG [341]. These conditions lead to the formation of 90° and 180° domain walls, which separate regions with differing polarization orientations. Further details on the domain structure of BTO can be found in Refs. [341–345].

We note significant differences in the bulk substrate quality between (100)- and (001)-oriented crystals, as illustrated in Fig. C.3. The (100)-oriented substrates feature prominent 90° domain patterns and finer surface ridges (domain bundles). In contrast, (001)-oriented substrates exhibit a more uniform appearance with fewer domain boundaries. This discrepancy likely arises from the anisotropic strain in the in-plane directions of a -axis crystals during cooling, which promotes the formation of additional domain walls. The higher domain density in (100)-oriented substrates results in increased surface roughness. The elevated roughness carries over to spalled thin films, leading to a more irregular topography. By contrast, the smoother surface of (001)-oriented substrates yields spalled films with more controllable and uniform surface properties.

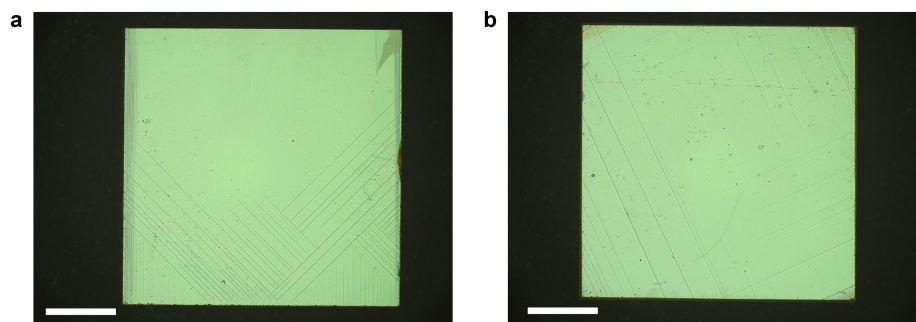


Figure C.3: **Single crystal BTO substrates with domains.** Optical microscope image of (a) (100)-oriented single crystal substrate with domains, and (b) (001)-oriented single crystal substrate with domains. Scale bar: 2.5 mm.

BIBLIOGRAPHY

1. Saleh, M. *et al.* *The Egyptian Museum, Cairo: Official Catalogue* (1987).
2. Enoch, J. M. First known lenses originating in Egypt about 4600 years ago. *Documenta ophthalmologica* **99**, 303 (1999).
3. McManamon, P. *et al.* Optical phased array technology. *Proceedings of the IEEE* **84**, 268–298. ISSN: 1558-2256 (Feb. 1996).
4. Doylend, J. K. *et al.* Two-dimensional free-space beam steering with an optical phased array on silicon-on-insulator. *Optics Express* **19**, 21595. ISSN: 1094-4087 (Oct. 2011).
5. Sun, J., Timurdogan, E., Yaacobi, A., Hosseini, E. S. & Watts, M. R. Large-scale nanophotonic phased array. *Nature* **493**, 195–199. ISSN: 1476-4687 (Jan. 2013).
6. Witzens, J. High-speed silicon photonics modulators. *Proceedings of the IEEE* **106**, 2158–2182. ISSN: 1558-2256 (Dec. 2018).
7. Aflatouni, F., Abiri, B., Rekhi, A. & Hajimiri, A. Nanophotonic projection system. *Optics Express* **23**, 21012. ISSN: 1094-4087 (Aug. 2015).
8. Hsu, C.-P. *et al.* A review and perspective on optical phased array for automotive LiDAR. *IEEE Journal of Selected Topics in Quantum Electronics* **27**, 1–16. ISSN: 1558-4542 (Jan. 2021).
9. Phare, C. T., Shin, M. C., Miller, S. A., Stern, B. & Lipson, M. Silicon optical phased array with high-efficiency beam formation over 180 degree field of view. *arXiv:1802.04624 [physics.app-ph]* (2018).
10. Poulton, C. V. *et al.* Long-range LiDAR and free-space data communication with high-performance optical phased arrays. *IEEE Journal of Selected Topics in Quantum Electronics* **25**, 1–8. ISSN: 1558-4542 (Sept. 2019).
11. Sharma, A. *et al.* Optimization of a programmable $\lambda/2$ -pitch optical phased array. *Nanophotonics* **13**, 2241–2249. ISSN: 2192-8614 (Mar. 2024).
12. Hutchison, D. N. *et al.* High-resolution aliasing-free optical beam steering. *Optica* **3**, 887. ISSN: 2334-2536 (Aug. 2016).
13. Fatemi, R., Khachaturian, A. & Hajimiri, A. A nonuniform sparse 2-D large-FOV optical phased array with a low-power PWM drive. *IEEE Journal of Solid-State Circuits* **54**, 1200–1215. ISSN: 1558-173X (May 2019).
14. Neff, J., Athale, R. & Lee, S. Two-dimensional spatial light modulators: A tutorial. *Proceedings of the IEEE* **78**, 826–855. ISSN: 0018-9219 (May 1990).

15. Takekawa, Y., Takashima, Y. & Takaki, Y. Holographic display having a wide viewing zone using a MEMS SLM without pixel pitch reduction. *Optics Express* **28**, 7392. ISSN: 1094-4087 (Feb. 2020).
16. Lazarev, G., Hermerschmidt, A., Krüger, S. & Osten, S. LCOS spatial light modulators: Trends and applications. *Optical Imaging and Metrology*, 1–29 (Aug. 2012).
17. Gong, C. (Invited) The journey of the DMD pixel design evolution. *ECS Transactions* **60**, 1141–1146. ISSN: 1938-6737 (Feb. 2014).
18. Zhu, Z. *et al.* Metasurface-enabled polarization-independent LCoS spatial light modulator for 4K resolution and beyond. *Light: Science & Applications* **12**. ISSN: 2047-7538 (June 2023).
19. Mansha, S. *et al.* High resolution multispectral spatial light modulators based on tunable Fabry-Perot nanocavities. *Light: Science & Applications* **11**. ISSN: 2047-7538 (May 2022).
20. Li, S.-Q. *et al.* Phase-only transmissive spatial light modulator based on tunable dielectric metasurface. *Science* **364**, 1087–1090. ISSN: 1095-9203 (June 2019).
21. Kuznetsov, A. I. *et al.* Roadmap for optical metasurfaces. *ACS Photonics* **11**, 816–865. ISSN: 2330-4022 (Feb. 2024).
22. Yu, N. & Capasso, F. Flat optics with designer metasurfaces. *Nature Materials* **13**, 139–150. ISSN: 1476-4660 (Jan. 2014).
23. Sun, S. *et al.* High-efficiency broadband anomalous reflection by gradient meta-surfaces. *Nano Letters* **12**, 6223–6229. ISSN: 1530-6992 (Dec. 2012).
24. Dorrah, A. H., Rubin, N. A., Zaidi, A., Tamagnone, M. & Capasso, F. Meta-surface optics for on-demand polarization transformations along the optical path. *Nature Photonics* **15**, 287–296. ISSN: 1749-4893 (Jan. 2021).
25. Paniagua-Domínguez, R. *et al.* A metalens with a near-unity numerical aperture. *Nano Letters* **18**, 2124–2132. ISSN: 1530-6992 (Feb. 2018).
26. Lalanne, P., Astilean, S., Chavel, P., Cambriel, E. & Launois, H. Blazed binary subwavelength gratings with efficiencies larger than those of conventional échelette gratings. *Optics Letters* **23**, 1081. ISSN: 1539-4794 (July 1998).
27. Lin, D., Fan, P., Hasman, E. & Brongersma, M. L. Dielectric gradient meta-surface optical elements. *Science* **345**, 298–302. ISSN: 1095-9203 (July 2014).
28. Wang, S. *et al.* Broadband achromatic optical metasurface devices. *Nature Communications* **8**. ISSN: 2041-1723 (Aug. 2017).
29. Arbabi, A., Horie, Y., Bagheri, M. & Faraon, A. Dielectric metasurfaces for complete control of phase and polarization with subwavelength spatial resolution and high transmission. *Nature Nanotechnology* **10**, 937–943. ISSN: 1748-3395 (Aug. 2015).

30. Huang, Y.-W. *et al.* Gate-tunable conducting oxide metasurfaces. *Nano Letters* **16**, 5319–5325. ISSN: 1530-6992 (Sept. 2016).
31. Benea-Chelmus, I.-C. *et al.* Gigahertz free-space electro-optic modulators based on Mie resonances. *Nature Communications* **13**. ISSN: 2041-1723 (June 2022).
32. Lewi, T., Evans, H. A., Butakov, N. A. & Schuller, J. A. Ultrawide thermo-optic tuning of PbTe meta-atoms. *Nano Letters* **17**, 3940–3945. ISSN: 1530-6992 (June 2017).
33. Thyagarajan, K., Sokhoyan, R., Zornberg, L. & Atwater, H. A. Millivolt modulation of plasmonic metasurface optical response via ionic conductance. *Advanced Materials* **29**. ISSN: 1521-4095 (June 2017).
34. Kim, Y. *et al.* Phase modulation with electrically tunable vanadium dioxide phase-change metasurfaces. *Nano Letters* **19**, 3961–3968. ISSN: 1530-6992 (May 2019).
35. Komar, A. *et al.* Dynamic beam switching by liquid crystal tunable dielectric metasurfaces. *ACS Photonics* **5**, 1742–1748. ISSN: 2330-4022 (Feb. 2018).
36. Shcherbakov, M. R. *et al.* Ultrafast all-optical tuning of direct-gap semiconductor metasurfaces. *Nature Communications* **8**. ISSN: 2041-1723 (May 2017).
37. Ou, J.-Y., Plum, E., Zhang, J. & Zheludev, N. I. An electromechanically reconfigurable plasmonic metamaterial operating in the near-infrared. *Nature Nanotechnology* **8**, 252–255. ISSN: 1748-3395 (Mar. 2013).
38. Arbabi, E. *et al.* MEMS-tunable dielectric metasurface lens. *Nature Communications* **9**. ISSN: 2041-1723 (Feb. 2018).
39. Ju, L. *et al.* Graphene plasmonics for tunable terahertz metamaterials. *Nature Nanotechnology* **6**, 630–634. ISSN: 1748-3395 (Sept. 2011).
40. Li, J., Chen, Y., Hu, Y., Duan, H. & Liu, N. Magnesium-based metasurfaces for dual-function switching between dynamic holography and dynamic color display. *ACS Nano* **14**, 7892–7898. ISSN: 1936-086X (Apr. 2020).
41. Chu, C. H. *et al.* Active dielectric metasurface based on phase-change medium. *Laser & Photonics Reviews* **10**, 986–994. ISSN: 1863-8899 (Oct. 2016).
42. Shirmanesh, G. K., Sokhoyan, R., Wu, P. C. & Atwater, H. A. Electro-optically tunable multifunctional metasurfaces. *ACS Nano* **14**, 6912–6920. ISSN: 1936-086X (Apr. 2020).
43. Salary, M. M., Farazi, S. & Mosallaei, H. A dynamically modulated all-dielectric metasurface doublet for directional harmonic generation and manipulation in transmission. *Advanced Optical Materials* **7**. ISSN: 2195-1071 (Sept. 2019).

44. Shaltout, A., Kildishev, A. & Shalaev, V. Time-varying metasurfaces and Lorentz non-reciprocity. *Optical Materials Express* **5**, 2459. ISSN: 2159-3930 (Oct. 2015).
45. Ishio, H., Minowa, J. & Nosu, K. Review and status of wavelength-division-multiplexing technology and its application. *Journal of Lightwave Technology* **2**, 448–463. ISSN: 0733-8724 (1984).
46. Thureja, P. *et al.* Array-level inverse design of beam steering active metasurfaces. *ACS Nano* **14**, 15042–15055. ISSN: 1936-086X (Oct. 2020).
47. Schwarz, B. Mapping the world in 3D. *Nature Photonics* **4**, 429–430. ISSN: 1749-4893 (July 2010).
48. Feng, F., White, I. H. & Wilkinson, T. D. Free space communications with beam steering a two-electrode tapered laser diode using liquid-crystal SLM. *Journal of Lightwave Technology* **31**, 2001–2007. ISSN: 1558-2213 (June 2013).
49. Yu, N. *et al.* Flat optics: Controlling wavefronts with optical antenna metasurfaces. *IEEE Journal of Selected Topics in Quantum Electronics* **19**, 4700423–4700423. ISSN: 1558-4542 (May 2013).
50. Yaacobi, A. *et al.* Integrated phased array for wide-angle beam steering. *Optics Letters* **39**, 4575. ISSN: 1539-4794 (July 2014).
51. Yu, N. *et al.* Light propagation with phase discontinuities: Generalized laws of reflection and refraction. *Science* **334**, 333–337. ISSN: 1095-9203 (Oct. 2011).
52. Shalaev, M. I. *et al.* High-efficiency all-dielectric metasurfaces for ultracompact beam manipulation in transmission mode. *Nano Letters* **15**, 6261–6266. ISSN: 1530-6992 (Aug. 2015).
53. Kafaie Shirmanesh, G., Sokhoyan, R., Pala, R. A. & Atwater, H. A. Dual-gated active metasurface at 1550 nm with wide (300°) phase tunability. *Nano Letters* **18**, 2957–2963. ISSN: 1530-6992 (Mar. 2018).
54. Han, S. *et al.* Complete complex amplitude modulation with electronically tunable graphene plasmonic metamolecules. *ACS Nano* **14**, 1166–1175. ISSN: 1936-086X (Jan. 2020).
55. Sell, D., Yang, J., Doshay, S., Yang, R. & Fan, J. A. Large-angle, multifunctional metagratings based on freeform multimode geometries. *Nano Letters* **17**, 3752–3757. ISSN: 1530-6992 (May 2017).
56. Pestourie, R. *et al.* Inverse design of large-area metasurfaces. *Optics Express* **26**, 33732. ISSN: 1094-4087 (Dec. 2018).
57. Molesky, S. *et al.* Inverse design in nanophotonics. *Nature Photonics* **12**, 659–670. ISSN: 1749-4893 (Oct. 2018).

58. Jafar-Zanjani, S., Inampudi, S. & Mosallaei, H. Adaptive genetic algorithm for optical metasurfaces design. *Scientific Reports* **8**. ISSN: 2045-2322 (July 2018).
59. Inampudi, S. & Mosallaei, H. Neural network based design of metagratings. *Applied Physics Letters* **112**. ISSN: 1077-3118 (June 2018).
60. Kudyshev, Z. A., Kildishev, A. V., Shalaev, V. M. & Boltasseva, A. Machine-learning-assisted metasurface design for high-efficiency thermal emitter optimization. *Applied Physics Reviews* **7**. ISSN: 1931-9401 (May 2020).
61. Egorov, V., Eitan, M. & Scheuer, J. Genetically optimized all-dielectric metasurfaces. *Optics Express* **25**, 2583. ISSN: 1094-4087 (Feb. 2017).
62. Jiang, J. & Fan, J. A. Global optimization of dielectric metasurfaces using a physics-driven neural network. *Nano Letters* **19**, 5366–5372. ISSN: 1530-6992 (July 2019).
63. Elsayw, M. M. R. *et al.* Global optimization of metasurface designs using statistical learning methods. *Scientific Reports* **9**. ISSN: 2045-2322 (Nov. 2019).
64. Chung, H. & Miller, O. D. Tunable metasurface inverse design for 80% switching efficiencies and 144° angular deflection. *ACS Photonics* **7**, 2236–2243. ISSN: 2330-4022 (July 2020).
65. Balanis, C. A. *Antenna theory. Analysis and design* 3. ed. 1117 pp. ISBN: 9780471667827 (Wiley-Interscience, Hoboken, N.J., 2005).
66. Hansen, R. C. *Phased array antennas* 2nd ed. 1547 pp. ISBN: 9780470529188 (Wiley, Hoboken, N.J., 2009).
67. Feigenbaum, E., Diest, K. & Atwater, H. A. Unity-order index change in transparent conducting oxides at visible frequencies. *Nano Letters* **10**, 2111–2116. ISSN: 1530-6992 (May 2010).
68. Dionne, J. A., Diest, K., Sweatlock, L. A. & Atwater, H. A. PlasMOSstor: A metal-oxide-Si field effect plasmonic modulator. *Nano Letters* **9**, 897–902. ISSN: 1530-6992 (Jan. 2009).
69. Forouzmand, A. *et al.* Tunable all-dielectric metasurface for phase modulation of the reflected and transmitted light via permittivity tuning of indium tin oxide. *Nanophotonics* **8**, 415–427. ISSN: 2192-8606 (Jan. 2019).
70. Goldberg, D. E. *Genetic algorithms in search, optimization, and machine learning* (ed Goldberg, D. E.) 412 pp. ISBN: 9780201157673 (Addison-Wesley, Boston, 2012).
71. Johnson, J. & Rahmat-Samii, V. Genetic algorithms in engineering electromagnetics. *IEEE Antennas and Propagation Magazine* **39**, 7–21. ISSN: 1045-9243 (1997).

72. Mishra, S., Yadav, R. N. & Singh, R. P. Directivity estimations for short dipole antenna arrays using radial basis function neural networks. *IEEE Antennas and Wireless Propagation Letters* **14**, 1219–1222. ISSN: 1548-5757 (2015).
73. Saleem, S. S., Ahmed, M. M., Rafique, U. & Ahmed, U. F. Optimization of linear antenna array for low SLL and high directivity. *19th International Multi-Topic Conference (INMIC)* (Dec. 2016).
74. Sokhoyan, R., Thureja, P., Sisler, J., Grajower, M., Shayegan, K., Feigenbaum, E., Elhadj, S. & Atwater, H. A. Electrically tunable conducting oxide metasurfaces for high power applications. *Nanophotonics* **12**, 239–253. ISSN: 2192-8614 (Jan. 2023).
75. Wu, P. C. *et al.* Dynamic beam steering with all-dielectric electro-optic III–V multiple-quantum-well metasurfaces. *Nature Communications* **10**. ISSN: 2041-1723 (Aug. 2019).
76. Belleville, J., Thureja, P. & Atwater, H. A. Active metasurface designs for lensless and detector-limited imaging. *Nanophotonics* (2025).
77. Malek, S. C., Overvig, A. C., Shrestha, S. & Yu, N. Active nonlocal metasurfaces. *Nanophotonics* **10**, 655–665. ISSN: 2192-8606 (Sept. 2020).
78. Shastri, K. & Monticone, F. Nonlocal flat optics. *Nature Photonics* **17**, 36–47. ISSN: 1749-4893 (Dec. 2022).
79. Malek, S. C., Overvig, A. C., Alù, A. & Yu, N. Multifunctional resonant wavefront-shaping meta-optics based on multilayer and multi-perturbation nonlocal metasurfaces. *Light: Science & Applications* **11**. ISSN: 2047-7538 (Aug. 2022).
80. Sokhoyan, R., Hail, C. U., Foley, M., Grajower, M. Y. & Atwater, H. A. All-dielectric high-Q dynamically tunable transmissive metasurfaces. *Laser & Photonics Reviews* **18**. ISSN: 1863-8899 (Feb. 2024).
81. Chakraborty, R. D. *et al.* Optical properties of electrochemically gated $\text{La}_{1-x}\text{Sr}_x\text{CoO}_{3-\delta}$ as a topotactic phase-change material. *Advanced Optical Materials* **11**. ISSN: 2195-1071 (May 2023).
82. De Jong, D. *et al.* Electrically switchable metallic polymer metasurface device with gel polymer electrolyte. *Nanophotonics* **12**, 1397–1404. ISSN: 2192-8614 (Jan. 2023).
83. Brongersma, M. L. The road to atomically thin metasurface optics. *Nanophotonics* **10**, 643–654. ISSN: 2192-8606 (Nov. 2020).
84. Tokpanov, Y. *Towards next generation of optoelectronics: From quantum plasmonics and 2D materials to advanced optimization techniques of nanophotonic devices* PhD thesis (California Institute of Technology, 2020).
85. Phan, T. *et al.* High-efficiency, large-area, topology-optimized metasurfaces. *Light: Science & Applications* **8**. ISSN: 2047-7538 (May 2019).

86. Mansouree, M. *et al.* Multifunctional 2.5D metastructures enabled by adjoint optimization. *Optica* **7**, 77. ISSN: 2334-2536 (Jan. 2020).
87. Mansouree, M., McClung, A., Samudrala, S. & Arbabi, A. Large-scale parametrized metasurface design using adjoint optimization. *ACS Photonics* **8**, 455–463. ISSN: 2330-4022 (Jan. 2021).
88. Ma, W. *et al.* Pushing the limits of functionality-multiplexing capability in metasurface design based on statistical machine learning. *Advanced Materials* **34**. ISSN: 1521-4095 (Mar. 2022).
89. Xie, J. *et al.* Designing semiconductor materials and devices in the post-Moore era by tackling computational challenges with data-driven strategies. *Nature Computational Science* **4**, 322–333. ISSN: 2662-8457 (May 2024).
90. Mounet, N. *et al.* Two-dimensional materials from high-throughput computational exfoliation of experimentally known compounds. *Nature Nanotechnology* **13**, 246–252. ISSN: 1748-3395 (Feb. 2018).
91. Choubisa, H. *et al.* Interpretable discovery of semiconductors with machine learning. *npj Computational Materials* **9**. ISSN: 2057-3960 (June 2023).
92. Liu, Z. *et al.* Machine learning with knowledge constraints for process optimization of open-air perovskite solar cell manufacturing. *Joule* **6**, 834–849. ISSN: 2542-4351 (Apr. 2022).
93. Zhang, L. *et al.* Space-time-coding digital metasurfaces. *Nature Communications* **9**. ISSN: 2041-1723 (Oct. 2018).
94. Taravati, S. & Eleftheriades, G. V. Microwave space-time-modulated metasurfaces. *ACS Photonics* **9**, 305–318. ISSN: 2330-4022 (Jan. 2022).
95. Sisler, J. *et al.* Electrically tunable space–time metasurfaces at optical frequencies. *Nature Nanotechnology*. ISSN: 1748-3395 (July 2024).
96. Thureja, P. *et al.* Toward a universal metasurface for optical imaging, communication, and computation. *Nanophotonics* **11**, 3745–3768. ISSN: 2192-8614 (Aug. 2022).
97. Fan, Y. *et al.* Phase-controlled metasurface design via optimized genetic algorithm. *Nanophotonics* **9**, 3931–3939. ISSN: 2192-8606 (June 2020).
98. Sanchez-Lengeling, B. & Aspuru-Guzik, A. Inverse molecular design using machine learning: Generative models for matter engineering. *Science* **361**, 360–365. ISSN: 1095-9203 (July 2018).
99. Zunger, A. Inverse design in search of materials with target functionalities. *Nature Reviews Chemistry* **2**. ISSN: 2397-3358 (Mar. 2018).
100. Yuan, L., Dutt, A. & Fan, S. Synthetic frequency dimensions in dynamically modulated ring resonators. *APL Photonics* **6**. ISSN: 2378-0967 (July 2021).

101. Galiffi, E. *et al.* Photonics of time-varying media. *Advanced Photonics* **4**, ISSN: 2577-5421 (Feb. 2022).
102. Harwood, A. C. *et al.* Super-luminal Synthetic Motion with a Space-Time Optical Metasurface. *arXiv:2407.10809 [physics.optics]* (2024).
103. Hecht, E. *Optics* 5 ed. 722 pp. ISBN: 9781292096933 (Pearson, Boston, 2017).
104. Wong, A. M. H. & Eleftheriades, G. V. Perfect anomalous reflection with a bipartite Huygens' metasurface. *Physical Review X* **8**, 011036. ISSN: 2160-3308 (Feb. 2018).
105. Wang, X. *et al.* Simultaneous realization of anomalous reflection and transmission at two frequencies using bi-functional metasurfaces. *Scientific Reports* **8**. ISSN: 2045-2322 (Jan. 2018).
106. Khorasaninejad, M. *et al.* Metalenses at visible wavelengths: Diffraction-limited focusing and subwavelength resolution imaging. *Science* **352**, 1190–1194. ISSN: 1095-9203 (June 2016).
107. Chen, W. T. *et al.* A broadband achromatic metalens for focusing and imaging in the visible. *Nature Nanotechnology* **13**, 220–226. ISSN: 1748-3395 (Jan. 2018).
108. Arbabi, A., Horie, Y., Ball, A. J., Bagheri, M. & Faraon, A. Subwavelength-thick lenses with high numerical apertures and large efficiency based on high-contrast transmitarrays. *Nature Communications* **6**. ISSN: 2041-1723 (May 2015).
109. Deng, Y., Wu, C., Meng, C., Bozhevolnyi, S. I. & Ding, F. Functional metasurface quarter-wave plates for simultaneous polarization conversion and beam steering. *ACS Nano* **15**, 18532–18540. ISSN: 1936-086X (Nov. 2021).
110. Devlin, R. C., Ambrosio, A., Rubin, N. A., Mueller, J. P. B. & Capasso, F. Arbitrary spin-to-orbital angular momentum conversion of light. *Science* **358**, 896–901. ISSN: 1095-9203 (Nov. 2017).
111. Balthasar Mueller, J. P., Rubin, N. A., Devlin, R. C., Groever, B. & Capasso, F. Metasurface polarization optics: Independent phase control of arbitrary orthogonal states of polarization. *Physical Review Letters* **118**, 113901. ISSN: 1079-7114 (Mar. 2017).
112. Tirole, R. *et al.* Double-slit time diffraction at optical frequencies. *Nature Physics* **19**, 999–1002. ISSN: 1745-2481 (Apr. 2023).
113. Wu, Z. & Grbic, A. Serrodyne frequency translation using time-modulated metasurfaces. *IEEE Transactions on Antennas and Propagation* **68**, 1599–1606. ISSN: 1558-2221 (Mar. 2020).
114. Cardin, A. E. *et al.* Surface-wave-assisted nonreciprocity in spatio-temporally modulated metasurfaces. *Nature Communications* **11**. ISSN: 2041-1723 (Mar. 2020).

115. Guo, X., Ding, Y., Duan, Y. & Ni, X. Nonreciprocal metasurface with space–time phase modulation. *Light: Science & Applications* **8**. ISSN: 2047-7538 (Dec. 2019).
116. Hadad, Y., Sounas, D. L. & Alu, A. Space-time gradient metasurfaces. *Physical Review B* **92**, 100304. ISSN: 1550-235X (Sept. 2015).
117. Taravati, S. & Eleftheriades, G. V. Generalized space-time-periodic diffraction gratings: Theory and applications. *Physical Review Applied* **12**, 024026. ISSN: 2331-7019 (Aug. 2019).
118. Wang, X., Asadchy, V. S., Fan, S. & Tretyakov, S. A. Space-time metasurfaces for power combining of waves. *ACS Photonics* **8**, 3034–3041. ISSN: 2330-4022 (Sept. 2021).
119. Salary, M. M. & Mosallaei, H. Time-modulated conducting oxide metasurfaces for adaptive multiple access optical communication. *IEEE Transactions on Antennas and Propagation* **68**, 1628–1642. ISSN: 1558-2221 (Mar. 2020).
120. Sabri, R., Salary, M. M. & Mosallaei, H. Quasi-static and time-modulated optical phased arrays: Beamforming analysis and comparative study. *Advanced Photonics Research* **2**. ISSN: 2699-9293 (July 2021).
121. Taravati, S., Chamanara, N. & Caloz, C. Nonreciprocal electromagnetic scattering from a periodically space-time modulated slab and application to a quasisonic isolator. *Physical Review B* **96**, 165144. ISSN: 2469-9969 (Oct. 2017).
122. Taravati, S. Aperiodic space-time modulation for pure frequency mixing. *Physical Review B* **97**, 115131. ISSN: 2469-9969 (Mar. 2018).
123. Tien, P. K. Parametric amplification and frequency mixing in propagating circuits. *Journal of Applied Physics* **29**, 1347–1357. ISSN: 1089-7550 (Sept. 1958).
124. Zhang, L. & Cui, T. J. Space-time-coding digital metasurfaces: Principles and applications. *Research* **2021**. ISSN: 2639-5274 (Jan. 2021).
125. Zhang, L. *et al.* Breaking reciprocity with space-time-coding digital metasurfaces. *Advanced Materials* **31**. ISSN: 1521-4095 (Aug. 2019).
126. Karimi, M., Alam, M. Z., Upham, J., Reshef, O. & Boyd, R. W. Time-varying gradient metasurface with applications in all-optical beam steering. *Nanophotonics* **12**, 1733–1740. ISSN: 2192-8614 (Mar. 2023).
127. Lustig, E. *et al.* Time-refraction optics with single cycle modulation. *Nanophotonics* **12**, 2221–2230. ISSN: 2192-8614 (May 2023).
128. Gui, Y. *et al.* 100 GHz micrometer-compact broadband monolithic ITO Mach–Zehnder interferometer modulator enabling 3500 times higher packing density. *Nanophotonics* **11**, 4001–4009. ISSN: 2192-8614 (Apr. 2022).

129. Amin, R. *et al.* Sub-wavelength GHz-fast broadband ITO Mach–Zehnder modulator on silicon photonics. *Optica* **7**, 333. ISSN: 2334-2536 (Apr. 2020).
130. Wattellier, B., Bétourné, A., Doudet, I., Ghesquière, B. & Pallares, A. Mid-Wave InfraRed metrology using quadriwave lateral shearing interferometry wave front sensing with low coherence quantum cascade laser sources, 41 (July 2023).
131. LaserFocusWorld. *Optics for automotive LiDAR: Metasurface beam steering enables solid-state, high-performance LiDAR* <https://www.laserfocusworld.com/optics/article/14036818/metasurface-beam-steering-enables-solid-state-high-performance-lidar>.
132. Andersen, T. I. *et al.* Beam steering at the nanosecond time scale with an atomically thin reflector. *Nature Communications* **13**. ISSN: 2041-1723 (June 2022).
133. Hadad, Y., Soric, J. C. & Alu, A. Breaking temporal symmetries for emission and absorption. *Proceedings of the National Academy of Sciences* **113**, 3471–3475. ISSN: 1091-6490 (Mar. 2016).
134. Taravati, S. & Eleftheriades, G. V. Full-duplex nonreciprocal beam steering by time-modulated phase-gradient metasurfaces. *Physical Review Applied* **14**, 014027. ISSN: 2331-7019 (July 2020).
135. Thureja, P. *et al.* Spalled barium titanate single crystal thin films for functional device applications. *arXiv:2505.04045 [physics.app-ph]* (2025).
136. McMahon, P. L. The physics of optical computing. *Nature Reviews Physics* **5**, 717–734. ISSN: 2522-5820 (Oct. 2023).
137. Hu, J. *et al.* Diffractive optical computing in free space. *Nature Communications* **15**. ISSN: 2041-1723 (Feb. 2024).
138. Miller, D. A. B. Attojoule optoelectronics for low-energy information processing and communications. *Journal of Lightwave Technology* **35**, 346–396. ISSN: 1558-2213 (Feb. 2017).
139. Karvounis, A., Timpu, F., Vogler-Neuling, V. V., Savo, R. & Grange, R. Barium titanate nanostructures and thin films for photonics. *Advanced Optical Materials* **8**. ISSN: 2195-1071 (Nov. 2020).
140. Margalit, N. *et al.* Perspective on the future of silicon photonics and electronics. *Applied Physics Letters* **118**. ISSN: 1077-3118 (May 2021).
141. Dutt, A., Mohanty, A., Gaeta, A. L. & Lipson, M. Nonlinear and quantum photonics using integrated optical materials. *Nature Reviews Materials* **9**, 321–346. ISSN: 2058-8437 (May 2024).
142. Li, N. *et al.* Large-area metasurface on CMOS-compatible fabrication platform: driving flat optics from lab to fab. *Nanophotonics* **9**, 3071–3087. ISSN: 2192-8606 (Apr. 2020).

143. Marris-Morini, D. *et al.* Recent progress in high-speed silicon-based optical modulators. *Proceedings of the IEEE* **97**, 1199–1215. ISSN: 0018-9219 (July 2009).
144. Li, M., Hail, C. U., Biswas, S. & Atwater, H. A. Excitonic beam steering in an active van der Waals metasurface. *Nano Letters* **23**, 2771–2777. ISSN: 1530-6992 (Mar. 2023).
145. Huang, L. *et al.* Enhanced light–matter interaction in two-dimensional transition metal dichalcogenides. *Reports on Progress in Physics* **85**, 046401. ISSN: 1361-6633 (Mar. 2022).
146. Yariv, A. *Optical waves in crystals. Propagation and control of laser radiation* (ed Yeh, P.) 589 pp. ISBN: 0471430811 (Wiley, Hoboken, NJ, 2003).
147. Burla, M. *et al.* 500 GHz plasmonic Mach-Zehnder modulator enabling sub-THz microwave photonics. *APL Photonics* **4**. ISSN: 2378-0967 (May 2019).
148. Zhu, D. *et al.* Integrated photonics on thin-film lithium niobate. *Advances in Optics and Photonics* **13**, 242. ISSN: 1943-8206 (May 2021).
149. Boes, A. *et al.* Lithium niobate photonics: Unlocking the electromagnetic spectrum. *Science* **379**. ISSN: 1095-9203 (Jan. 2023).
150. Thomaschewski, M., Zenin, V. A., Wolff, C. & Bozhevolnyi, S. I. Plasmonic monolithic lithium niobate directional coupler switches. *Nature Communications* **11**. ISSN: 2041-1723 (Feb. 2020).
151. Weis, R. S. & Gaylord, T. K. Lithium niobate: Summary of physical properties and crystal structure. *Applied Physics A Solids and Surfaces* **37**, 191–203. ISSN: 1432-0630 (Aug. 1985).
152. Klopfer, E., Dagli, S., Barton, D., Lawrence, M. & Dionne, J. A. High-quality-factor silicon-on-lithium niobate metasurfaces for electro-optically reconfigurable wavefront shaping. *Nano Letters* **22**, 1703–1709. ISSN: 1530-6992 (Feb. 2022).
153. Kuo, Y.-H. *et al.* Strong quantum-confined Stark effect in germanium quantum-well structures on silicon. *Nature* **437**, 1334–1336. ISSN: 1476-4687 (Oct. 2005).
154. Lee, J. *et al.* Ultrafast electrically tunable polaritonic metasurfaces. *Advanced Optical Materials* **2**, 1057–1063. ISSN: 2195-1071 (July 2014).
155. Yu, J. *et al.* Electrically tunable nonlinear polaritonic metasurface. *Nature Photonics* **16**, 72–78. ISSN: 1749-4893 (Dec. 2021).
156. Li, N. *et al.* Aluminium nitride integrated photonics: A review. *Nanophotonics* **10**, 2347–2387. ISSN: 2192-8606 (June 2021).
157. Smolyaninov, A., El Amili, A., Vallini, F., Pappert, S. & Fainman, Y. Programmable plasmonic phase modulation of free-space wavefronts at gigahertz rates. *Nature Photonics* **13**, 431–435. ISSN: 1749-4893 (Feb. 2019).

158. Kischkat, J. *et al.* Mid-infrared optical properties of thin films of aluminum oxide, titanium dioxide, silicon dioxide, aluminum nitride, and silicon nitride. *Applied Optics* **51**, 6789. ISSN: 2155-3165 (Sept. 2012).
159. Barton, D., Lawrence, M. & Dionne, J. Wavefront shaping and modulation with resonant electro-optic phase gradient metasurfaces. *Applied Physics Letters* **118**. ISSN: 1077-3118 (Feb. 2021).
160. *Precision Micro-optics, "Lithium Niobate (LiNbO₃)"* Mar. 2022. https://www.pmoptics.com/lithium_niobate.html.
161. Heni, W. *et al.* Silicon-organic and plasmonic-organic hybrid photonics. *ACS Photonics* **4**, 1576–1590. ISSN: 2330-4022 (June 2017).
162. Kieninger, C. *et al.* Record-high in-device electro-optic coefficient of 359 pm/V in a silicon-organic hybrid (SOH) modulator. *Conference on Lasers and Electro-Optics, STu3N.2* (2017).
163. Baehr-Jones, T. *et al.* Nonlinear polymer-clad silicon slot waveguide modulator with a half wave voltage of 0.25V. *Applied Physics Letters* **92**. ISSN: 1077-3118 (Apr. 2008).
164. Heni, W. *et al.* Nonlinearities of organic electro-optic materials in nanoscale slots and implications for the optimum modulator design. *Optics Express* **25**, 2627. ISSN: 1094-4087 (Feb. 2017).
165. Abel, S. *et al.* Large Pockels effect in micro- and nanostructured barium titanate integrated on silicon. *Nature Materials* **18**, 42–47. ISSN: 1476-4660 (Nov. 2018).
166. Hsu, M.-H. M. *et al.* Orientation-dependent electro-optical response of BaTiO₃ on SrTiO₃-buffered Si(001) studied via spectroscopic ellipsometry. *Optical Materials Express* **7**, 2030. ISSN: 2159-3930 (May 2017).
167. Jin, T. & Lin, P. T. Efficient mid-infrared electro-optical waveguide modulators using ferroelectric barium titanate. *IEEE Journal of Selected Topics in Quantum Electronics* **26**, 1–7. ISSN: 1558-4542 (Sept. 2020).
168. Frigerio, J. *et al.* Giant electro-optic effect in Ge/SiGe coupled quantum wells. *Scientific Reports* **5**. ISSN: 2045-2322 (Oct. 2015).
169. Klein, H. *Integrated InP Mach-Zehnder modulators for 100 Gbit/s ethernet applications using QPSK modulation* en. PhD thesis (Technische Universität Berlin, 2010).
170. Adediji, Y. B., Adeyinka, A. M., Yahya, D. I. & Mbelu, O. V. A review of energy storage applications of lead-free BaTiO₃-based dielectric ceramic capacitors. *Energy, Ecology and Environment* **8**, 401–419. ISSN: 2363-8338 (June 2023).

171. Jiang, B. *et al.* Barium titanate at the nanoscale: Controlled synthesis and dielectric and ferroelectric properties. *Chemical Society Reviews* **48**, 1194–1228. ISSN: 1460-4744 (2019).
172. Berlincourt, D. & Jaffe, H. Elastic and piezoelectric coefficients of single-crystal barium titanate. *Physical Review* **111**, 143–148. ISSN: 0031-899X (July 1958).
173. Abel, S. *et al.* A hybrid barium titanate-silicon photonics platform for ultraefficient electro-optic tuning. *Journal of Lightwave Technology* **34**, 1688–1693. ISSN: 1558-2213 (Apr. 2016).
174. Girouard, P. *et al.* $\chi^{(2)}$ Modulator with 40-GHz modulation utilizing BaTiO₃ photonic crystal waveguides. *IEEE Journal of Quantum Electronics* **53**, 1–10. ISSN: 1558-1713 (Aug. 2017).
175. Sun, D. *et al.* Theoretical feasibility demonstration for over 100 GHz electro-optic modulators with c-axis grown BaTiO₃ crystal thin-films. *Journal of Lightwave Technology* **33**, 1937–1947. ISSN: 1558-2213 (May 2015).
176. Palik, E. D. *Handbook of optical constants of solids* Includes bibliographical references. 1804 pp. ISBN: 0080523757 (Academic Press, San Diego, 1998).
177. Fontana, M., Laabidi, K., Jannot, B., Maglione, M. & Jullien, P. Relationship between electro-optic, vibrational and dielectric properties in BaTiO₃. *Solid State Communications* **92**, 827–830. ISSN: 0038-1098 (Dec. 1994).
178. Winiger, J. *et al.* PLD epitaxial thin-film BaTiO₃ on MgO – dielectric and electro-optic properties. *Advanced Materials Interfaces* **11**. ISSN: 2196-7350 (Oct. 2023).
179. Dong, Z. *et al.* Monolithic barium titanate modulators on silicon-on-insulator substrates. *ACS Photonics* **10**, 4367–4376. ISSN: 2330-4022 (Nov. 2023).
180. Kormondy, K. J. *et al.* Microstructure and ferroelectricity of BaTiO₃ thin films on Si for integrated photonics. *Nanotechnology* **28**, 075706. ISSN: 1361-6528 (Jan. 2017).
181. Weigand, H. C. *et al.* Nanoimprinting solution-derived barium titanate for electro-optic metasurfaces. *Nano Letters* **24**, 5536–5542. ISSN: 1530-6992 (Apr. 2024).
182. Chen, J. & Packard, C. E. Controlled spalling-based mechanical substrate exfoliation for III-V solar cells: A review. *Solar Energy Materials and Solar Cells* **225**, 111018. ISSN: 0927-0248 (June 2021).
183. Miura, H., Ohta, H., Okamoto, N. & Kaga, T. Crystallization-induced stress in silicon thin films. *Applied Physics Letters* **60**, 2746–2748. ISSN: 1077-3118 (June 1992).
184. Hutchinson, J. & Suo, Z. in *Advances in Applied Mechanics Volume 29* 63–191 (Elsevier, 1991). ISBN: 9780120020294.

185. Lee, Y. H., Kim, J. & Oh, J. Wafer-scale ultrathin, single-crystal Si and GaAs photocathodes for photoelectrochemical hydrogen production. *ACS Applied Materials & Interfaces* **10**, 33230–33237. ISSN: 1944-8252 (Sept. 2018).
186. Bedell, S. W. *et al.* Kerf-less removal of Si, Ge, and III–V layers by controlled spalling to enable low-cost PV technologies. *IEEE Journal of Photovoltaics* **2**, 141–147. ISSN: 2156-3403 (Apr. 2012).
187. Bedell, S. W. *et al.* Layer transfer by controlled spalling. *Journal of Physics D: Applied Physics* **46**, 152002. ISSN: 1361-6463 (Mar. 2013).
188. Crouse, D. R. *Controlled spalling in (100)-oriented germanium by electroplating* MA thesis (Colorado School of Mines, 2017).
189. Sweet, C. A. *Spalling fracture behavior in (100) gallium arsenide* PhD thesis (Colorado School of Mines, 2016).
190. Prasad, V. C. S. & Subbarao, E. C. Deformation and stress relaxation of single crystal BaTiO₃. *Ferroelectrics* **15**, 143–147. ISSN: 1563-5112 (Jan. 1977).
191. Meschke, F., Kolleck, A. & Schneider, G. R-curve behaviour of BaTiO₃ due to stress-induced ferroelastic domain switching. *Journal of the European Ceramic Society* **17**, 1143–1149. ISSN: 0955-2219 (Jan. 1997).
192. Hamze, A. K., Reynaud, M., Geler-Kremer, J. & Demkov, A. A. Design rules for strong electro-optic materials. *npj Computational Materials* **6**. ISSN: 2057-3960 (Aug. 2020).
193. Chelladurai, D. *et al.* Barium titanate and lithium niobate permittivity and Pockels coefficients from MHz to sub-THz frequencies. arXiv: 2407.03443 [physics.optics] (July 2024).
194. Gunter, P. Electro-optical effects in dielectric crystals. *Ferroelectrics* **75**, 5–23. ISSN: 1563-5112 (Sept. 1987).
195. Teng, C. C. & Man, H. T. Simple reflection technique for measuring the electro-optic coefficient of poled polymers. *Applied Physics Letters* **56**, 1734–1736. ISSN: 1077-3118 (Apr. 1990).
196. Schildkraut, J. S. Determination of the electrooptic coefficient of a poled polymer film. *Applied Optics* **29**, 2839. ISSN: 1539-4522 (July 1990).
197. Kang, T. D. *et al.* Large electro-optic effect in single-crystal Pb(Zr,Ti)O₃ (001) measured by spectroscopic ellipsometry. *Journal of Applied Physics* **104**. ISSN: 1089-7550 (Nov. 2008).
198. Adachi, H., Kawaguchi, T., Setsune, K., Ohji, K. & Wasa, K. Electro-optic effects of (Pb, La)(Zr, Ti)O₃ thin films prepared by rf planar magnetron sputtering. *Applied Physics Letters* **42**, 867–868. ISSN: 1077-3118 (May 1983).
199. Hoerman, B. H., Nichols, B. M., Nystrom, M. J. & Wessels, B. W. Dynamic response of the electro-optic effect in epitaxial KNbO₃. *Applied Physics Letters* **75**, 2707–2709. ISSN: 1077-3118 (Nov. 1999).

200. Petraru, A., Schubert, J., Schmid, M., Trithaveesak, O. & Buchal, C. Integrated optical Mach Zehnder modulator based on polycrystalline BaTiO₃. *Optics Letters* **28**, 2527. ISSN: 1539-4794 (Dec. 2003).
201. Lee, Y. S. *et al.* Hybrid Si-LiNbO₃ microring electro-optically tunable resonators for active photonic devices. *Optics Letters* **36**, 1119. ISSN: 1539-4794 (Mar. 2011).
202. Abel, S. *Electro-optic photonic devices based on epitaxial barium titanate thin films on silicon* Theses (Université de Grenoble, Feb. 2014). <https://theses.hal.science/tel-01230124>.
203. Inoue, A., Inoue, S.-i. & Yokoyama, S. Enhanced electro-optic response of a poled polymer in a reflective microcavity. *Optics Communications* **283**, 2935–2938. ISSN: 0030-4018 (July 2010).
204. Fuchs, K. The conductivity of thin metallic films according to the electron theory of metals. *Mathematical Proceedings of the Cambridge Philosophical Society* **34**, 100–108. ISSN: 1469-8064 (Jan. 1938).
205. Sondheimer, E. H. The mean free path of electrons in metals. *Advances in Physics* **50**, 499–537. ISSN: 1460-6976 (Sept. 2001).
206. Castera, P., Tulli, D., Gutierrez, A. M. & Sanchis, P. Influence of BaTiO₃ ferroelectric orientation for electro-optic modulation on silicon. *Optics Express* **23**, 15332. ISSN: 1094-4087 (June 2015).
207. Hu, X. & Wang, J. Ultrabroadband compact graphene-silicon TM-pass polarizer. *IEEE Photonics Journal* **9**, 1–10. ISSN: 1943-0655 (Apr. 2017).
208. Wemple, S., Didomenico, M. & Camlibel, I. Dielectric and optical properties of melt-grown BaTiO₃. *Journal of Physics and Chemistry of Solids* **29**, 1797–1803. ISSN: 0022-3697 (Oct. 1968).
209. Hail, C. U., Foley, M., Sokhoyan, R., Michaeli, L. & Atwater, H. A. High quality factor metasurfaces for two-dimensional wavefront manipulation. *Nature Communications* **14**. ISSN: 2041-1723 (Dec. 2023).
210. Philipp, H. R. Optical properties of silicon nitride. *Journal of The Electrochemical Society* **120**, 295. ISSN: 0013-4651 (1973).
211. Kim, J. Y. *et al.* Full 2π tunable phase modulation using avoided crossing of resonances. *Nature Communications* **13**. ISSN: 2041-1723 (Apr. 2022).
212. Joo, W.-J. *et al.* Metasurface-driven OLED displays beyond 10,000 pixels per inch. *Science* **370**, 459–463. ISSN: 1095-9203 (Oct. 2020).
213. Devlin, R. C., Khorasaninejad, M., Chen, W. T., Oh, J. & Capasso, F. Broadband high-efficiency dielectric metasurfaces for the visible spectrum. *Proceedings of the National Academy of Sciences* **113**, 10473–10478. ISSN: 1091-6490 (Sept. 2016).

214. Qi, Y. & Li, Y. Integrated lithium niobate photonics. *Nanophotonics* **9**, 1287–1320. ISSN: 2192-8606 (Apr. 2020).
215. Kim, S. *et al.* Electronically tunable perfect absorption in graphene. *Nano Letters* **18**, 971–979. ISSN: 1530-6992 (Jan. 2018).
216. Park, J. *et al.* All-solid-state spatial light modulator with independent phase and amplitude control for three-dimensional LiDAR applications. *Nature Nanotechnology* **16**, 69–76. ISSN: 1748-3395 (Oct. 2020).
217. Wu, P. C., Sokhoyan, R., Shirmanesh, G. K., Cheng, W.-H. & Atwater, H. A. Near-infrared active metasurface for dynamic polarization conversion. *Advanced Optical Materials* **9**. ISSN: 2195-1071 (June 2021).
218. Chen, H.-T. *et al.* Active terahertz metamaterial devices. *Nature* **444**, 597–600. ISSN: 1476-4687 (Nov. 2006).
219. Jun, Y. C. *et al.* Active tuning of mid-infrared metamaterials by electrical control of carrier densities. *Optics Express* **20**, 1903. ISSN: 1094-4087 (Jan. 2012).
220. Park, J., Kang, J.-H., Liu, X. & Brongersma, M. L. Electrically tunable epsilon-near-zero (ENZ) metafilm absorbers. *Scientific Reports* **5**. ISSN: 2045-2322 (Nov. 2015).
221. Kim, S. I. *et al.* Two-dimensional beam steering with tunable metasurface in infrared regime. *Nanophotonics* **11**, 2719–2726. ISSN: 2192-8614 (Feb. 2022).
222. Park, J. *et al.* Dynamic thermal emission control with InAs-based plasmonic metasurfaces. *Science Advances* **4**. ISSN: 2375-2548 (Dec. 2018).
223. Caldwell, J. D. *et al.* Low-loss, extreme subdiffraction photon confinement via silicon carbide localized surface phonon polariton resonators. *Nano Letters* **13**, 3690–3697. ISSN: 1530-6992 (July 2013).
224. Aryaee Panah, M. E., Semenova, E. S. & Lavrinenko, A. V. Enhancing optical forces in InP-based waveguides. *Scientific Reports* **7**. ISSN: 2045-2322 (June 2017).
225. Streyer, W., Feng, K., Zhong, Y., Hoffman, A. J. & Wasserman, D. Engineering the Reststrahlen band with hybrid plasmon/ phonon excitations. *MRS Communications* **6**, 1–8. ISSN: 2159-6867 (Mar. 2016).
226. Kinsey, N., DeVault, C., Boltasseva, A. & Shalaev, V. M. Near-zero-index materials for photonics. *Nature Reviews Materials* **4**, 742–760. ISSN: 2058-8437 (Sept. 2019).
227. Lu, Y.-J. *et al.* Dynamically controlled Purcell enhancement of visible spontaneous emission in a gated plasmonic heterostructure. *Nature Communications* **8**. ISSN: 2041-1723 (Nov. 2017).

228. Smoleński, T. *et al.* Interaction-induced Shubnikov-de Haas oscillations in optical conductivity of monolayer MoSe₂. *Physical Review Letters* **123**, 097403. ISSN: 1079-7114 (Aug. 2019).
229. Ni, P. *et al.* Gate-tunable emission of exciton-plasmon polaritons in hybrid MoS₂-gap-mode metasurfaces. *ACS Photonics* **6**, 1594–1601. ISSN: 2330-4022 (June 2019).
230. Lien, D.-H. *et al.* Electrical suppression of all nonradiative recombination pathways in monolayer semiconductors. *Science* **364**, 468–471. ISSN: 1095-9203 (May 2019).
231. Dai, S. *et al.* Tunable phonon polaritons in atomically thin van der Waals crystals of boron nitride. *Science* **343**, 1125–1129. ISSN: 1095-9203 (Mar. 2014).
232. Datta, I. *et al.* Low-loss composite photonic platform based on 2D semiconductor monolayers. *Nature Photonics* **14**, 256–262. ISSN: 1749-4893 (Feb. 2020).
233. Scuri, G. *et al.* Large excitonic reflectivity of monolayer MoSe₂ encapsulated in hexagonal boron nitride. *Physical Review Letters* **120**, 037402. ISSN: 1079-7114 (Jan. 2018).
234. Back, P., Zeytinoglu, S., Ijaz, A., Kroner, M. & Imamoğlu, A. Realization of an electrically tunable narrow-bandwidth atomically thin mirror using monolayer MoSe₂. *Physical Review Letters* **120**, 037401. ISSN: 1079-7114 (Jan. 2018).
235. Li, M., Biswas, S., Hail, C. U. & Atwater, H. A. Refractive index modulation in monolayer molybdenum diselenide. *Nano Letters* **21**, 7602–7608. ISSN: 1530-6992 (Sept. 2021).
236. Ling, X., Wang, H., Huang, S., Xia, F. & Dresselhaus, M. S. The renaissance of black phosphorus. *Proceedings of the National Academy of Sciences* **112**, 4523–4530. ISSN: 1091-6490 (Mar. 2015).
237. Biswas, S., Grajower, M. Y., Watanabe, K., Taniguchi, T. & Atwater, H. A. Broadband electro-optic polarization conversion with atomically thin black phosphorus. *Science* **374**, 448–453. ISSN: 1095-9203 (Oct. 2021).
238. Van de Groep, J. *et al.* Exciton resonance tuning of an atomically thin lens. *Nature Photonics* **14**, 426–430. ISSN: 1749-4893 (Apr. 2020).
239. Masubuchi, S. *et al.* Autonomous robotic searching and assembly of two-dimensional crystals to build van der Waals superlattices. *Nature Communications* **9**. ISSN: 2041-1723 (Apr. 2018).
240. Mannix, A. J. *et al.* Robotic four-dimensional pixel assembly of van der Waals solids. *Nature Nanotechnology* **17**, 361–366. ISSN: 1748-3395 (Jan. 2022).

241. Whitney, W. S. *Electrically-tunable light-matter interactions in quantum materials* en. PhD thesis (California Institute of Technology, 2019).
242. Naeem, T., Khaliq, H. S., Zubair, M., Tauqeer, T. & Mehmood, M. Q. Engineering tunability through electro-optic effects to manifest a multifunctional metadvice. *RSC Advances* **11**, 13220–13228. ISSN: 2046-2069 (2021).
243. Jazbinšek, M. & Zgonik, M. Material tensor parameters of LiNbO₃ relevant for electro- and elasto-optics. *Applied Physics B: Lasers and Optics* **74**, 407–414. ISSN: 1432-0649 (Apr. 2002).
244. Weigand, H. *et al.* Enhanced electro-optic modulation in resonant metasurfaces of lithium niobate. *ACS Photonics* **8**, 3004–3009. ISSN: 2330-4022 (Sept. 2021).
245. Weiss, A. *et al.* Tunable metasurface using thin-film lithium niobate in the telecom regime. *ACS Photonics* **9**, 605–612. ISSN: 2330-4022 (Jan. 2022).
246. Haffner, C. *et al.* Low-loss plasmon-assisted electro-optic modulator. *Nature* **556**, 483–486. ISSN: 1476-4687 (Apr. 2018).
247. Xu, H. *et al.* Design and synthesis of chromophores with enhanced electro-optic activities in both bulk and plasmonic–organic hybrid devices. *Materials Horizons* **9**, 261–270. ISSN: 2051-6355 (2022).
248. Kieninger, C. *et al.* Ultra-high electro-optic activity demonstrated in a silicon-organic hybrid modulator. *Optica* **5**, 739. ISSN: 2334-2536 (June 2018).
249. Jin, J. *et al.* Topologically enabled ultrahigh-Q guided resonances robust to out-of-plane scattering. *Nature* **574**, 501–504. ISSN: 1476-4687 (Oct. 2019).
250. Koshelev, K., Lepeshov, S., Liu, M., Bogdanov, A. & Kivshar, Y. Asymmetric metasurfaces with high-Q resonances governed by bound states in the continuum. *Physical Review Letters* **121**, 193903. ISSN: 1079-7114 (Nov. 2018).
251. Koshelev, K. *et al.* Subwavelength dielectric resonators for nonlinear nanophotonics. *Science* **367**, 288–292. ISSN: 1095-9203 (Jan. 2020).
252. Salary, M. M. & Mosallaei, H. Tunable all-dielectric metasurfaces for phase-only modulation of transmitted light based on quasi-bound states in the continuum. *ACS Photonics* **7**, 1813–1829. ISSN: 2330-4022 (June 2020).
253. Sautter, J. *et al.* Active tuning of all-dielectric metasurfaces. *ACS Nano* **9**, 4308–4315. ISSN: 1936-086X (Mar. 2015).
254. Buchnev, O., Podoliak, N., Kaczmarek, M., Zheludev, N. I. & Fedotov, V. A. Electrically controlled nanostructured metasurface loaded with liquid crystal: Toward multifunctional photonic switch. *Advanced Optical Materials* **3**, 674–679. ISSN: 2195-1071 (Jan. 2015).

255. Savo, S., Shrekenhamer, D. & Padilla, W. J. Liquid crystal metamaterial absorber spatial light modulator for THz applications. *Advanced Optical Materials* **2**, 275–279. ISSN: 2195-1071 (Jan. 2014).
256. Hwang, C.-S. *et al.* Achieving 1 μ m pixel pitch display for electronic holography in *Advances in Display Technologies X* (eds Lee, J.-H., Wang, Q.-H. & Yoon, T.-H.) (SPIE, Feb. 2020), 21.
257. Zhang, Y. *et al.* Electrically reconfigurable non-volatile metasurface using low-loss optical phase-change material. *Nature Nanotechnology* **16**, 661–666. ISSN: 1748-3395 (Apr. 2021).
258. Butakov, N. A. *et al.* Broadband electrically tunable dielectric resonators using metal-insulator transitions. *ACS Photonics* **5**, 4056–4060. ISSN: 2330-4022 (Sept. 2018).
259. Michel, A.-K. U. *et al.* Reversible optical switching of infrared antenna resonances with ultrathin phase-change layers using femtosecond laser pulses. *ACS Photonics* **1**, 833–839. ISSN: 2330-4022 (Sept. 2014).
260. Yin, X. *et al.* Beam switching and bifocal zoom lensing using active plasmonic metasurfaces. *Light: Science & Applications* **6**, e17016–e17016. ISSN: 2047-7538 (June 2017).
261. Kim, Y. *Light modulation with vanadium dioxide-based optical devices* PhD thesis (California Institute of Technology, 2022).
262. Shalaginov, M. Y. *et al.* Design for quality: Reconfigurable flat optics based on active metasurfaces. *Nanophotonics* **9**, 3505–3534. ISSN: 2192-8606 (July 2020).
263. Tanriover, I., Hadibrata, W., Scheuer, J. & Aydin, K. Neural networks enabled forward and inverse design of reconfigurable metasurfaces. *Optics Express* **29**, 27219. ISSN: 1094-4087 (Aug. 2021).
264. Lin, C.-H. *et al.* Automatic inverse design of high-performance beam-steering metasurfaces via genetic-type tree optimization. *Nano Letters* **21**, 4981–4989. ISSN: 1530-6992 (June 2021).
265. Gigli, C. *et al.* Fundamental limitations of Huygens' metasurfaces for optical beam shaping. *Laser & Photonics Reviews* **15**. ISSN: 1863-8899 (June 2021).
266. Hodge, J. A., Mishra, K. V. & Zaghoul, A. I. Deep inverse design of reconfigurable metasurfaces for future communications. *arXiv:2101.09131* (2021).
267. Yao, Y. *et al.* Wide wavelength tuning of optical antennas on graphene with nanosecond response time. *Nano Letters* **14**, 214–219. ISSN: 1530-6992 (Dec. 2013).
268. Benea-Chelms, I.-C. *et al.* Electro-optic spatial light modulator from an engineered organic layer. *Nature Communications* **12**. ISSN: 2041-1723 (Oct. 2021).

269. Komar, A. *et al.* Electrically tunable all-dielectric optical metasurfaces based on liquid crystals. *Applied Physics Letters* **110**. ISSN: 1077-3118 (Feb. 2017).
270. Liu, L. *et al.* Temperature control of terahertz metamaterials with liquid crystals. *IEEE Transactions on Terahertz Science and Technology* **3**, 827–831. ISSN: 2156-3446 (Nov. 2013).
271. Wang, Y. *et al.* Electrical tuning of phase-change antennas and metasurfaces. *Nature Nanotechnology* **16**, 667–672. ISSN: 1748-3395 (Apr. 2021).
272. Gholipour, B., Piccinotti, D., Karvounis, A., MacDonald, K. F. & Zheludev, N. I. Reconfigurable ultraviolet and high-energy visible dielectric metamaterials. *Nano Letters* **19**, 1643–1648. ISSN: 1530-6992 (Feb. 2019).
273. Driscoll, T. *et al.* Memory metamaterials. *Science* **325**, 1518–1521. ISSN: 1095-9203 (Sept. 2009).
274. She, A., Zhang, S., Shian, S., Clarke, D. R. & Capasso, F. Adaptive metalenses with simultaneous electrical control of focal length, astigmatism, and shift. *Science Advances* **4**. ISSN: 2375-2548 (Feb. 2018).
275. Roy, T. *et al.* Dynamic metasurface lens based on MEMS technology. *APL Photonics* **3**. ISSN: 2378-0967 (Feb. 2018).
276. Berto, P. *et al.* Tunable and free-form planar optics. *Nature Photonics* **13**, 649–656. ISSN: 1749-4893 (July 2019).
277. Li, G., Zhang, S. & Zentgraf, T. Nonlinear photonic metasurfaces. *Nature Reviews Materials* **2**. ISSN: 2058-8437 (Mar. 2017).
278. Zhang, J., MacDonald, K. F. & Zheludev, N. I. Controlling light-with-light without nonlinearity. *Light: Science & Applications* **1**, e18–e18. ISSN: 2047-7538 (July 2012).
279. Wang, Q. *et al.* Optically reconfigurable metasurfaces and photonic devices based on phase change materials. *Nature Photonics* **10**, 60–65. ISSN: 1749-4893 (Dec. 2015).
280. Lazarev, G., Chen, P.-J., Strauss, J., Fontaine, N. & Forbes, A. Beyond the display: phase-only liquid crystal on Silicon devices and their applications in photonics [Invited]. *Optics Express* **27**, 16206. ISSN: 1094-4087 (May 2019).
281. Zhang, Z., You, Z. & Chu, D. Fundamentals of phase-only liquid crystal on silicon (LCOS) devices. *Light: Science & Applications* **3**, e213–e213. ISSN: 2047-7538 (Oct. 2014).
282. Savage, N. Digital spatial light modulators. *Nature Photonics* **3**, 170–172. ISSN: 1749-4893 (Mar. 2009).
283. Choi, J. H. *et al.* The new route for realization of 1- μ m-pixel-pitch high-resolution displays. *Journal of the Society for Information Display* **27**, 487–496. ISSN: 1938-3657 (June 2019).

284. Yeom, H.-I. *et al.* 60-3: Distinguished paper: Oxide vertical TFTs for the application to the ultra high resolution display. *SID Symposium Digest of Technical Papers* **47**, 820–822. ISSN: 0097-966X (May 2016).
285. Baek, Y. J. *et al.* Vertical oxide thin-film transistor with interfacial oxidation. *Scientific Reports* **12**. ISSN: 2045-2322 (Feb. 2022).
286. Li, S.-Q. *et al.* Dynamic control of visible light with dielectric nanoantennas: towards next-gen spatial light modulators (Conference Presentation) in *High Contrast Metastructures IX* (SPIE, Mar. 2020), 45.
287. Apter, B., Efron, U. & Bahat-Treidel, E. On the fringing-field effect in liquid-crystal beam-steering devices. *Applied Optics* **43**, 11. ISSN: 1539-4522 (Jan. 2004).
288. Bouvier, M. Analysis of nematic-liquid-crystal binary gratings with high spatial frequency. *Optical Engineering* **39**, 2129. ISSN: 0091-3286 (Aug. 2000).
289. Wong, H.-S. P. *et al.* Phase change memory. *Proceedings of the IEEE* **98**, 2201–2227. ISSN: 1558-2256 (Dec. 2010).
290. Anbarasu, M. & Wuttig, M. Understanding the structure and properties of phase change materials for data storage applications. *Journal of the Indian Institute of Science* **91**, 259–274 (2012).
291. Davoyan, A. & Atwater, H. Perimeter-control architecture for optical phased arrays and metasurfaces. *Physical Review Applied* **14**, 024038. ISSN: 2331-7019 (Aug. 2020).
292. Oh, D. K. *et al.* Nanoimprint lithography for high-throughput fabrication of metasurfaces. *Frontiers of Optoelectronics* **14**, 229–251. ISSN: 2095-2767 (Apr. 2021).
293. Meta Materials Inc. *Lithography 2022*. <https://metamaterial.com/technologies/lithography/>.
294. Chen, X. *et al.* Dual-polarity plasmonic metalens for visible light. *Nature Communications* **3**. ISSN: 2041-1723 (Nov. 2012).
295. Ni, X., Ishii, S., Kildishev, A. V. & Shalaev, V. M. Ultra-thin, planar, Babinet-inverted plasmonic metalenses. *Light: Science & Applications* **2**, e72–e72. ISSN: 2047-7538 (Apr. 2013).
296. Aieta, F., Kats, M. A., Genevet, P. & Capasso, F. Multiwavelength achromatic metasurfaces by dispersive phase compensation. *Science* **347**, 1342–1345. ISSN: 1095-9203 (Mar. 2015).
297. Khorasaninejad, M. *et al.* Achromatic metalens over 60 nm bandwidth in the visible and metalens with reverse chromatic dispersion. *Nano Letters* **17**, 1819–1824. ISSN: 1530-6992 (Feb. 2017).

298. Arbabi, E., Arbabi, A., Kamali, S. M., Horie, Y. & Faraon, A. Controlling the sign of chromatic dispersion in diffractive optics with dielectric metasurfaces. *Optica* **4**, 625. ISSN: 2334-2536 (June 2017).
299. Shrestha, S., Overvig, A. C., Lu, M., Stein, A. & Yu, N. Broadband achromatic dielectric metalenses. *Light: Science & Applications* **7**. ISSN: 2047-7538 (Nov. 2018).
300. Chen, W. T., Zhu, A. Y., Sisler, J., Bharwani, Z. & Capasso, F. A broadband achromatic polarization-insensitive metalens consisting of anisotropic nanostructures. *Nature Communications* **10**. ISSN: 2041-1723 (Jan. 2019).
301. Chen, W. T. *et al.* Broadband achromatic metasurface-refractive optics. *Nano Letters* **18**, 7801–7808. ISSN: 1530-6992 (Nov. 2018).
302. Shalaginov, M. Y. *et al.* Reconfigurable all-dielectric metalens with diffraction-limited performance. *Nature Communications* **12**. ISSN: 2041-1723 (Feb. 2021).
303. Ahmed, R. & Butt, H. Strain-multiplex metalens array for tunable focusing and imaging. *Advanced Science* **8**. ISSN: 2198-3844 (Jan. 2021).
304. Holsteen, A. L., Lin, D., Kauvar, I., Wetzstein, G. & Brongersma, M. L. A light-field metasurface for high-resolution single-particle tracking. *Nano Letters* **19**, 2267–2271. ISSN: 1530-6992 (Mar. 2019).
305. Lin, R. J. *et al.* Achromatic metalens array for full-colour light-field imaging. *Nature Nanotechnology* **14**, 227–231. ISSN: 1748-3395 (Jan. 2019).
306. Colburn, S. & Majumdar, A. Metasurface generation of paired accelerating and rotating optical beams for passive ranging and scene reconstruction. *ACS Photonics* **7**, 1529–1536. ISSN: 2330-4022 (May 2020).
307. Quirin, S. & Piestun, R. Depth estimation and image recovery using broadband, incoherent illumination with engineered point spread functions [Invited]. *Applied Optics* **52**, A367. ISSN: 2155-3165 (Dec. 2012).
308. Guo, Q. *et al.* Compact single-shot metalens depth sensors inspired by eyes of jumping spiders. *Proceedings of the National Academy of Sciences* **116**, 22959–22965. ISSN: 1091-6490 (Oct. 2019).
309. Berlich, R., Bräuer, A. & Stallinga, S. Single shot three-dimensional imaging using an engineered point spread function. *Optics Express* **24**, 5946. ISSN: 1094-4087 (Mar. 2016).
310. Zheng, G. *et al.* Metasurface holograms reaching 80% efficiency. *Nature Nanotechnology* **10**, 308–312. ISSN: 1748-3395 (Feb. 2015).
311. Huang, L. *et al.* Three-dimensional optical holography using a plasmonic metasurface. *Nature Communications* **4**. ISSN: 2041-1723 (Nov. 2013).
312. Li, J. *et al.* Addressable metasurfaces for dynamic holography and optical information encryption. *Science Advances* **4**. ISSN: 2375-2548 (June 2018).

313. Li, L. *et al.* Electromagnetic reprogrammable coding-metasurface holograms. *Nature Communications* **8**. ISSN: 2041-1723 (Aug. 2017).
314. Overvig, A. C. *et al.* Dielectric metasurfaces for complete and independent control of the optical amplitude and phase. *Light: Science & Applications* **8**. ISSN: 2047-7538 (Oct. 2019).
315. Castaldi, G. *et al.* Joint multi-frequency beam shaping and steering via space-time-coding digital metasurfaces. *Advanced Functional Materials* **31**. ISSN: 1616-3028 (Oct. 2020).
316. Sabri, R., Salary, M. M. & Mosallaei, H. Broadband continuous beam-steering with time-modulated metasurfaces in the near-infrared spectral regime. *APL Photonics* **6**, 086109. ISSN: 2378-0967 (Aug. 2021).
317. Salary, M. M., Jafar-Zanjani, S. & Mosallaei, H. Nonreciprocal optical links based on time-modulated nanoantenna arrays: Full-duplex communication. *Physical Review B* **99**, 045416. ISSN: 2469-9969 (Jan. 2019).
318. Minzioni, P. *et al.* Roadmap on all-optical processing. *Journal of Optics* **21**, 063001. ISSN: 2040-8986 (May 2019).
319. Abdollahramezani, S., Hemmatyar, O. & Adibi, A. Meta-optics for spatial optical analog computing. *Nanophotonics* **9**, 4075–4095. ISSN: 2192-8606 (Sept. 2020).
320. Kulce, O., Mengu, D., Rivenson, Y. & Ozcan, A. All-optical synthesis of an arbitrary linear transformation using diffractive surfaces. *Light: Science & Applications* **10**. ISSN: 2047-7538 (Sept. 2021).
321. Mohammadi Estakhri, N., Edwards, B. & Engheta, N. Inverse-designed metastructures that solve equations. *Science* **363**, 1333–1338. ISSN: 1095-9203 (Mar. 2019).
322. Silva, A. *et al.* Performing mathematical operations with metamaterials. *Science* **343**, 160–163. ISSN: 1095-9203 (Jan. 2014).
323. AbdollahRamezani, S., Arik, K., Khavasi, A. & Kavehvas, Z. Analog computing using graphene-based metalines. *Optics Letters* **40**, 5239. ISSN: 1539-4794 (Nov. 2015).
324. Cordaro, A. *et al.* High-index dielectric metasurfaces performing mathematical operations. *Nano Letters* **19**, 8418–8423. ISSN: 1530-6992 (Nov. 2019).
325. Zhu, T. *et al.* Generalized spatial differentiation from the spin Hall effect of light and its application in image processing of edge detection. *Physical Review Applied* **11**, 034043. ISSN: 2331-7019 (Mar. 2019).
326. Bykov, D. A. *et al.* First-order optical spatial differentiator based on a guided-mode resonant grating. *Optics Express* **26**, 10997. ISSN: 1094-4087 (Apr. 2018).

327. Zangeneh-Nejad, F., Khavasi, A. & Rejaei, B. Analog optical computing by half-wavelength slabs. *Optics Communications* **407**, 338–343. ISSN: 0030-4018 (Jan. 2018).
328. Youssefi, A., Zangeneh-Nejad, F., Abdollahramezani, S. & Khavasi, A. Analog computing by Brewster effect. *Optics Letters* **41**, 3467. ISSN: 1539-4794 (July 2016).
329. Zhu, T. *et al.* Plasmonic computing of spatial differentiation. *Nature Communications* **8**. ISSN: 2041-1723 (May 2017).
330. Liu, Y., Zhao, T., Ju, W. & Shi, S. Materials discovery and design using machine learning. *Journal of Materiomics* **3**, 159–177. ISSN: 2352-8478 (Sept. 2017).
331. Schmidt, J., Marques, M. R. G., Botti, S. & Marques, M. A. L. Recent advances and applications of machine learning in solid-state materials science. *npj Computational Materials* **5**. ISSN: 2057-3960 (Aug. 2019).
332. Cai, J., Chu, X., Xu, K., Li, H. & Wei, J. Machine learning-driven new material discovery. *Nanoscale Advances* **2**, 3115–3130. ISSN: 2516-0230 (2020).
333. Faraji-Dana, M. *et al.* Compact folded metasurface spectrometer. *Nature Communications* **9**. ISSN: 2041-1723 (Oct. 2018).
334. Xie, Y.-Y. *et al.* Metasurface-integrated vertical cavity surface-emitting lasers for programmable directional lasing emissions. *Nature Nanotechnology* **15**, 125–130. ISSN: 1748-3395 (Jan. 2020).
335. Wang, Q.-H. *et al.* On-chip generation of structured light based on metasurface optoelectronic integration. *Laser & Photonics Reviews* **15**. ISSN: 1863-8899 (Feb. 2021).
336. Qiu, C.-W., Zhang, T., Hu, G. & Kivshar, Y. Quo vadis, metasurfaces? *Nano Letters* **21**, 5461–5474. ISSN: 1530-6992 (June 2021).
337. Kort-Kamp, W. J. M., Azad, A. K. & Dalvit, D. A. R. Space-time quantum metasurfaces. *Physical Review Letters* **127**, 043603. ISSN: 1079-7114 (July 2021).
338. Deep, K., Singh, K. P., Kansal, M. & Mohan, C. A real coded genetic algorithm for solving integer and mixed integer optimization problems. *Applied Mathematics and Computation* **212**, 505–518. ISSN: 0096-3003 (June 2009).
339. *MTI Corporation, BaTiO3* <https://mtixtl.com/collections/batio3>.
340. Garrett, M. & Mnushkina, I. Techniques for top-seeded solution growth of BaTiO₃. *Journal of Crystal Growth* **166**, 550–557. ISSN: 0022-0248 (Sept. 1996).
341. Garrett, M. H., Chang, J. Y., Jenssen, H. P. & Warde, C. A method for poling barium titanate, BaTiO₃. *Ferroelectrics* **120**, 167–173. ISSN: 1563-5112 (Aug. 1991).

342. Bednyakov, P. S., Sluka, T., Tagantsev, A. K., Damjanovic, D. & Setter, N. Formation of charged ferroelectric domain walls with controlled periodicity. *Scientific Reports* **5**. ISSN: 2045-2322 (Oct. 2015).
343. Howell, J. A., Vaudin, M. D., Friedman, L. H. & Cook, R. F. Stress and strain mapping of micro-domain bundles in barium titanate using electron backscatter diffraction. *Journal of Materials Science* **52**, 12608–12623. ISSN: 1573-4803 (Aug. 2017).
344. Howell, J. A., Vaudin, M. D., Friedman, L. H. & Cook, R. F. Lamellar and bundled domain rotations in barium titanate. *Journal of Materials Science* **54**, 116–129. ISSN: 1573-4803 (Aug. 2018).
345. Bednyakov, P. S., Rafalovskyi, I. & Hlinka, J. Fragmented charged domain wall below the tetragonal-orthorhombic phase transition in BaTiO₃. *Applied Physics Letters* **126**. ISSN: 1077-3118 (Jan. 2025).

